UNIVERSITY OF STRATHCLYDE

Department of Electronic & Electrical Engineering

Centre for Ultrasonic Engineering

Bio-inspired Acoustic Sensors and Systems - From Biology to Engineering Exploiting Feedback Computation

José M. F. Guerreiro

(Thesis submitted in the fulfilment of the requirements for the degree of Doctor of Philosophy in Electronic & Electrical Engineering)

Supervisors:

Prof. James Windmill

Dr. Joseph Jackson

Examination committee:

Convenor:	Dr. Benjamin Tiller
External examiner:	Dr. William Whitmer
Internal examiner:	Dr. Charles MacLeod

November 2018

This thesis is the result of the author's original research. It has been composed by the author and has not been previously submitted for examination which has led to the award of a degree.

Signed:

Date:

Abstract

In order to design sensors and systems that can be sensitive to small signal levels even when immersed by background noise, may require out-of-the-box thinking. Biology can provide inspiration to achieve that, allowing the engineering landscape to borrow interesting ideas with the aim to solve current human problems. Biological sensor, system and signal processing designs are a result of many million years of evolutionary processes, which make them very-power efficient and well-adapted to perform their functions in a living organism. This thesis is an example of how acoustic engineering can look into biology in order to get inspiration to design novel ways for detecting, encoding and processing sound information. Sometimes the challenges behind innovation are on finding the proper tools to conceptualize and prototype novel ideas. Bio-inspired engineering offers a possible pathway for new technological advances using theoretical reasoning and appropriate physical modelling. Therefore, this body of work is a research study, which borrows ideas from biology and employs engineering techniques to prototype some new concepts of sensors, systems and signal processing. Moreover, it suggests an unconventional methodology in acoustic engineering, aiming to demonstrate that novel acoustic sensor system concepts can perform peripheral signal processing at the transducer level such like some natural sensory systems do. Here, from the engineering perspective, the aim is to delay as much as possible the digitalization task while exploiting analogue mechanical-electrical-feedback based computations, therefore, a smart acoustic sensory system concept can be created

targeting real-time signal processing applications.

Acknowledgements

At first, I would like to thank my supervisors Prof. James Windmill and Dr. Joseph Jackson for all the great and magnificent support throughout my Ph.D. research journey in Strathclyde University, Glasgow, Scotland, UK. Since the beginning (back to January 12, 2015), they have given positive feedback into my research questions and supplied always useful and meaningful discussions, directing my work in the best possible manner. I have got a great supervisor-student relationship, which allowed me to go in pursuit of my own research interests, and opportunities to engage and nourish from an international landscape and research community.

Moreover, I would give my words of gratitude to the Centre of Ultrasonic Engineering and Electronic & Electrical Engineering staff at University of Strathclyde for the excellent support and research facilities that supply a great research environment. Nevertheless, this research was funded by the European Research Council under the European Union's Seventh Framework Programme (FP/2007-2013) / ERC Grant Agreement n. [615030].

Foremost, I would like to thank my family namely my parents Maria and Manuel and my sister Marina for all the support and love that often make my life easier to manage, allowing to put my focus on desired academic goals. To my dear and lovely girlfriend Floriane, and my friends and mates for all the good moments and healthy relationships developed in the last few years abroad. You always provided significant emotional support and good synergies, feeding my

purpose for a healthy and well-balanced life-style.

Last but not least, I would like to devote my words of great gratitude to my godparents Gertrudes and José for their unconditional dedication and love during my childhood in Azinhaga do Ribatejo, Santarém, Portugal. Both contributed to the development of great and important pillars of discipline and generosity, balance and courage, to pursue a honest life. Rest peacefully.

Mòran taing dhuibh uile!

Muito obrigado!

Contents

List of Figures

List of Tables

Chapter 1

Introduction

1.1 Motivation

Advances in recent decades in acoustic sensors, systems and signal processing methodologies, have been mainly focused on digitally processing the acoustic information received by a microphone – therefore, known as digital audio systems. Conventionally, microphones are designed with a broad and static frequency response, aiming to cover the spectrum of frequencies related to the human auditory system (e.g., 20 – 20 kHz). Their designs are meant to be simple to address general purpose applications, which might not be as flexible or adaptable enough to deal with some signal requirements.

Generally, the basic audio signal processing framework approach follows a static feed-forward configuration, with the sound detected by the microphone being fed to the digital signal processor and then to a receiver, which can be a loudspeaker, headphones or any kind of output signal interface associated to a particular system application. The microphone is meant to perform the first stage of signal processing such as detecting and mechanically filtering the signal; the digital processor digitises it, enhances it - to suit a particular application, for instance by computing noise-reduction algorithms, including filtering, compress-

ing and amplifying the signals; and then converting the signals into the receiver's dynamic range such as sounds that can be perceivable by the human hearing system, at best.

In this current state, a fully-digital and static feed-forward signal processing approach may encounter some challenges to further improve some fundamental system requirements such as power consumption and processing latency in the main signal pathway (e.g., microphone → processor → receiver). Moreover, digital audio signal processing is incurred by analogue-digital and digital-analogue conversions, which consume energy, and the time latency that is spent on computation such as processing and streaming data between digital buffers. Therefore, there might be some potential for the creation of new paradigms on signal processing methodologies based on novel and bio-inspired sensory-system technologies.

1.2 Thesis Proposal and Novelty

The work described throughout this thesis aims to present a novel concept of signal processing framework in acoustic sensors and systems, where the detector, which can be considered any kind of sound detector or transducer at audio or ultrasonic range, or both, can be adaptable and therefore capable of computing input information. The novelty of this signal processing methodology relies on a recursive approach that is inspired by nature. For instance, some auditory systems can adapt the acoustic response of their front-end sensors through feedback mechanisms based on previous acoustic inputs, which help them to detect or predict signals of interest. Therefore, improving their ability to hear sounds masked by noise. In contrast with the feed-forward processing approach of man-made systems – Figure 1.1 (A), in nature there is evidence of feedback loops used for signal computation between the front-end acoustic detector and the back-end signal processors - Figure 1.1 (B).

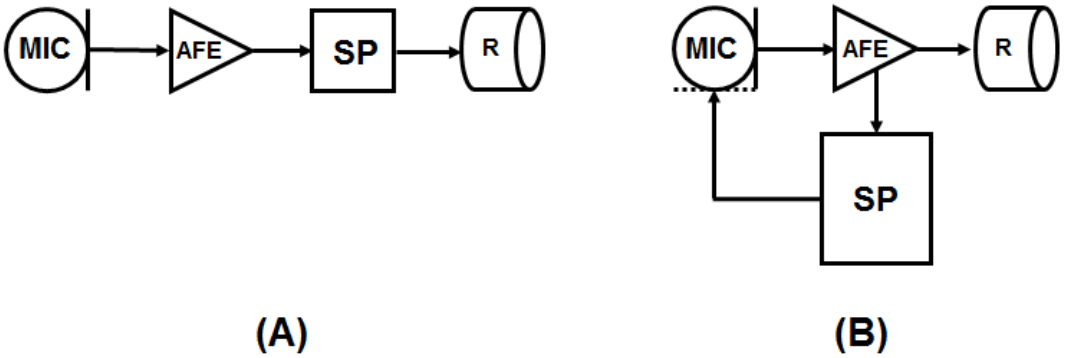

Figure 1.1: Sound processing framework approaches. (A) Standard feed-forward signal processing approach; (B) Bio-inspired based feedback signal processing approach. Where MIC represents the acoustic sensor such as a microphone, AFE is the analogue front-end circuits and systems used for the signal conditioning stage, SP represents any kind of signal processor either analogue, digital or both combined, and R represents any kind of system's output interface such as a loudspeaker.

The bio-inspired feedback processing approach that is illustrated in Figure 1.1 (B) is a concept where the transducer becomes part of the signal processing chain by exploiting feedback control processes (e.g., slow and fast mechanisms) between mechanical (e.g., microphone's diaphragm) and electrical systems (e.g., analogue, digital or both back-end processor types) that together can enhance peripheral signal processing, while changing the effective mechanical characteristics of the front-end sensor such as the spring constant and quality factor. The goal is to provide a new methodology for sound processing that may help to improve the performance of a signal processing task while keeping low-power consumption levels and reduced latencies on processing sensory signals as the following describes:

1. Adaptive analogue computation at the sensor level, which can potentially improve both, sound detection in noisy environments and output signals much faster than digital based computation as employed by conventional man-made feed-forward digital sound processing systems;

2. Reducing the amount of digital signal processing operations within the main signal path so that the overall power consumption spent on digital computation might be less demanding – balancing digital usage with further analogue computation when applied;

3. Decreasing the signal processing latency by reducing both the amount of data processing and data streaming exchanged between digital buffers – therefore, exploiting analogue computation in the main signal path, exclusively;

4. Moving the digital processing operations to the feedback signal path may allow the use of more sophisticated signal-detection and noise-reduction algorithms such as the ones based on statistical methods – trade-off with point (2).

Assuming a basic configuration, then the above-mentioned signal feedback computation methodology is intended to include at least two main functions:

- Frequency agile tuning: adapting the spring factor, hence the resonance frequency (ω_0) of the front-end detector (e.g., microphone or ultrasonic transducer). This function is intended to be based on a slow-feedback adaptation process, which feedbacks compatible signals to a custom-designed microphone (e.g., sound detector) based on previous n-cycles of the input sound signal. This is a modality that can be used, for instance, to tune the frequency response of the microphone(s) with a targeted sound(s), or to set a desired resonant response of the sensor upon fabrication;

- Active nonlinear amplification: adapting the Q-factor of the front-end sensor (e.g., microphone or ultrasonic transducer). This function is meant to be a fast-feedback adaptation process, which feedback compatible signals to a custom-designed microphone based on cycle-by-cycle computation of

previous inputs. This modality might be used, for instance, to compress and amplify acoustic signals at the transducer level.

Nevertheless, these two feedback computation modalities can either be supported by analogue systems, digital systems, or both without interfering with the main signal path, therefore they are meant to be compatible with critical and real-time signal processing applications.

1.3 Research Objectives

The aim of research was essentially to broadly understand how natural sensors and systems detect and process acoustic information, which allow living organisms to explore and being aware of the surrounded environment. Topics covered by this Ph.D. research study include:

- **Modelling acoustic sensors and systems inspired by nature:** firstly, it was fundamentally important to start the study from how natural sensors and systems transform sound into bio-electrical signals. Thereafter, that knowledge and understanding were translated into the engineering point of view. Concurrently, it was essential to outline some mathematical methods, which allowed the creation of theoretical models to evaluate sensory responses based on the bio-inspired acoustic sensors and systems studied;

- **Transduction and design methods:** conversion of acoustic/mechanical energy into a form of electrical information. Transducer design techniques were outlined and state-of-the-art models, materials, fabrication, and transduction methods that could be integrated in the creation of new physical prototypes based on biological acoustic sensors and systems designs were considered;

- **Signal processing:** nature has magnificent ways to process acoustic signals. For instance, frequency selectivity, and nonlinear amplification can be considered interesting functions to enhance signal-to-noise conditions in the ears of some animals. Certain elements were studied from the biological reports and used as inspiration to develop a new kind of signal processing framework based on slow and fast feedback computation processes;

- **Computational methods:** engineering tools can be used in multiple ways to approach identical problems. However, it is necessary to evaluate whether a system is efficient or not in order to optimize computational costs versus the amount of information processed, while executing a particular task. Therefore, some computational methods were studied with particular emphasis on methods inspired by nature that are considered by the literature as efficient to address some engineering problems as the work developed in this research thesis aims to aspire.

1.4 Contributions

The main contributions of this Ph.D. research thesis include the development of a novel theoretical model approach based on feedback control theory applied to acoustic sensors and systems, which was derived from the study and understanding of the biological counterparts. Additionally, there was creation of physical embedded system setups, including three new sensor designs and associated purpose-built circuits and systems that faithfully replicate some acoustic responses as similarly reported from biological studies. Overall, a smart acoustic sensor system concept is prototyped, which potentially allow sensor, circuit and system designers to address real-time sound processing applications in an unconventional way. During the realization of this thesis two IEEE journal articles were published and another one is in preparation, and three other IEEE confer-

ence papers were presented to three different international audiences and another one is correctly in review process to be potentially presented in another IEEE upcoming conference, among other abstract papers also presented, as follows:

1.4.1 Journal articles:

- J. Guerreiro, J. C. Jackson and J. F. C. Windmill, "Simple Ears Inspire Frequency Agility in an Engineered Acoustic Sensor System". IEEE Sensors Journal, 17(22): 7298 – 7305, 2017;

- J. Guerreiro, A. Reid, J. C. Jackson and J. F. C. Windmill, "Active Hearing Mechanisms Inspire Adaptive Amplification in an Acoustic Sensor System". IEEE Transactions on Biomedical Circuits and Systems Journal, 12(3): 655 - 664, June 2018;

- J. Guerreiro, A. Reid, J. C. Jackson and J. F. C. Windmill, "Frequency Agile Tuning and Nonlinear Compressive Amplification Embedded in a Hybrid Piezo-Capacitive MEMS Microphone". (In preparation, November 2018).

1.4.2 Conference papers:

- J. Guerreiro, J. C. Jackson and J. F. C. Windmill, "Bio-inspired Frequency Agile Acoustic System". Proceedings on IEEE Sensors Conference 2016, Orlando, Florida, USA;

- J. Guerreiro, A. Reid, J. C. Jackson and J. F. C. Windmill, "Bio-inspired Active Amplification in a MEMS Microphone using Feedback Computation", Proceedings on IEEE Biomedical Circuits and Systems Conference 2017, Turin, Italy;

- J. Guerreiro, A. Reid, J. C. Jackson and J. F. C. Windmill, "Towards the Development of a Frequency Agile MEMS Acoustic Sensor System".

Proceedings on IEEE Sensors Conference 2017, Glasgow, UK;

- J. Guerreiro, J. C. Jackson and J. F. C. Windmill, “Enhancing Acoustic Sensor Responsiveness Exploiting Bio-inspired Feedback Computation”. (Currently in review process, November 2018).

1.4.3 Conference abstracts:

- J. Guerreiro, A. Reid, J. C. Jackson and J. F. C. Windmill, “Bio-inspired Frequency-Adaptive Acoustic System”, Proceedings on Speech is Noise Workshop 2018, Glasgow, UK;

- J. Guerreiro, A. Reid, J. C. Jackson and J. F. C. Windmill, “Fully-Adaptive Embedded MEMS Acoustic Sensor System”, Proceedings on International Hearing Aid Research Conference 2018, Tahoe City, California, USA.

1.4.4 Awards:

- Best student paper award for the paper entitled: "Bio-Inspired Frequency Agile Acoustic System" at IEEE Sensors Conference 2016, Orlando, Florida, USA;

- 1^{st} position award at the IEEE International "Sensors and Measurements" student contest, presenting a live demo of the project entitled: "Multimodal Sensing System for Hearing Enhancement and Research", IEEE Sensors Conference 2017, Glasgow, Scotland, UK;

- Student scholarship travel award to sponsor the work presented: "Fully-Adaptive Embedded MEMS Acoustic Sensor System" at the International Hearing Aid Research Conference 2018, Tahoe City, California, USA.

1.5 Document Organization

The remainder of this document is organized as follows:

- **Chapter 2** outlines the background knowledge relating to fundamentals of acoustics, biological sensors, circuits and systems, as well as some state-of-the-art in engineering trends based on MEMS microphones technology;
- **Chapter 3** describes a novel bio-inspired frequency agile acoustic sensor system concept exploiting feedback computation (e.g., slow adaptation process);
- **Chapter 4** presents a bio-inspired active nonlinear amplification concept in acoustic sensors and systems based on cycle-by-cycle feedback computation (e.g., fast adaptation process);
- **Chapter 5** presents the experimental results of a novel embedded acoustic sensor system and signal processing framework, combining the concepts described in Chapter 3 and 4;
- **Chapter 6** describes the design and architecture of a new embedded acoustic sensor system, including a MEMS microphone and the analogue conditioning, driving and computational circuits and systems used to provide real-time results based on a novel bio-inspired audio signal processing framework;
- **Chapter 7** summarizes the main conclusions of this research work.

Chapter 2

Background Knowledge

Fundamentals of Acoustic Signals and Biological Sensors and Systems

Sound is produced by nature as a form of mechanical energy (i.e., acoustic information) that typically propagates through a medium (e.g. air, water, etc.). When available within the medium, acoustic information can be detected by means of an appropriate sensory apparatus. Sound perception or audition (hearing) is considered as one of the fundamental senses available in living organisms, humans included. Biological sensors and systems are masters of finely resolve specific sound signatures within a broad spectrum of acoustic information. The aim of this chapter is to describe some fundamental and background knowledge related to signals and sensory apparatus required to detect and process acoustic signals, focusing on biological sensors and systems. Additionally, it highlights the fact that acoustic engineering can take inspiration from nature in order to design novel and unconventional ways to detect and process sounds.

2.1 The Physics of Sound

Acoustic signals are produced by nature and they can be at different frequency ranges. For instance, infrasound signals are the ones composed of low-frequencies such as below 20 Hz (e.g., elephant's communication, earthquake sounds, etc.); audio signals are considered the ones compatible with the human hearing system, which are located at frequencies between 20 Hz and 20 kHz; and ultrasound signals are normally frequencies above 20 kHz up to hundreds of kHz (e.g., bat echolocation calls, dolphins communicating signals, etc.). Nevertheless, within engineered systems, ultrasonic frequencies can reach up to GHz range such as the ones used in acoustic microscopy applications [22].

There is broad literature related to acoustics, showing that sounds can be transmitted exploiting the physical properties of materials [23]. For instance, some matters can propagate sounds faster than others, namely water (c_0 = 1460 m/s @ 20^o C) and air (c_0 = 343 m/s @ 20^o C), respectively. Many studies support the fact that sound is a form of mechanical energy that can be propagated through some media such as gases, liquids or solids due to intrinsic particle interactions [24]. It means that in the absence of matter, sound cannot be propagated such as in outer space or vacuum. Fundamental principles of sound detection and transduction have been reported in several works in biology and also within engineering fields [25], [26]. Nevertheless, the physical principles used to retrieve acoustic information from the environment are phenomena widely evolved and resolved by biological acoustic sensors [27]. Many millions of years of biological evolution enabled the creation of the most energy-efficient and size-adapted acoustic detectors ever invented, which faithfully suit individual needs. Biological sensors and systems have been shaped by genetic replications and modifications throughout many generations in order to overcome the challenges imposed by the laws of physical acoustics. Therefore, biological acoustic sensors are well-adapted

to retrieve sounds from the environment such as very small mechanical vibrations, which resonate within someone's ears.

Part of the acoustic energy that is produced is lost through the process of signal transmission and reception. In other words, part of the signals generated by a sound source are attenuated due to intrinsic absorption imposed by the communication channel - the medium (e.g. air); and also reflected and lost when reaching the receptor. Sound intensity is decreased as a function of distance travelled mainly due to the relative air humidity, and it is also frequency and temperature dependent [28]. For instance, considering atmospheric air as the communication channel, thus acoustic energy can propagate as a longitudinal travelling wave containing two components such as sound pressure and sound particle velocity. Acoustic pressure appears due to the compression and rarefaction (expansion) of the air particle movements within the acoustic wave, whereas, sound particle velocity is related to the intrinsic fluctuation of particles back-and-forth that favours the propagation of sound, as illustrated in Figure 2.1. Nevertheless, it is important to note that at longer distances the pressure component of sound should be easier to detect than the particle velocity component, since they follow different attenuation tendencies in respect to distance ($\frac{1}{d}$ vs $\frac{1}{d^2}$, respectively, where d is the distance travelled by sound) [9], ignoring any obstacles that would obstruct the signal path and/or scatter the energy, which might interfere with the signal strength as well [29].

As mentioned before, some amount of acoustic energy is lost at the interface between different materials due to the mismatch of acoustic impedances [23]. This is a phenomenon well-known in acoustics while transferring energy between media with different material properties. As a result, only part of that acoustic energy generated by a transmitter can likely be retrieved by the receiver, since some of the energy is lost during the process of signal generation, propagation (absorbed by the medium, obstructed or scattered) and detection (reflected at the boundary

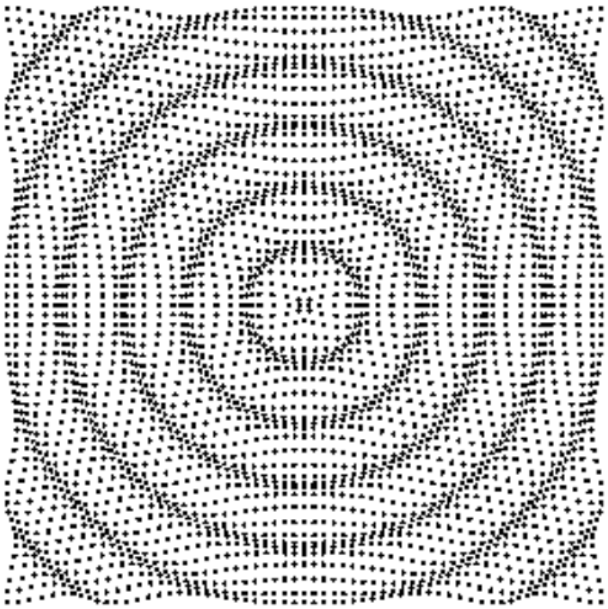

Figure 2.1: Longitudinal acoustic traveling waves, showing compression and expansion/rarefaction of particles in the medium (e.g., air). The signal source is located at the centre of the image. Image adapted from [1].

region of the receiver – acoustic impedance mismatching), consequently. Overall, these are some of the challenges imposed by the laws of physical acoustics on sound detection (i.e. sound is an analogue signal in nature). Therefore, it might be hypothesized that an acoustic receiver either biological or artificially-engineered should be well-evolved or designed to overcome the challenges imposed by the physics of sound, respectively. They should be able to translate very "weak" and "noisy" analogue signals into faithful information (e.g., bioelectrical or electrical signals, respectively), which can be interpreted by entities, either biological or artificial systems. Biological acoustic sensors and systems have evolved to be capable of retrieving either of the sound components, showing interesting sensing properties that maximize sound detection and consequent transduction. Some examples of biological acoustic sensors and systems are discussed in the following sections of this chapter, including sound pressure and sound particle velocity methods. Moreover, it is important to note that any acoustic signals

referred to further in the text are related to airborne sound signals within audio range (e.g., 20 Hz and 20 kHz), unless otherwise specified. Some examples of biological sensors, circuits and systems designs and associated mechanical, chemical and electrical responses are then presented, including details about sound detection, transduction and processing within human [30] and some insects' hearing systems [31].

2.2 Biological Acoustic Sensors, Circuits and Systems

This section outlines some of the background knowledge about biological acoustic sensors, circuits and systems as the foundations that inspired the work presented in this thesis. The main topic of discussion in this section is related to hearing systems in general, focusing on some interesting mechanisms exhibited by the human as well as the insects' auditory organs. Particular emphasis is made on the principles of sound transduction, signal conditioning and processing. Most interestingly, biology exploits the natural wiring of circuits and systems with multiple levels of feedback mechanisms in order to enhance several tasks of signal processing within the auditory pathway. Moreover, the process of sound conditioning includes the coupling of mechanical with electrical systems. That faithfully enables sensory adaptation such as tuning and active amplification achieved at the peripheral sensory level. These are fundamental topics exploited in this Ph.D. research study. A bio-inspired electromechanical feedback mechanism as a method to enable adaptive signal processing capabilities performed at the transducer level, and that can be implemented with engineered acoustic sensor and system techniques as further presented later in this thesis. The sense of hearing is accomplished through the use of highly evolved and complex mechanisms of sound detection, transduction and processing, which faithfully facilitate communication between animals,

humans included [32]. The ability to perceive acoustic signals is an important feature to survive and prosper [33]. There are several features composing acoustic information such as, sound intensity (or signal amplitude – energy; may quantify the distance between the receiver and transmitter), frequency (associated to the period of sound traveling through the medium; also it might give indication about specific features within the sound pattern, specie specific such as speech in humans, including the pitch of a sound signal) and directivity (the direction of sound propagation; may quantify the direction or location of the transmitter in respect to the receiver). In order to retrieve important acoustic information from the environment, biological acoustic sensors have evolved interesting properties to face the challenges imposed by the laws of physics [34].

It has been shown that some auditory systems may differ in the components of sound that they specialise to retrieve from the environment such as pressure or particle velocity component. However, they might use similar strategies in order to discriminate the intensity and frequency components of sound. In general, mechanical structures that are able to effectively couple acoustic energy are present at the front-end sensory apparatus. For instance, mechanosensory cells (hair cells (in vertebrates) and scolopidia (in invertebrates)) with ciliary elements - fluid-coupled systems that have robustness in the task of transducing mechanical energy into bio-electrical signalling as a result of stereocilia displacements. Nevertheless, sound perception is accomplished as a combination of passive, active, adaptive, electromechanical and chemical processes throughout multiple stages of signal transformation, including feedback and feed-forward computation across the chain of auditory pathway, as summarized as follows and as Figure 2.2 illustrates:

- **Signal detection an sound transduction:** acousto-mechanical energy is transformed into bio-electro-chemical signals;
- **Signal conditioning:** electromechanical amplification and filtering, en-

hance signals at the sensor periphery, pre-processing stage;

- **Signal encoding:** electrochemical filtering, signal encoding and compression of sensory input information;
- **High-level signal processing systems:** feature extraction and pattern recognition, regulate and adapt local parameters of the peripheral sensory system to enhance hearing responsiveness based on past sensory information processed.

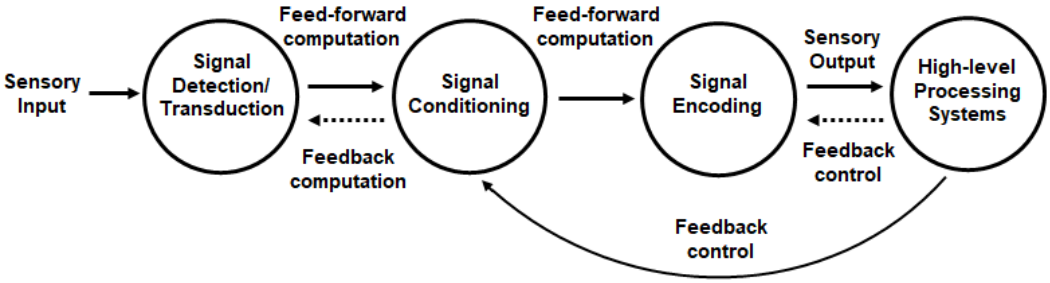

Figure 2.2: Simplified scheme of feed-forward and feedback mechanisms within a peripheral auditory signal processing chain.

2.2.1 The Human Hearing System

The human peripheral hearing system is composed of three different regions, as following described and illustrated in Figure 2.3:

1. **The outer ear:** pinna and auditory canal are responsible for receiving and conducting the acoustic energy to the middle ear, respectively;
2. **The middle ear:** tympanic membrane (also called as eardrum or tympanum) and the three ossicles (malleus, incus and stapes), which together perform an important levering mechanism, as illustrated in Figure 2.4 that effectively transfer energy from air-coupled sounds received by the eardrum

to the fluid-filled organ – the cochlea, also thought to work as an impedance matching mechanism;

3. **The inner ear or cochlea:** it is the end-point of the peripheral auditory system, which works as a transducer, exploiting the movement of fluids as mechanical energy (vibrations) that can be converted into equivalent electrical pulses compatible with the nervous system communication protocol.

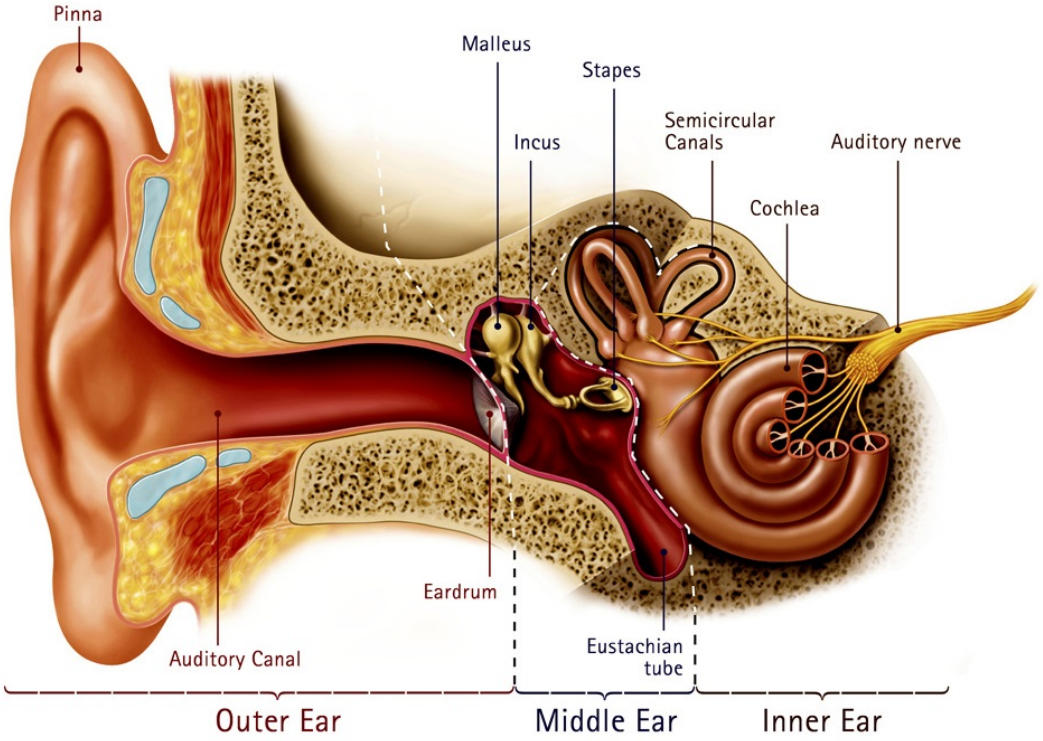

Figure 2.3: Anatomy of the human ear. © 2018 Frequency Therapeutics.

It is important to note that the function of the middle ear is very significant in order to maximize the energy transfer received by the tympanic membrane to the cochlea. That is thought to rely on two main mechanisms:

1. A scaling factor (≈17×, thus +25 dB gain) between the area of the tympanic membrane (≈50 mm^2) and the input of the cochlea - the oval window (≈3 mm^2);

2. A lever action performed by the three ossicles that can force (≈1.3×, thus +2 dB gain) the oval window to move. Together, both factors are thought to have an effect of increasing the overall pressure (+27 dB gain, overall) at the oval window compared to that on the tympanal membrane in order to compensate the impedance mismatch between airborne sounds and the fluids inside the cochlea (-30 dB loss) [35].

Therefore, received signals are then transferred into the cochlea structure with possibly minimum losses performed by this biological middle ear design, as illustrated in Figure 2.4.

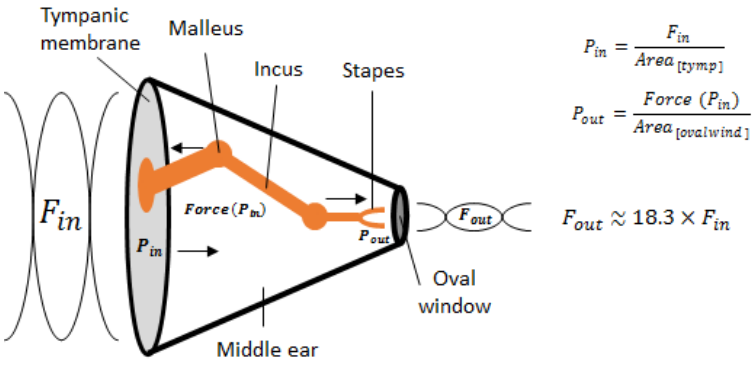

Figure 2.4: A simplified schematic of the human middle ear. Input sound waves (F_{in}) are received by the tympanic membrane, which exerts an input pressure (P_{in}) over the membrane. That pressure is then transformed by the levering action of the three ossicles into a force that pushes the oval window back-and-forth. Consequently, the output pressure (P_{out}) at the oval window is then injected into the cochlea as a travelling force (F_{out}) that is carried by the movement of fluids.

The shape of the cochlea looks like a shell of a snail. It is a bony structure that protects thousands of delicate hearing cells in its interior; in the centre (viewing through a cross-section image – Figure 2.5 northwest) are the three fluid-filled chambers – scalae separated by the Reissner's and basilar membranes. Figure 2.5 shows the organ of Corti, where the auditory receptor cells (e.g., mechanoreceptors) are located in between the basilar and the tectorial membranes. Every

turn-step of the cochlea sets out a different scale of frequency coding, as the following describes.

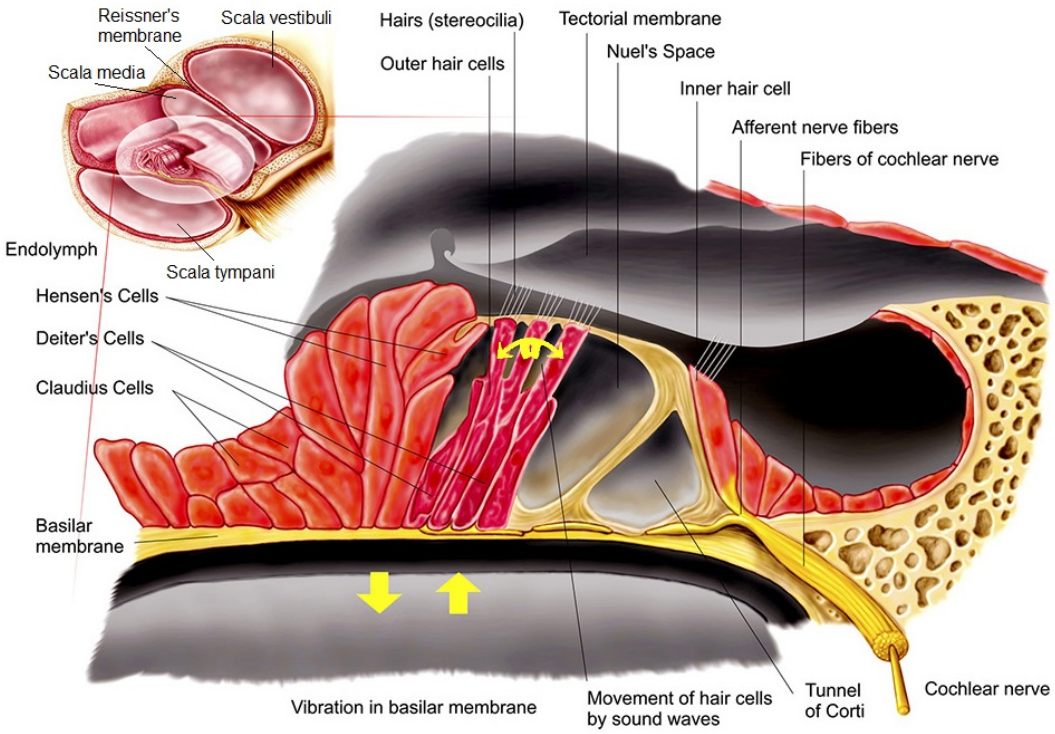

Figure 2.5: Zoom into the Organ of Corti highlighting a cross-section of the cochlea (northwest image showing the three scalae and the organ of Corti separated by the Reissner's membrane and the basilar membrane). Additional cells and structures (e.g., Hensen's, Deiter's and Claudius cells) that compose the auditory organ are also represented in this image, which are used by the hearing system to give support to sound transduction tasks. © 2018 Frequency Therapeutics.

The acoustic energy that is injected to the inner hear generates travelling waves that propagate from the base to the apex of the cochlea [36]. The peak of the induced travelling vibrations changes along with the basilar membrane size and stiffness. Therefore, the acoustic properties of the organ of Corti change according to the position in the cochlea. For instance, the basilar membrane is narrower and stiffer at the base and wider and less stiff as it goes towards the apex. Therefore, local resonant vibrations appear to represent a place code for

each independent sound frequency, as illustrated in Figure 2.6 A. In order words, there is a sort of frequency analysis represented at the basilar membrane level – low frequencies apically and higher frequencies basilary. Additionally, there is also a local time code inside the cochlea – higher frequencies make the membrane vibrate more quickly and lower frequencies more slowly. Consequently, that is reflected in the speed of charging of associated neuronal cells. Fundamentally, the basilar membrane and associated sensory neurons become somehow locally tuned at each specific frequency, and hence it might be seen as a system that mechanically filters the input sound signals, as illustrated in Figure 2.6 B, showing evidence of signal processing capabilities that are performed at the peripheral sensory system level, as follows.

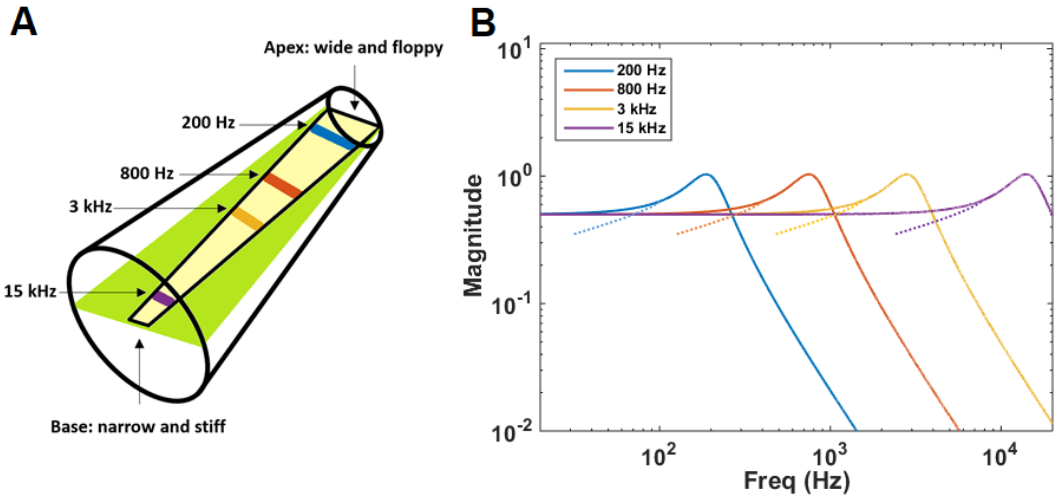

Figure 2.6: A simplified schematic of the uncoiled cochlea structure (e.g., its natural dimensions are about 32 mm long and 2 mm in diameter) showing the basilar membrane in the middle (e.g., light yellow colour) that exhibits a place code for each sound frequency according to its size and stiffness [2]. That exhibits a kind of bandpass response, accordingly (e.g., mechanical filtering) [3].

In the middle of the cochlea the auditory nerve (cochlear nerve) is found coming in (see Figure 2.3 and Figure 2.5). Basically, its function is to receive and send messages from the peripheral sensory system (cochlea) to the brain, and vice-versa. The neuronal system is capable of keeping track of both codes (e.g.,

local code and time code) induced by the sensory cells also known as hair cells.

Mechanoreceptor Cells

Hair cells are mechanosensory machines capable of sensing/actuating (with specificity, as explain later in the text) from/to the input vibrations coupled onto the basilar membrane. They transduce and conduct the received signals into the nerve fibers attached onto them. Nerve fibers are considered the highway of neuronal information to/from high-level neuronal networks in the auditory pathway. There are two types of hair cells in the cochlea, inner hair cells (IHC – around 3,500 cells/ear) and outer hair cells (OHC – around 14,000 cells/ear). Both have different roles in the process of auditory signal transduction. Nevertheless, they both have prominent stereocilia, also called microvilli, seated on top of their cuticular plate that enable the mechanically-induced transduction action [37]. Furthermore, the stereocilia on a single hair cell (in both IHC and OHC), are linked together at the top of each other (tip-links - proteins) forming a bundle that is called as hair bundle. In humans, there are about 40 stereocilia elements, in a bundle, for a given IHC, and about 140 for a single OHC [37]. Each bundle tends to move together in a pivoting way in response to sound. That is thought to be the triggering action, activating the mechanically-gated ion channels (e.g. potassium K^+) within the stereocilia. Every time a bundle moves in response to sound, it opens up ion channels located at the top of each stereocilia, enabling K^+ influx to the hair cell. These are called as the transduction channels, which convert mechanical displacements of stereocilia into reciprocal electrical charge signalling. That happens because the influx of K^+ caused by stereocilia movements tends to positively charge the cell, and therefore evokes receptor potentials, which are voltage-dependent conductances (e.g. voltage-gated calcium Ca^{2+} channels) in the basolateral membrane of the hair cells. Consequently, more Ca^{2+} channels are open leading to the increase of neurotransmitter synthe-

sis of the synaptic vesicles at the bottom-end of each hair cell [4]. Excitatory neurotransmitter (e.g., L-Glutamate) is then released as the input information received by afferent neurons (via postsynaptic neurite of spiral ganglion neurons) [4], as illustrated in Figure 2.7. These dynamics are normally called the "passive" responses exhibited by the interactions between the basilar membrane (from mechanical stimuli), mechanoreceptors (from mechanical to electrical to chemical) and afferent neurons (from chemical to electrical).

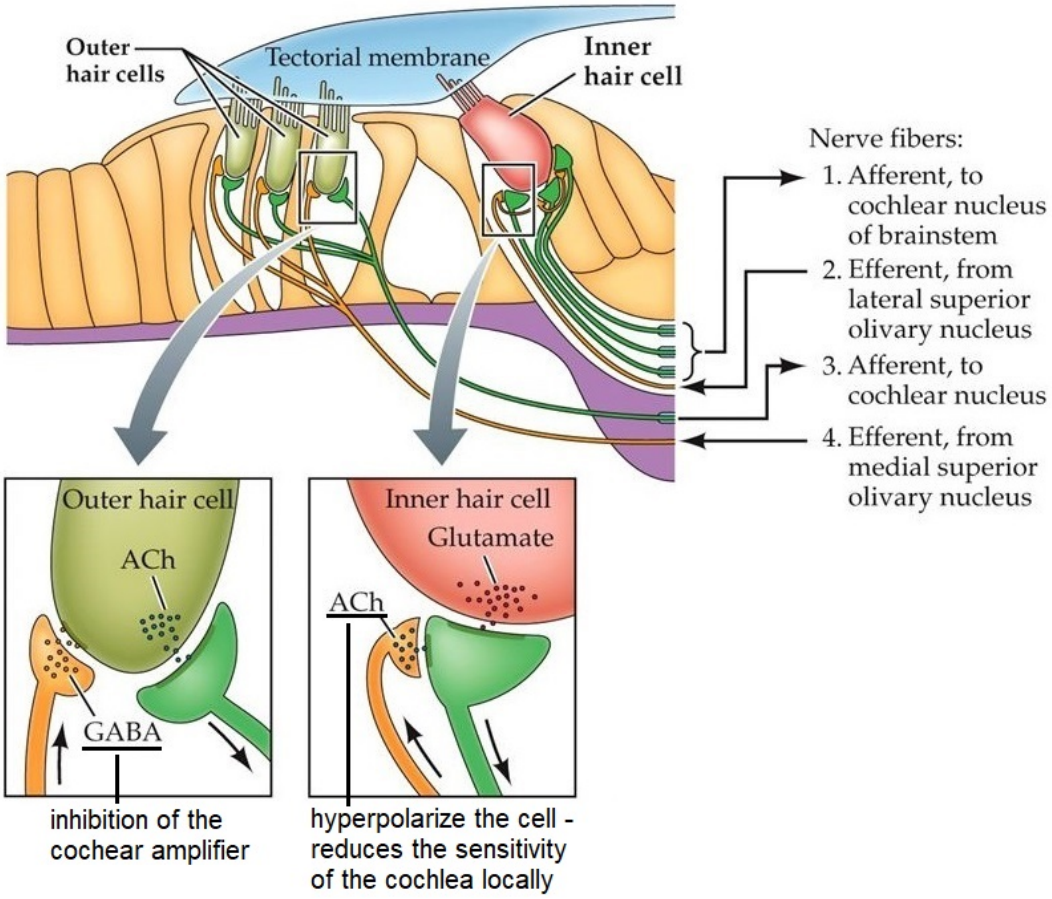

Figure 2.7: Auditory nerve fibers and synapses in the organ of Corti, showing the release of neurotransmitters - e.g., excitatory such as Glutamate or Acetylcholine (ACh) and inhibitory such as gama-Aminobutyric acid (GABA) from/to hair cells to/from the nerve fibers (via afferent and efferent, respectively) as a function of regulation of the peripheral sensory transduction and encoding of signals. Image adapted from [4]. © 2013 Sinauer Associates, Inc.

When the level of excitatory neurotransmitters present at the synaptic interface between hair cells and afferent nerve fibers is raised, the process of neuronal depolarization of the afferents starts until the point that action potentials are fired, and then conducted to the cochlear nucleus (CN). This is the mechanism used by the auditory system to encode sound in a form of electrical pulses. Typically, these are the signals used for communication between neurons that are compatible with overall brain network communication protocol. This process also works in the opposite direction, high-level neuronal networks in the auditory pathway can often send regulatory and control signals out to the peripheral organ, conducted by efferent nerve fibers that innervate both mechanoreceptor cells (IHCs and OHCs). Additionally, some other efferent regulatory signals are sent to the middle ear muscles in order to enable *attenuation reflexes*. These actions are conducted by the small muscles attached to the ossicles, which then control the acoustic conductivity (transmission of acoustic energy) of the middle ear (e.g., stiffening effect) [38]. Both mechanisms are thought to provide peripheral sensory adaptation, and therefore to further enhance signal processing capabilities at early stages (e.g., example of slow feedback adaptation processes). For instance, in order to enable speech understanding in noisy environments [39], and also as a mechanism of protection against very loud sounds/vibrations that otherwise would saturate the inner hearing system or in the worst case damage it [40].

OHCs are motile, which means that they can move and alter their dimensions such as, stretching or shortening. They have piezoelectric-like properties, which allow them to change their size according to the ionic gradients across their cell membrane or if stimulated electrically [37]. As emphasized before, every time that acoustic energy is fed into the cochlea it is propagated throughout the movement of fluids as a travelling wave. This travelling energy can make the hair bundles to move and so, activating the transducer channels, which consequently alters the cell's voltage potential. The OHCs shorten when depolarised, however, when the

sound phase reverses, the hair bundle moves in the opposite direction, and so the ion channels deactivate, which make the cells return back to their normal length. These back-and-forth movements (e.g., stretching and shortening of the cell) are likely to provide additional mechanical energy to the system. Nevertheless, this process relies on a motor protein, called *Prestin*, which is present in the lateral membrane of OHCs. It may be hypothesized that if adding more energy to the system it might result in an amplified output response. If that is true, additional force is injected into the system, which then triggers more bending of the stereocilia. More depolarization of the hair cells occurs and even more electro-motility happens in a sort of a locally-tuned positive feedback loop mechanism inside the cochlea [41] (e.g., example of a fast feedback adaptation process). That may be a good reason to call the OHCs the cochlea amplifiers, which can provide gains of 40 – 60 dB when preserved in a healthy condition [41]. Moreover, since OHCs are motile due to the presence of the protein *Prestin*, it means that they would move even when there is no sound coming into the auditory organ, as such they can self-generate signals, also called otoacoustic emissions [42]. Normally, these sounds are self-produced by the cochlea due to the electro-motility of the OHCs, which radiate externally from a healthy hearing system enabling recordings that can be interpreted by medical examinations to test some hearing conditions [42]. These dynamics are normally known as the "active" responses exhibited by the interactions between the efferent neurons, OHCs and basilar membrane.

IHCs are not motile (e.g., no evidence of the motor protein *Prestin* in their cell membrane), suggesting that they might not contribute to the amplifying capabilities inside the cochlea. However, they have stretching sensitive cells (stereocilia) used as the mechanical transducers that allow external mechanical stimulus to be converted into reciprocal bioelectrical-biochemical signals. Similarly to OHCs, alternating displacements inside the cochlea can cause consequent cycles of increase and decrease forces of the stereocilia. On the one hand, positive cycles induce

the ion channels to open (mainly K^+), which depolarise the cells by increasing their voltage potential. On the other hand, negative cycles induce the channels to close. This process seems like an on-off mechanism with a consequent capacitive charging effect. In general, the cellular membrane of the mechanoreceptor cells is thought to behave like a small leaky capacitor with equivalent capacitance (C) and resistance (R), which charges every time strain increases and discharges when it decreases [5]. This might resemble the response of a RC circuit system (with limited bandwidth such as low-pass response) imposed by the cell membrane characteristics. It means that when the frequency of the input stimuli increases more than the cut-off frequency of that RC filter, say a few kHz, the hair cells are not able to cope entirely with the phase of the input signal. As said before, that is the charging time ($\tau = R.C$) associated to the transduction process imposed by the cell membrane characteristics. It is thought that at low frequencies (e.g., below 1 kHz) the hair cells operate in AC mode, at high frequencies (e.g. above 3 kHz) they operate in DC mode, whereas at middle frequencies between 1 and 3 kHz they operate using both AC and DC modes at the same time, as illustrated in Figure 2.8.

It should be further emphasized that electrical signalling is a fundamental property that underlies many aspects of signal transduction, processing and communication between mechanoreceptors and neuronal cells in general. Biological cells consume energy in order to establish a potential gradient between intracellular and extracellular fluids. In general, neuronal cells have evolved passive and active mechanisms to exploit the electrochemical potential.

Auditory Neurons

There are two types of nerve fibers in the auditory nerve, innervating both IHCs and OHCs [37]:

- **Type I:** 95% of the neurons, bipolar and myelinated), which are normally

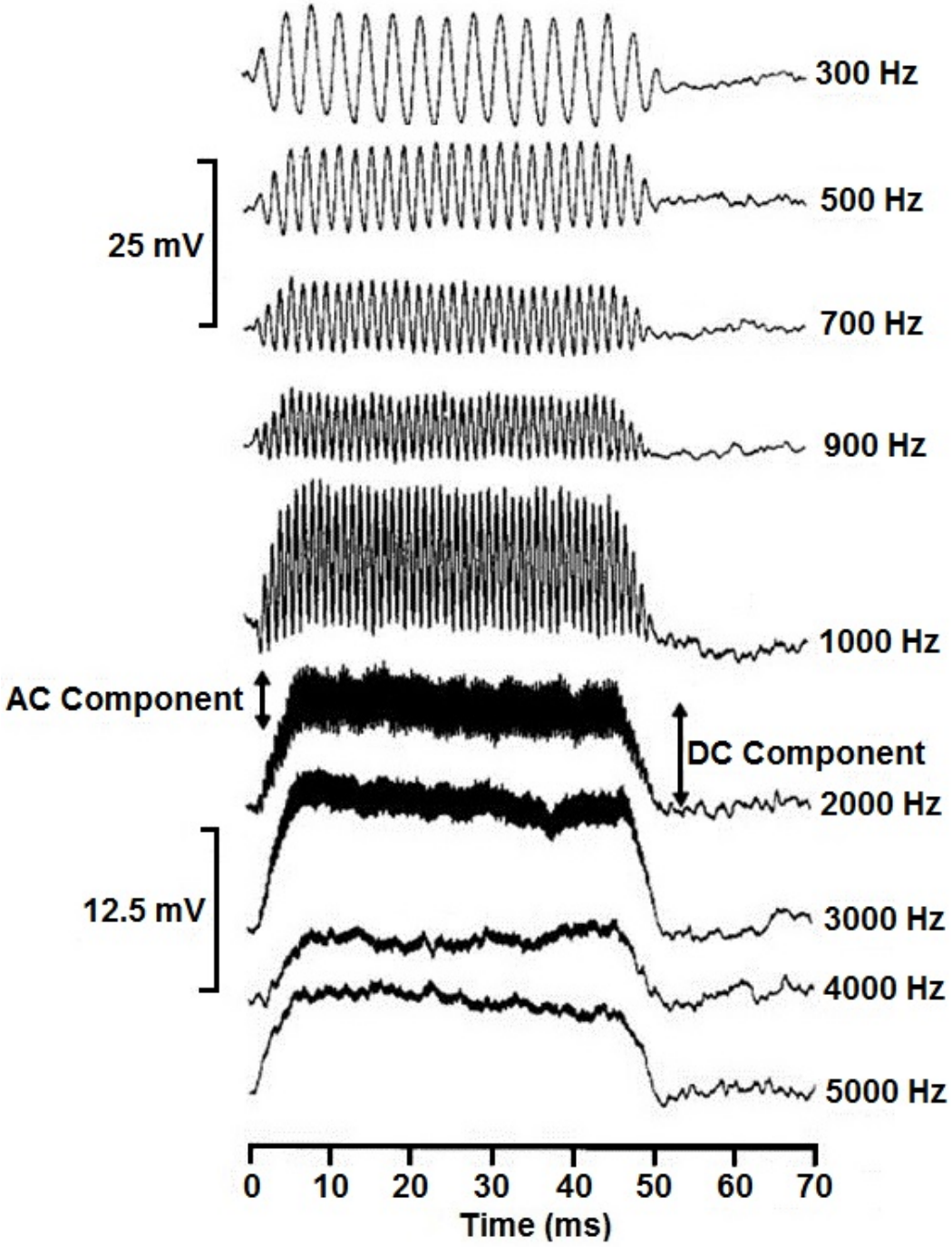

Figure 2.8: Receptor voltage potentials for different frequencies of stimuli. Image redrawn and adapted from [5].

attached to a single IHCs, but each IHC can have several of these fast type I nerve fibers connected to them (e.g., up to 30). Type I neurons are normally called afferent nerve fibers, which generally send information from the cochlea to the auditory pathway (e.g., CN);

- **Type II:** 5% of the cochlear neurons, unipolar and unmyelinated) are generally attached to OHCs (e.g., up to 3). These are normally called efferent nerve fibers (medial olivocochlear efferents), which mainly downstream information from the auditory pathway (e.g., superior olivary complex) to the cochlea, sending control signals [43] – e.g., control of cochlear gain [44].

The number of nerve fibers of both types I and II, which can be found innervating the cochlea, differs in quantity depending on their location inside the auditory organ. However, there are on average 30,000 fibers within the human cochlear nerve.

The postsynaptic afferent neurons can also be charged via ionic influx and efflux of molecules (e.g., sodium Na^+, potassium K^+, chloride Cl^- and calcium Ca^{2+}) across their cell membrane, according to the amount of excitatory neurotransmitter received from the hair cells or from synaptic contacts with efferents as illustrated previously in Figure 2.7. When the neuroreceptors in the afferent neurons detect the presence of higher levels of neurotransmitters in their synaptic clefts, they initiate protein synthesis, which activates the ion channels at their cell membrane. That follows a similar ionic exchange mechanism as previously described at the depolarization process in the hair cells. Again, different concentrations of ions establish different potential gradients between the inside and outside of the neuron. Generally, at the equilibrium state, also called resting potential, the inner side of the cell is more negative compared to the outside, which may vary between -40 mV and -90 mV [37]. As said before, auditory neurons are then able to be stimulated chemically through their synaptic connections with the hair cells. The presence of neurotransmitter stimulations may alter the ionic

gradients across the cell membrane and therefore, a neuron can hyperpolarize or depolarize. Hyperpolarization occurs when the cell potential becomes more negative than its resting potential. Depolarization is the opposite response, occurring when the cell increases its voltage potential. These dynamics are normally called the "passive" responses happening at the cellular level. However, when strongly stimulated (e.g., depolarized), neurons can also become "active" generators of electrical signals, so called action potentials, as illustrated in Figure 2.9.

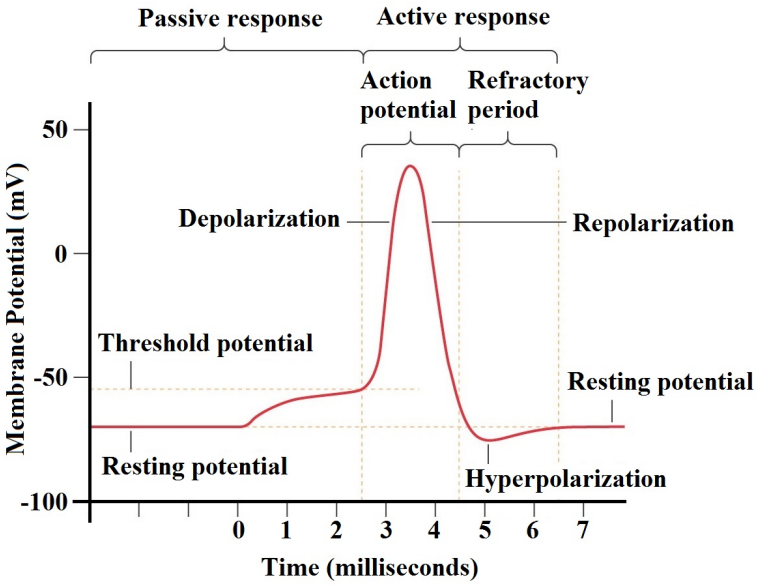

Figure 2.9: Example of an action potential from a neuron that looks like a spike type signal or an electrical pulse. Image adapted and redrawn from [6].

These are spike-type signals that occur every time the cell potential reaches a certain voltage threshold. After crossing this threshold, a cascade of electrochemical dynamics occurs, resulting in a sudden increase of the cell's potential level, followed by its cellular machinery counteracting that by imposing an automatic control mechanism to discharge (i.e., repolarize) and reset the cell, towards its equilibrium state (e.g., resting potential). A neuron can spontaneously generate electrical pulses, or action potentials, as often as input stimuli are presented to it, such as a neurotransmitter released from other sensory cells (or also via

electrical stimulation). However, a neuron normally requires a refractory period. That is the time spent by the cell machinery to recover after firing an action potential. Recalibration of the ionic equilibrium is required until the neuron is able to fire again. The action potential is induced by depolarization of the cell, and is sometimes a spontaneous event in which the duration can vary based upon many factors differing between cell type and function. Typically, firing rates are within the millisecond range in sensory neurons [37]. A typical neuron is thought to be subdivided in five different sections or zones as the following outlines and as illustrated in Figure 2.10:

1. **Dendrites:** that are generally protoplasmic extensions of the cell body, which provide the majority of the electrochemical inputs to the neuron from receptor cells or other neuronal cells;

2. **Soma or cell body:** it is where the majority of the electrochemical synthesis occur - the cell nucleus is located here;

3. **Trigger zone:** cellular region where the electrical responses (e.g., action potentials) are initiated/triggered;

4. **Axons:** which are thin and long neuronal branches that extend the cell body. Axons are usually used as communication channels to carry electrical signals between different nerve cells;

5. **Axon terminals:** provide the synaptic contacts with adjacent neuronal cells to deliver information.

Nevertheless, synaptic connections between neuronal cells can either be excitatory or inhibitory, depending on their type and function. Moreover, the type of synaptic contacts can either be chemical (e.g., neurotransmitter based) or electrical. However, in the inner hear the synaptic connections between mechanore-

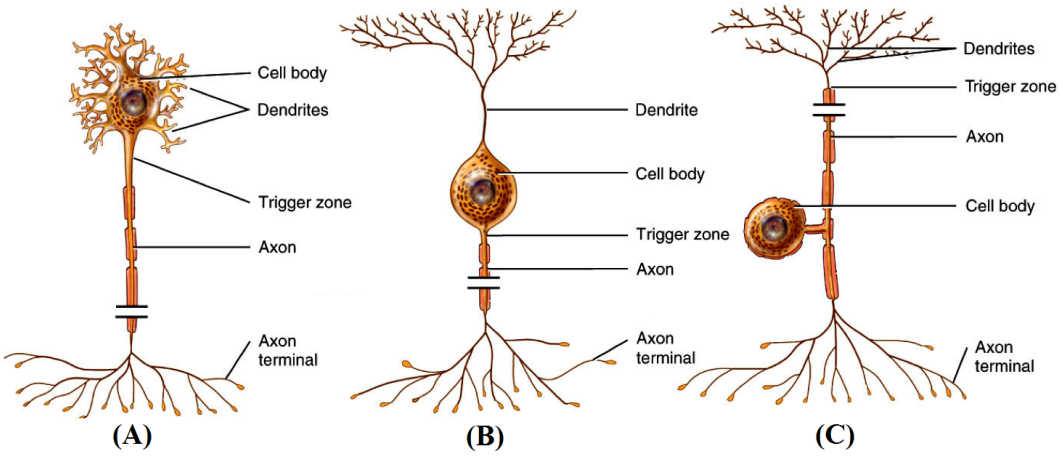

Figure 2.10: Examples of a neuronal cells. (A) Multipolar neuron; (B) Bipolar neuron; (C) Unipolar neuron. Image adapted from [7]. © 2013 John Wiley & Sons, Inc.

ceptors (hair cells) and the afferents or efferent neurons are typically chemical synapses [37].

Different types of neurons might show different spiking patterns or may change their firing rates proportionally to the intensity of the stimuli provided to the cell body. For instance, sensory neurons, such as the ones innervating the hair cells in the cochlea, encode sounds into a specific neuronal firing pattern. It should be clear that hair cells do not fire action potentials themselves, but instead do synthetize glutamatergic agents, which are then released through synaptic contacts with spiral ganglion nerve fibers (e.g., afferent nerve fibers that are normally attached to the bottom-end of each hair cell) that form the auditory nerve. This is called as the VIIIth cranial nerve, which transports synthetized action potentials to the CN.

It is thought that peripheral auditory system has developed three interesting strategies to encode sound [25]:

1. A place code that is associated to the fact that each frequency component of the input sound has a specific place of enhanced vibration at the basilar membrane level (e.g., tonotopy). Moreover, it is said that each incoming

sound has a characteristic frequency (CF), which is related to the tonotopic organization of mechanoreceptors and associated neuronal cells firings;

2. A frequency code, also known as temporal code, which relates the ability of the primary auditory neurons to fire action potentials according to the timing or phase of the input waveform (also known as the phase-locking principle);

3. A volley code, which is described in the literature as the ability of the hearing system to combine the firing responses of multiple neurons in order to be able to perceive sounds with frequencies greater than the firing rates of each individual neuronal cells (e.g., bandwidth limitation). The volley principle get use of the frequency code as illustrated in Figure 2.11.

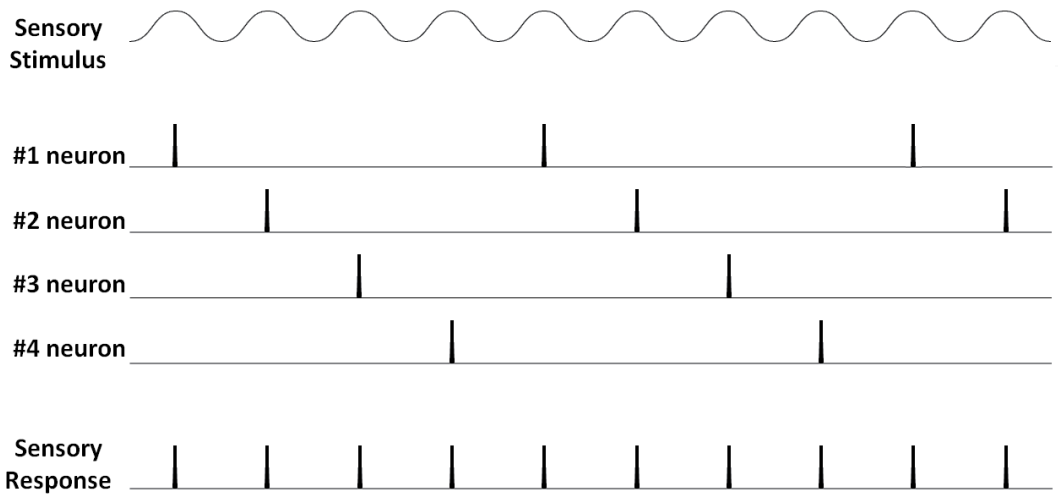

Figure 2.11: Example of the volley principle shown by a group of 4 auditory neurons that fire in-phase with the input stimulus waveform, which then result in a combined pulse train response of the sensory system with equivalent frequency as presented by the input signal. Image adapted and redrawn from [8].

When the input sound frequency is much greater (e.g., above 5 kHz) than the firing rates of afferent neurons, only intensity information is able to be encoded,

because temporal acuity of signals can no longer be kept by the afferent auditory neurons bandwidth. Therefore, auditory signals are only represented by the tonotopic mapping [25].

Concurrently, some other studies agree with the fact that it might be advantageous, in terms of the total cost of computation, to distribute the task of computing or communicating large amount of sensory information by using parallel processing systems and many sensors with reduced bandwidth, as from the research of Carver Mead in neuromorphic electronic systems [45] and also by Rahul Sarpeshkar [46] based on biological circuits and systems, and also relating to Shannon's information theory [47], respectively. This parallel processing approach is clearly exploited by natural sensory systems as it has been described previously. Moreover, biology has evolved many other ways to optimise the cost of computation versus communication and information to process. For instance, signals in the brain that are exchanged between neuronal cells are noisy and stochastic. However, natural wiring make each neuron capable of communicating with several other neurons at low speed, therefore the cost of computation can be cheap, such that might be more efficient to compute noisy signals while having collective interactions (e.g., longer delays on averaging and feedback systems to dynamically update local system's variable states) between lots of computational machines rather than to make every device very precise and fast, or simply following a feed-forward system architecture. Therefore, it would be more expensive to maintain in terms of its power consumption, since that is greatly dependent on system's speed and precision [48].

In biological systems different levels of feedback can be found, as well as parallel feed-forward neuronal circuits and systems in the brain [37], both part of the so-called bottom-up and top-down auditory signal processing pathways. For instance, considering bottom-up mechanisms the CN is considered the first auditory relay station for the signals coming from the auditory organ [25]. As

said before, each afferent nerve fiber is a dedicated channel (neuronal cable) that carries information from each mechanoreceptor cell (e.g., IHC). All that parallel information, from multiple nerve fibers, is then merged into the CN for further signal processing. Interneurons in the CN have synaptic connections with the primary nerve fibers in order to integrate (e.g., average) the incoming information [4], which then forward the signals to other auditory operations such as coincidence detection [49]. Averaging is a fundamental process performed by neuronal cells in general, thought to be a filtering mechanism of background noises between neuronal circuits and systems communications [50].

In contrast, top-down auditory processing relies on prior knowledge (e.g., memory) of previous sound events and their footprint and acoustic signatures, and therefore, predictive neuronal signalling is sent downwards from higher-level neuronal networks to the peripheral sensory system, which may help to further enhance hearing capabilities such as sound perception in noisy environments or tuning to a speaker within the presence of competitive signals (e.g., cocktail party effect) [51]. Nevertheless, attention and efferent neural health are rich fields of hearing research.

2.2.2 The Moth Auditory System

It has been mentioned previously that natural hearing is a result of intertwined interactions between mechanical, bioelectrical and chemical processes inside the auditory system [52]. Focusing on the feedback coupling between mechanical and electrical mechanisms that have evolved to enhance signal transduction and subsequent processing capabilities. Another good example of that has been reported in research involving insect's ears [53]. Due to their relatively reduced complexity, insect's ears have been used as a model for hearing research in the last decades [54], [55], for instance, moths that have a tympanum-like ear [10]. Generally, moths have two tympanic membranes, one on each side of the body to allow

some directional hearing information. A tympanum acts like a pressure sensor for sound detection [9]. Moths are thought to present one of the simplest, morphologically speaking, ears found in nature [56]. Maybe because of the reduced number of mechanoreceptors (e.g., 1–4 sensory neuron(s), depending on specie) that are available for signal transduction, which directly attach to the back-side of the tympanic membrane, as illustrated in schematic example of Figure 2.12 (Left).

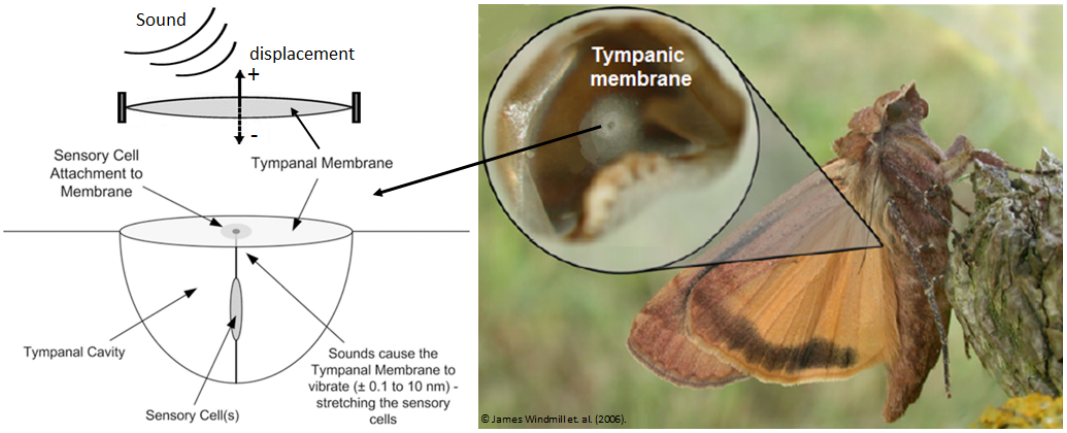

Figure 2.12: The morphology of the moth *Noctua pronuba* auditory system includes a tympanal/tympanic membrane and a cavity that houses an ensemble of 1–4 sensory neuron(s). (Left) a simplified schematic of the moth's ear morphology [9]; (Right) a moth *Noctua pronuba* and a microscopic picture of one of its ears (inset) [10].

In contrast with the human peripheral auditory system, which is subdivided in three well-defined parts such as outer ear, middle ear and inner ear, rather in this case: "moths have simply the outer ear directly connected to the inner ear". It means that the mechanosensory neuron(s) attach directly onto the back-side of the tympanal membrane [9]. This ear layout can be seen as simple as an air-coupled resonant membrane exposed to the outside environment and that is typically located under the wing body parts (also specie dependent). However, this sensory simplicity comes with a cost - generally moths cannot finely discriminate between different frequencies as their auditory system is not designed

as the human is (e.g., cochlea function) with a place code for each independent frequency component of sound. Instead, their hearing system is able to capture signals within a higher bandwidth but has a limited frequency resolution, showing greater sensitivity at certain ultrasonic frequencies that can range from 20-60 kHz. Moreover, a particular moth specie – the greater wax moth, *Galleria mellonella* is capable of hearing sounds within a wider spectrum of frequencies, from 10 kHz up to 300 kHz, but still show greater sensitivities around 60 kHz [56]. Conceptually, these ears have evolved to be more tuned to the ultrasonic signals from bats (echolocation calls) while in predatory actions. Moreover, in some *Noctuid* moths (refer to Figure 2.12 (Right)), their ears may show active tuning capabilities with hysteretic responses [10]. These moths are able to dynamically adapt their tympanal responses to track the spectral changes within the signalling of bat echolocation calls. For instance, for quiet sounds, the *Noctuid* moth ears show higher sensitivity at low frequencies, however, when exposed to loud ultrasonic signals (e.g., imminent attack from a close-by bat), they appear to have their natural mechanical tuning shifting towards higher frequencies, as illustrated in Figure 2.13. This phenomenon might be seen as a strategic mechanism of defence used to trigger behaviour (e.g., avoidance) to counteract against a bat's fatal catch.

These *simple-passive* tympanic membranes may become *smart-active* through the presence of a feedback mechanism involving back-end neuronal processing that dynamically actuates directly onto the front-end acoustic detector (tympanal membrane), as the possible example illustrated in Figure 2.14. Therefore, the natural resonance properties of that system can be altered. It is important to note that it is not completely clear yet how the *Noctuid* moth hearing system tunes up [10]. However, it might be hypothesized the following:

- Either during the charging process of mechanoreceptor cells may become stiffer (e.g., shortening) pulling somehow on the tympanic membrane – thus,

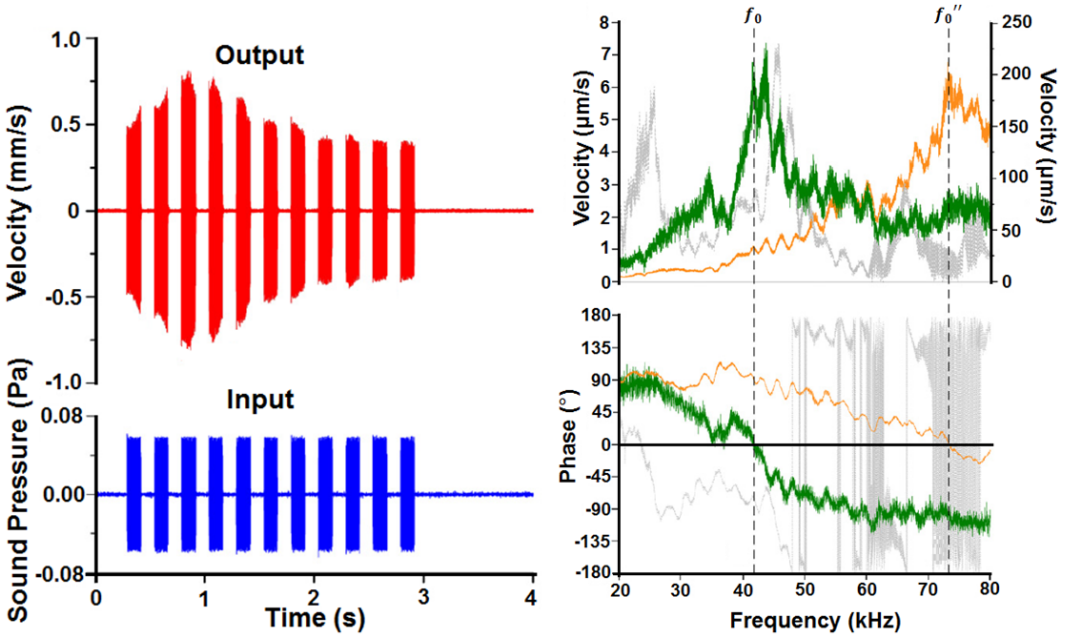

Figure 2.13: Tympanal membrane tuning response in the moth *Noctua pronuba*; (Left) mechanical response measured using laser Doppler vibrometer techniques (red trace) of the tympanic membrane to a bat-like incoming ultrasonic signal (blue trace); (Right) frequency response of the tympanic membrane for low intensity stimuli (green trace), showing tuning at f_0 and for high-intensity stimuli (orange trace), showing tuning at f_0''. Redrawn and adapted with kind permission from [10].

once pulled the tympanic membrane might stretch and so its mechanical structure and frequency response is altered;

- Or it might be due to feedback processing using efferent neurons controlling muscles attached to the tympanic membrane that play the role of acting on the supporting/edging structure instead (e.g., stretching), and therefore affecting the signal transmission as the possibly basis for this *peripheral sensory reflex*.

This particular example of sensory feedback adaptation seems to be considered as a slow-adaptation process. Since there might be a constant time associated to the feedback computation to settle and that would influence the transient time

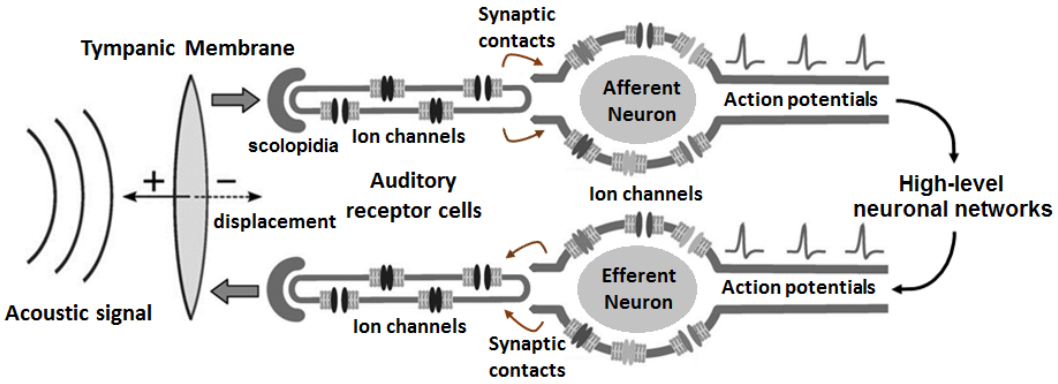

Figure 2.14: Example of a tympanic-like auditory system (e.g., moth) showing transmission (mechanical front-end) and transduction of acoustic signals into electrical pulses, which are then processed and fed back by high-level neuronal networks (back-end signal processing) to enhance peripheral conditioning and signal processing capabilities such as active tuning. Redrawn and adapted from [11].

of the sensory system response overall. This adaptive tuning response seems to be delayed (e.g., lagging) when compared with the period of the input signal waveform, also showing hysteresis within a few seconds range [10]. It means that signals are computed over time (e.g., integration of signals using previous n-cycles of the input waveform), before feedback actuation onto the tympanal structure (e.g., front-end acoustic detector). The possible dynamics of this electromechanical sensory system are approximated to the ones of a mass-spring system (e.g., passive resonator) such as a driven damped harmonic oscillator while the active processes, which vary the system's resonance frequency can be modelled as adapting the equivalent stiffness (e.g., spring constant of the structure) according to the input force applied to the system [10], [57], as illustrated in Figure 2.15.

Overall, a feedback mechanism acting over the tympanic membrane in the *Noctuid* moth ears is possibly the method used by this adaptive acoustic sensor system to achieve its frequency agile tuning response.

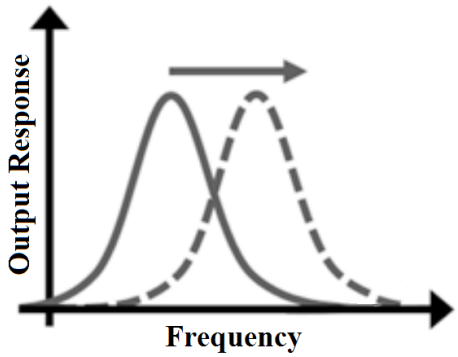

Figure 2.15: Changes in the equivalent stiffness of a mechanical system can alter its resonance frequency, also referred as frequency agile tuning. Image adapted and redrawn from [9].

2.2.3 The Mosquito Hearing System

Another model example of interest in biological acoustic sensory studies is the mosquito auditory system. Mosquitoes exhibit remarkable hearing mechanisms for sound perception. Their ears evolved to be very sensitive sensors to detect the particle velocity component of sound, achieving an acute sensitivity with displacements of ≈1 nm at the front-end detectors – antennae [58]. These sound receptors are composed of antenna-like structures exposed outside the body, called plumose flagella, located on top of the head, as illustrated in Figure 2.16 (A).

This type of sensor can detect sound when the motion of particles viscously drags the external mechanical structures (antennae) that protrude from a chordotonal organ called the Johnston's organ (JO). The sound-induced mechanical motion on each antenna drives up to 16,000 force sensitive cells (mechanosensory neurons (n)) inside the pedicel, as illustrated in Figure 2.16 (B) and Figure 2.16 (C). When stimulated, these mechanosensory neurons convert the mechanical energy into electrical signalling in a form of spike-type neuronal responses commonly called action potentials, as similarly described in the previous Section 2.2.1 for the human hearing system model. Importantly, mosquitoes rely on their hearing system in order to increase their mating successes. Preferentially, males

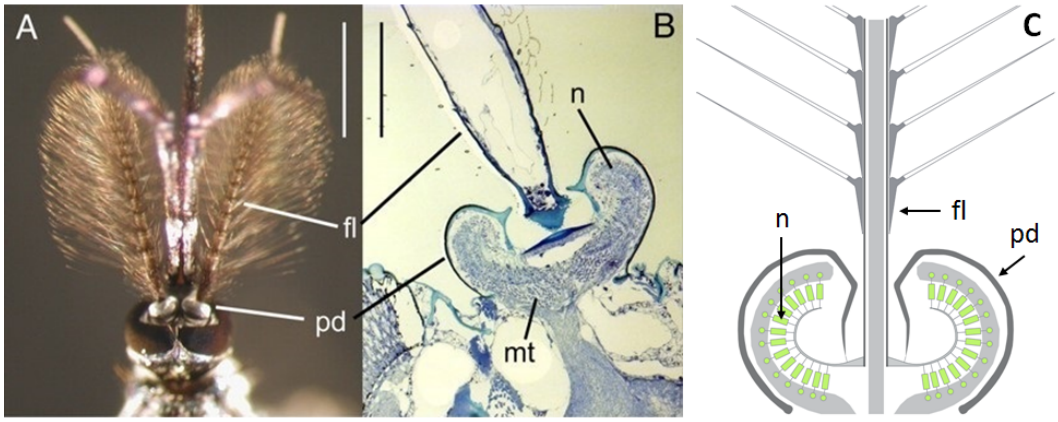

Figure 2.16: Auditory organ of a male mosquito *Toxorhynchites brevipalpis*, showing the antennae and Johnston's organ. (A) Male antennae, highlighting the plumose flagella (fl) and the pedicel (pd) – scale bar 1 mm (adapted from [12]). (B) Cross-section of the antennal pedicel – scale bar 200 μm (picture by H. Kohler and D. Robert), the pedicel houses an ensemble of mechanosensory neurons (n) which are surrounded by mitochondria (mt) as the supply source of metabolic energy. (C) Simplified schematic of the mosquito's auditory organ (adapted from [13]).

can detect the sound particle displacements generated by a flying female of 3.5 nm from a distance of 10 cm away, within the frequency range of 350 - 450 Hz [58]. Intuitively, for a male mosquito to detect and pursue a flying target, its sound receptors may need to transit between two modes of operation:

- Fast transient time response, which allows the sensory system to quickly detect a close-by target;
- Frequency-selective sensing mode, which enhances the system intelligibility when sounds are generated by a selected/targeted source.

A dynamic transition between these two modes of operation might not be achieved entirely by a conventional passive mechanical detector (e.g., front-end acoustic sensor) alone such as a driven damped harmonic oscillator. Biological studies based on the mosquito hearing system [12] along with complementary

mathematical models [13], [59] report the fact that the presence of a positive-feedback mechanism using a set of synchronized neurons pumping additional energy to the front-end detector (e.g., antenna structure) may be the reason for the dynamical adaptation exhibited by this hearing system, when exposed to an input sound stimulus, as illustrated in Figure 2.17.

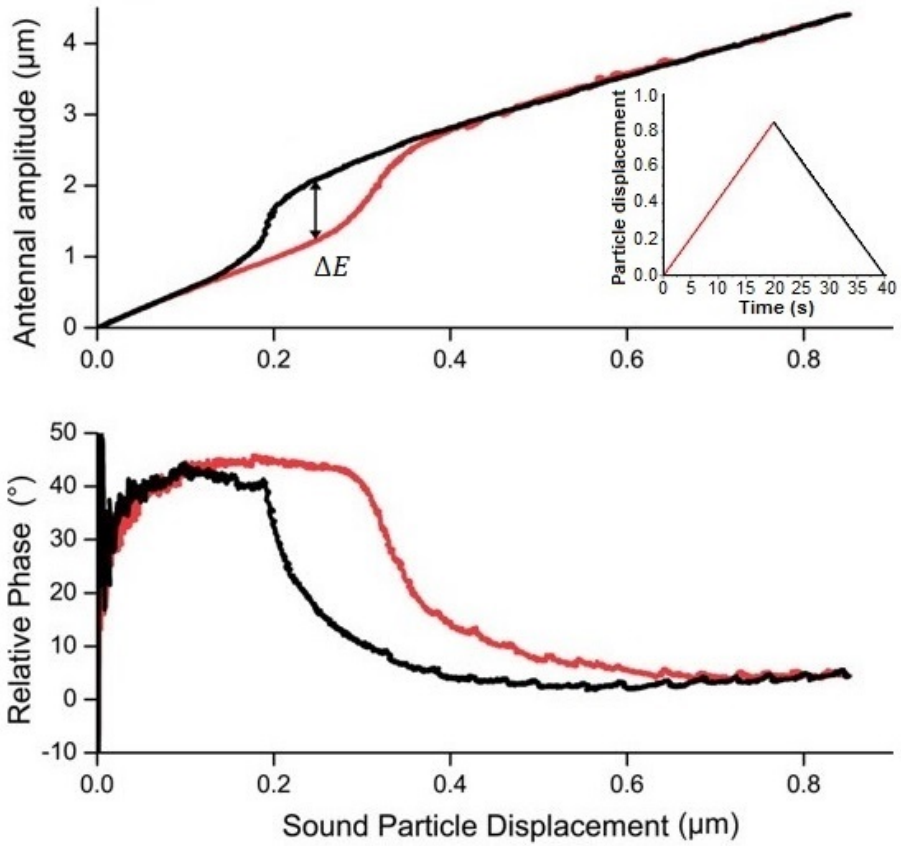

Figure 2.17: Antennal nonlinear response showing amplification and hysteretic behaviour. ΔE is the rational energy of oscillation between the hysteretically amplified and the initial (passive) non-amplified response. Inset image is the envelop of a single-tone stimulus used to test this sensory system response while increasing (red trace) and decreasing (black trace) sound intensity. Adapted from [12].

It is thought that signals can be amplified in a nonlinear fashion due to the presence of an unconventional feedback mechanism between the front-end acoustic detector (antenna structure) and a set of back-end computational machines

(neuronal cells), resulting in hysteretic output responses. The assumption is that the active hearing responsiveness to input acoustic signals (female's wing beat sounds) is greatly enhanced by synchronized neuronal cells (efferent neurons within the JO [60]) pumping additional energy entrained with the front-end detector through a cycle-by-cycle positive-feedback mechanism [12], therefore this is meant to be a fast feedback mechanism. This seems to be an unconventional but advantageous technique to adapt the sensory responsiveness to a desired input stimulus. Therefore, frequency selectivity, nonlinear compressive responses, and hysteresis of such a sensory system may result [12]. These active amplification and frequency selective responses have also been reported from other studies including insects with tympanal ears such as the ones of the tree cricket, which are thought to exploit similar nonlinear-like mechanisms using neuronal feedback computation in order to enhance signal detection and processing capabilities [61].

2.2.4 Compressive Nonlinear Gain

Generally, active amplification and sharp frequency selectivity are thought to be the most important functions taking place at the initial stages of signal conditioning performed by an auditory system. The ability to amplify and tune at specific frequencies can benefit such a sensory system to separate desired but sometimes weak signals from undesired background noises. Studies based on the vertebrate inner ear report that a healthy hearing organ can provide gains up to 60 dB [41]. As described before, that is thought to be a consequence of energy injection provided by synchronized electromotile cells, which putatively increase the magnitude of their mechanical inputs in a sort of positive-feedback mechanism. Moreover, the hearing system is more likely to amplify low level sounds and can be less responsive proportionally, as they become louder. This function is generally known as the compressive nonlinearity that can be achieved by a hearing organ, and that is a fundamental mechanism that greatly enhances overall

dynamic range. For instance, in humans the dynamic range can be up to 120 dB when preserved in a healthy condition [52]. The assumption is that the process of active hearing is thought to be related to a kind of critical oscillatory behaviour, which enables signals to be quickly amplified and in a nonlinear fashion through a positive feedback control technique between the front-end mechanical sensor and a back-end electrical computational system, which in that case can also provide hysteretic responses [12], as illustrated in Figure 2.18.

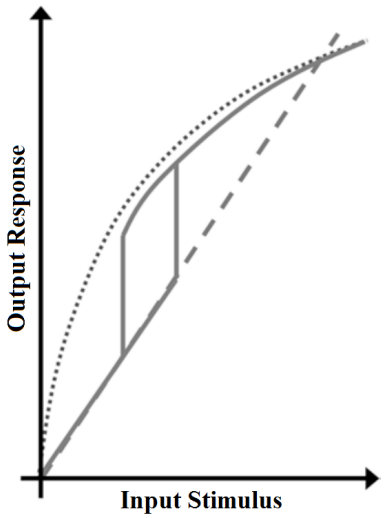

Figure 2.18: Examples of hearing responses; (dash line) represents a system with a linear response, such as a driven damped harmonic oscillator; (dot line) is a typical vertebrate hair bundle nonlinear response; and (solid line) is a hysteretic nonlinear response such as reported from the mosquito hearing system. Image adapted and redrawn from [9].

2.2.5 Passive Sensory Responses

Conventionally, the resonant mechanical response exhibited by the passive mechanical responses in biological acoustic sensors may resemble the ones given by the driven damped harmonic oscillators also called passive resonators [3]. Normally, those are classified as 2^{nd} order systems, which may simply be expressed in Laplace form by the following transfer functions, where s represents the Laplace

term ($s = i\omega$), as expressed in Table 2.1:

Table 2.1: A 2^{nd} order system as the possible basic model to study passive acoustic sensory responsiveness [3]. ($H_{lp}(s)$) Low-pass response such as pressure like acoustic detector - e.g., the moth hearing system [10]; ($H_{bp}(s)$) Band-pass response such as sound velocity detector - e.g., the mosquito hearing system [21].

Low-pass response	**Band-pass response**
$H_{lp}(s) = \frac{\omega_0}{s^2+s\frac{\omega_0}{Q}+\omega_0^2}$	$H_{bp}(s) = \frac{s\frac{\omega_0}{Q}}{s^2+s\frac{\omega_0}{Q}+\omega_0^2}$

These kinds of mechanical detectors/resonators can be characterized either by structural mechanical properties such as stiffness (k), mass (m) and dissipation/losses, or by physical properties such as resonance frequency ($\omega_0 = \sqrt{\frac{k}{m}}$) and quality factor ($Q = \frac{\omega_0}{\gamma}$), where γ represents the damping coefficient and $\omega_0 = 2 \times \pi \times f_0$ is the resonant frequency term. The Q-factor expresses how quickly the energy supplied to the passive detector/sensor/resonator can be dissipated in it.

This means that an underdamped system (high-Q detector) exhibits a slower temporal resolution compared to an overdamped one (low-Q detector) that may achieve a faster temporal responsiveness when subject to an applied acoustic stimulus. The resonance frequency (ω_0) is defined as the preferred frequency where the system exhibits greater responsiveness or sensitivity.

Additionally, a passive detector/sensor of this kind exhibits linear sensitivity and its bandwidth can be expressed by the ratio between resonance frequency and quality factor, $\Delta\omega = \frac{\omega_0}{Q}$. Therefore, that sets a trade-off between time versus frequency responsiveness of a given front-end acoustic detector/sensor of this kind, as summarized in the following Table 2.2:

Overall, a sensor designed with low-Q can achieve fast temporal resolution with the cost of a poor frequency selectivity, whereas, a high-Q sensor design has a slower temporal transient responsiveness with the benefit of a higher frequency selectivity, as illustrated in Figure 2.19.

Table 2.2: Summary of time vs frequency resolution/response of a resonant acoustic sensor.

	Time (resolution/response)	**Frequency (resolution/response)**
Low-Q sensor	high/fast	low/wide
High-Q sensor	low/slow	high/narrow

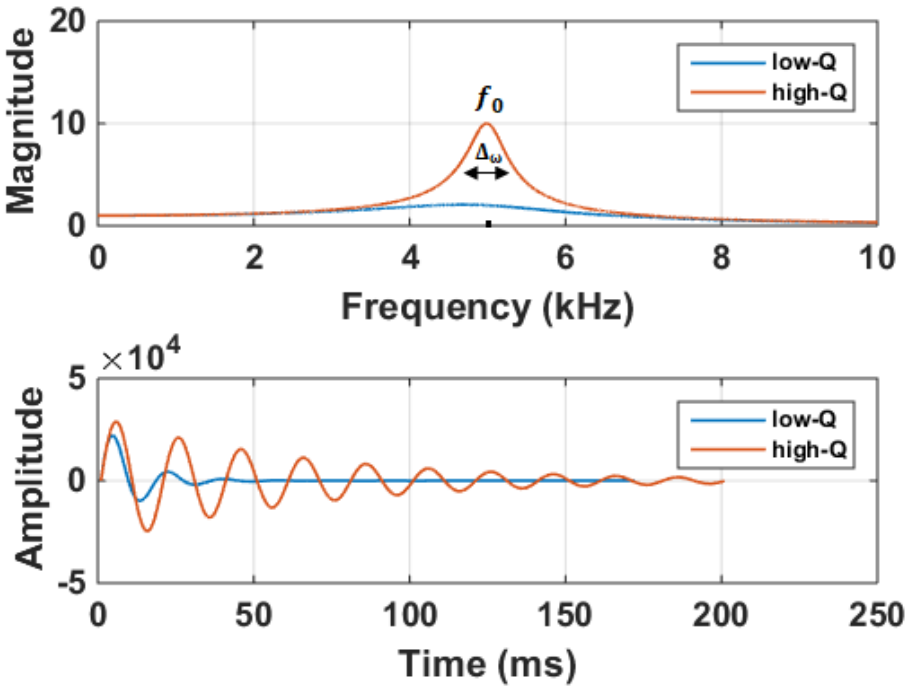

Figure 2.19: A 2^{nd} order system as the possible basic model for a passive acoustic sensor front-end. Frequency selectivity and transient time response might be adapted by manipulating the Q-factor of the system.

Additionally, when the stiffness parameter (k, also known as spring factor) of this kind of system is altered, consequently it affects the natural resonance frequency of the system, since $\omega_0^2 = \frac{k}{m}$, as illustrated in Figure 2.20.

This acoustic sensory system modelling approach is exploited in the work presented in Chapters 3 and 4 of this thesis.

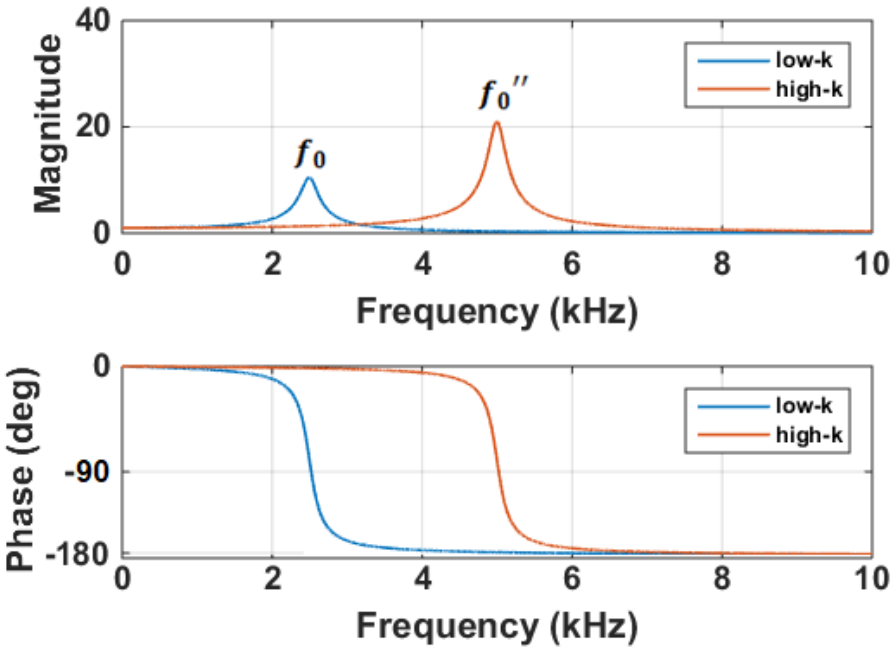

Figure 2.20: A 2^{nd} order system as the basic model for a passive acoustic receiver front-end. Resonance frequency (ω_0) may be adaptable by altering the equivalent stiffness (k) of the system.

2.2.6 Neuronal Models and Artificial Systems

Motivated by the biological mechanisms of signal transduction and processing within mechanoreceptors and neuronal cells, neuroscientists have developed some mathematical methods and computational models, which may help to study the dynamics of the brain and its peripheral sensory systems. Therefore, it led to the development of discrete computational models with different levels of granularity that incorporate some of the dynamics behind neuronal encoding and firings, for instance the Hodgkin-Huxley [62], Leaky Integrate-and-Fire (LIF) [63], Izhikevich [64]; and others that focus more on the transduction processes in mechanoreceptors (e.g., hair cells) [65]; and also higher-level models that faithfully replicate some of the output responses as similarly seen in the mammalian auditory system [66]. Most interestingly, the use of some of these neuronal models, such as

the LIF neuron, can be implemented in a very efficient way in terms of computational costs, and therefore it can be exploited as a computational mechanism within engineered and real-time signal processing systems [57], [67], as the following describes.

The LIF neuron is a simplified model that resembles the behaviour of a single neuron. It ignores the conductances of Na^+ and K^+ responsible for the action potential generation, which are normally included in more complete neuronal models such as the Hodgkin-Huxley [62]. Instead, the LIF model replaces that by assuming an equivalent membrane's capacitance (C) and resistance (R), and evolving the membrane's voltage potential over time according to the differential equation as following presented in Equation 2.1:

$$C\frac{dV_m}{dt} = -\frac{V_m}{R} + I, t > 0 \tag{2.1}$$

Solving Equation 2.1, by applying the Euler method which considers the approximation: $V_m(t_{n+1}) - V_m(t_n) \approx h(\frac{dV_m}{dt})$, where $h = dt$ (i.e., step size), thus:

$$V_m(t_{n+1}) = V_m(t_n).\left(1 - \frac{dt}{\tau}\right) + R.I(t_{n+1}).\left(\frac{dt}{\tau}\right) \tag{2.2}$$

Where $\tau = R.C$ represents the membrane's time constant; V_m represents the membrane's voltage potential, I is the input stimulus, which might be associated to any input current reaching the cell body (i.e., soma). By computing Equation 2.2 over time (t_n), an action potential can be fired when a voltage threshold is reached. As said before, real neurons hold some time before they are capable of firing again. This refractoriness is normally composed of two periods: a hard (absolute) and a soft (relative) period. A hard refractory period is a time in which a neuron cannot fire absolutely, whereas a soft refractory period is time during which the threshold is generally more elevated than its steady-state voltage value such that an action potential may not be likely to occur. Overall in a LIF

model, an absolute refractory period can generally be set by a constant time whereas a relative refractoriness can be set by a sudden increase (i.e., arbitrarily) of the threshold voltage value, which may decay over time towards its basal level (steady-state) after each firing. It is shown that the mathematical implementation of the LIF neuron using the Euler method can be very efficient in terms of its computational cost when compared with other methods while computing neuronal models [68], therefore, it is applied to the work presented in Chapter 4 of this thesis.

Artificial cochlear circuits and systems have been presented in the last decades that integrate and/or replicate several of the auditory responses as similarly reported within biological studies based on the mammalian auditory system [69]. And some of that knowledge has also been used within speech processing algorithms for hearing aid technology [70], for instance digital and analogue filter-bank systems [71] that mimic the mammalian basilar membrane frequency tuning response and automatic gain control system that try to replicate the function of the OHCs as the active amplification mechanism in the cochlea [72]; and among other bio-inspired works including silicon cochlea systems [73], and silicon neurons [74], and circuit and system interfaces for bio-inspired sensors [75], [76].

Moreover, many other studies based on feature extraction and pattern recognition fields have shown promising results on speech enhancement while using machine learning and statistical methods, the so-called Artificial Intelligence (AI) [77], [78]; some other studies use deep learning algorithms (e.g., deep neuronal networks) for environmentally robust speech recognition [79]; and among others that can extract different sound features within competitive signals [80], [81]; and also showing robustness on speaker identification [82]. These are promising results, however mostly relied on "big-computational-machines" with high-power requirements, large memory (e.g. databases), and with time delays on the signal processing tasks, which up-to-date may not be compatible with some real-time

processing applications. For instance, within battery limited systems such as wearable devices, hearing aids or cochlear implants that require very low power system consumption (< 1 mW), small hardware packaging for sensors, circuits and systems; and reduced latency (< 10 ms) on digital signal processing routines and data buffering in order to avoid signal distortions within enhanced hearing applications [83].

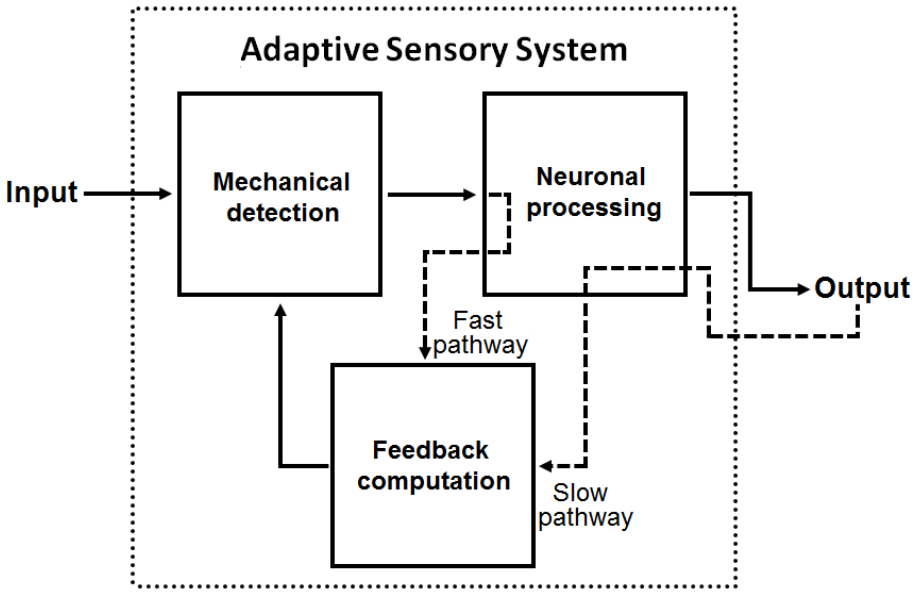

Figure 2.21: Schematic diagram of a possible basis for an engineered adaptive sensory system showing the flow of signal information that is influenced by slow and fast feedback control with neuronal based computation of signals using efficient computational methods.

2.2.7 Active Feedback Computation

The sensitivity of a passive acoustic detector/sensor is greatest when operated at its resonance frequency (ω_0), and that is also proportionally dependent on the Q-factor. Physical constraints are imposed by the sensor's design on the Q-factor and resonance frequency that can be achieved, such that one might not have much flexibility and control over these parameters when and after designing an

acoustic detector/sensor. However, some natural hearing systems overcome that limitation through the use of feedback control mechanisms in order to dynamically adapt those physical parameters such as Q-factor and resonance frequency (ω_0). In order to accomplish the above-mentioned adaptations, two types of feedback processes have been identified that allow biological acoustic sensors to adapt their physical parameters as the following describes and illustrated in Figure 2.21:

- **Slow feedback adaptation**, which is performed based on n-cycles computation. The output responses are delayed from the input stimuli due to integration of past n-cycles of the input signal. Potentially applied on frequency agile tuning (adapting the spring factor of the sensor, therefore, affecting ω_0) - Figure 2.22 A;
- **Fast feedback adaptation**, is intended to be based on cycle-by-cycle computation, which means that the output responses given by this method are performed at every cycle of the input stimuli. Potentially applied on nonlinear compressive amplification (adapting the Q-factor of the sensor) - Figure 2.22 B.

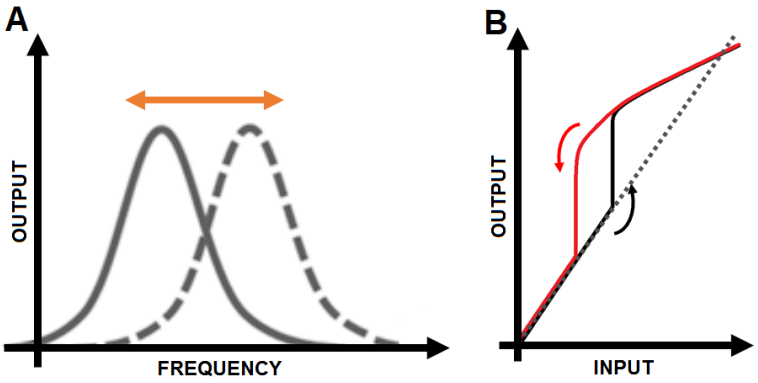

Figure 2.22: Adaptive sensory system responses based on slow and fast feedback computation. (A) Frequency agile tuning and (B) nonlinear active amplification.

For instance, some studies using engineered resonant sensors, circuits and systems, likely support the use of positive-feedback control techniques, which also

enable adaptive nonlinearities in low-powered filtering applications [84], hysteretic behaviour applied to speech in noise applications [85], and that the Q-factor of sensors can be enhanced exploiting the feedback control technique so-called parametric amplification, for instance, used in atomic force microscopy [86], [87]. Moreover, frequency agile tuning can be either described as a function of a sensor system that cleverly adjusts its operating frequency to overcome the influence of interfering sources such as noise, or rather its adaptation to be tuned with desired signals of interest. This technique has already been exploited among radar and general radio applications to account for jamming or adverse atmospheric conditions [88].

Therefore, feedback computation can be seen as a potential method to be used in order to maximize sensory responsiveness, converging the system's operating state the best possible detection rate output. It is important to note that this might be possible if the front-end detector and transduction method used are designed in such a way that allows signals to be fed back into the sensor. That sets an important requirement for an adaptive acoustic sensory system front-end design, i.e. the readout and actuation on the transducer using a combination of standard or perhaps novel sensing and actuation techniques, which can be optic (readout only), piezoelectric (readout and/or actuation) and capacitive (readout and/or actuation), with their associated demands for electrical signal conditioning with respect to each one of those transduction methods.

2.2.8 Discussion I

Several biological sensor system examples were highlighted in this section. Passive and active mechanisms within hearing sensors and systems showing evidence of analogue signal processing performed at the peripheral sensory system such as mechanical filtering, active amplification, and transduction of signals that are sampled and compressed by the nervous system as action potentials. Moreover,

supporting previous studies on that line of thought - it might be advantageous to pre-process signals at the periphery, considering that many signal processing tasks can possibly be made more energy efficient when exploiting some analogue based functions and delaying the digitalization process for later [89]. Nevertheless, there might be a size/area cost trade-off on the front-end sensory systems associated to it [48]. Increasing the number of elements (detectors/sensors) placed in an array fashion for a distributed processing task, and the area used for feedback control systems and back-end computation may increase the size of overall front-end system architecture - nevertheless, that is dependent on technology and design strategies used.

To conclude this section about natural hearing and related sensory systems, it is important to note that any acoustic stimuli detected/sensed and pre-processed by the peripheral auditory system may or may not be useful information. Mainly, it is meant to sense and transduce signals faithfully at a specific time-frame, and deliver output signals to be processed by higher-level reasoning systems. Therefore, any decision making based upon any incoming sound information requires sophisticated signal processing capabilities in order to trigger reliable output behaviour. Feature extraction and pattern recognition based on different neuronal firings are encoded and processed by the nervous system. Behavioural outputs typically rely on coordinated and synchronized high-level circuits and networks of neurons that merge multiple sensory information (e.g., sensory integration) in the brain. Moreover, feature extraction and pattern recognition of sounds are tasks performed and subdivided by a set of specialized neuronal networks that learn throughout time (getting learning experience) how to make sense of sound. However, the presence of optimized analogue computation at the front-end sensory level and the use of feedback mechanisms with power-efficient neuronal circuits and systems (inhibitory or excitatory responses) may likely enhance distinct features within a specific sound pattern and its reasoning. Therefore, a simplified

but important note to retain from this section is that - the first stage of sound processing in biological acoustic sensors and systems is likely to be performed by the front-end transducer - electromechanical computation. That is mainly relied on analogue computation, which includes signal detection, impedance matching of acoustic signals, and filtering and nonlinear amplification. Moreover, the front-end sensory system should be well-designed with feedback system mechanisms to enable adaptation such as frequency agile tuning and active nonlinear amplification that best suit a particular signal processing task.

2.3 State-of-the-Art in Acoustic Sensors, Circuits and Systems - Engineering Trends and Designs

This section presents some state-of-the-art in recent advances on microphones technology with particular attention on Microelectromechanical Systems (MEMS), including different transduction methods, electronic circuitry and systems.

2.3.1 Microelectromechanical Systems (MEMS) Microphones

Many developments in sensor technology are based on MEMS, and this is very true of microphones, as illustrated in Figure 2.23. Nowadays, MEMS microphones can be fabricated in a very small form factor on batch-processes at very low cost, allowing the integration of these little microphones (e.g., mm^3 scale) within almost all sorts of consumable electronics such as smartphones, tablets, laptops, headsets, smart-speakers, automotive, wearables, smart-TVs, etc. Moreover, this new trend in sensory technology is bringing forward the possibility for new kind of audio-activated applications including speech recognition, authentication, and voice controlled and activated systems, among several other ways to optimise

communications; and the emergence of new business solutions and products [90]. Additionally, MEMS microphones have also the potential to be integrated within biomedical applications such as Hearing Aids (HA) and Cochlear Implants (CIs), allowing these prosthetic systems to be further optimised in terms of their integration in miniaturized solutions to better address individual needs [91].

Figure 2.23: Example of a silicon top sound port condenser MEMS microphone (amplified 10×, approx.) fabricated by Infineon Technologies AG, showing the top MEMS package with and without the metal case, and the connection pads on the bottom side. Image adapted from [14].

The MEMS microphone market has grown every year since 2005, and with predictions of growth until 2022 as shown in Figure 2.24, and perhaps beyond that, it might be hypothesized that the number of units manufactured may follow an exponential growing trend (e.g., *the law of accelerating returns* by Ray Kurzweil), as similarly seen within other technological advances in the last few years, and lead by technologies relied on microelectronics and integrated circuits [92].

2.3.2 Capacitive MEMS Microphones

The widely used and perhaps most fabricated MEMS microphone so far, is based on the capacitive transduction modality [93]. The condenser MEMS microphone has been a topic of research for many years [94], [95], but it was only introduced and faithfully accepted in the market of consumer electronics in the early 2000s, replacing the electret type microphone - possibly due to the smaller form factor,

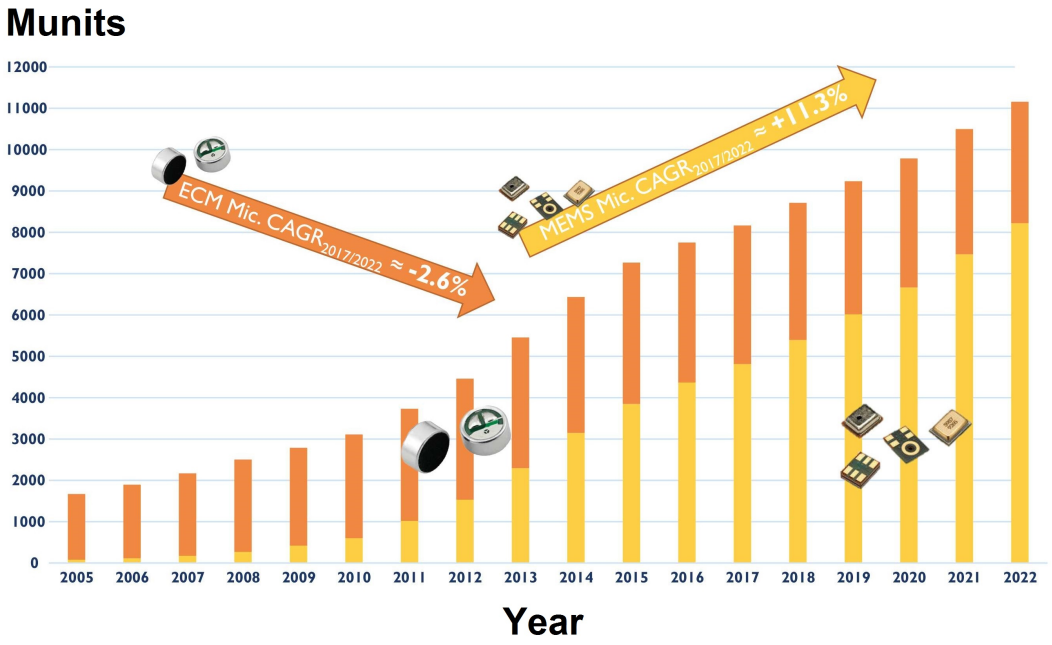

Figure 2.24: Microphone's market predictions from 2005 until 2022, showing a decrease of the amount of Electret devices and an increase of MEMS microphones that are manufactured per year, where Munits represents Million of devices manufactured. Image adapted and redrawn from [15].

and reduced manufacturing and processing costs [96], [97]. The condenser microphone working principles are based on the capacitive transduction method. In its basic form, this transduction modality consists of two parallel plates (e.g. a flexible membrane or diaphragm and a rigid/fixed back plate) separated by an air gap acting as a dielectric material to form a variable capacitor. The capacitor is permanently charged by means of an imposed constant supply voltage called a DC bias. Alternating acoustic waves can force/press the flexible membrane to move up and down, which consequently vary the effective capacitance between the two parallel plates (e.g. causing the bending of the flexible diaphragm forced by the acoustic energy coupled onto it), as illustrated in Figure 2.25 (Top). As a consequence, a variable electrical charge signal output is generated, as an equivalent AC electrical signal that can be acquired and further processed by means of an appropriate electronic system. Moreover, another possible design of this

transduction method is to place the flexible membrane in between two back-plates, as illustrated in Figure 2.25 (Bottom). This symmetric design provides a differential output signal (e.g., two complementary output signals with opposite polarities), showing some advantages in comparison with the single-ended designs (e.g., single back-plate design) such as, higher immunity to common noises (e.g., RF interference) and higher dynamic range [98].

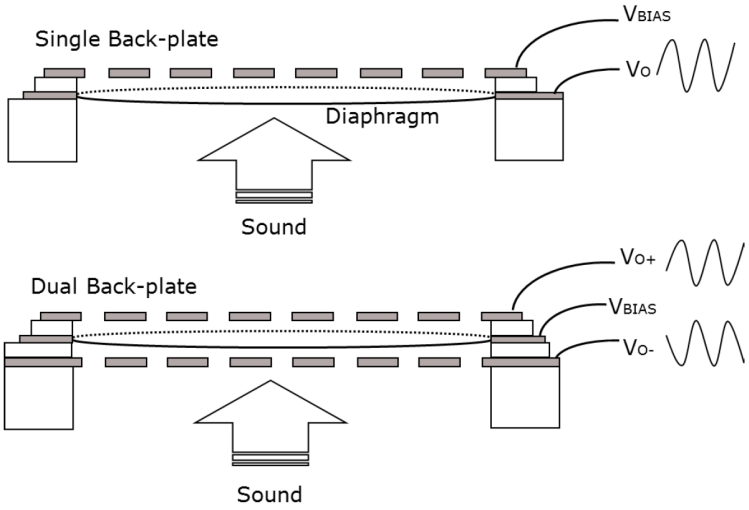

Figure 2.25: Electrical output from two standard capacitive transduction design methods used in commercial MEMS microphones. (Top) single-ended output; (Bottom) differential-ended output. Where V_{BIAS} represents the constant supply voltage and V_o the electrical output signal resulted from the diaphragm displacements. © C. Lillelund, Infineon Technologies AG.

The standard parallel plate microphone design is based on the electrostatic transduction method, which is *per se* nonlinear. The output signal (electrical force, F_e) resulting from the diaphragm's displacement is nonlinear, following an inverse square relationship with the size of the variable dielectric gap that is in between the two parallel plates, as expressed in Equation 2.3 [99]:

$$F_e = \frac{1}{2}\frac{\epsilon.A.V_b^2}{(x_0 - x)^2} \tag{2.3}$$

Where ϵ is the dielectric permittivity; A is the area of the diaphragm (top

capacitor's plate); V_b is the constant supply voltage across the parallel plates (e.g., DC bias); x_0 is the thickness/size of the dielectric gap; and x represents the diaphragm's displacement.

Nevertheless, the magnitude of the restoring mechanical force (F_m) given by this system has a linear relationship with the diaphragm's displacement such that $F_m = -k_m.x$ (Hooke's law), as illustrated in Figure 2.26. Therefore, it is assumed that the parallel plate system behaves like a mass-spring system (2^{nd} order system). Where k_m represents the mechanical spring constant associated to the restoring mechanical force (F_m) of the system.

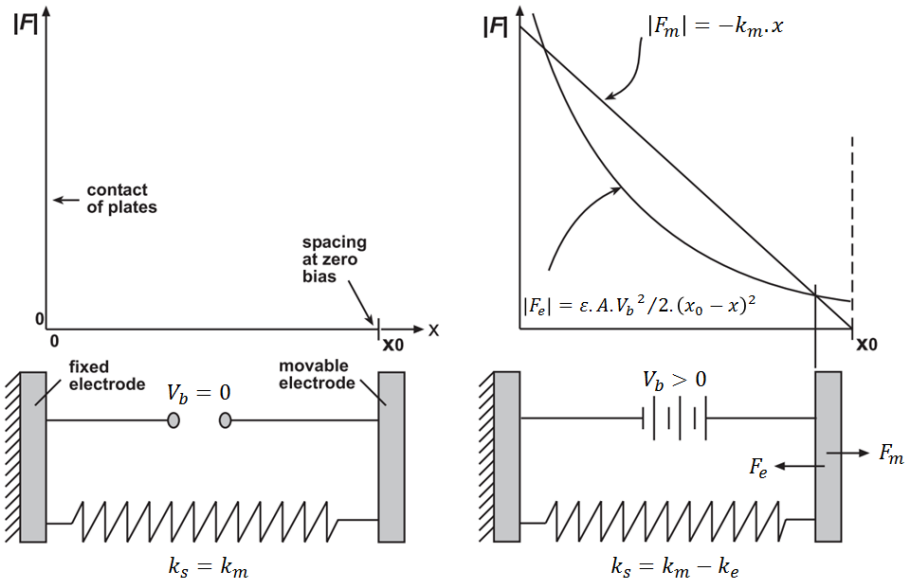

Figure 2.26: Magnitude of the mechanical and electrical forces as a function of the distance between the parallel plates [16], where k_s represents the overall effective stiffness of the diaphragm.

Moreover, when a constant voltage is applied across the parallel plate capacitor system, it develops an additional spring constant (electrical spring factor - k_e) due to the electrostatic attraction force applied (DC voltage) that modifies the overall static stiffness of the structure, engaging the movable plate at its equilibrium state, as expressed in Equation 2.4 [99]:

$$k_e = \frac{\epsilon.A.V_b^2}{(x_0 - x)^3} \tag{2.4}$$

Therefore, the effect of the DC bias has an impact in this system's resonance frequency (ω_0) – softening effect, as expressed in Equation 2.5 [99]:

$$\omega_0 = \sqrt{\frac{k_s}{m}} = \sqrt{\frac{1}{m}(k_m - k_e)} \tag{2.5}$$

Where m represents the equivalent mass of the system. Additionally, if the constant voltage (DC bias) applied to the system exceeds a certain value (e.g., pull-in voltage, V_{PI}), the diaphragm and the back plate may snap in and collapse, and so the equivalent capacitor is short-circuited, as expressed in Equation 2.6 [99]:

$$V_{PI} = \sqrt{\frac{8.k_s.x_0^3}{27.\epsilon.A}} \tag{2.6}$$

Overall, the electrostatic transduction method exploited by the standard capacitive MEMS microphone designs has a nonlinear relationship with the diaphragm displacement. Moreover, a constant supply voltage (DC bias) is a requirement for the electrostatic transduction method, however, caution should be taken to ensure that the voltage applied across the structure is compatible with the magnitude of the diaphragm's expected displacements, while driving the system acoustically. Otherwise, the pull-in limits are compromised and the overall structure may collapse as the parallel plates stick together, short-circuiting the equivalent capacitor [16]. Additionally, the bias voltage sets-up an electrical spring constant that modifies the effective static stiffness of the overall system (e.g., softening the system [16]), which therefore alters its resonance frequency. These are some of the limitations imposed by the standard back-plate microphone's designs.

2.3.3 Piezoelectric MEMS Microphones

Another sensing modality that has been topic of investigations within the MEMS research community and acoustic sensors in general is the piezoelectric transduction method [17], [100], [101]. This principle is based on mechanical deformations of structural parts (e.g. exploiting the stiffness mode or bending mode of materials) such as membranes or cantilevers that are shaped and coated with some sort of piezoelectric layers to transduce displacements into equivalent electrical signals. Devices are custom-designed to allow an effective coupling of acoustic energy onto their surfaces. For instance, mechanical-bending of structures can induce stress onto the piezoelectric layers, which consequently can generate electrical signals due to the direct-piezoelectric effect. The opposite is also possible such that an applied voltage (building up an electrical charge) on the piezoelectric materials has the effect of changing their dimensions (e.g., reverse piezoelectric effect) [102].

Piezoelectric materials such as aluminium nitride (AIN), zinc oxide (ZnO) or lead zirconate titanate (PZT), among others [103], can be used as transduction layers over the device's structure, exploiting their piezoelectric capabilities. As previously mentioned, one of the most relevant properties of these piezoelectric materials is their ability to become electrically polarized when strain is applied onto them, allowing the use of these smart materials in several sensory and actuation applications such as in energy harvesting, medical technology, pumping and dosing machines, ultrasonic transducers, force measurement systems, etc. Moreover, piezoelectric capabilities can also be integrated within micromachined transducer designs for instance in ultrasonic applications [104]. Some advantages of using piezoelectric materials for sensing acoustic signals include:

- No requirement for a DC bias voltage to be built-in the device to operate, which may reduce the overall power consumption of the system;

- Allow more robust transducer designs when performances are compared against the standard parallel-plate electrostatic transduction designs under some acoustical conditions [17].

It is important to note that a piezoelectric based transducer might be less sensitive when compared with an equivalent capacitive one, however it may compete against with more reliable electromechanical compliance under some specific acoustic conditions such as acoustic overloading. And, they are also compatible with commercial acoustic applications [17], [105].

Recently, a combination of novel fabrication processes with clever design principles enabled the creation of a microphone with high immunity to environmental contaminants, high shock-resistances and waterproofing. Now, it is possible to integrate and operate MEMS microphones within wet and dirty conditions. These are some of the features claimed by the inventors (e.g., [17]) of the Vesper's omni-directional MEMS microphone, which is thought to be the first piezoelectric based MEMS microphone available in the market [105], as illustrated in Figure 2.27.

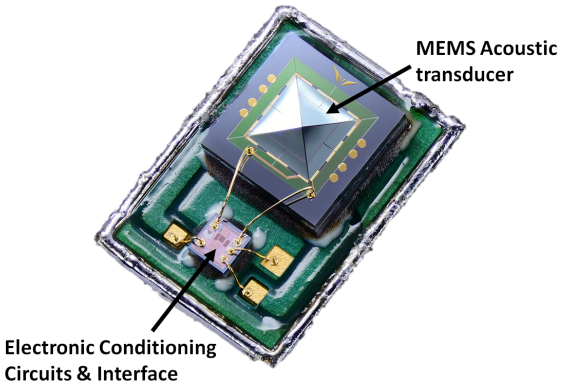

Figure 2.27: Vesper's omni-directional MEMS microphone (amplified 20×, approx.) based on piezoelectric transduction method [99]. This device is a bottom port piezoelectric MEMS microphone with package size of 3.76 mm × 2.95 mm × 1.1 mm. © 2018 Vesper Technologies, Inc.

Some studies from the sensors community using piezoelectric materials report the fact that the piezoelectric transduction method can behave linearly at

reduced and moderate mechanical deformations, however when subject to very high electrical fields some nonlinearities may appear. That is the case for the ferroelectric hysteresis effect in PZT [106], [107], and among other nonlinear responses of dielectric polarizations to electric fields [108]. However, in the context of piezoelectric sensing in MEMS microphones, nonlinearities are normally related to extreme stresses applied on the sensor's mechanical structure (e.g., large deflections or deformations). That can happen due to acoustical overloading, or restricting movement of the mechanical parts (from which the electrostatic based microphones are also affected). Therefore, that is not primarily related to any nonlinear behaviour from the piezoelectric transduction method itself [17], meaning that at small mechanical deflections a linear relationship between force and displacement can be preserved, as illustrated in Figure 2.28.

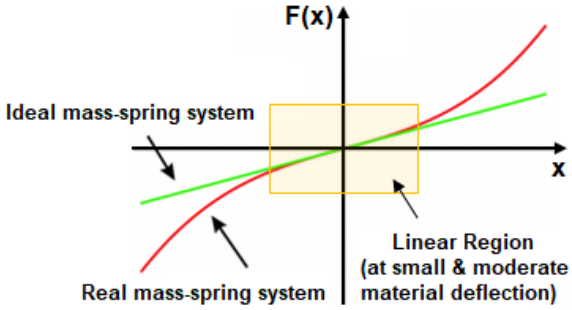

Figure 2.28: Mass-spring system referred mechanical restoring force vs displacement.

2.3.4 MEMS Microphone Specifications

Presently, several omni-directional MEMS microphones are available in the market, including both analogue and digital system packages. MEMS microphone manufacturers report a number of parameters that quantify the overall performance of their devices such as sensitivity, signal-to-noise ratio (SNR), linearity, bandwidth, and also other factors such as power consumption and package size.

Sensitivity is normally referred to as the minimum detectable signal given by

a device. It relates the analogue output voltage or a digital value to a specified input sound pressure. Typically, a microphone's sensitivity is measured with a *pure* tone at 1 kHz sine wave reference signal at 94 dB SPL, or 1 Pa [109]. It is important to note that the sensitivity factor is measured at the output signal after the electronic conditioning stage. This means that one is able to increase the sensitivity of a given device by adding a little extra of amplification to the output signal through proper electronic conditioning, with an increase cost on the power consumption of the overall system.

Moreover, the sensitivity parameter is commonly used as a metric relating the mechanical and electrical performance of a given device over its referred noise floor (both mechanical and electrical noise contribute to it [110], [111]) for the SNR calculation. Electrical noise is mainly associated to random thermal fluctuation of electrical charge carriers and also referred as electrical thermal noise or Johnson-Nyquist noise in an electrical system [112], [113]. Whereas, acoustic noise is associated to mechanical dissipation and also referred as structural damping – acoustic thermal noise [111]; and radiation resistance due to air drag or friction at the moving parts of the acoustic elements [17]. Nevertheless, it is also good practice to perform acoustic measurements such as the ones related to the microphone's noise floor levels, within a quiet anechoic chamber at room controlled temperature [114].

The SNR in a microphone is calculated by the ratio of the sensitivity to its output referred noise floor. Generally described in microphone's datasheets, the SNR value is normalised on an A-weighted scale (dBA) as a standard procedure applied on systems that are used for measuring acoustic signals in human applications. The A-weighted function is a mathematical operation, which faithfully maps the microphone's response to the sensitivity of the human hearing system [115].

These quantitative measurements are important to quantify the device's acousto-

electrical performance. The sensitivity and the noise floor are inherent properties of each specific device, imposed by its mechanical design, transduction method used, fabrication processes, and electronic interfaces and packaging setup, even though, the system's sensitivity can also be refined in order to fit specific application requirements through proper electronic adjustments upon manufacturing stage. A high SNR device is essential at high fidelity acoustic applications. Currently, the industry-leading SNR values achieved by MEMS microphones are up to 70 dBA (94 dBSPL @ 1 kHz) in consumer electronics.

Another key parameter referred to by microphone designers and manufacturers is the device's dynamic range. Ideally, a microphone is designed to behave as linearly as possible within its dynamic range, at small and moderate diaphragm's deflections, as previously mentioned. However at high sound levels some nonlinearities may be evoked after a particular point – Acoustic-Overload-Point (AOP), where the system's acoustic performance can be fairly compromised and so nonlinearities may quickly arise after that specified point, for instance a form of harmonic distortions [98].

Harmonic distortions are commonly nonlinear combination of tones at multiple frequencies and they are normally noted as undesired behaviour in high quality audio systems. In MEMS microphones, the Total-Harmonic-Distortion (THD) factor may rise for two main reasons [99]:

- The mechanical structures such as diaphragms or membranes when exposed to high level mechanical forces from acoustic fields or environmental conditions (e.g., wind) may deform in a nonlinear and uncontrolled fashion or exhibit total collapse of the structure;

- The electronic circuits are normally designed to be operated within specified signal limits, which otherwise result in saturated levels or distorted output signals (e.g., clipping effect), therefore, degrading the THD factor of the overall system.

The THD value is given as a percentage of the distortion levels measured at the system's output for an applied input signal (e.g., a *pure* tone at 1 kHz). Normally, THD is expressed as the ratio of the sum of the powers of all the harmonic components referred to the input signal power [98]. Therefore, the AOP value is normally described in MEMS microphones datasheets to quantify the nonlinearities of the system. This value is presented in decibel Sound Pressure Level (dB SPL) units for a given THD percentage. Essentially, the AOP parameter informs about the performance of a given device, when subject to a high mechanical stress (e.g. high displacements or uncontrolled deformations) and the capacity of the electronic circuits to be compatible with the signal levels supplied by the acoustic elements.

An interesting note is that at near field applications, one may choose a microphone that can offer a high AOP value since the device might be exposed to very loud acoustic fields - since the device might be placed near the acoustic sources. Currently, the AOP values offered by the industry-leading MEMS microphones are up to 130 dB SPL (10% THD @ 1 kHz) in consumer electronics.

Another important parameter intrinsic to any acoustic system is the operational bandwidth. That is commonly specified for MEMS microphones in between the -3 dB low frequency roll-off and the +3 dB frequency point towards its resonance frequency peak. Sometimes, manufacturers can also report the bandwidth as the region where the device have a flatter or constant frequency response, which is at least in between 0.1 - 10 kHz for standard MEMS microphones applied to consumer electronic applications. The device's full bandwidth is commonly set by the design and fabrication methods of the acoustic elements (e.g., mechanical response) and generally it can be kept unaltered by the electronic conditioning circuits to suit a desired application, at best. In standard microphone designs the value of the resonance frequency is set to be well above the upper frequency limit of the desired audio signals in order to avoid output signal distortions in

general purpose consumer acoustic applications.

The power consumption of a MEMS microphone is generally related to the electronic circuits and systems that are integrated within the MEMS package, and less related to the acoustic element itself. However, as mentioned before, electrostatic devices have the need for a DC voltage bias to be applied as a requirement of that transduction method to operate properly. Additionally, it can be noticed when comparing different device systems that the power consumption of digital MEMS microphones is normally higher than their analogue counterparts. Essentially, that is due to the inclusion of additional integrated circuits into the overall MEMS package such as Analog-Digital (A/D) converters and other circuits for signal control and communication that substantially increase the overall power consumption of the system.

2.3.5 MEMS Microphones Circuitry, Signal Conditioning and Interfaces

Microphones are the first interface between the surrounding acoustic environment and the audio signal processing chain. Recent audio applications rely mainly on digital computational machines [116]. These digital computers can be programmed with some sort of digital artificial intelligence in order to process sound. Essentially, exploiting the use of mathematical functions (e.g. digital signal processing algorithms) implemented in the discrete domain with the aim to retrieve or enhance desired acoustic information. Commonly, sound is an analogue signal in its natural form, detected by means of an acoustic sensor, transmitted to a homologous analogue electrical circuit for signal conditioning and then delivered to a digital machine for further processing. In other words, signals are acquired by digital units (e.g. A/D converted) at some point of the signal processing chain. However, analogue interfacing is required by means of an analogue circuit front-end (AFE) to prepare the signal before analog-to-digital conversion (ADC).

An AFE can be described as an analogue electronic system that is used to interface signals between the acoustic element and a digital machine. Whether using capacitive or piezoelectric based transduction, both principles require output signals to be prepared before digital sampling. The aim is to interface the signals without compromising a system's performance, including the parameters previously described such as sensitivity, dynamic range, linearity, bandwidth, and noise floor and power consumption [110]. Usually in MEMS devices, the acoustic element has to be wire-bonded using some sort of conductive wires or electrodes to an AFE that is placed and mounted nearly on a common PCB laminate, as illustrated in Figure 2.29. Regardless the microphone's output type, either analogue or digital, the MEMS acoustic element and its associated electronic circuitry are currently able to be integrated within the same manufacturing process using recent MEMS-CMOS technologies [100], [117].

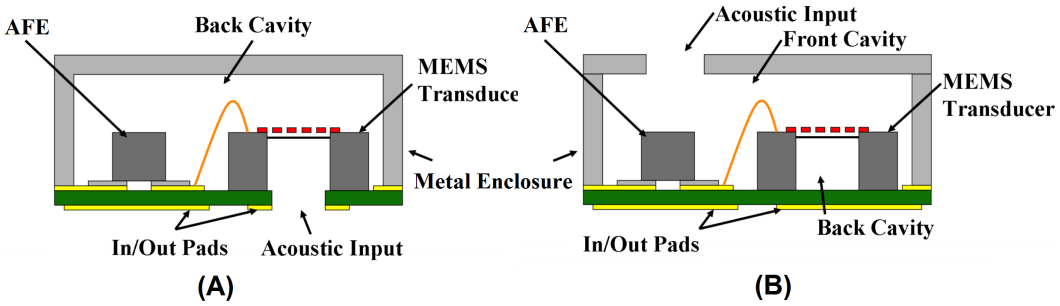

Figure 2.29: Simplified schematic examples of MEMS microphone packaging, showing a bottom-port (A) and a top-port (B) setups. A typical MEMS microphone package size is around 12 mm^3. Image redrawn and adapted from [17].

The casing (e.g., metal enclosure) also plays an important role in the device's acoustic performance. It is meant to protect the diaphragms or membranes and the electronic circuits against adverse atmospheric factors that otherwise would compromise the overall performance of the system (e.g. dust particles, water, shock, handling, etc.). Moreover, the metal casing can be grounded with the external embedded system, which then works as a faraday-cage shielding against

radio-frequency (RF) and electromagnetic interference (EMI) - undesired signals coupled from surrounding electrical appliances.

Generally, a custom-designed AFE is used to effectively convert the signal impedance from the acoustic element to best suit the impedance of the acquisition system (A/D converter input circuitry). Regardless of the transduction method used, either capacitive or piezoelectric, the equivalent output impedance of these types of transducers are typically high, in the range of thousands of Ω up to MΩ [9], [118]. Therefore, a good candidate to provide that high impedance interface role is the Junction Field-Effect Transistor (JFET) device. JFETs can normally be interfaced to the acoustic element following different circuit configurations such as buffer circuits (unity-gain configurations as source followers) or as voltage amplifiers (common-drain configurations). For instance, if the signal conditioning stage requires some sort of amplification and filtering before digital sampling, other circuit examples can be used as presented in [117], [118]. Circuits using discrete electronic devices can also be combined with integrated level systems (e.g. Op-Amps) [119], and other methods of analogue signal conditioning can also be exploited such as charge amplifier circuits [120].

JFET devices offer interesting characteristics that make them very suitable to interface with high equivalent impedance MEMS microphones [17]. For instance, two of the JFETs main characteristics include:

- High equivalent input impedance;
- Very low input referred noise at high impedance signal sources (kΩ - MΩ range).

As previously mentioned, the main goal of using a proper circuit interface attached to the transducer element is to maximize the transfer of signals between a high equivalent impedance signal output (transmitter – e.g., microphone's signals) and the equivalent impedance of the input receiver such as an A/D con-

verter, which is typically a low impedance port, when compared to the equivalent electrical impedance of the acoustic element transduction method used.

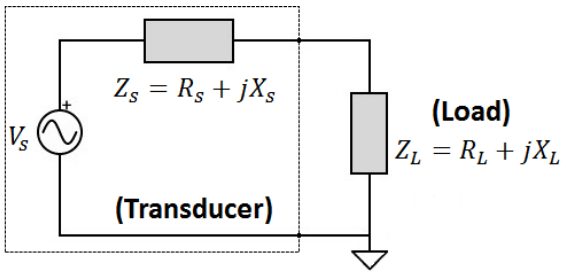

Figure 2.30: Thévenin equivalent circuit when loading an acoustic element following a voltage-mode analysis.

Considering the following exercise: a transmitter (acoustic element) is a non-ideal signal voltage source with an internal electrical impedance (Z_S), which generates signals to be sensed by a system with equivalent internal electrical impedance (Z_L), as presented in Figure 2.30. It might be clear through simple circuit analysis that in order to maximize the transfer/sensing of voltage signals by the load element under these conditions means that its electrical impedance (Z_L) should be much greater than the electrical impedance of the source ($Z_L >> Z_S$). Important to note that this analysis is valid only if aiming to maximize the sensing of voltage signals and not the power transfer between elements. It is well-known that in AC circuit analysis, in order to ensure maximum power transfer between electrical elements, the equivalent electrical impedance of the load and the source should be matched namely, complex conjugated, $Z_L = Z_S{}^*$ (e.g., $R_L = R_S$ and $X_L = -X_S$). This approach is usually applied to high-power ultrasonic transducers by the use of "matching networks" as the interface between the transducer element and its driving circuits [121].

From this simple exercise, it might be concluded that in order to minimize the effect of circuit loading (receptor's impedance), considering a voltage-sensing analysis and at low frequencies (e.g., audio frequencies), the electrical impedance of the load (Z_L) needs to be much greater than the electrical impedance of the

signal source (Z_S). Ignoring any parasitic elements (e.g., wiring) and reactive terms such as intrinsic input capacitances of a typical JFET device, which essentially would limit the bandwidth of that interface [118]. Therefore, a buffer circuit configuration using a discrete JFET device might suit most of the above requirements, as illustrated in Figure 2.31.

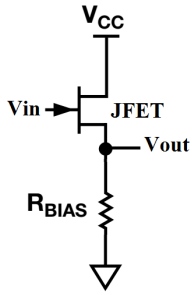

Figure 2.31: Common-drain circuit using a n-channel JFET device in a buffer amplifier configuration.

Moreover, as mentioned before, MEMS microphones are available in hardware packages that sometimes integrate the A/D converters in it – hence digital microphones. In those case, it is said that these provide a digital audio signal output, which can be expressed in a form of pulse-density modulation (PDM) data formats, or pulse-code modulation (PCM) data formats transmitted through I^2S protocol. $\Delta\Sigma$ modulators are often used as a method for A/D conversion integrated within MEMS microphones [122].

2.3.6 Actuation Method for a MEMS Microphone

Novel differential MEMS microphones have been designed in the past few years, exploiting methods of signal transduction including piezoelectric [101], electrostatic [19] and optic [123], showing some innovation on sensing capabilities in the creation of a new kind of directional MEMS microphones [124]. More interesting for the work presented in Chapter 6 of this thesis is the capacitive interdigitated comb fingers system that has been exploited for a while in MEMS for actuation

purposes [125], [126] and [18]. The basic design principle of this actuation method includes a set of comb fingers attached on a movable membrane. Moreover, an equivalent capacitance can be created by the overlap area with a complementary set of interdigitated fingers attached to a fixed substrate, when an electrostatic force is applied, as illustrated in Figure 2.32. When supplying AC signals to the comb fingers structure that can make a MEMS membrane to move. And, if applying a DC voltage bias across that same system, then it might affect its equivalent stiffness seen as a stiffening effect [19].

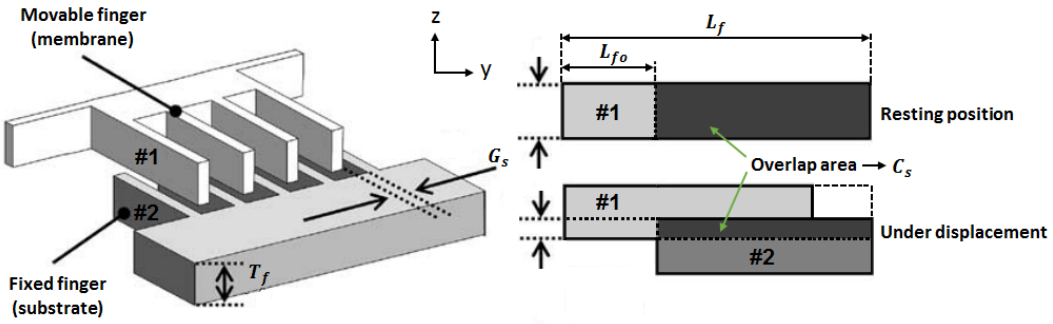

Figure 2.32: Simplified design schematic of a vertical comb-drive actuator, where #1 represents a movable membrane and #2 the fixed substrate. Image adapted and redrawn from [18].

In this comb-drive actuator design the DC bias applied provides a stiffening effect to the spring constant of the system. In contrast with the parallel plate capacitor system, where an applied DC bias has the opposite effect - softening the spring constant of the microphone's diaphragm.

The equivalent capacitance of a vertical comb-drive actuator system can be derived from [16], and simplified as described in Equation 2.7:

$$C_s = 2 \times n \times \epsilon \times \frac{y_0 - z}{G_s} \tag{2.7}$$

Where n is the number of moving comb fingers; (y_0 is the initial lateral overlap area ($y_0 = (L_f - L_{fo}) \times T_f$); T_f is the thickness of the substrate; G_s represents the gap spacing between the movable and fixed set of comb fingers; and z repre-

sents the reduced area of overlap due to the vertical displacement of the movable membrane (e.g., microphone diaphragm), which at resting position thus $z = 0$. In this system case design, the electrostatic attraction force is not likely to affect the distance between adjacent comb fingers (e.g., there is a balanced forcing between them), therefore, the equivalent electrical spring of the system is thought to change proportionally with the amount of DC voltage applied and the equivalent capacitance set by the comb fingers structure [16], as expressed in Equation 2.8:

$$K_s \propto C_s \times V_b^2 \tag{2.8}$$

Reports suggest that this design approach is robust in terms of the amount of constant bias voltage that can be applied to it [19]. This is in contrast with the conventional parallel plate capacitive system where DC bias voltages might become more prone to instability or total collapse [99]. Therefore, the capacitive comb fingers design approach might be an attractive driving method, for instance, in DC bias mode for dynamically adapting the resonance frequency of a purpose-built MEMS microphone, as illustrated in Figure 2.33, without compromising the system's integrity as suggested in [19], and in AC bias mode it can be used to enable Q-factor control, as exploited by this thesis work presented in Chapters 4 and 6 of this thesis.

2.3.7 DC Driving Circuit

An essential requirement when using capacitive type microphones is a circuit that can provide the DC bias voltage. Recent capacitive based MEMS microphone designs incorporate the Dickson voltage converter (DC-DC voltage converter) in the package. This system is also known as charge-pump circuit [20], as in the example illustrated in Figure 2.34.

Optimised designs of this type of circuit can ensure efficient voltage conver-

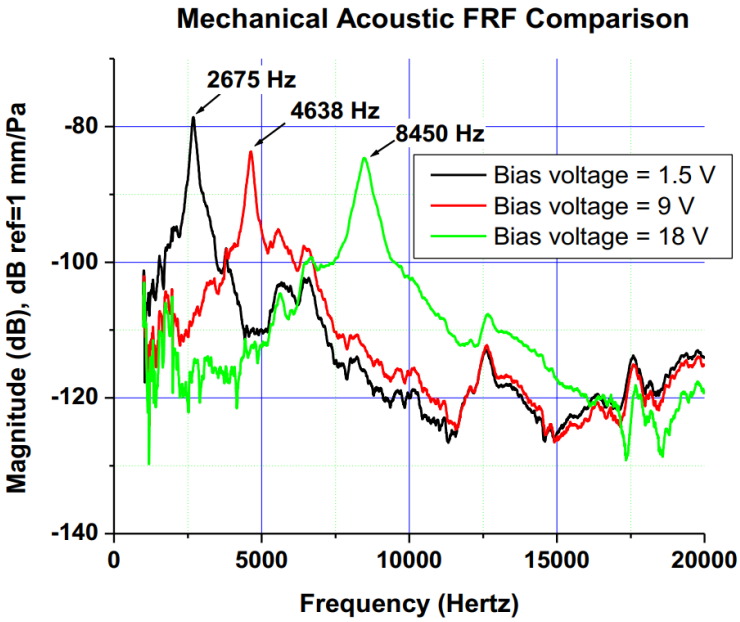

Figure 2.33: Microphone's frequency response can be changed proportionally to the constant bias voltage applied to the comb fingers system – stiffening effect. Image adapted from [19].

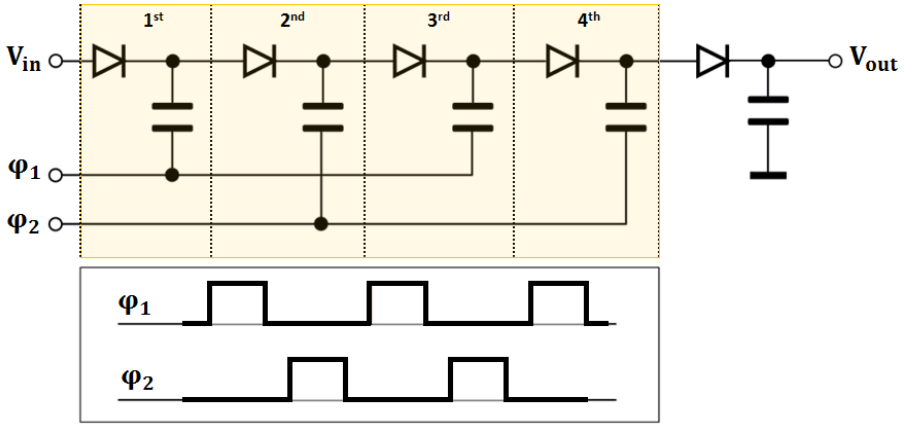

Figure 2.34: Standard Dickson charge-pump voltage multiplier circuit with 4 stages – 5× multiplier, where V_{in} is the input DC voltage; V_{out} is the output DC voltage given by the circuit (e.g., $V_{out} = 5 \times V_{in}$); Φ1 and Φ2 are the auxiliary high-frequency clock signals used to carry-out (build-up) the charge between capacitors [20].

sions while exploiting integrated circuit design techniques compatible with CMOS processes [117], [127].

2.3.8 Discussion II

When comparing MEMS microphone specifications, it is important to consider that manufacturers report referred parameters from test controlled measurements that combine both acoustic and electrical element's performances. However, the choice for the right device should be based on the specific application. For instance, in near field applications the AOP value might be the most important parameter to take into consideration for a MEMS microphone, whereas in far field applications a highly sensitivity device might be the one to choose. It is important to note that the overall sensitivity of a microphone system can be increased by providing appropriate electronic conditioning upon fabrication, while care is taken to not compromise the overall system's noise floor, linearity, bandwidth, package size and power consumption. A desire to have a device with very low noise floor is always very likely to suit any kind of application.

Regarding design considerations, conventional MEMS microphones for consumer electronic applications are designed and aimed to be operated below the resonance frequency (e.g. stiffness-controlled region), aiming to cover audio signal frequencies. Regardless of the sensory transduction method used, the sensitivity of the device is meant to be controlled by the elastic properties of the mechanical elements. Therefore, care is taken to provide enough spacing for the mechanical parts (e.g. membranes, diaphragms or cantilevers) to move freely and evenly, which otherwise would compromise the device's linear acoustic performance; and perhaps exposing the total collapse of the system if operated under high stress conditions – piezoelectric based MEMS microphones appear to be more robust to than standard parallel plate capacitive counterparts [17] - e.g., cantilever based designs.

The parallel plate condenser type microphone design relies on the electrostatic transduction method, which has a nonlinear relationship between the acoustic force and the distance between the parallel plates, whereas the piezoelectric MEMS design appears to ensure better linearity response as for under controlled stress conditions. Additionally, this transduction method has already been integrated in commercial MEMS microphone designs [105], therefore, it is seen as a potential feature to be exploited in a purpose-built MEMS microphone design, as presented in Chapter 6 of this thesis.

Furthermore, the parallel plate condenser type microphone relies on a constant supply voltage applied to enable transduction. This design requires some special considerations to ensure enough back cavity spacing when elevated electrostatic forces are supplied (e.g., high DC voltages) that otherwise would stick the parallel plates together. In contrast, the capacitive comb-drive actuator design seems to ensure higher robustness due to the balance of the electrostatic force between adjacent fingers. Moreover, this method has already been integrated in MEMS microphone designs [19], therefore it is seen as a potential feature to be used to dynamically adapt the output response of a MEMS microphone such as its resonance frequency, without compromising its acoustic performance, as presented in Chapter 6 of this thesis.

In general, MEMS microphone technology benefits and follows the growing trend of CMOS technological advances. Devices are getting smaller and relatively cheaper to manufacture, following similar exponential technological trends such as predicted by *Moore's law* - allowing easier integration of sensors, circuits and systems almost everywhere. Nevertheless, trade-offs should always be considered, and probably the biggest challenges in acoustic sensors and system applications at the moment is finding new methods and techniques to further improve their performances under some complex conditions. Therefore, the next generation of acoustic sensors and systems, including further innovation in MEMS microphone's

technology may rely on fundamental research in the subject areas summarized as follows:

- Exploiting multiple methods of signal transduction such as piezoelectric and capacitive in the same device system;
- Combination of novel design ideas while integrating conventional sensing and actuation capabilities in the same device;
- New prototyping techniques;
- Unconventional methods of signal processing, for instance bio-inspired computation, applied on sensors, circuits and systems;
- Adaptive acoustic front-ends exploiting the use of feedback computation at the sensor level, aiming to achieve best-possible acoustic-electrical performances, while also using standard micro-fabrication and manufacturing processes.

There is potential for technological innovation in acoustic sensors, circuits and systems in order to address problems related to real-time audio signal processing in complex environments, while keeping devices small and operating at low power demands. Therefore, these are some of the topics of current research interests and developments involving different engineering disciplines, which in part, the bio-inspired work presented in this thesis aims to consider.

Chapter 3

Bio-Inspired Frequency Agile Acoustic Sensor System

Standard microphones and ultrasonic devices are generally designed with a broad and static frequency response in order to address multiple acoustic applications. Therefore, they may not be flexible or adaptable enough to deal with some requirements. For instance, when operated in noisy environments such devices might be vulnerable to wideband background noise or interfering signals, which might require further signal processing techniques to remove them, generally relying on digital signal processors (DSP).

In this chapter, it is considered if microphones or acoustic sensors in general could be designed to be sensitive only at selected frequencies of interest, whilst also providing flexibility in order to adapt their electromechanical responses to track signals of interest or to deal with environmental demands, noise or interfering signals. This line of thought is developed under the assumption that a "transducer can be part of the signal processing chain" by exploiting feedback processes between mechanical and electrical mechanisms that together can enhance peripheral sound processing. This capability is present within a biological acoustic system, namely in the ears of certain moths as noted in Chapter 2. That

is to be used as a model of inspiration for a smart acoustic sensor system concept, which enables dynamic adaptation of the front-end transducer's frequency response.

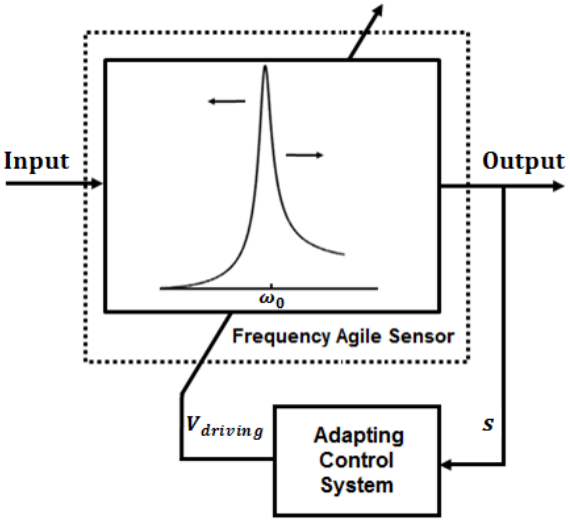

Figure 3.1: Diagram overview of the feedback control system that can be used to implement the concept of a frequency agile transducer. Where s represents the reference signal used to provide a processing response from the feedback system computation and $V_{driving}$ represents the control signal used to alter the frequency response of the front-end transducer.

From the engineering point-of-view, the *Noctuid* moth hearing system that was introduced in Chapter 2 might be represented as a system composed of an acoustic sensor with feedback computation capabilities as presented in Figure 3.1, where the "Frequency Agile Sensor" system represents the tympanic membrane (i.e., passive acoustic front-end detector); and the "Adaptive Control System" block represents a back-end neuronal processing (i.e., feedback computation), which enables the dynamic adaptations of the front-end sensory structure in order to alter its frequency response.

3.1 Theoretical Model

Recalling Chapter 2, hearing responsiveness is greatly dependent on interactions between mechanical and electrical processes inside the auditory system. Natural passive responses of front-end mechanical detectors (e.g., ear tympanic membranes) may show active responses due to incorporated feedback mechanisms, which then affect their mechanical structures for sound detection. For instance, moths have a tympanum-like ear that acts as a pressure sensor for sound sensing, which in some species shows adaptive capabilities such as frequency agile tuning. In some *Noctuid* moths, their ears show high sensitivity for quiet sounds at low frequencies, and when stimulated with loud sounds, sensitivity is shifted towards higher frequencies instead. This auditory system automatically adapts its sensitivity towards higher frequencies in order to become frequency tuned with the hunting signals of bats. This adaptable mechanism is seen as an active tuning system with interesting features, and possibly with great benefits to acoustic engineering.

Motivated by the dynamics and active processes reported from the auditory system of moths, a feedback control system framework was developed in order to prototype this concept of a frequency agile acoustic sensor system. First of all, it might be hypothesised that the moth's tympanic membrane is represented as a mass-spring system (e.g., a 2^{nd} order system, as noted in Chapter 2), which the natural resonance frequency is directly proportional to its spring's stiffness and mass. Modelling one of these elements (e.g., reactive terms) would allow the frequency response of the system to be altered since, ${\omega_0}^2 = \frac{k}{m}$. Furthermore, the Q-factor might also change along with the natural resonance frequency of the system, because $Q = \frac{\omega_0}{\gamma}$. It is reported in the literature [10] that the tympanic membrane of *Noctuid* moths might be somehow mechanically stretched to allow that dynamic tuning adaptation. Stretching might be provided to the system

by increasing tension over it (i.e., adding an external pulling force), which then expands the membrane and consequently changes its natural frequency response. From the engineering point of view, this assumption can be simply generalised as a thin membrane fixed on both sides while stretching is provided by adding a transverse tension at those points (e.g., pulling apart), as illustrated in Figure 3.2, which ideally expands the membrane uniformly and consequently alters the frequency response of this system, as illustrated in Figure 3.3.

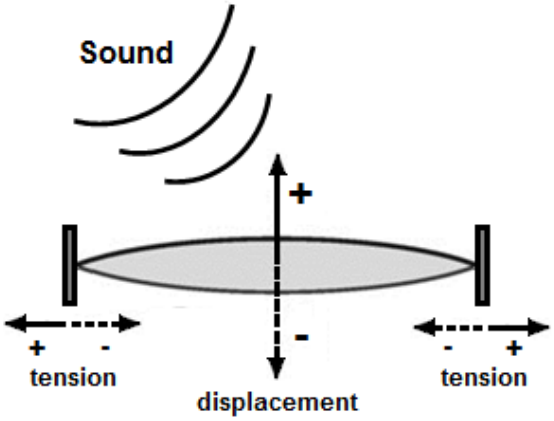

Figure 3.2: A fixed-fixed membrane structure as a simple system (2^{nd} order system) to model the tuning response of the tympanic membrane of moths.

Therefore, the structural acoustics (e.g., vibrational behaviour) of this system used as a front-end acoustic detector is approximated to a linear single degree of freedom oscillatory response (i.e. z-axis), which for the purposes of this study can be expressed mathematically as a 2^{nd} order system as presented in Laplace form in Equation 3.1:

$$H(s) = \frac{\omega_0}{s^2 + s\frac{\omega_0}{Q} + \omega_0^2} \tag{3.1}$$

Refer to Chapter 2 and [128] for further fundamental discussions about the behavioural responses given by a 2^{nd} order system of this type.

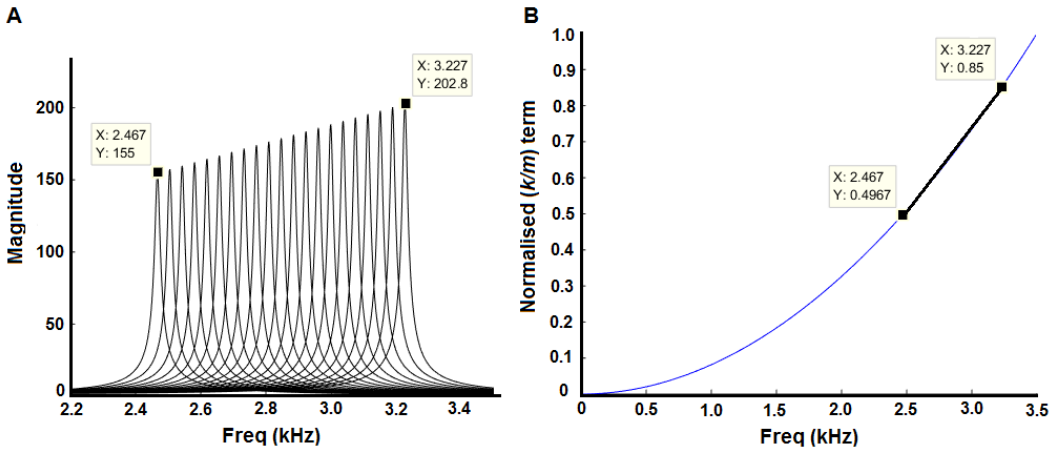

Figure 3.3: (A) Frequency response of a 2^{nd} order system, while ω_0 term is altered as a hypothetical consequence of providing additional tension over the mechanical structure, which consequently affects its stiffness – shifting resonance frequency. (B) Graphical representation of ${\omega_0}^2 = \frac{k}{m}$ – highlighting the region between two resonance frequencies, which shows a quasi-linear profile within that frequency-frame.

3.2 Frequency Agile Sensor (Front-end Acoustic Transducer – physical model)

For the prototyping purposes of this concept, and with the aim to investigate and better understand the behaviour given by a real acoustic system (e.g., physical model), an electromechanical setup was designed. A front-end acoustic transducer was fabricated using off-the-shelf materials, including a thin Kapton membrane (polyimide film: width = 22 mm; height = 3 mm; thickness = 50 μm) that is placed and glued on top of a piezoelectric (PZT) stack device. The PZT stack is used to provide the pulling force to expand and consequently to stretch the Kapton membrane, as illustrated in Figure 3.4. The PZT stack used in this prototype device is the PICMA® stack multilayer piezo actuator (ref: P-885.51) from PI Ceramic.

Theoretically, when providing additional tension (upon the pre-set equilibrium conditions after the device's fabrication stage) over the membrane by pulling the

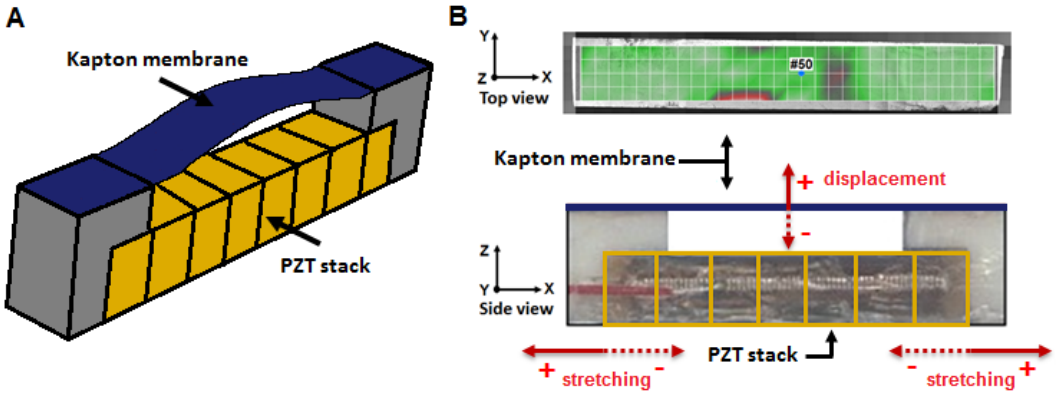

Figure 3.4: (A) 3D view of the purpose-built acoustic transducer that is manufactured using a Kapton membrane (50 μm thick) and a PZT stack (length = 18 mm; height = 3 mm; width = 3 mm). (B) Top-view of the transducer outlining a central point over the Kapton membrane (#50). Side-view of the transducer illustrating the polarity of displacement when the membrane is driven by sound and also the stretching direction, which the PZT stack can provide to alter the behaviour of the sensor system.

structure apart (at the side points), it should change the effective stiffness and consequently alter its natural resonance frequency response. Therefore, evaluation tests were conducted to investigate and analyse the acoustic-structural interactions in the purpose-built transducer using laser Doppler vibrometer (LDV) measurements as well as performing finite-element modelling in COMSOL. In order to predict the acousto-strutural interactions in the device before its fabrication, finite element modelling using COMSOL Multiphysics was performed using the acoustics and structural mechanics modules, as illustrated in Figure 3.5.

The frequency response resulting from COMSOL simulations is presented in Figure 3.6 (A). It shows a prediction of the frequency response given by the purpose-built transducer before its fabrication. It is important to have an approximation of its resonant eigenvalues since the dimensions of the structure can play a significant role in that. The membrane is also scanned using LDV techniques during acoustic stimuli and multiple resonance modes are identified, as

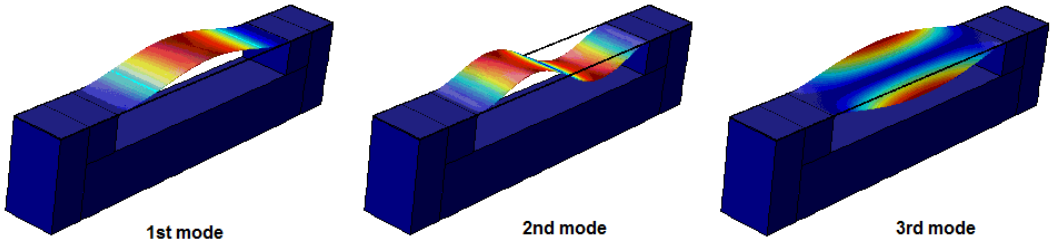

Figure 3.5: COMSOL model of the purpose-built device, showing the dynamical movement of the front-end membrane with three resonant behaviours.

illustrated in Figure 3.6 (B).

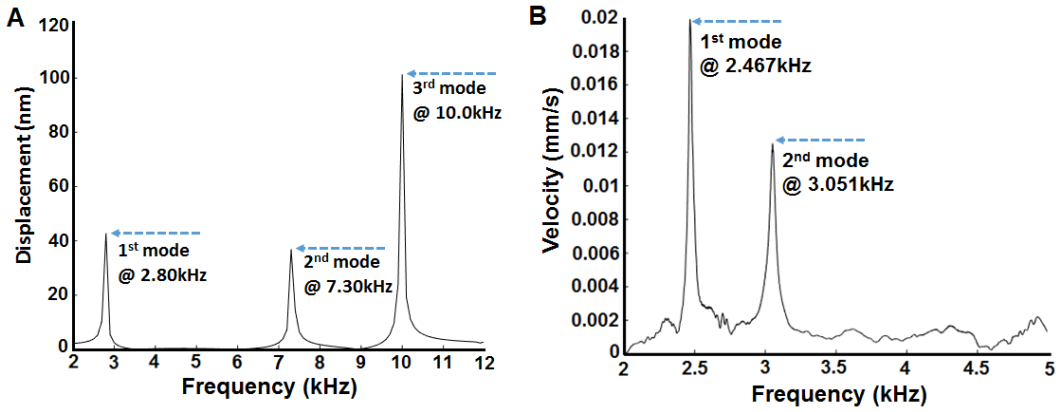

Figure 3.6: COMSOL and LDV measurement results. (A) COMSOL simulation showing the frequency response of the modelled transducer, presenting 3 resonant modes between 2 – 12 kHz. (B) Frequency response of the transducer measured with LDV, showing 2 resonant modes between 2 – 5 kHz related to outlined central point (#50) over the Kapton membrane (refer to Figure 3.4).

As previously described, the frequency response of the Kapton membrane can be altered by increasing tension over it and that was tested experimentally as presented in Figure 3.7. The tension effect over the purpose-built transducer is tested by driving the PZT stack with DC voltages between 0 – 100 V with 5 V step increments. A proportional shift of the natural resonance frequency and enhanced sensitivity of the sensor responsiveness was recorded. Experimental tests concentrated around the 1^{st} resonance frequency mode revealed that it can be shifted from 2.467 kHz to 3.227 kHz ($\Delta\omega$ = 760 Hz, where $\Delta\omega$ represents

the frequency shifting window in which the transducer can be operated). This evaluation test validates the transducer's design and fabrication processes through LDV techniques (refer to Figure 3.8 for the LDV setup used). The transducer's responsiveness faithfully matches the behaviour of a mass-spring system model - 2^{nd} order system response (refer to Figure 3.3), which is considered acceptable for the purposes of this study.

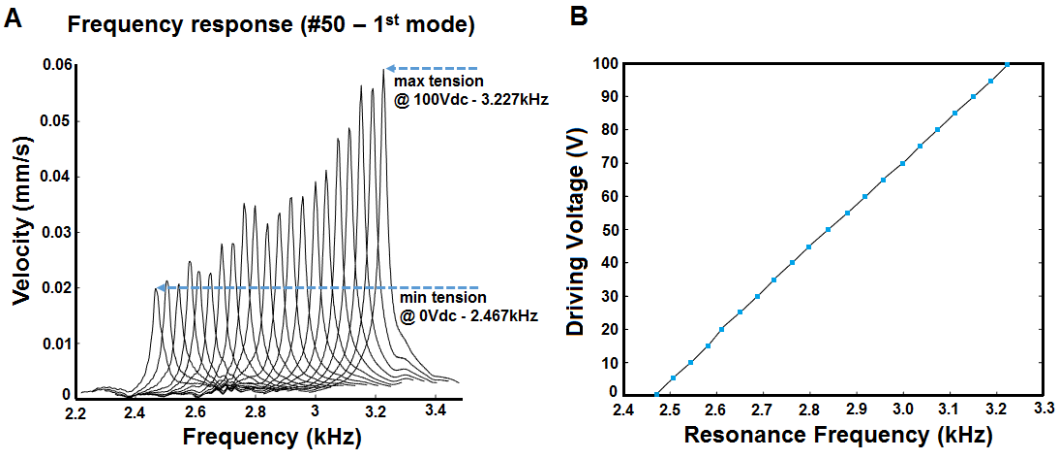

Figure 3.7: LDV measurement results while DC voltages are applied to the PZT stack terminals: (A) Plot representation of the 1^{st} resonant frequency mode of the Kapton membrane while providing different tensions (e.g., driving forces from 0 – 100 V with 5 V step increments); (B) Approximation to a quasi-linear shifting of the natural resonance frequency - $\Delta f \approx 38$ Hz @ $\Delta V = 5$ V. These plots show a favourable matching between the physical front-end transducer with its theoretical model as a 2^{nd} order system response (recall to Figure 3.3 for comparison). These evaluation tests required sound to be driven, using a sound transmitter/speaker (ESS HEIL Air-Motion Transformer) that was placed perpendicularly to the device, at a distance of 50 cm, which was excited by the internal signal generator of the LDV machine.

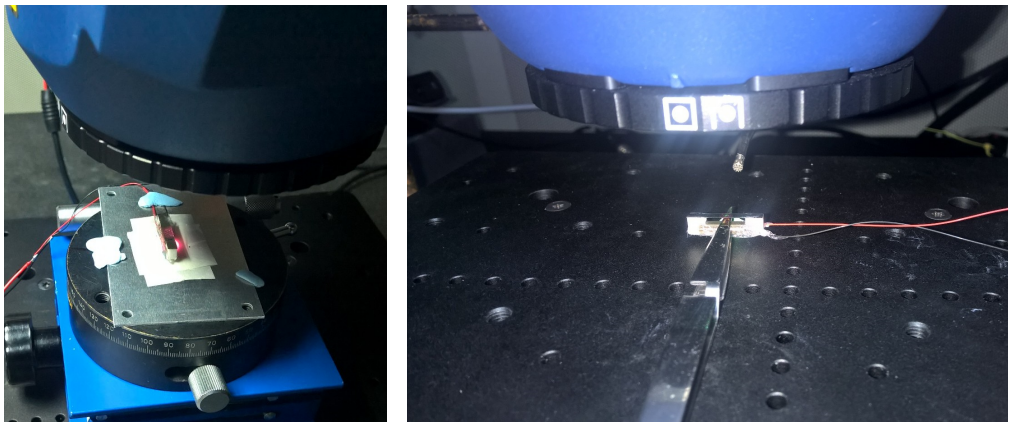

Figure 3.8: Images of the device under the LDV measurement machine (Polytec sensor head MSA-100-3D) ready for a scan.

3.3 Adapting Control System (Back-end Neuronal Computation)

In the moth hearing system, as reported in [10], the effective stiffness of the tympanic membrane might be physically dependent on the amplitude of the input acoustic stimuli reaching it (i.e., stiffness as a function of the input sound intensity). Following a similar approach, it is proposed that a back-end signal processing algorithm can be computed within a processing unit to progressively adapt the resonance frequency of the purpose-built acoustic transducer presented in Section 3.2. The algorithm is time and amplitude dependent to be similarly matched with the moth's hearing response and designed to be easily executed while providing real-time results. The workflow of signal processing is presented in Figure 3.9, which mimics some of the mechanisms of signal transduction within auditory sensory receptors, as the first two block systems represent the "Mechanoreceptor cells role" and the following two blocks the "Neuronal cells role" - refer to Chapter 2 (e.g., [5]) for biological background details.

The algorithm evolves as follows: the output signal s (readout from the sensor) is averaged over time and once the pre-defined threshold is reached, the

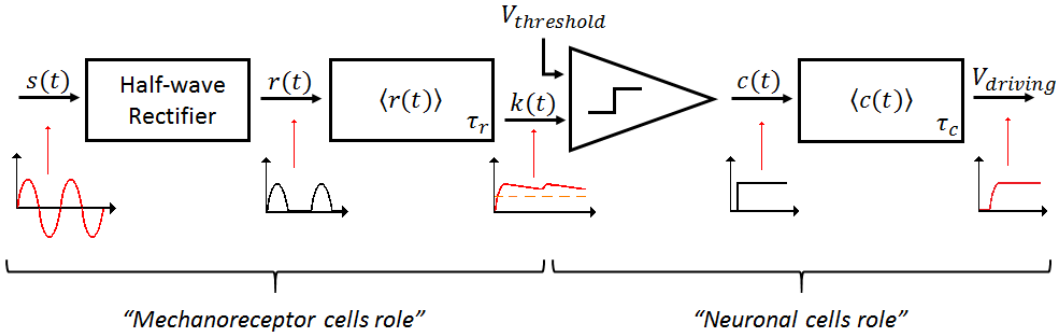

Figure 3.9: Schematic diagram of the "Adapting Control System" algorithm. Where s represents the output signal of the sensory system (refer to Figure 3.1), which is fed through the feedback pathway of signal processing; r represents the half-wave rectifier output signal; k shows the lowpass response outcome from the mechanoreceptor cells charging effect; c represents the on-off neuronal response (e.g., threshold based computation), which is then smoothed ($V_{driving}$) in order to provide a progressive control of the transducer's resonance frequency adaptation. τ_r and τ_c represent the time factors associated to $\langle r(t)\rangle$ and $\langle c(t)\rangle$ averaging block systems, respectively.

computational algorithm drives output signals ($V_{driving}$) to control the front-end transducer's frequency response (e.g., stretching the membrane – changing its stiffness). In this engineered version of "hearing" – the time averaging blocks $\langle r(t)\rangle$ and $\langle c(t)\rangle$ are implemented using a first order IIR (Infinite Impulse Response) system with transfer function given in Z-domain by Equation 3.2:

$$H(z) = \frac{\alpha}{1 - Z^{-1}(1-\alpha)} \tag{3.2}$$

Where $\alpha = \frac{dt}{\tau}$ represents the moving-average window coefficient and τ is the average time constant associated to this function, and dt is the time step resolution.

3.4 Numerical Simulation of the Purpose-Built Sensor System

The concept illustrated in Figure 3.1, and introduced previously as a theoretical model was then implemented through a numerical simulation in MatLab R2014b, and tested using synthetic signals with sampling time resolution of $dt = 20\mu$s.

First, the "Adapting Control System" algorithm was tested in an open-loop configuration with synthetic input signals as follows. As explained before, the algorithm is divided in two parts: "Mechanoreceptor cells role" and "Neuronal cells role". It has been reported in the literature [5] that when increasing frequency of the input stimuli, mechanoreceptor cells gradually alter their response from alternating mode (AC) to direct mode (DC) – that behaviour is included in this model, and is achieved by the coupling between the initial two blocks (half-wave rectifier + lowpass filtering) of this computational algorithm. In Figure 3.10 the top graphs illustrate four examples of $s(t)$ signals (i.e., reference/readout signals from the sensor, which are used to feed the workflow of signal processing). The processing shows a gradual change from AC to DC mode of operation while increasing signal frequency. This behaviour is illustrated in Figure 3.10 bottom graphs with $k(t)$ signal plot. This charging effect is dependent on $\langle r(t) \rangle$ time constant - τ_r.

The "Neuronal cells role" is then the next step performed by the algorithm. It is set by a comparison between a threshold previously defined with the resultant signal $k(t)$ followed by an additional lowpass filtering - $\langle c(t) \rangle$. Figure 3.11 (A) presents three examples of signal processing outputs using different threshold values (i.e., 0.01, 0.025 and 0.04 – from Bottom to Top). The output of the comparator is defined by $c(t)$, which is essentially an on-off output signal. If $k(t)$ presents an oscillatory signature at the input of the comparator around its threshold value ($V_{threshold}$), as illustrated in Figure 3.11 (A): Top and Middle

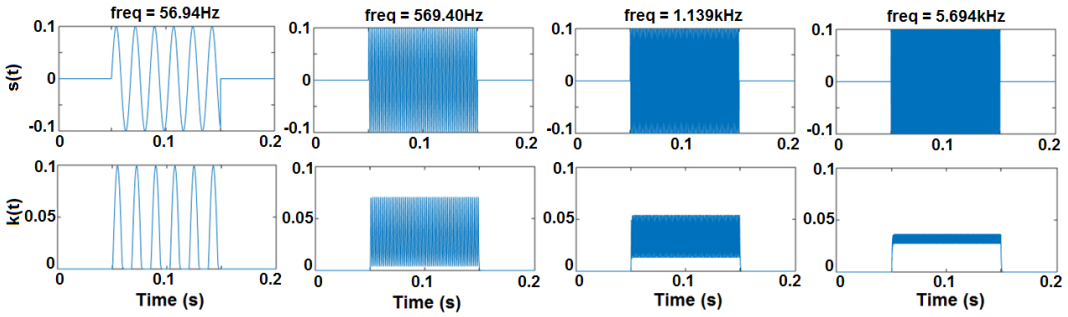

Figure 3.10: Mechanoreceptor cells role" signal processing response showing gradual changing from AC to DC mode of operation when frequency of the input stimuli is increased – with $\tau_r = 0.351$ ms.

graphs, that will trigger an oscillatory on-off response of $c(t)$, as illustrated in Figure 3.11 (B): Top and Middle graphs. So, the role that $\langle c(t) \rangle$ plays to ensure a more stable and smoothed output signal ($V_{driving}$) of the algorithm is essential for the sake of overall system stability. On the one hand, low averaging times within $\langle c(t) \rangle \rightarrow \tau_c$ will set faster overall responses (e.g., onset of the algorithm), however it will make the system less robust to fast switching at the comparator stage – Figure 3.11 (B): Top and Middle plots on the left shows $c(t)$ signal with some ripple when $\tau_c = 1$ ms. On the other hand, higher averaging time constants will improve the system's robustness against fast switching, however it might cause the system to react slower – spending more time to achieve its steady-state, Figure 3.11 (B): Top and Middle plots on the right show $c(t)$ signal more immune to fast switching but with slow convergence time when $\tau_c = 50$ ms. When the threshold is fully achieved with a DC component at $k(t)$ that will set a smoothed and progressive output response of the algorithm, as illustrated in Figure 3.11 – Bottom plots for $Vth = 0.01$. The overall time response of the algorithm is then mainly dependent on τ_c, since τ_r is kept significantly smaller in comparison, ensuring DC modes of operation at low frequencies.

In order to analyse the system's overall dynamics, a model using a front-end acoustic receiver expressed by Equation 3.1 is placed within a feedback loop

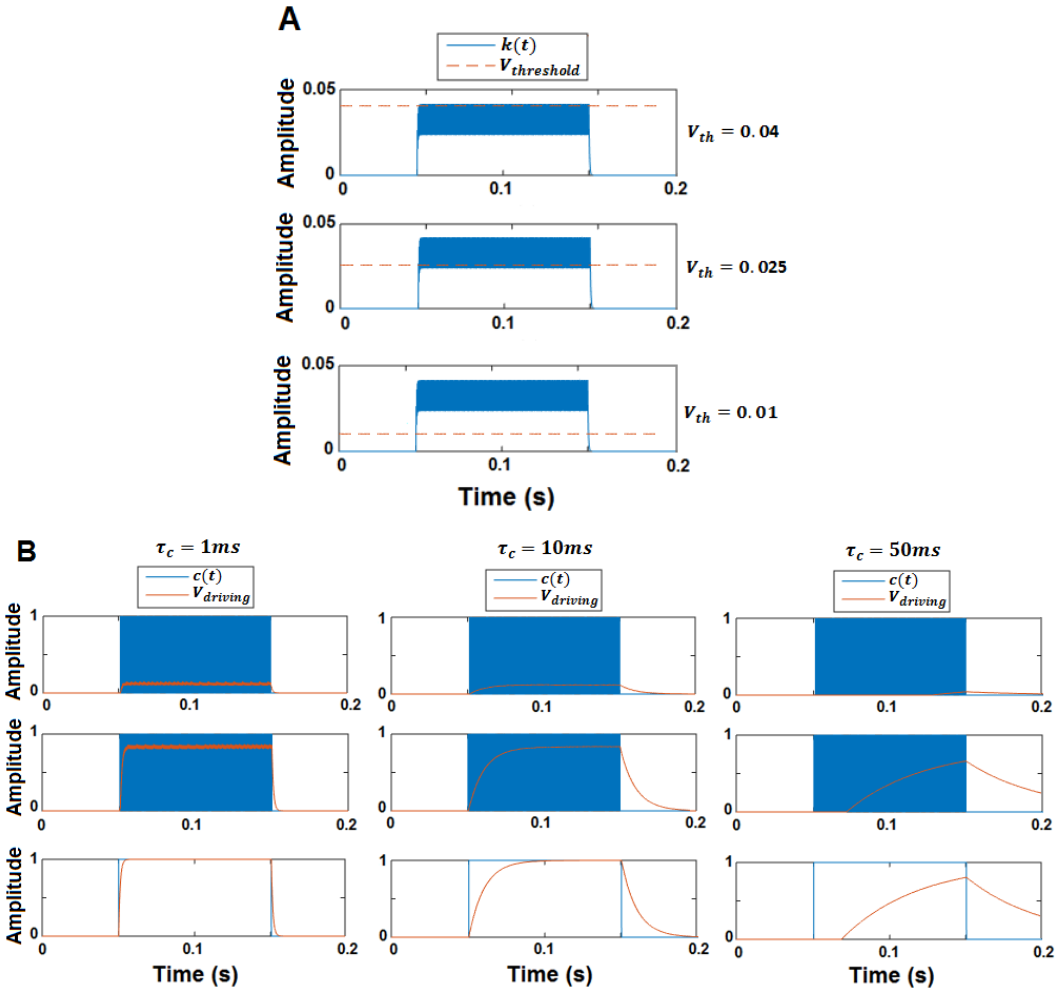

Figure 3.11: "Neuronal cells role" signal processing response showing threshold and time dependency settled mainly by the comparator and $\langle c(t) \rangle$ blocks, respectively. (A) Shows three examples of $k(t)$ signal using different thresholds; (B) illustrates the correspondent signals $c(t)$ showing the influence of τ_c in the algorithm's performance and stability.

fashion controlled by the computational chain of signal processing blocks as the "Adapting Control System" algorithm introduced in Figure 3.9. Three different synthetized sound signals are presented to the system's input to trigger frequency tuning that travels from f_0 towards f_0'', as illustrated in Figure 3.12.

First of all in (a), tuning is seen at the beginning of the input signal with frequency f_0, however once the algorithm starts to be iterated that will initi-

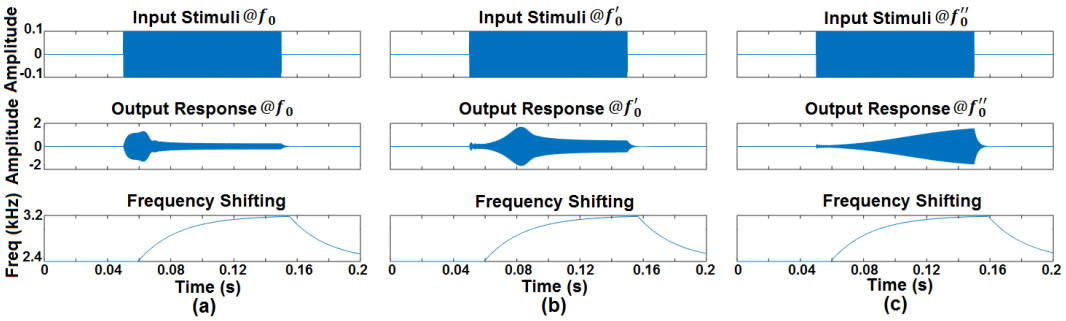

Figure 3.12: Modelling the feedback control system that is illustrated in Figure 3.1, showing three different resonance tuning responses (a), (b) and (c) at $f_0 = 2.467$ kHz, $f_0' = 2.847$ kHz and $f_0'' = 3.227$ kHz, respectively with $Q = 10$. Using $\tau_r = 0.351$ ms, $V_{threshold} = 0.01$ and $\tau_c = 25$ ms.

ate its influence over the front-end sensor frequency response (i.e., showing the mechanical properties of the front-end transducer being changed) and so after approximately 25 ms the system's tuning becomes off-resonance. Secondly, in (b) the input signal with frequency f_0' is not initially matched with the initial resonant frequency of the system f_0, however after approximately 25 ms of the input stimulus being presented, the system shows resonant tuning matched with the input signal at frequency f_0', due to feedback adaptation. Thirdly, in (c) the resonance tuning response of the system is matched with the input signal at frequency f_0''. This happens when the algorithm reaches its steady-state adaptation. If there is no acoustic input presented to the sensory system, the threshold will not be reached and so the front-end sensor frequency response will return back to its initial resonance at f_0.

The impulse response of the overall system was also tested, as presented in Figure 3.13, and that shows higher immunity to fast transients of the input signal when using higher values of τ_c. So, the overall stability given by the feedback control algorithm is dependent on those three parameters: τ_r, $V_{threshold}$ and τ_c. However, it can be mainly controlled by τ_c when kept higher than the settling time of the front-end sensor itself (e.g., approximately 5 ms for a $Q = 10$), in detriment to the algorithm's time of convergence. For instance, in Figure 3.13

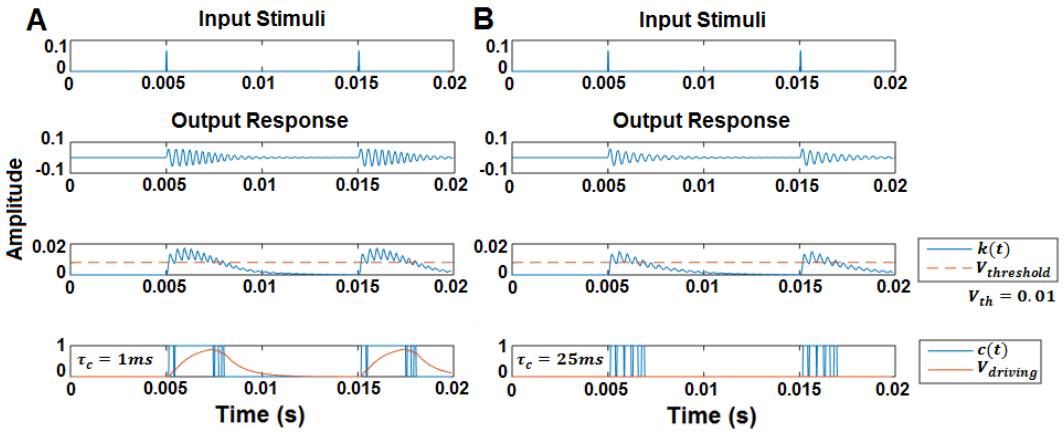

Figure 3.13: Impulse response of the overall feedback control system has a settling time ≈ 5ms – see "Output Response" plots; with $Q = 10$; $\tau_r = 0.351$ ms and $V_{threshold} = 0.01$. (A) $\tau_c = 1$ ms; and (B) $\tau_c = 25$ ms.

(B) – when $\tau_c = 25$ ms, the algorithm accounts for the transducer's settling time to occur, which then improves the system's stability when fast input transient appears, compared to when $\tau_c = 1$ ms, as illustrated in Figure 3.13 (A).

It is important to note that the criterion used to define the value of τ_r is based on the input signal frequency to set the transition between AC and DC mode, for instance $\tau_r = 0.351$ ms sets this transition when $f_{in} = f_0' = 2.847$ kHz. Furthermore, the criterion used to define τ_c is based on the assumption that this concept is meant to be a slow adaptation process. Therefore, τ_c is defined to be 5x greater than the settling time of the front-end receiver impulse response, which is $\tau_c = 25$ ms for a $Q = 10$ with setting time ≈ 5ms, as shown in Figure 3.13.

3.5 Experimental Embedded System Setup

In order to implement the concept experimentally (e.g., physical model), a feedback control system that ensures results in real-time was prototyped through an embedded system setup, as illustrated in Figure 3.14. As previously described,

the acoustic transducer, which is built with Kapton and PZT materials, and the feedback control algorithm proposed were both integrated in this experimental setup.

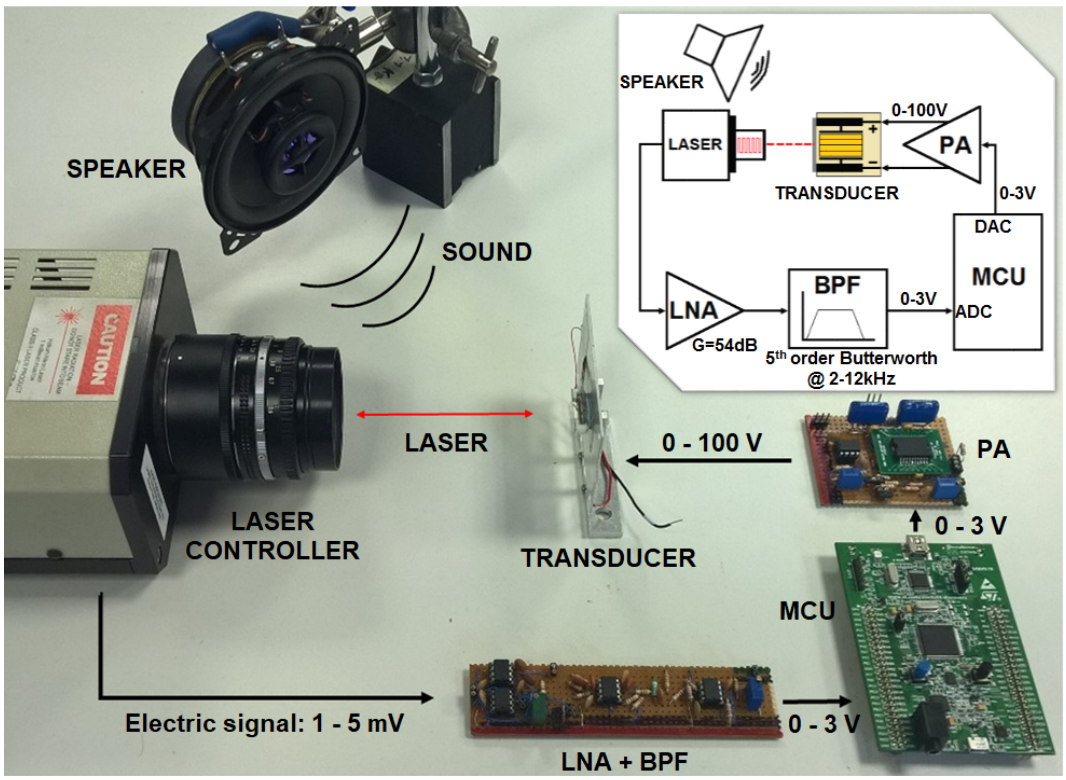

Figure 3.14: Experimental setup and schematic overview (inset) of the embedded system and circuit blocks used to implement the frequency agile concept in a real-time processing scenario.

A laser vibrometer (head + controller: Polytec OFV 2700) providing an analogue output was used as a reference measurement signal of the displacements induced on the Kapton membrane from acoustic stimuli. A 32-bit Micro-controller Unit (MCU) from STMicroelectronics (STM32F4) running with a clock frequency of 168 MHz is used to acquire signals and to compute the feedback control algorithm. Pre-amplification and filtering are provided that are integrated on an analogue conditioning circuit for the output signals coming from the laser controller. Signal acquisition is done using an on-board A/D converter (e.g., 12-bit

resolution, unipolar input [0 – 3 V]) with a sampling frequency of 50 kHz. Data is acquired and managed using interrupt-based routines. The threshold based algorithm is executed inside the Central Processing Unit (CPU), which is set according to the intensity of the input sound signals measured, such that the feedback control system can dynamically adapt the structural mechanics of the front-end transducer in real-time. The PZT stack is actuated using a D/A converter (e.g., 12-bit resolution, single-ended output [0 – 3 V]) with an additional analogue driving circuit to amplify compatible output signals.

3.5.1 Acquisition Workflow

As previously mentioned, the aim of this purpose-built embedded system setup is to implement the concept of a frequency agile acoustic sensor system, which can provide results in a real-time scenario, so the setup should ensure real-time signal processing capabilities with accurate data sampling. The approach is based on hard and soft interrupt routines, which allow prioritization of the acquisition task. The sampling rate of the A/D required three hardware interrupt routines (e.g., computational operations without CPU intervention) configured as follows and presented in Figure 3.15:

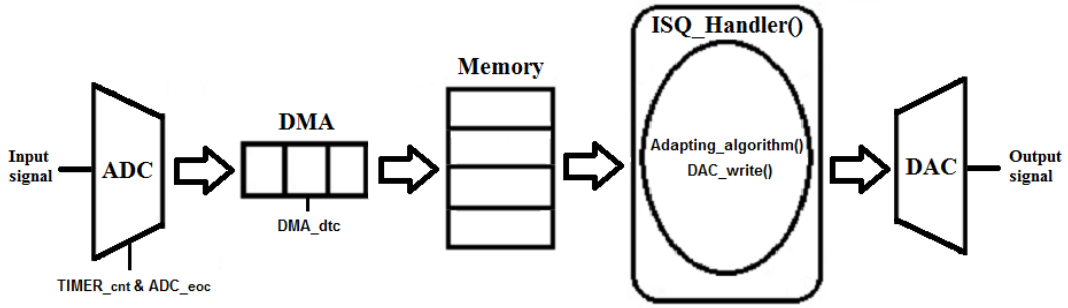

Figure 3.15: Diagram overview of the acquisition and real-time signal processing workflow that is relied on a sample-by-sample computation.

1. Timer interrupt (configured in counter mode – e.g., $TIMER_{cnt}$) is used to

trigger the A/D to start acquisition/sampling;

2. A/D end-of-conversion flag (e.g., ADC_{eoc}) is used to signal the DMA controller to collect and transfer data samples from the A/D register to memory (RAM);

3. DMA data-transfer-complete flag (e.g., DMA_{dtc}) is used to signal the CPU through a software interrupt routine (e.g., $ISQ_{Handler()}$) when data is ready to be processed.

4. The CPU computes the algorithm (e.g., $Adapting - algorithm()$), which outputs the results through the D/A controller that drives compatible signals (e.g., $DAC - write()$) to the transducer.

3.5.2 Analogue Conditioning Circuits

Signals relating to the Kapton membrane's displacements are measured using an optical readout. Due to the inherent setup (e.g., manual alignment of the laser head + laser light, etc.), the output signals given by the laser controller can exhibit low signal-to-noise ratio levels. In order to ensure suitable discrimination of signals acquired by the A/D stage, amplification and filtering were required.

Figure 3.16 shows the schematic of the circuit used to perform the conditioning of signals from the laser controller. Amplification is performed using an instrumentation amplifier (INA) front-end with a variable gain, up to 54 dB, including an additional filter stage for low frequency suppression, with cut-off frequency approximately 2 kHz. Lowpass filtering is also provided using a Butterworth 4^{th} order filter, with cut-off frequency approximately 12 kHz, in a Sallen-Key configuration – this is for anti-aliasing filtering as well as high frequency suppression. Its frequency response is presetned in Figure 3.17. The final stage of this conditioning circuit is a variable DC level-shift circuit, which provides single-ended output from this circuit to the MCU's on-board A/D unipolar input (0 – 3 V) as

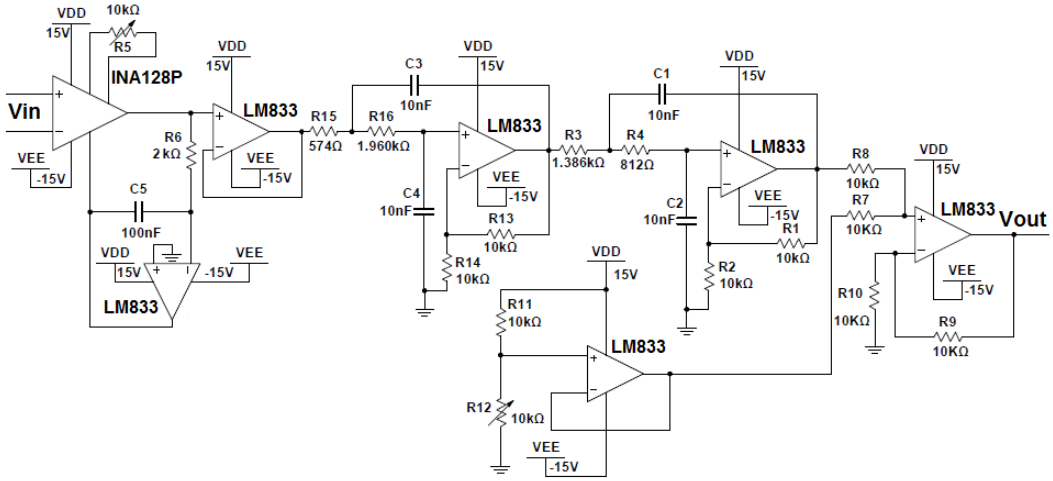

Figure 3.16: Schematic overview of the circuit used for readout from the laser controller – LNA, BPF, and DC level shift.

well as to correct any DC-offset errors added from the previous stages of signal conditioning.

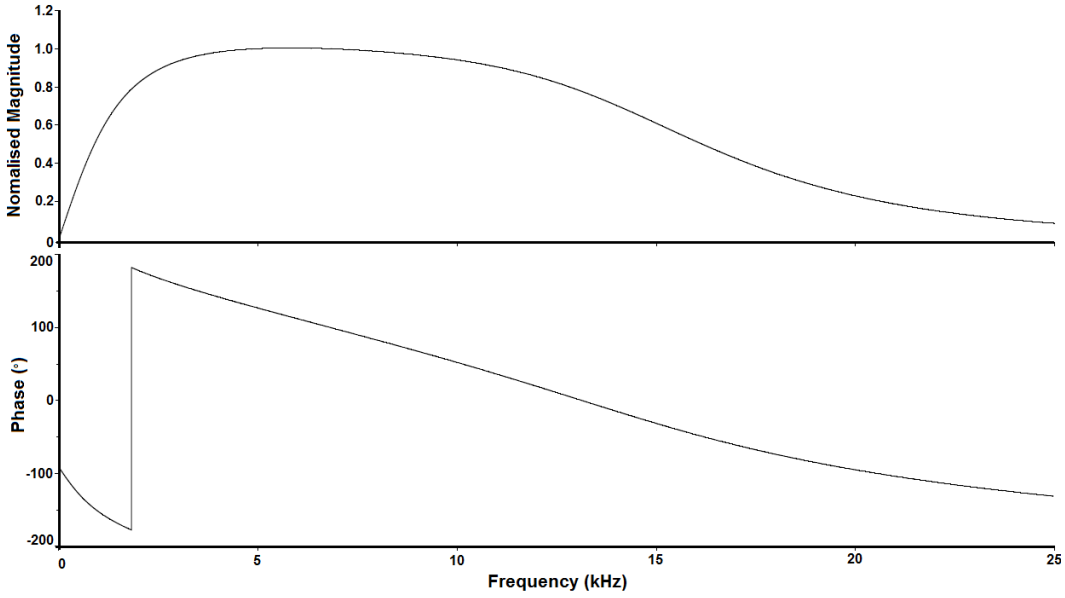

Figure 3.17: Frequency response of the analogue conditioning circuit to provide a bandpass filtering with a quasi-linear phase response between 2 and 12 kHz.

In order to operate the PZT stack within a voltage range of 0 V up to 100 V, it was necessary to design a circuit to amplify, with up to 30 dB of gain, the

output signals from the D/A (unipolar 0 – 3 V). A non-inverter amplifier circuit configuration using the PA78 device from Apex Microtechnology was used, as illustrated in Figure 3.18.

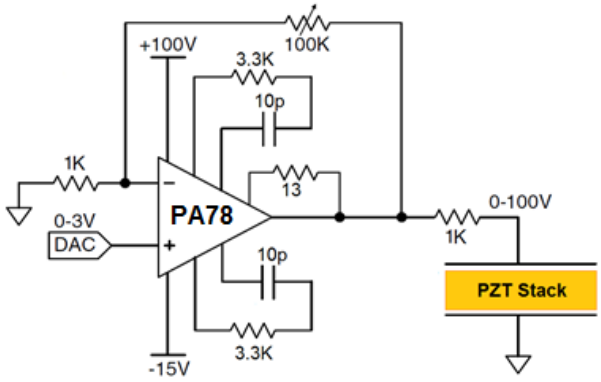

Figure 3.18: Schematic overview of the driver circuit used to amplify the output signals from the D/A converter (0 – 3 V) to operate the PZT stack (0 – 100 V).

3.6 Experimental Results of the Closed-Loop Sensory System

The embedded system setup was also tested integrating all its parts, including the acoustic transducer placed within the embedded closed-loop system, as illustrated in Figure 3.14. The MCU was loaded with the code of the feedback control algorithm following the processing workflow as presented in Figure 3.9. Figure 3.19 shows three different tuning responses given by the presented embedded system setup. Frequency tuning travels from f_0 towards f_0'', similarly to that presented through numerical simulation from the theoretical model as illustrated in Figure 3.12. Firstly in (a), tuning is seen at the beginning of the input signal with frequency f_0, however once the membrane starts being stretched with a transverse positive tension, the mechanical properties of the membrane are changed and so is its frequency response – after approximately 25 ms the system

tuning becomes off-resonance. Secondly in (b), the input signal with frequency $f_0^{'}$ is not matched with the initial resonant frequency of the transducer f_0, however, after approximately 25 ms of the input stimulus being presented, and due to mechanical adaptations of the membrane, the system shows resonant tuning matched with the input signal at frequency $f_0^{'}$. Thirdly in (c), the resonance tuning response of the system is matched with the input signal at frequency $f_0^{''}$ when the membrane is fully stretched (e.g., max. tension provided). If there is no acoustic input presented to the system setup, the algorithm will set no stretching output (e.g., min. tension provided) to the front-end sensor, which will return back to its initial resonance frequency at f_0.

The processing time spent while computing the feedback control algorithm was measured at approximately 5 μs running the CPU at 168 MHz, which is far smaller than the sampling time of the computational system - 20 μs (e.g., time window between consecutive data samples), which ensures reliable real-time signal processing conditions. Quantitative tests were also performed in order to characterize the temporal uncertainty of the data acquired by the purpose-built computational embedded acquisition setup (refer to Fig. 13), during the experimental stage, while following the technique proposed in [129], and the results are summarized in Table 3.1, for an applied triangular signal from 0 – 3V at 1 kHz as a reference signal driven by a digital Agilent Waveform Generator (33250A) with output resolution of 14-bit.

Table 3.1: Temporal uncertainty of the purpose-built acquisition system at Fs = 1 kHz as a reference test signal.

Fs (real) [Hz]	**Aperture Delay (skew)** [%]	**Aperture Jitter** [%]
1000.1611 ± 0.054	-0.01611	0.0054

The power consumption of the overall embedded system was estimated at around 500 mW – based on the expected operating conditions of the CPU and

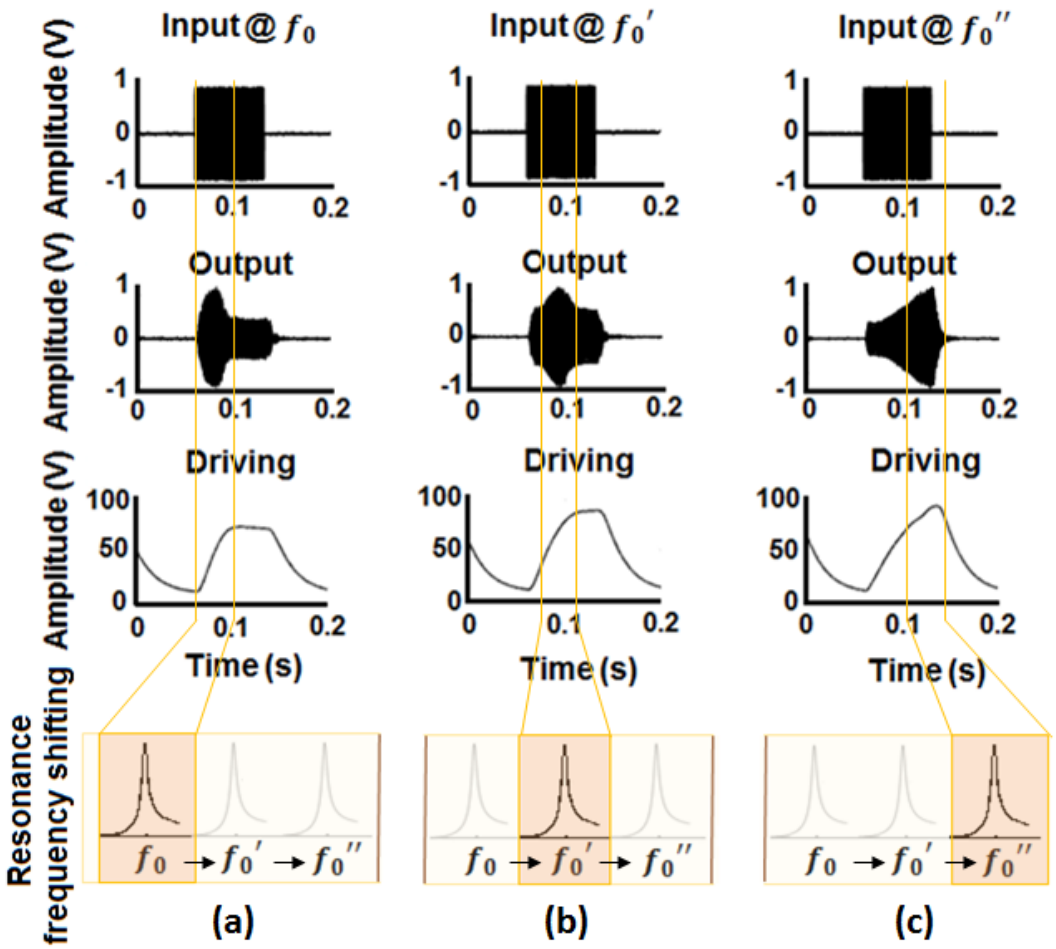

Figure 3.19: Experimental results showing dynamic frequency adaptation given by the embedded system setup in a closed-loop configuration, presenting time ($\tau = \tau_r + \tau_c \approx 25$ ms) and amplitude ($V_{th} = 0.5$ V) dependencies (recall to Figure 3.12 for comparison with the numerical simulation of the purpose-built system).

digital hardware cores configured for processing tasks as well as the analogue circuitry used for signal conditioning and driving.

3.7 Discussion

Inspired by the feedback mechanisms used to achieve frequency agile tuning in the *Noctuid* moth ears [10], a novel engineered acoustic transducer concept is

introduced combining mechanical signal processing with a complementary electrical feedback computation - *the transducer therefore computes, as the natural sensory system does*, to enhance peripheral signal conditioning and processing capabilities. This is the first prototype version for a frequency agile tuning concept that describes, models and validates the design of an acoustic sensor system, a combination of Kapton and piezoelectric ceramic materials. The use of materials such as PZT was fundamental to achieve the adaptations of the front-end transducer due to its electromechanical properties. Other smart materials such as polymers (e.g., EFOAM, PVDF or EAP) are also promising materials to exploit and use within new sensor-actuator designs in active control applications since they are light weight, flexible, low-cost, give easy integration into any size or material shape, among other characteristics [103]. The use of novel manufacturing processes may also be considered based on 3D printing techniques [130]. Furthermore, feedback computation was also applied in order to process acoustic signals based on "simple" mechanisms of auditory signal processing [5]. Moreover, an embedded system setup was prototyped in a feedback control loop to compute the algorithm that dynamically adapts the frequency response of the front-end transducer. Experimental results given by the purpose-built sensor system are faithfully matched with their simulated model equivalents, which are used to better describe and characterize the concept and its overall frequency agile tuning behaviour.

The purpose-built acoustic transducer follows a quasi-linear resonant-shifting response over a dynamic frequency range of 760 Hz. It has 38 Hz of frequency resolution for each 5 V step, and the embedded system response time was set to be approximately 25 ms, which is the time defined for the sensor to operate from f_0 to $f_0^{''}$ using 0 to 100 V, respectively. The system stability was evaluated by simulation and it is mainly controlled by the algorithm's time constant τ_c. It is concluded that the τ_c time constant can ensure higher immunity to fast

transients of the input signal if kept higher than the settling time of the front-end transducer itself (e.g., dependent on the Q-factor of the sensor) – here a slow adaptation process is considered.

The work described in this chapter introduces the fundamentals of a novel concept of signal processing at the sensor level that can potentially be exploited by sensor and system designers in the future developments of acoustic devices. An acoustic signal processing framework integrating a functional prototype system was engineered to support the concept of a frequency agile sensor, however further improvements may be included in the next generation (e.g., advanced prototyping stages such as miniaturization) of this concept in order to address real world applications, outlined as follows:

- **Front-end transducer**: in this initial prototype version for a frequency agile acoustic sensor system, a transducer is made with a Kapton membrane (50 μm thick) glued on top of a PZT stack (length = 18 mm; height = 3 mm; width = 3 mm) is used to sense acoustic signals, using an optical readout signal, and actuating through the piezoelectric functionality embedded in the sensor itself. Further developments at the transducer level should be to make the device (e.g., acoustic detector/sensor) smaller and easier to integrate with integrated circuits and systems, for instance by exploiting micro fabrication techniques towards the design of miniaturised microphones or ultrasonic devices based on MEMS technology. Some ideas should be highlighted in this regard:

  This concept of frequency agile tuning might be more advantageous when using a high-Q transducer/detector/sensor, so the design and fabrication requirements should accomplish that;

  Readout and actuation on the transducer can be done by using a combination of standard sensing and actuation techniques, which can be optic (readout only), piezoelectric (readout and/or actuation) and capacitive

(readout and/or actuation), with all the advantages and disadvantages associated to them as well as the demands of custom design for the analogue front-end signal conditioning circuits with respect to each one of those transduction/actuation modalities.

- **Feedback computation**: with proper revision, the feedback control algorithm or any computational approach, either analogue, digital or both modalities combined, can be designed to scan and hold at desired frequencies of interest instead of just moving up and down in the spectrum based on the intensity level of the input signal detected. Additional ideas can also be exploited in this regard are:

  Other variables for decision making and adaptation can be used rather than only based on a static threshold. The threshold might be adaptable over time and this algorithm or any kind of computation technique chosen (e.g., digital, analogue, or both) can evolve according to selected features of the input signal. For instance its amplitude and frequency signatures that if combined with the transducer's response may allow the system to track more complex signals instead of only single tone frequencies. Moreover, a combination of multiple agile sensors of this kind that can be placed in an array fashion can be exploited to address the processing of more complex signals such as human speech, tuning with the specific peaks of their sound spectrum - formants. In that case, tracking speech-formants would require multiple bands with differing widths and shifting capabilities;

  An acoustic sensor might be also adaptable to deal with environmental changes such as atmospheric pressure and temperature gradients, which can affect the transducer's natural response and its overall performances over time. So, making a sensor adaptable over time might be of great importance to increase sensing fidelity in an audio measurement device system [131],

[132];

The algorithm presented in this study includes computational operations such as rectification, averaging and comparisons, which can be performed without the need for a digital computational unit executing DSP operations. Thus, the overall power consumption of such an adaptable audio system might be reduced if exploiting feedback computation between the front-end acoustic transducer/detector and its back-end systems using low power electronics based on integrated circuits and analogue signal processing techniques such like some of the examples presented in [89].

Chapter 4

Bio-inspired Active Amplification in an Acoustic Sensor System

Over many millions of years of evolution, nature has developed some of the most adaptable sensors and sensory systems possible, capable of sensing, conditioning and processing signals in a very power- and size-effective manner. By looking into biological sensors and systems as a source of inspirations, this chapter presents a study of a bio-inspired concept of signal processing performed at the transducer level. By exploiting a feedback control mechanism between the front-end acoustic sensor and back-end neuronal based computation, a nonlinear active amplification with hysteretic behaviour is created. Moreover, the transient response of the front-end acoustic sensor can also be controlled and enhanced. A theoretical model is proposed and the concept is prototyped experimentally through an embedded system setup that can provide dynamic adaptations of a sensory system comprising a MEMS microphone placed in a closed-loop positive feedback configuration. It faithfully mimics the mosquito's active hearing response as a function of the input sound intensity (refer to Chapter 2 for details about mosquito's hearing and active processes). Inspired by that unconventional mechanism of signal detection and conditioning, an engineered system using a cycle-by-cycle feedback

based computation can be developed to manipulate the response of the front-end acoustic detector, as illustrated in Figure 4.1.

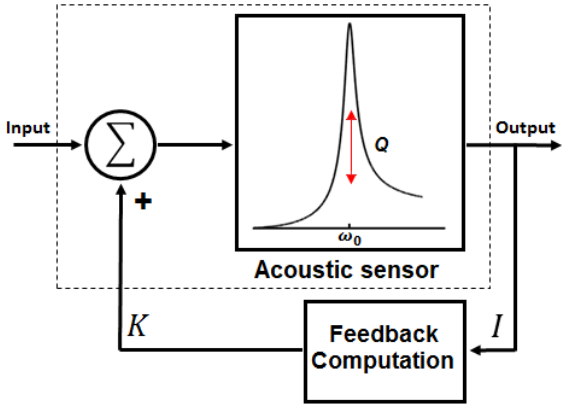

Figure 4.1: Diagram overview of the feedback control system that can be used to implement the concept of active nonlinear amplification such as for Q-factor control. That is inspired by the mosquito's hearing system. "Acoustic sensor" represents the front-end acoustic detector/sensor/transducer such as a MEMS microphone; "Feedback Computation" represents the back-end feedback control based on a cycle-by-cycle signal processing used to pump additional energy (K) to the front-end detector/sensor/transducer dependent on past signals detected (I).

The assumption is that the active amplification responsiveness to acoustic signals can be greatly enhanced by synchronized pulsatile signals supplying additional energy per cycle entrained (e.g., phase-locking) with the front-end acoustic detector through a positive feedback mechanism.

4.1 Theoretical Model

A bio-inspired concept for sensory signal detection and conditioning such as active nonlinear amplification that exploits feedback computation at the sensor level is proposed and described as follows. It faithfully describes an active process that is inspired by the possible physical basis for the mosquito hearing. From the engineering point of view, this concept can be illustrated by the closed-loop

diagram presented in Figure 4.2 and its transfer function is expressed by Equation 4.1:

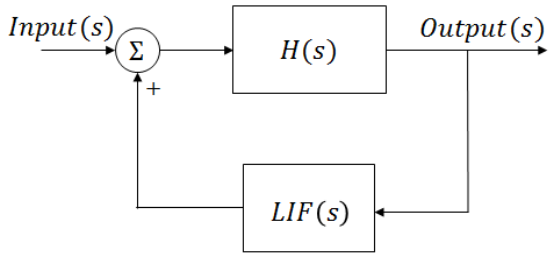

Figure 4.2: Diagram overview of the closed-loop feedback system used to model the concept of active nonlinear amplification. $H(s)$ represents the transfer function of a front-end acoustic sensor (e.g., MEMS microphone) and $LIF(s)$ is the transfer function of a smart pulse generator (e.g., back-end neuronal system response outputted by a computational machine) that is placed in a positive-feedback fashion. $Input(s)$ represents mechanical vibrations due to acoustic energy coupled with the sound detector structure (e.g., microphone's diaphragm) and $Output(s)$ is the signal readout from the acoustic sensor (e.g., signal resulted from the transduction method used, for instance optical readout using laser light can be used to measure the diaphragm displacements. Other transduction methods are also valid such as piezoelectric or capacitive, as exploited in Chapter 6).

$$\frac{Output(s)}{Input(s)} = \frac{H(s)}{1 - LIF(s).H(s)} \tag{4.1}$$

This concept is based on the assumption of a feedback system architecture considering two fundamental elements:

1. **A front-end acoustic sensor**, which has the role to detect sound, performing the first stage of signal detection and conditioning (e.g., mechanical filtering and transduction of energy from mechanical to an electrical form); And, this sensor's design should include actuation capabilities;

2. **A back-end computational system (e.g., either analogue or digital, or both)**, which assists in the process to further enhance the sensor responsiveness to a targeted stimulus.

Therefore, the overall response of this sensory system concept is greatly dependent on the coupling between these two elements (e.g., front-end acoustic sensor + back-end computational system), which once combined can result in a nonlinear active amplification with hysteretic behaviour.

Theoretically, if the damping of a front-end acoustic sensor can be changed dynamically, that might have a consequent effect on its sensitivity to sound (e.g., Q-factor is altered, as noted in Chapter 2). This principle can be achieved through the entrainment of pulsatile energy, a form of square-shaped pulses that are injected to the front-end acoustic detector in a synchronized and cycle-by-cycle manner (e.g. phase-locking), for instance, exploiting 1:1 resonance mode, as illustrated in Figure 4.3.

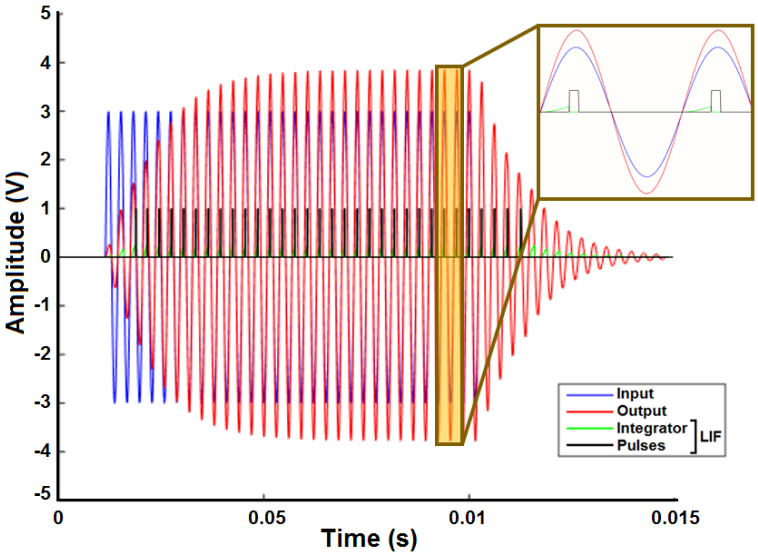

Figure 4.3: Example of 1:1 resonance mode entrainment of the input signal (blue trace) with square pulses (black trace). Pulses are generated after the integration of signals (green trace) reaching a defined threshold level. Overall, the coupling of both signals may result in an amplified and mechanically filtered output response (red trace) performed at the sensor level.

Generally speaking, it means that feedback signals (e.g., pulses) are entrained with the input signal at the same frequency and polarity. Therefore, an amplified and filtered response can likely result from an in-phase summation of signals

that are mechanically coupled by the front-end acoustic sensor. For instance in a real system (e.g., a physical model), it means that the mechanical vibrations induced by the input sound waves into, say a microphone's diaphragm are likely to be added to the vibrations generated by the pulsatile actuation imposed by the feedback system mechanism (e.g., back-end neuronal system response outputted by a computational machine). Therefore, the summation of signals is done at the mechanical level of the microphone's diaphragm itself (refer to the experimental setup in Section 4.3 for a practical implementation of this active nonlinear amplification concept). Additionally, under certain conditions it may behave like a critical acoustic sensor – an active system that operates near the oscillatory instability [133]. This behaviour has been described from within several studies on biological acoustic sensors and hearing systems [134], and has also been included within state-of-the-art auditory models [66].

4.1.1 Front-end Acoustic Sensor

Conventionally, the resonant response exhibited by a front-end acoustic detector (e.g. when approximated to a linear single degree of freedom oscillator) resembles the one given by a driven damped harmonic oscillator [41], which for the purposes of this study can simply be expressed by the transfer function in Equation 4.2, where s represents the Laplace term ($s = i\omega$):

$$H(s) = \frac{s\frac{\omega_0}{Q}}{s^2 + s\frac{\omega_0}{Q} + \omega_0^2} \tag{4.2}$$

Refer to Chapter 2 for further discussion about passive acoustic sensor/resonator modelled as 2^{nd} order system.

4.1.2 Back-end Feedback Computation

How can we visualize and perhaps implement the back-end feedback computational function using control-systems theory? The simplest and most well-known control mechanism is the On-Off controller. This method of control is based on a continuous comparison between a defined threshold with the input that is presented to the system, which may result in a switching output response. At some degree this might reflect the "all-or-none" behaviour of a LIF neuron, as presented in Chapter 2. However, the response exhibited by a neuron is more sophisticated than purely a switching mechanism. Its dynamics can be self-controlled showing a sort of oscillatory behaviour as a consequence of: (i) a growth of some quantity; (ii) until reaching a threshold: (iii) followed by a self-reset. The process can repeat itself in the form of a continuous sequence of cycles being produced by the system. These kind of responses are commonly exhibited by relaxation oscillators that describe many phenomena across different disciplines [133].

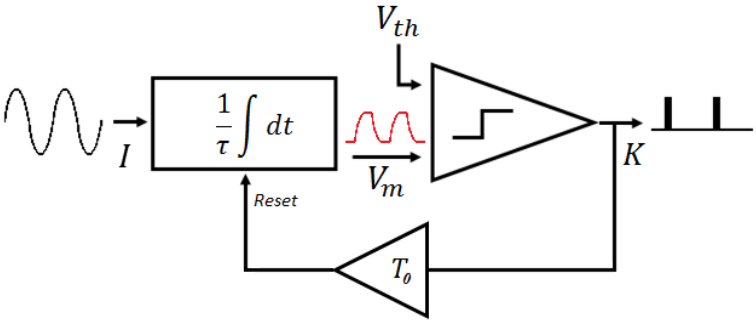

Figure 4.4: Simplified diagram overview of a LIF system, where τ represents the integrator constant, T_0 is the refractory time (e.g., delay) that is used to reset the leaky integrator. V_m is the system's voltage potential. V_{th} is the comparator threshold, which for the purposes of this study it only assumes a positive value. The output signal of the comparator is composed of square pulses with amplitude K and positive polarity, which can also be referred as the feedback signal to be injected to the front-end acoustic sensor.

A diagram overview of a LIF system is faithfully represented by Figure 4.4. The system is composed of a leaky integrator (e.g., linear or not), a comparator

(e.g., with static or variable threshold) and a reset time delay (e.g., constant or variable) in the feedback pathway. For instance, by tuning the system for a defined function, pulses can be generated according to the phase of the input signal that is presented to it. Therefore, the LIF system can then be considered as a smart generator of pulses and perhaps be exploited as a control mechanism for an adaptable sensory system. The output response ($LIF_{1:1}$) of this LIF system (e.g., smart generator of positive pulses in an 1:1 resonance mode) can then be expressed in Laplace form as described in Equation 4.3:

$$LIF_{1:1}(s) = \frac{K.e^{-(\tau.dt).s}}{\tau_r.s+1} - \frac{K.e^{-(W+\tau.dt).s}}{\tau_r.s+1} \tag{4.3}$$

Where K represents the amplitude of the pulse, $\tau.dt$ is the time delay before a pulse is generated (e.g., time spent by the integrator function), τ_r is the constant time associated to the rising of the output signal (i.e., pulses generated by a non-ideal driver circuitry), which should be much smaller than W ($\tau_r \ll W$) in order to provide a faithful square-shaped pulse, and W is the pulse with (e.g., duration in seconds).

4.2 Numerical Simulation Approach

This section summarizes the theoretical model of the proposed sensory system concept that is simulated using a numerical approach through MatLab R2014b. In order to better understand the system's dynamics, a model using a front-end acoustic sensor described by Equation 4.2 is placed within a positive-feedback loop system controlled by a computational function exploiting the On-Off mechanisms presented in Figure 4.2 that is implemented mathematically using the "Leaky Integrate-and-Fire" neuronal model introduced in Chapter 2, as expressed by Equation 4.4:

$$V_m(t_{n+1}) = V_m(t_n).\left(1 - \frac{dt}{\tau}\right) + R.I(t_{n+1}).\left(\frac{dt}{\tau}\right) \tag{4.4}$$

Recalling the LIF neuronal model that is described in Chapter 2, $\tau = R.C$ represents the system's time constant; V_m represents the system's voltage potential, I is the input stimulus, which might be associated to any input signal reaching the system. By computing Equation 4.4 over time (t_n), a pulse can be fired when the voltage threshold is reached, followed by the system's reset state.

This modelling approach is directly derived from the mathematical implementation of Equation 4.2 and 4.4 computed in a recursive way as a closed-loop system. It is important to note that, Equation 4.2 is mapped from the analog-to-digital domain using bilinear transformation and implemented as an IIR filter using a biquadratic topology. First of all, the concept is tested using noise-free synthetic signals with $dt = 1$ μs that is the time-step resolution (i.e., sampling time constant - unless otherwise specified). The resonant frequency of the system is $f_0 = 3.3$ kHz and the LIF model features include: $T_0 = 0.303$ ms, $\tau = 10$ ms and $W = 20$ μs.

4.2.1 Checking for Stability

An evident consequence of using a control mechanism imposing pulses in a positive-feedback configuration with a resonant sensor front-end is how the stability of the overall system can vary under certain conditions. A system is found stable if its output tends to converge to an equilibrium state ($LIF(s).H(s) < 1$). It becomes unstable if the output appears to diverge without bound ($LIF(s).H(s) = 1$). A system can also be classified as critically stable when the output converges to a continuous and endless oscillatory state ($LIF(s).H(s) > 1$). Testing the system's stability is then a preliminary task in order to understand the nature of its behaviour under certain conditions.

Figure 4.5 shows the stability diagram calculated from a numerical implemen-

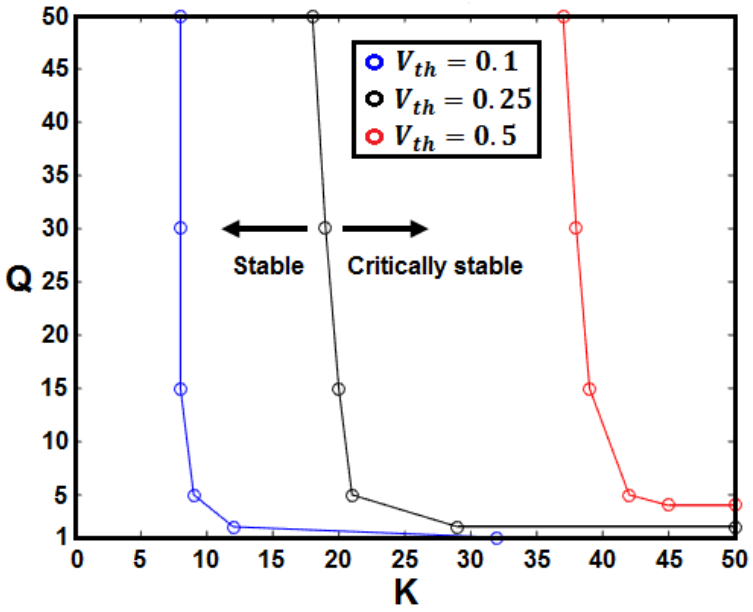

Figure 4.5: Stability diagram of the sensor system obtain by numerical simulation (e.g., based on the impulse response analysis of the overall system). Q represents the quality factor of the front-end acoustic sensor and K is the feedback signal gain, and V_{th} is the threshold that sets the feedback operation.

tation of the closed-loop system presented in Figure 4.2, while varying Q, K and V_{th}. As referred to in Chapter 2, the Q-factor of a system expresses how quickly the energy captured is dissipated by it, meaning that a sensor with a high-Q may oscillate by itself when a high feedback signal gain (K) configuration is applied to it, whereas a low-Q sensor may show a higher/faster level of convergence under the same K conditions. Additionally, V_{th} represents the threshold that sets the feedback operation, which can also play a role in the system's stability, since it can determine the position where the stability curve is located, as illustrated in Figure 4.5.

In order to have a better characterization of a given system's operating point, Figure 4.6 shows the bifurcation diagram obtained from a test while varying K, which sets the amplitude of pulses, assuming a front-end acoustic sensor with Q = 30 (i.e., for the custom-built sensor that is integrated within the experimen-

tal setup presented in Section 4.3) and feedback threshold, $V_{th} = 0.25$ V. The simulated system presents a Hopf bifurcation around the $\beta = 19$ point. Briefly, the Hopf bifurcation is defined as the critical region or point (β) where the system transits from a stable to an oscillating unstable or critically stable operating regime (refer to [41] for further details about the Hopf bifurcation related to hearing research). To ensure a stable system operation (e.g., convergent dynamics), it should function on the left side of the β point, and therefore the K chosen should obey that condition for a defined V_{th}.

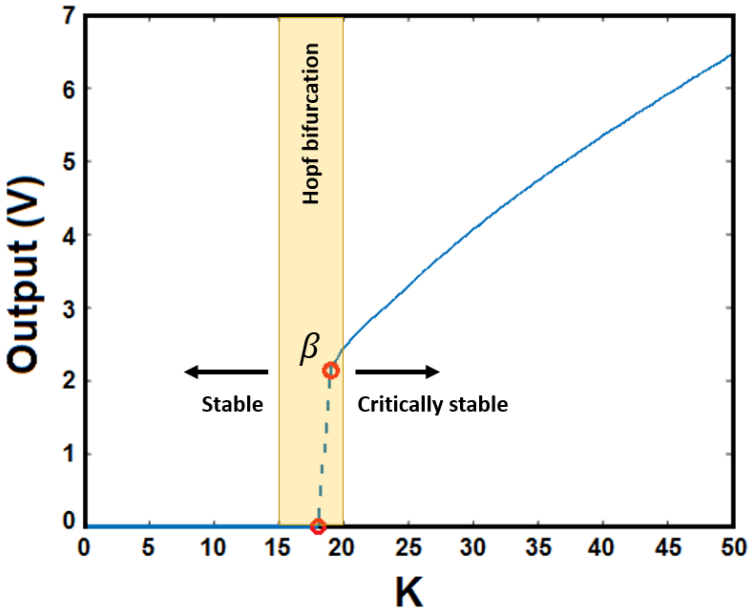

Figure 4.6: Bifurcation diagram of the sensor system obtained by numerical simulation using an impulse response analysis within the following conditions: $Q = 30$, $V_{th} = 0.25$ V and varying K.

Another interesting characteristic of this system's dynamics is that the time of entrainment between the pulses and the input signal may also affect the stability of the system, as illustrated in Figure 4.7. It means that the entrainment at the beginning of the input cycle may ensure a higher level of stability than entrainment at the middle or at the end of the input cycle.

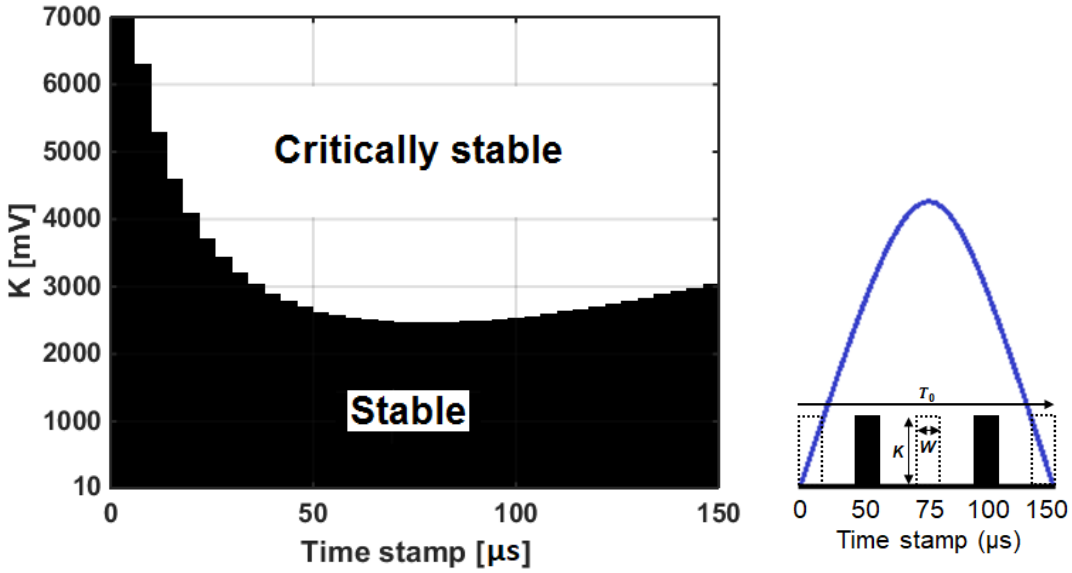

Figure 4.7: Stability of the system based on the phase-locking time under the following test conditions: $f_{in} = f_0 = 3.3$ kHz, $Q = 30$, $V_{th} = 0.25$ V, $T_0 = 0.303$ ms, $\tau = dt = 20$ μs, $W = 20$ μs.

4.2.2 Nonlinear Compressive Gain

One of the advantages of the feedback technique exploited in this study is the fact that it can provide a nonlinear compressive gain to the overall sensor responsiveness. For instance, when the K value is higher than the input signal itself, the contribution of the energy added to the system dynamics, from the pulsatile feedback signal, is higher than the reverse situation – when the input amplitude is higher than the feedback energy injected, therefore the system can exhibit a nonlinear compressive gain, as illustrated in Figure 4.8.

The system is operated within its stable regime using a 1:1 resonance mode (refer to Figure 4.3), hence the feedback signal gain should obey the condition $K < 19$, for $Q = 30$ and $V_{th} = 0.25$ V. Assuming $K = 15$, then a stable operation of the system is ensured that results in a peak-gain given by this system of about 6.2 dB at 1.76 V of the input amplitude (as shown in Figure 4.8). Therefore, the feedback contribution to the overall gain ($\frac{Vout}{Vin}$) is seen as nonlinear and it is also

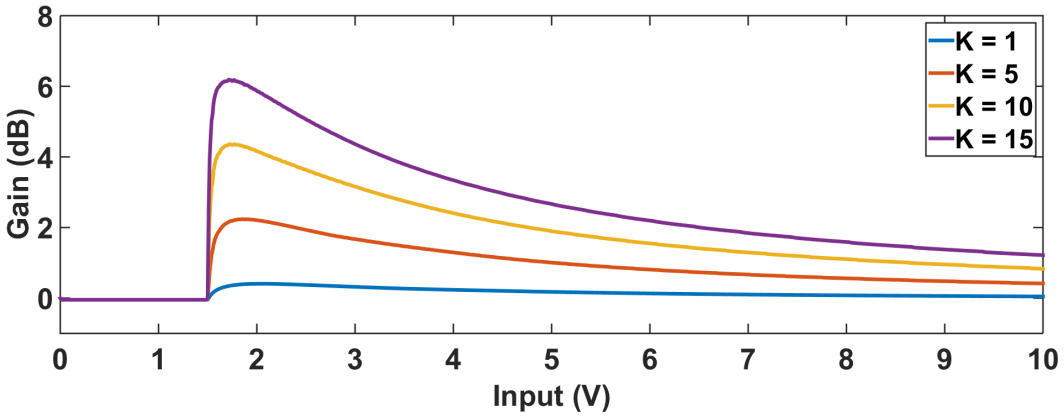

Figure 4.8: Example of the nonlinear compressive gain that can be provided by the sensor system using the following conditions: input signal frequency $f_{in} = f_0 =$ 3.3 kHz, $Q = 30$, $T_0 = 0.303$ ms, $\tau = dt = 20$ μs, $W = 20$ μs, and $V_{th} = 0.25$ V for $K = 1$, 5, 10 and 15.

dependent on the input signal amplitude following an experimentally determined exponential relationship expressed by Equation 4.5, where x represents the input signal amplitude (V), δ is the peak-gain (dB), θ is defined as the input amplitude for an achieved peak-gain (δ), and $\alpha = 1$ - $\left(\frac{maxGain}{minGain}\right)$ gives the gain compression rate factor.

$$Gain_{[dB]} = \begin{cases} \delta \times e^{-\alpha(x-\theta)} & x \geq \theta \\ 0 & x < \theta \end{cases} \tag{4.5}$$

This is a simplified equation used as a fitting curve to express the gain after a threshold, which follows an exponential decay when the input amplitude is increased, and vice-versa. It is important to note that V_{out} is equal to V_{in} when the system is without feedback operation as such $Gain = 0$ dB under that condition. Table 4.1 summarizes some of the gain features using different feedback thresholds. It can be seen that the system while operated under the stable region can achieve a peak-gain of 7.03 dB when $K = 35$ and $V_{th} = 0.5$. However, the maximum compression rate factor is $\alpha = 0.31$ obtained when the feedback signal gain and threshold are reduced to $K = 5$ and $V_{th} = 0.1$, respectively.

Table 4.1: Summary of the gain factors obtain under different feedback operations.

V_{th} **(V)**	K	θ **(V)**	α	δ **(dB)**
0.1	5	0.69	0.31	5.28
0.25	15	1.76	0.20	6.20
0.5	35	3.41	0.13	7.03

It highlights that the feedback contribution to the overall gain has a bigger impact at low levels of the input stimuli, as the compression of the gain response arises. V_{th} can also influence the overall gain given by the system, since it affects the timing of the pulses entrained within a given input signal amplitude (V_{in}). For instance, for a given V_{in} = 1.0 V while varying V_{th}, thus 0.2 < $Gain$ (dB) < 2.5 @ K = 15, as illustrated in Figure 4.9. At high V_{th} values, the system is more likely to fire pulses closer to the end of the input cycle, since it takes more time for integration to reach the threshold level, than for low V_{th}, which is more likely to set the firing at the beginning of the input cycle, for the same given input signal amplitude. However, a more effective locking appears when the pulses are entrained at the middle of the input cycle, thus the contribution to the overall gain can be maximized. It means that for each configuration V_{th} and K, the system has a defined input amplitude for which it maximizes the overall gain. Nevertheless, a trade-off with the stability diagram should be considered as referred in Figure 4.7.

It is interesting to note that V_{th} value should be chosen to be smaller than the input signal amplitude (V_{in}) in order to trigger feedback computation to the system. Moreover, when $V_{th} = V_{in}/2$, is when the overall feedback gain can provide its maximum output contribution.

4.2.3 Rise-time Analysis

Another important property of the positive-feedback technique exploited in this study is related to the fact that it can alter the effective time response of the

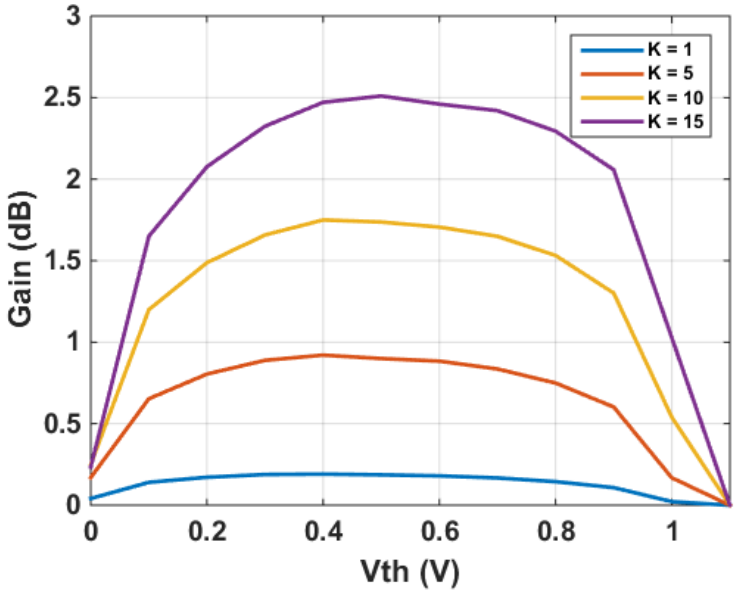

Figure 4.9: Impact on the overall gain response based on the time of entrainment, between input and feedback signals, which vary depending on V_{th} and K values; for the same given input signal amplitude.

overall system when subject to a step input stimulus. The rise time without feedback operation is 18.2 ms. Measured at 98% of the peak amplitude for an acoustic receiver with $Q = 30$. Table 4.2 presents a summary of the rise times of the system when operated under the influence of feedback computation, where Δ represents the minimum rise time that can be achieved by the system (milliseconds) and σ is the input amplitude (V) that is maximized in terms of the rise time under the defined system configuration set by V_{th} and K. Therefore, if a threshold detection method is required by a given application, the use of the positive-feedback process can provide a faster responsiveness ($\approx 4.0\times$) under these operating conditions.

Table 4.2: Summary of the rise time for different feedback operations.

V_{th} **(V)**	K	σ **(V)**	Δ **(ms)**
0.1	5	1.6	4.2
0.25	15	3.9	3.9
0.5	35	8.2	3.6

4.2.4 Hysteretic Response

The input-output relationship of the studied sensory system follows a distinct nonlinear response, dependent on whether the input amplitude is increasing or decreasing. A system showing this kind of behaviour is said to have a hysteretic output response. Hysteresis commonly originates due to the on-off feedback control mechanism applied to the system. It might be expected that the feedback operation imposes a switching behaviour to the overall system response. Therefore, a hysteretic behaviour is likely to appear as a direct consequence of the control mechanism exploited in this work. The control process is a threshold based computation that can lead to a bistable behaviour of the overall sensory system. Sensors that show hysteresis are nonlinear systems. For the purposes of this study it is assumed that hysteresis is a consequent feature of the proposed concept, which may be exploited by a given application. Biological sensors and systems also show evidence of hysteretic responses, which is exploited as a useful feature, such that it can be seen as a synonym of intrinsic residual memory of the sensory system to a previous targeted signal and perhaps can provide immunity to noise (e.g., random jitter) [10].

4.3 Results

This section presents the system's output response obtained from the implementation of the theoretical model, as used to characterize and test the behaviour of the sensory system while applying standard signals. It can be used to further validate the response of this concept obtained from the physical prototyped implementation that is also presented here.

4.3.1 Overall Response of the Sensor System from Numerical Simulation

Figure 4.10 shows the dynamic adaptation of the overall sensor system response under the following test conditions: $f_{in} = f_0 = 3.3$ kHz, $Q = 30$, $V_{th} = 0.25$ V, $T_0 = 0.303$ ms, $\tau = dt = 20$ μs, $K = 10$ and $W = 20$ μs. That provides a gain of about 1.52 ($Gain_{[dB]} = 3.63$ dB) under active feedback computation (A2 & B2).

Figure 4.11 shows the hysteretic response of the overall sensory system – when the input stimulus follows an amplitude modulation (e.g., increased and decreased level). It can be concluded that the feedback operation imposes a switching behaviour to the overall system response, which is mainly dependent on the threshold value V_{th} and feedback gain K value used, as illustrated in Figure 4.12.

4.3.2 Response of the Sensor System Obtain from an Experimental Setup

For validation purposes, the concept is then prototyped using a custom-built experimental setup as presented in Figure 4.13, which can perform real-time computation and provide a proof-of-concept for this parametric amplification applied to a MEMS microphone. The approach is similar to the previous embedded system setup design presented in Chapter 3. However, here the front-end acoustic receiver is a custom-built MEMS microphone (e.g., frequency-limited sensor), as illustrated in Figure 4.14.

This experimental setup is meant to be a direct implementation of the theoretical model presented previously, but in a practical manner. The system is prototyped using an electromechanical setup as following described. Firstly, the function ($H(s)$) of a front-end acoustic receiver is performed by a MEMS microphone. The design and characterization of this device are addressed in Chapter

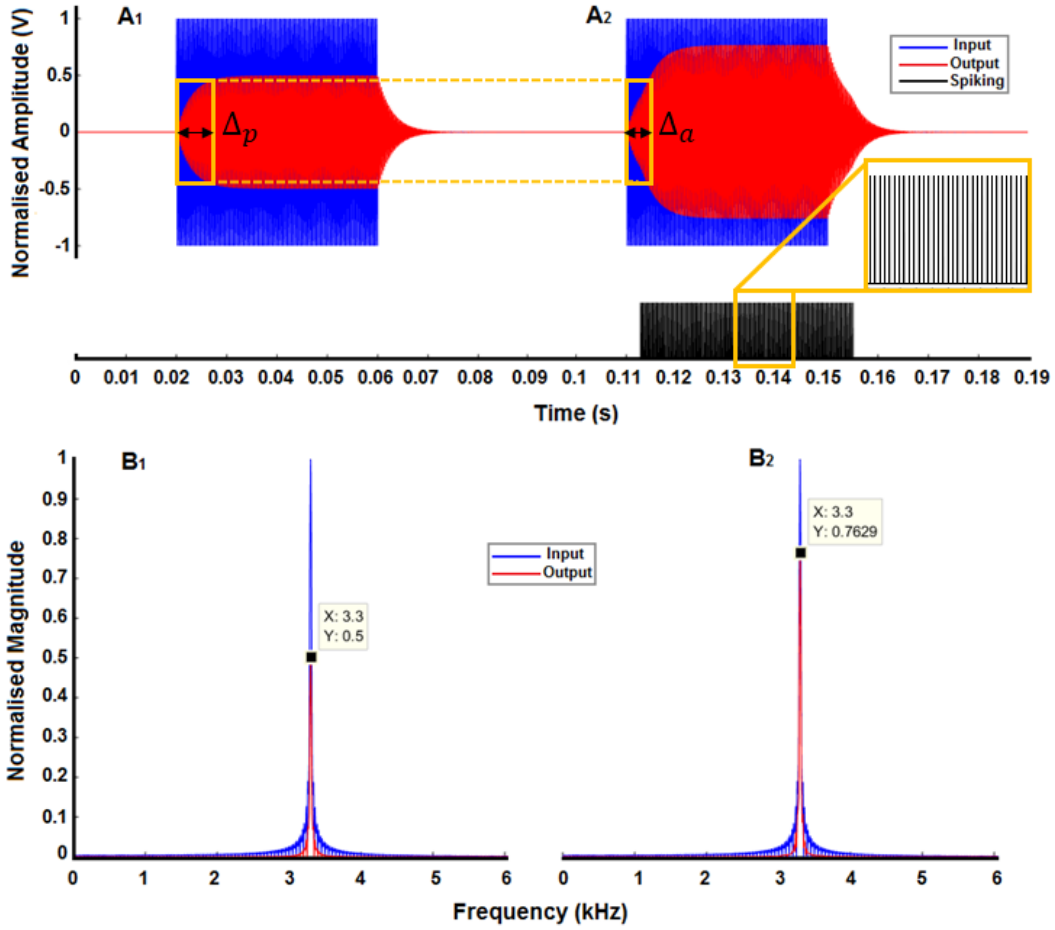

Figure 4.10: Example of an amplified response of the sensory system obtained by simulation. Time and frequency response of a single-tone input signal (blue trace); output response of the sensory system (red trace) without – (A1 & B1) and with – (A2 & B2) phase-locked pulses (black trace) using 1:1 resonance mode. It is shown that $\Delta_p < \Delta_a$, when comparing the rise time to reach a defined voltage level for passive and active operation of the system, respectively. The black signal trace in (A2) is rescaled for the sake of clarity and labelled - "Spiking" as short-pulses with square-shape that are entrained once per cycle with the "Input" signal.

6, where results of finite element modelling and practical experimentation are reported. Some of the device's main features include: the resonance frequency around 3.3 kHz and a Q-factor of 30 (refer to Chapter 6 for further details about the MEMS microphone, including its design and characterization). Secondly, the element of feedback computation and control ($LIF()$) is implemented through an

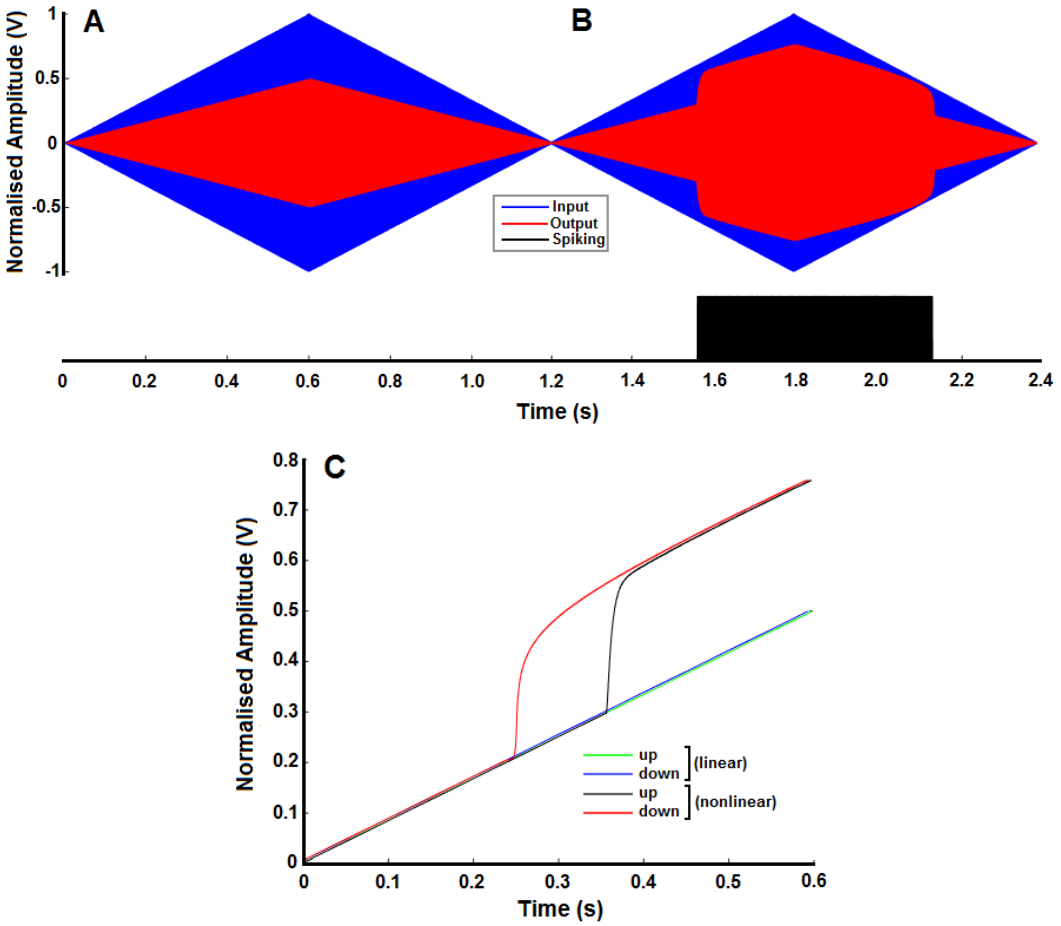

Figure 4.11: Example of the hysteretic response of the sensory system obtained by simulation using an amplitude modulated input signal, (A) without and (B) with feedback control operation; (C) linear vs nonlinear response of the sensor system. The black signal trace in (B) is rescaled for the sake of clarity and labelled - "Spiking" as short-pulses with square-shape that are entrained once per cycle with the "Input" signal.

embedded system setup. By computing a software routine based on the method described previously in Equation 4.4, the embedded system (e.g., a microcontroller) is able to generate pulses to be in-phase with a targeted input stimuli reaching the microphone's diaphragm. Feedback signals (e.g., pulses) are driven to the capacitive port (e.g., capacitive comb fingers) of the MEMS microphone.

Highlights of the embedded system setup features include: an optical read-out from the microphone's diaphragm displacements using a single-point laser

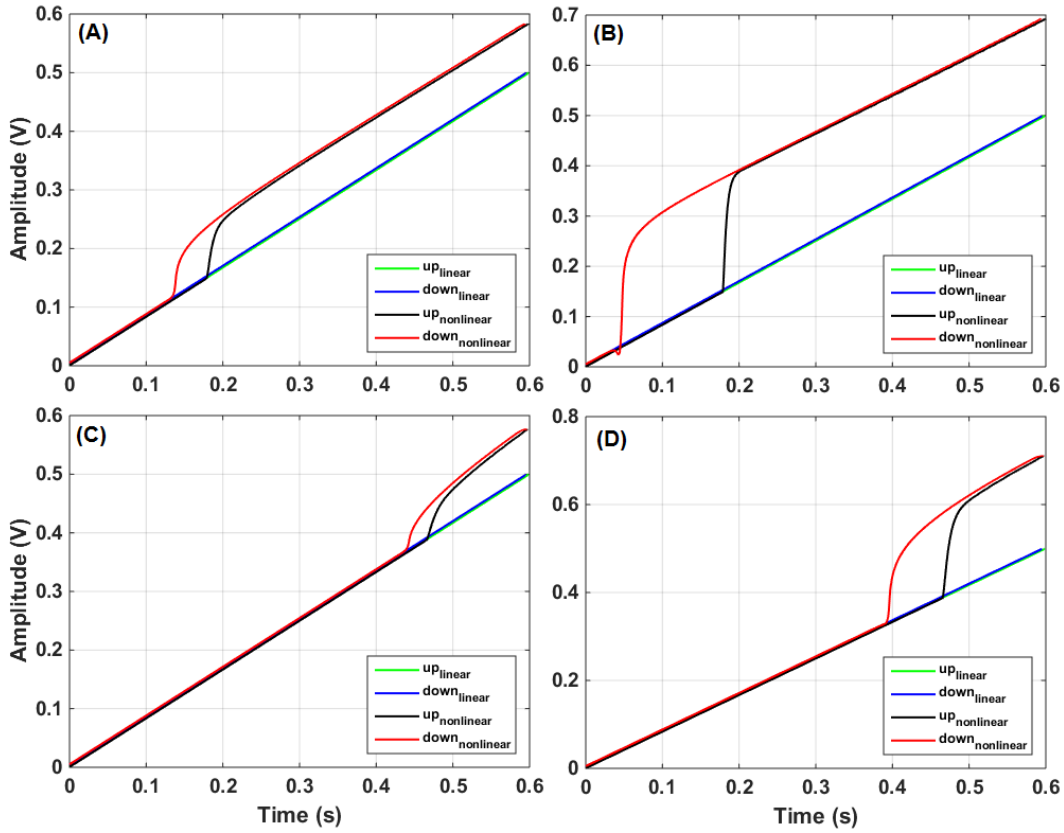

Figure 4.12: Hysteretic response of the sensory system to an amplitude modulated input signal while varying V_{th} and K values setup. (A) low K and low V_{th}; (B) high K and low V_{th}; (C) low K and high V_{th}; (D) high K and high V_{th}.

vibrometer device providing correspondent analogue output signals. Signal conditioning is performed on the laser output signals before A/D conversion (12-bit @ Fs = 50 kHz). Signals are acquired using a STM32F4 microcontroller board running at 168 MHz clock-speed. The purpose-built algorithm is then executed inside the processing unit (CPU) that can generate spike-type phase-locked signals using an on-board D/A converter (12-bit @ Fs = 50 kHz). The pulses can be entrained with the input signal at the microphone level (e.g., microphone's diaphragm), once an average and a voltage threshold are met, followed by a consequent auto-reset routine after each firing. Moreover, a refractory period is also defined to set the maximum firing rate of the pulse generator system. For in-

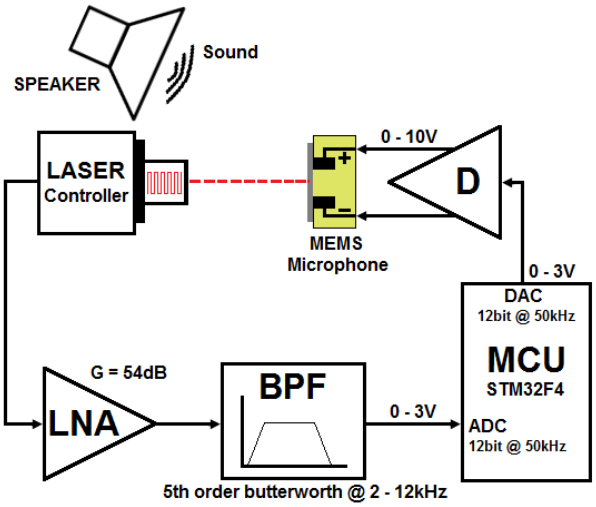

Figure 4.13: Schematic of the custom-built embedded system used to enable the experimental setup. A more complete description of circuits and systems can be accessed in the previous Chapter 3.

stance, the feedback system can be adjusted to lock and fire at a specific timing of the input signal, which allows that to be amplified as the Q-factor of the overall system can be increased, as follows.

The purpose-built sensor system is then tested by experimentation using the following parameters: input acoustic signals with frequency $f_{in} = f_0 = 3.3$ kHz are played by a standard audio speaker; and $V_{th} = 0.25$ V, $T_0 = 0.303$ ms, $\tau = 10$ ms, $dt = 20$ μs, $K < 7$ and $W = 20$ μs.

Figure 4.15 presents the response of the sensory system setup showing an output amplification (A2 & B2) of about 2.2 greater ($Gain_{dB} = 6.85$ dB), and the system's responsiveness to a step input stimuli is also enhanced (with rise time measured: $\Delta = 5.5$ ms), when compared with its passive response (A1 & B1 – with rise time measured: $\Delta = 16.7$ ms). Figure 4.16 shows the response of the system to an amplitude modulated input signal with sound level being increased and decreased consequently; with- (B) and without- (A) feedback control operation, respectively. When pulses are in-phase with the input signal, the output response shows amplification as predicted by the theoretical model and simulation results,

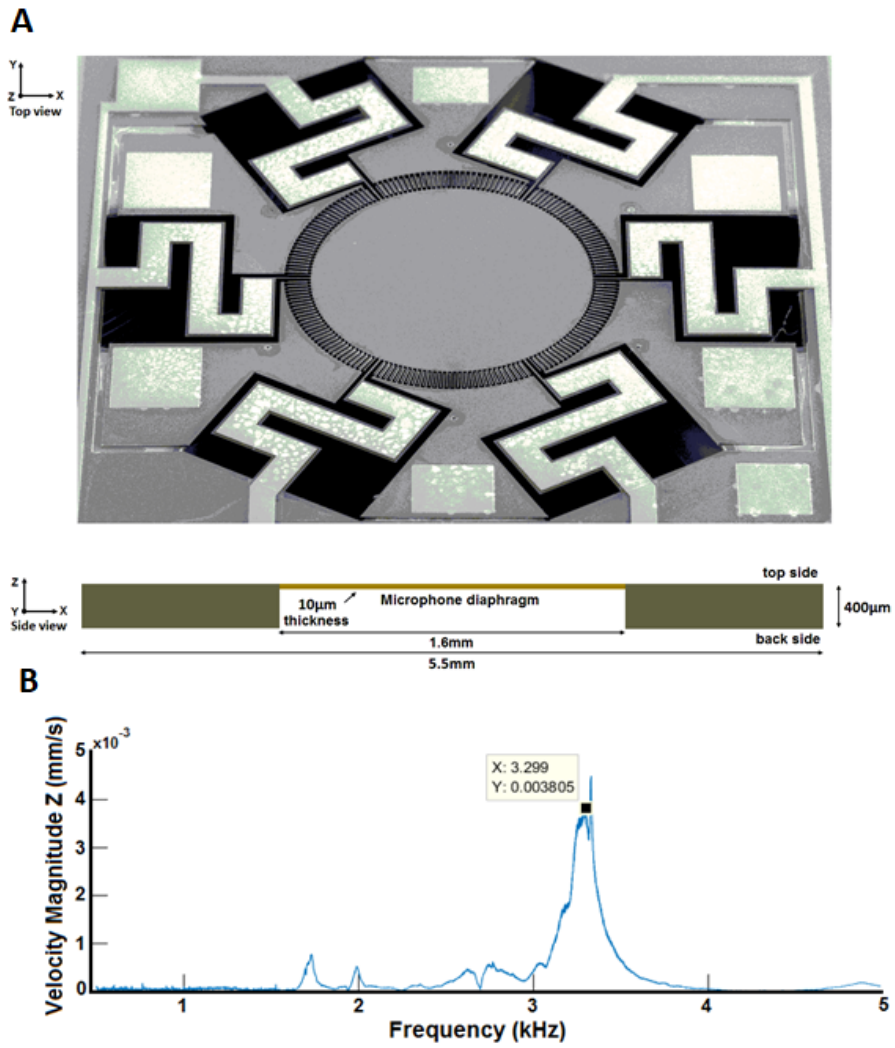

Figure 4.14: Custom-built MEMS microphone. (A) Microscopic picture and dimensions of the device; (B) its frequency response measured using LDV techniques.

and also exhibits similar behaviour to that reported for the mosquito's hearing system studies, as discussed in Chapter 2.

During the experimental tests, the system's operating regime is located within the stable zone. However, it is important to note that the stable region of the overall setup is found after experimentation by tuning the feedback signal gain value. Experimentally, the critical region/point of this purpose-built system is

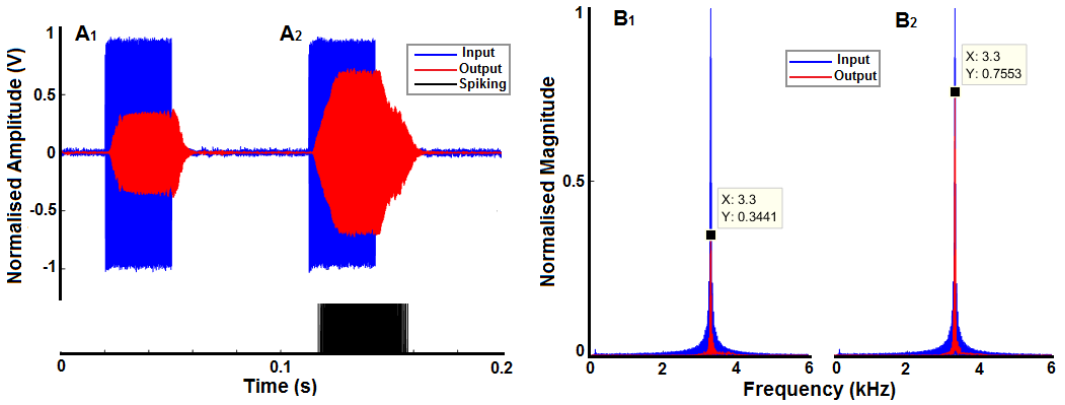

Figure 4.15: Adaptive response of the purpose-built sensor system setup. Time and frequency response of the system for a single-tone acoustic input at 3.3 kHz (blue trace); output response of the sensor system (red trace) without- (A1 & B1) and with- (A2 & B2) feedback contribution (black trace) with $K = 5$ V @ $V_{th} = 0.25$ V. The black signal trace is rescaled for the sake of clarity and labelled - "Spiking" as short-pulses with square-shape that are entrained once per cycle with the "Input" signal.

reached when K is approximately 7 V at $V_{th} = 0.25$ V. Therefore, in practical terms the critical region/point is reached at smaller K amplitudes when compared to what is predicted by simulation (for a $Q = 30$, hence $K = 19$ and $V_{th} = 0.25$ V, as presented in Figure 4.6). In practice, the critical point is expected to be shifted since in general a positive-feedback system configuration can be greatly affected by the background noise (e.g., acoustic and electrical) surrounding the experimental setup and within the computational system itself (e.g., digital noise: round-off errors). It means that noise can affect the system dynamics in several ways. For instance, noise within the system may impose some jittering response to the feedback control operation likely seen at the transitory states, as seen in Figure 4.15 (A2) – the pulse train (black trace) is kept active for a longer time at the downward slope of the system's response signal, which is not seen in a noise-free simulation at Figure 4.10 (A2). Additionally, when the system is operating near its threshold voltage, noise can make the system transit between the on-off states momentarily (Figure 4.16 (B) – black trace). This may result

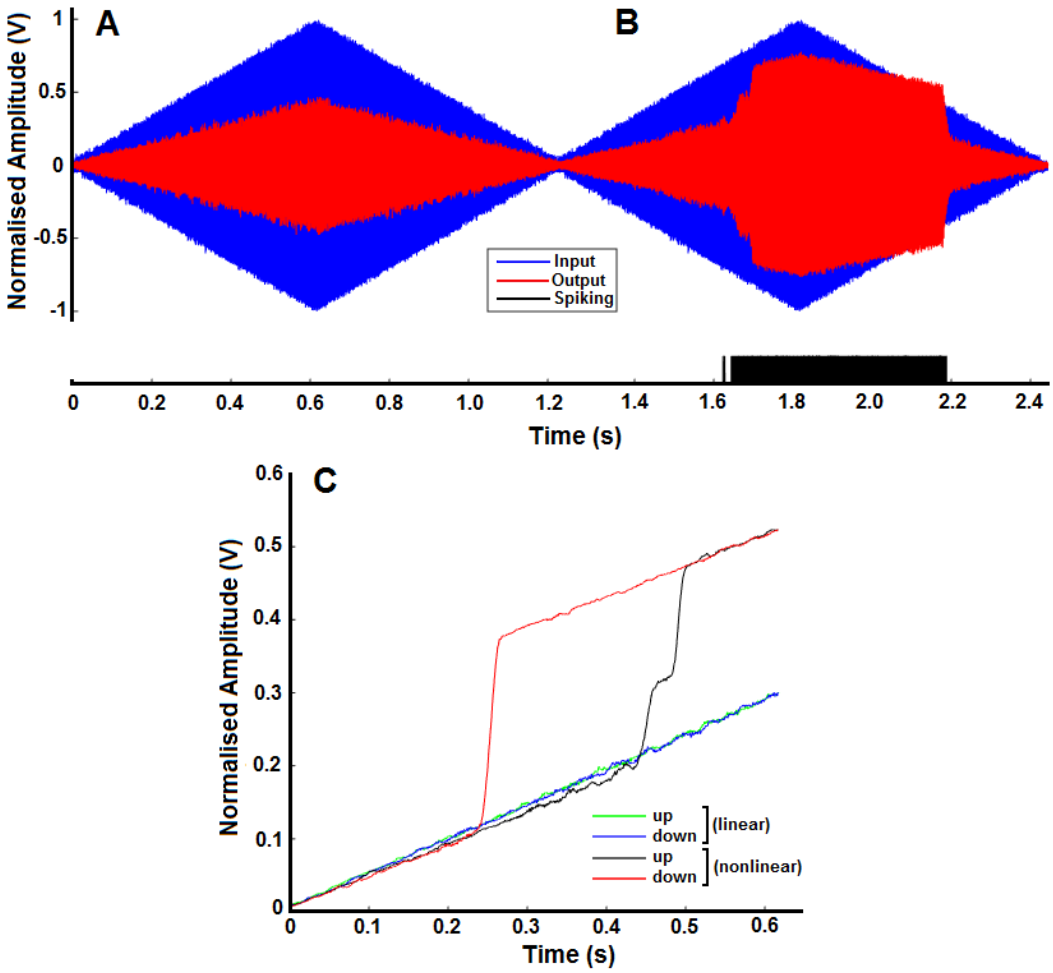

Figure 4.16: Hysteretic response of the purpose-built sensor system setup. The sound level at 3.3 kHz (blue trace) is increased and decreased consequently: (A) showing linear response – without feedback; and (B) showing hysteretic nonlinear response with feedback $K = 3$ V @ $V_{th} = 0.25$ V; (C) linear vs nonlinear response of the sensory showing the amplification and the hysteretic behaviour of the system. The black signal trace in B is rescaled for the sake of clarity and labelled - "Spiking" as short-pulses with square-shape that are entrained once per cycle with the "Input" signal.

in intermediate output fluctuations as the system jumps between the two states (Figure 4.16 (C), black trace onset). There is evidence that this is a separate state, which appears to be at the junction of stability between the two states.

4.4 Discussion I

This study presents a method to provide adaptive nonlinear amplification capabilities at the sensor/transducer level. The concept is theoretically described through a mathematical model that is implemented and validated using MatLab simulations and then physically prototyped using a custom-built setup as a proof-of-concept. It is clear that the positive-feedback mechanism exploited in this study can enhance signal conditioning at the sensor level, namely amplification and fast sensory responsiveness to sound when the sensor is subject to a step input stimulus. However, in a real scenario this type of system dynamics might be highly influenced by the noise surrounding the setup. Future investigations might address that topic, for instance by adding noise at the simulation level in order to have a better prediction of the system's dynamics in the presence of different types of noise (e.g., random noise or any kind of competitive signals that can be generated by electrical or acoustic sources). Moreover, the biological reports (noted in Chapter 2) that inspired this work describe the mosquito hearing response as greatly enhanced due to the "synchrony through twice-frequency forcing" – 2:1 resonance mode. It should be noted that this study, only explored the use of 1:1 resonance mode (e.g., one pulse per input cycle with positive polarity), however, one might hypothesize about the response of the proposed sensory system if configured at 2:1 resonance mode (e.g., entrainment at twice per cycle – one pulse phase-locked in the positive cycle of the input signal and another pulse phase-locked in its negative cycle with compatible polarity, respectively):

(a) It would drag the β point towards a lower value of K, for the same given threshold value as used with 1:1 resonance mode, meaning that the system might enter in a self-oscillatory condition quicker and at lower feedback signal gain values used;

(b) The overall performance of the system would benefit from the 2:1 resonance

more in terms of the nonlinear compressive gain and time response/resolution that can be achieved, since the feedback signal path can then supply twice the energy, per period of the input signal, when compared with 1:1 resonance mode.

Future investigations might address that modality further (2:1 resonance mode), which may add another level of versatility to the purpose-built system concept and to its outcomes. Additionally, it may be hypothesized that the feedback parameters such as V_{th} and K, which are kept as constant values in this study, can assume variable conditions (e.g., be adaptable). For instance, evolving dynamically to place the system operating point at its best SNR conditions as natural sensors and systems possibly do.

This work aims to support the positive cross-disciplinary synergy between biology and engineering based on previous and ongoing bio-inspired research studies. It provides a proof-of-concept of a bio-inspired acoustic sensor system that can potentially be exploited by both the sensors and the circuits and systems fields. The instrumentation and electronic circuits and systems that were embedded in this prototyped sensor-system are generic and they are mostly based on off-the-shelf and discrete-level components. Therefore, the next step for this research work would include a more advanced and matured prototyping stage such as, a higher level of integration of circuits and systems towards the development of a more compact experimental embedded system setup by exploiting the sensing and actuation capabilities (e.g., piezoelectric and capacitive) built-in the purpose-built MEMS microphone as presented in Chapter 6. The aim is towards the goal of creating a combined bio-inspired embedded acoustic sensor system, featuring active nonlinear amplification and frequency agile tuning to enhance sensory responsiveness while targeting signals of interest.

4.5 LIF Computational Model – Theoretical Revision

The biological reports that inspired the work previously described are based on the mosquito hearing response as greatly enhanced due to the "synchrony through twice-frequency forcing" – 2:1 resonance mode – refer to Figure 4.17 for a comparison between 1:1 and 2:1 resonance modes.

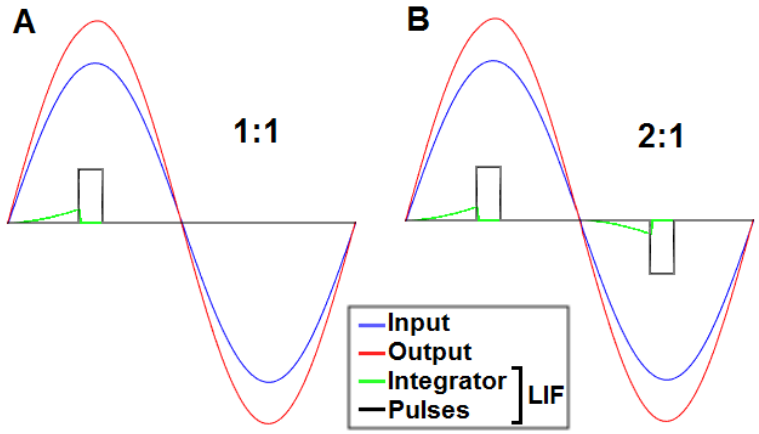

Figure 4.17: Entrainment of signals based on 1:1 and 2:1 resonance modes for comparison, (A) and (B) respectively.

Here, the LIF computational model presented previously in Figure 4.4 is revised in order to address the points (a) and (b) highlighted at the end of Section 4.4. Additional simulated results are presented in order to further characterize the dynamics of the system when configured in 2:1 resonance mode, mainly in the presence of competitive input signals and Additive Gaussian White Noise (AGWN) within the system.

The diagram overview of the new/revised LIF system is represented in Figure 4.18. The new system's architecture is composed by two identical leaky integrators, two identical comparators with similar auto-reset mechanism dependent on a time delay (T_0) as a feedback control. The aim is to configure this new system to generate positive and negative pulses according to the phase of the input signal

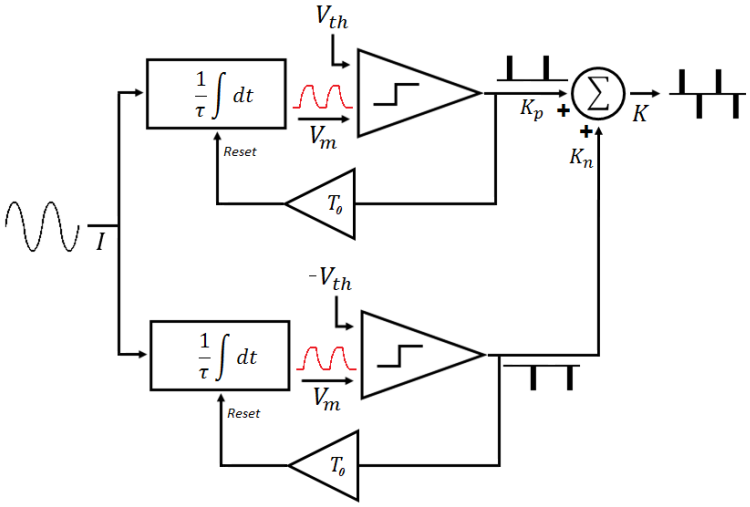

Figure 4.18: Diagram overview of the new/revised LIF system, where the top signal pathway enables the generation of square pulses with positive polarity; and the bottom signal pathway enables the generation of square pulses with negative polarity. It should be assumed that $K = K_p + K_n$, where $|K_p| = |K_n|$ in order to keep the pulses with symmetric polarity, identical width and same amplitudes.

that is presented to it. Therefore, this new LIF system can also be considered as a smart generator of pulses (e.g., biphasic), which can also be exploited as a control mechanism for an adaptable sensory system, as similarly done with the previous 1:1 resonance mode version. The output response ($LIF_{2:1}$) of the new LIF system (e.g., generator of biphasic pulses) can be expressed in Laplace form as described in Equation 4.6:

$$LIF_{2:1}(s) = \left(\frac{K_p.e^{-(\tau.dt).s}}{\tau_r.s+1} - \frac{K_p.e^{-(W+\tau.dt).s}}{\tau_r.s+1}\right) - \left(\frac{K_n.e^{-(T_0+\tau.dt).s}}{\tau_r.s+1} - \frac{K_n.e^{-(T_0+W+\tau.dt).s}}{\tau_r.s+1}\right) \tag{4.6}$$

Where K_p represents the amplitude of pulses with positive polarity, K_n represents the amplitude of pulses with negative polarity; T_0 is the time between two consecutive pulses (e.g., positive and negative, respectively), which normally is set as half of the value of the input signal period (e.g., $T_0 = T/2$, where T is the period of the input signal). Refer to Section 4.1 for further details about other

variables of this equation.

4.5.1 Simulation Results

A new study is then conducted to compare the performance of the proposed concept configured at 1:1 and 2:1 resonance modes, as following presented through simulated results. First of all, the response of the system when configured at 2:1 mode (e.g., entrainment at twice-per-cycle) places the critical point (β point) at the left-side of the 1:1 bifurcation region, for the same threshold value, as illustrated in Figure 4.19.

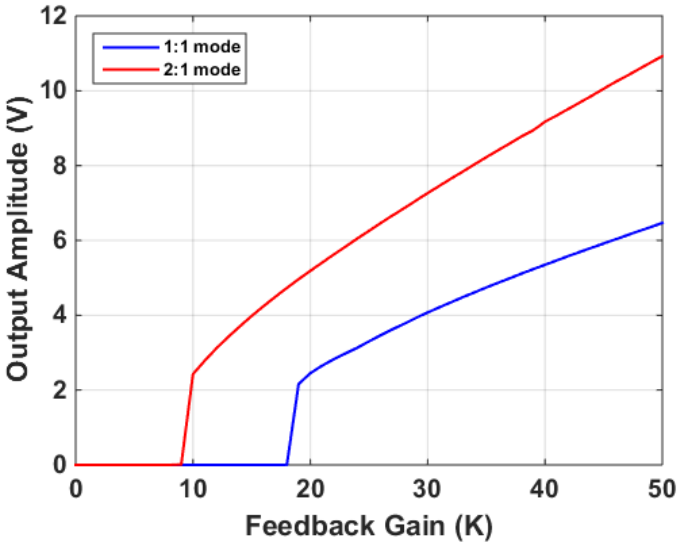

Figure 4.19: Hopf bifurcation of the system based on the feedback gain value (K). Comparison between 1:1 and 2:1 modes obtained by numerical simulation using an impulse response analysis within the following test conditions: $f_{in} = f_0 =$ 3.3 kHz, $Q = 30$, $V_{th} = 0.25$ V, $T_0 = 0.303$ ms (1:1) and $T_0 = 0.166$ ms (2:1), $\tau = dt = 20$ μs, $W = 20$ μs.

Table 4.3 provides a summary of the bifurcation points for different feedback configurations, where $\beta_{1:1}$ and $\beta_{2:1}$ represent the β point for each resonant mode, and $Out_{1:1}$ and $Out_{2:1}$ are the oscillatory output amplitudes when the sensory system is operated at that particular critical point $\beta_{1:1}$ or $\beta_{2:1}$, respectively.

Table 4.3: Summary of the bifurcation point (β) for different feedback thresholds at 1:1 and 2:1 synchronization modes for comparison.

V_{th} **(V)**	$\beta_{1:1}$ | $\beta_{2:1}$	$Out_{1:1}$ | $Out_{2:1}$
0.1	8 | 4	0.981 | 0.971
0.25	19 | 10	2.160 | 2.427
0.5	38 | 19	4.319 | 4.382

Another important point to this system's dynamics is that under the same feedback conditions (V_{th} and K) - the 2:1 resonance mode can maximize the performance of the sensory system in terms of the nonlinear compressive gain that can be obtained, as illustrated in Figure 4.20; and also the time response/resolution that can be achieved, as further summarized in Table 4.4.

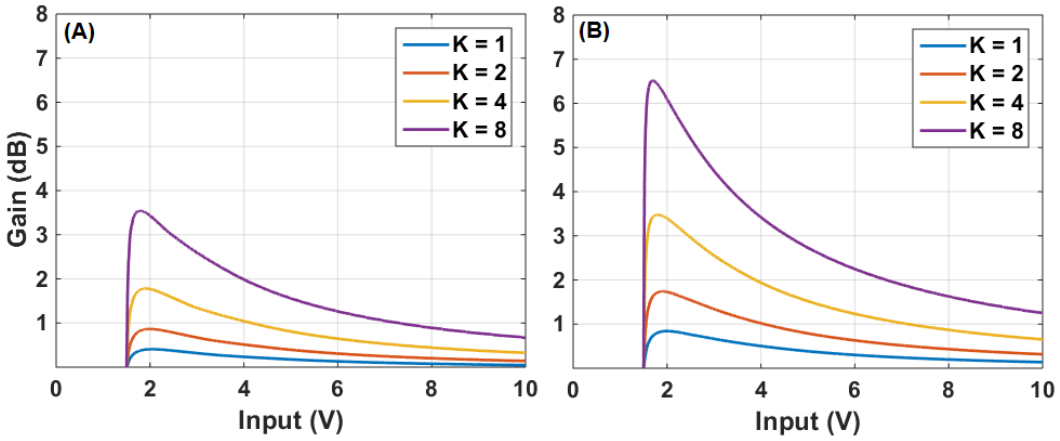

Figure 4.20: Nonlinear compressive gain response under the following test conditions: $f_{in} = f_0 = 3.3$ kHz, $Q = 30$, $V_{th} = 0.25$ V, $T_0 = 0.303$ ms (1:1) and $T_0 = 0.166$ ms (2:1), $\tau = dt = 20$ μs and $W = 20$ μs; for $K = 1$, 2, 4 and 8. (A) 1:1 resonance mode; (B) 2:1 resonance mode.

Figure 4.21 shows three different feedback gain configurations such as passive, 1:1 and 2:1 modes, respectively, as a comparison. It illustrates that 2:1 mode can provide greater feedback gain contribution and faster rise time response than 1:1 configuration under the same feedback variable conditions (V_{th} and K), as summarized in Table 4.4.

The hysteretic response is also affected by different feedback configurations

Table 4.4: Summary of the gain and rise times for different feedback thresholds at 1:1 and 2:1 synchronization modes for comparison.

V_{th} **(V)** $K_{1:1} = K_{2:1}$	0.1 1	0.25 5	0.5 15
$\theta_{1:1}$ | $\theta_{2:1}$ **(V)**	0.80 | 0.75	1.89 | 1.75	3.33 | 3.4
$\alpha_{1:1}$ | $\alpha_{2:1}$	0.41 | 0.34	0.21 | 0.20	0.13 | 0.13
$\delta_{1:1}$ | $\delta_{2:1}$ **(dB)**	1.10 | 2.18	2.23 | 4.30	3.59 | 6.20
$\sigma_{1:1}$ | $\sigma_{2:1}$ **(V)**	1.1 | 1.2	3.0 | 3.3	6.0 | 7.8
$\Delta_{1:1}$ | $\Delta_{2:1}$ **(ms)**	7.1 | 5.8	5.8 | 4.5	5.0 | 3.9

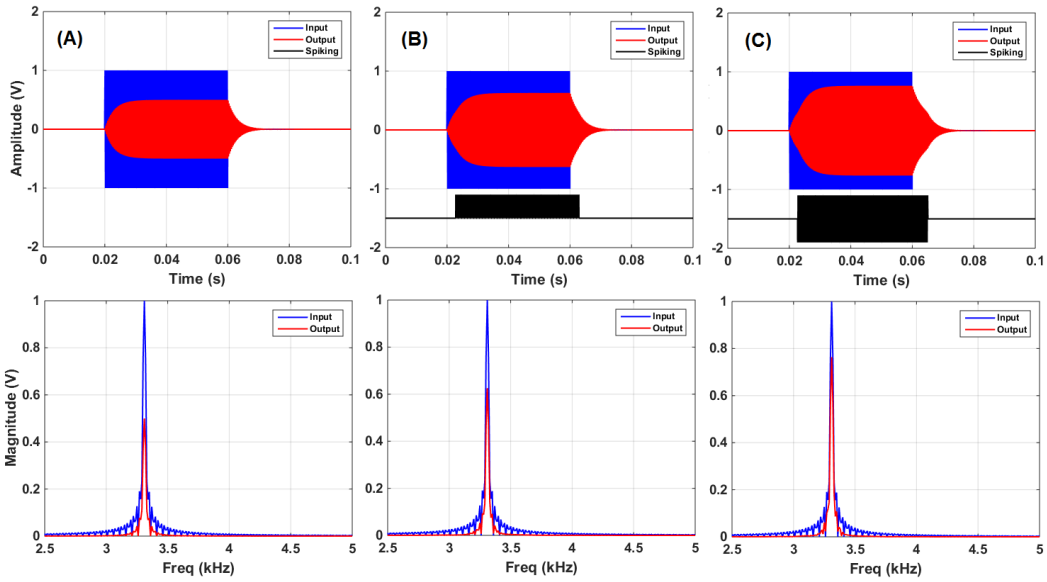

Figure 4.21: Gain response of the system is greater at 2:1 resonance mode. Test under the following conditions: $f_{in} = f_0 = 3.3$ kHz, $Q = 30$, $V_{th} = 0.25$ V, $T_0 = 0.303$ ms (1:1) and $T_0 = 0.166$ ms (2:1), $\tau = dt = 20$ μs, and $W = 20$ μs; (A) $K = K_p = K_n = 0$; (B) $K = K_p = +5$ and $K_n = 0$; (C) $K = K_p - K_n = \pm 5$; The black signal trace in (B) and (C) is rescaled for the sake of clarity.

namely V_{th} and K values, as previously mentioned in Section 4.2. However, the 2:1 resonance mode has the property of approximately doubling the amount of energy that is injected per cycle, which consequently appears to further impact the on-off behaviour set by the feedback control mechanism. And, therefore alters the hysteretic response, as illustrated in Figure 4.22 (C). Additionally, changing the polarity of the feedback signal ($K = K_n$), while keeping phase-

locking compatibility with the input signal, while operating the system at 1:1 mode, does not appear to affect the gain and hysteretic response of the overall system, as illustrated in Figure 4.22 (A) and (B), respectively, as a comparison.

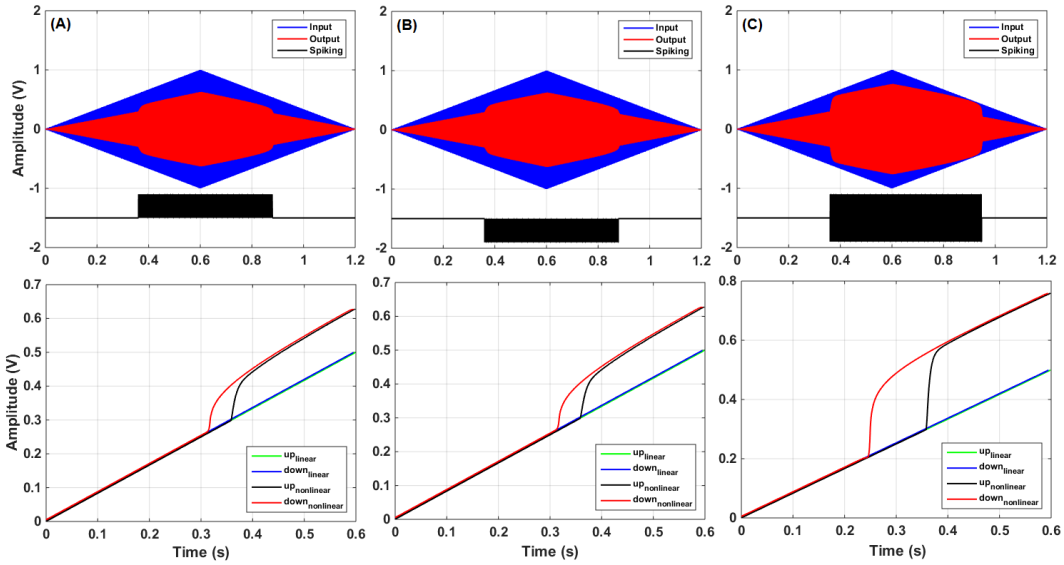

Figure 4.22: Hysteresis of the overall sensor system response under the following test conditions: $f_{in} = f_0 = 3.3$ kHz, $Q = 30$, $V_{th} = 0.5$ V, $T_0 = 0.303$ ms (1:1) and $T_0 = 0.166$ ms (2:1), $\tau = dt = 20$ μs, and $W = 20$ μs; (A) $K = K_p = 10$ and $K_n = 0$; (B) $K = -K_n$ = -10 and $K_p = 0$; (C) $K = K_p - K_n = \pm 10$; The black signal trace in (A), (B) and (C) is rescaled for the sake of clarity.

Importantly, inverting the polarity of the pulses (e.g., firing pulses without compatible polarity as the input signals phase), in both 1:1 or 2:1 mode, appears to greatly impact the overall gain of the system, as illustrated in Figure 4.23. It seems to have an attenuation effect when compared with Figure 4.21 (C) and Figure 4.22 (C), respectively. Therefore, it might be noted that perhaps signal attenuation or suppression may also be another functionality that can be exploited by this proposed system concept.

Competitive signals that are presented to the system and within its bandwidth can result in intermodulation output responses as a consequence of the nonlinearities imposed by the feedback system operation, as illustrated in Figure

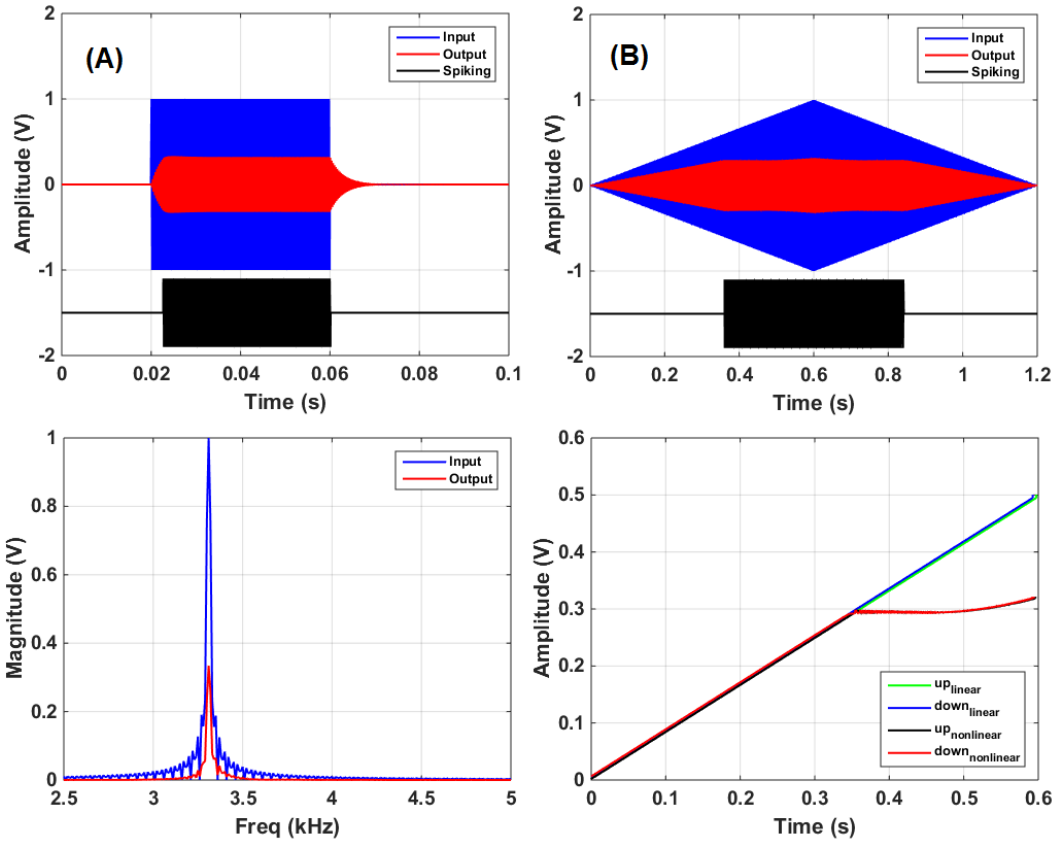

Figure 4.23: The gain response of the system is greatly affected by the pulse's polarity. In this case the pulses were set to fire with their phase reversed. (A) To compare with Figure 4.21 (C); (B) To compare with Figure 4.22 (C). According with the following test conditions: $f_{in} = f_0 = 3.3$ kHz, $Q = 30$, $V_{th} = 0.25$ V, $T_0 = 0.166$ ms, $\tau = dt = 20$ μs, $W = 20$ μs; (A) $K = -K_p + K_n = \pm 5$; (B) $K = -K_p + K_n = \pm 10$; The black signal trace in (A) and (B) is rescaled for the sake of clarity.

4.24. Intermodulation products are typical phenomena that result from this kind of nonlinear system, as similarly reported in biological studies related to active processes in hearing systems [41], [134].

Table 4.5 summarizes the intermodulation distortion products for a $\Delta f = |f_1 - f_2| = 50$ Hz, as illustrated in Figure 4.25 (zoom in of Figure 4.24 (B), highlighting the distortion products frequency region).

In conventional (e.g. man-made) high quality audio systems, harmonic dis-

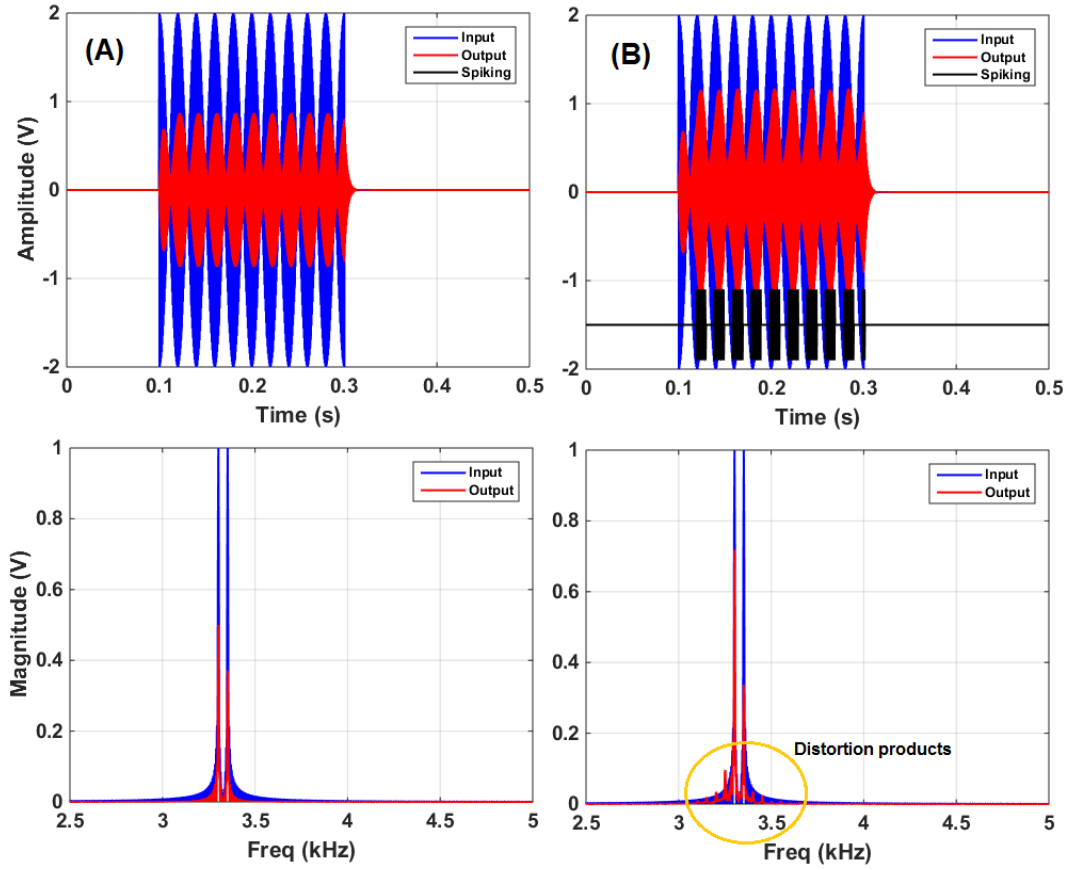

Figure 4.24: Intermodulation response given by the system under the following test conditions: $f_{in} = f_1 + f_2$, $f_1 = f_0 = 3.3$ kHz and $Q = 30$, $f_2 = 3.35$ kHz, $V_{th} = 0.25$ V, $T_0 = 0.166$ ms, $\tau = dt = 20$ μs, and $W = 20$ μs and $K = \pm 10$ (2:1 mode). (A) Without feedback computation; (B) With feedback computation, therefore, highlighting the distortion products as a consequence of the nonlinearities imposed by the feedback system operation.

Table 4.5: Intermodulation distortion products at $\Delta f = |f_1 - f_2| = 50$ Hz.

f_1	f_2	$2f_1 - f_2$	$3f_1 - 2f_2$	$2f_2 - f_1$	$3f_2 - 2f_1$
3302 Hz	3352 Hz	3252 Hz	3202 Hz	3402 Hz	3452 Hz

tortions are not desired, however, there is some evidence that the natural hearing system of mosquitoes use this intermodulation distortion products to hear desired signals. That seems to be another unconventional signal processing technique to identify the presence of signals of interest [135]. Distortion products are thought to be a consequence of nonlinear dynamics in the peripheral sensory system,

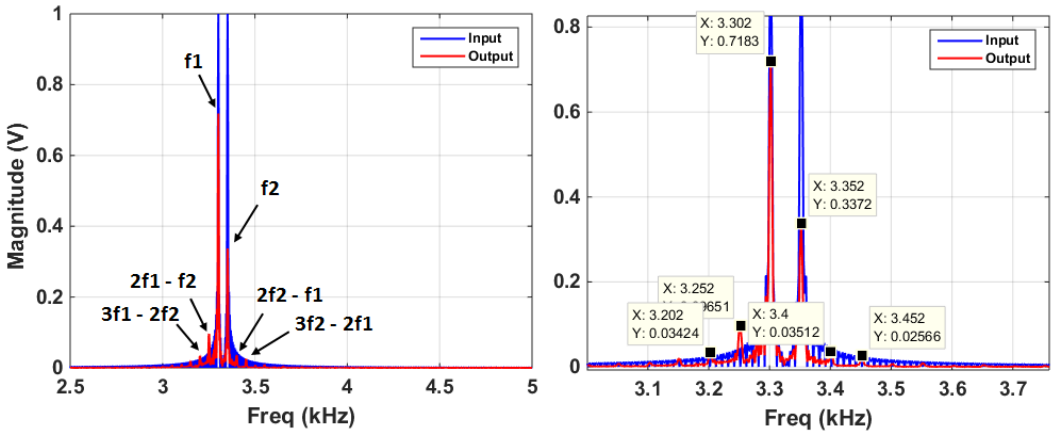

Figure 4.25: Intermodulation response given by the system under the same test conditions as in Figure 4.24, highlighting the intermodulation output response such as distortion products for $\Delta f = |f_1 - f_2| = 50$ Hz.

which can be interpreted by higher level signal processing stages, and used as useful information to trigger behavioural responses.

Moreover, AWGN within the system may impose some timing errors caused by random jittering behaviour at the feedback control operation likely seen at the transitory states (e.g., between the on-off states) as previously noted in Section 4.4. The feedback control operation is dependent on a threshold based mechanism, which can be affected by different AWGN amplitude levels. This means that the uncertainty in the threshold crossing setting at each input wave cycle is increased proportionally with the AWGN level – hence SNR is decreased, as illustrated in Figure 4.26.

4.6 Discussion II

A theoretical revision of the LIF model study including the 2:1 resonance mode is implemented and validated through MatLab simulations, and compared with the 1:1 configuration introduced in Section 4.1. It can be concluded that the 2:1 positive-feedback mechanism studied can maximize the nonlinear amplification

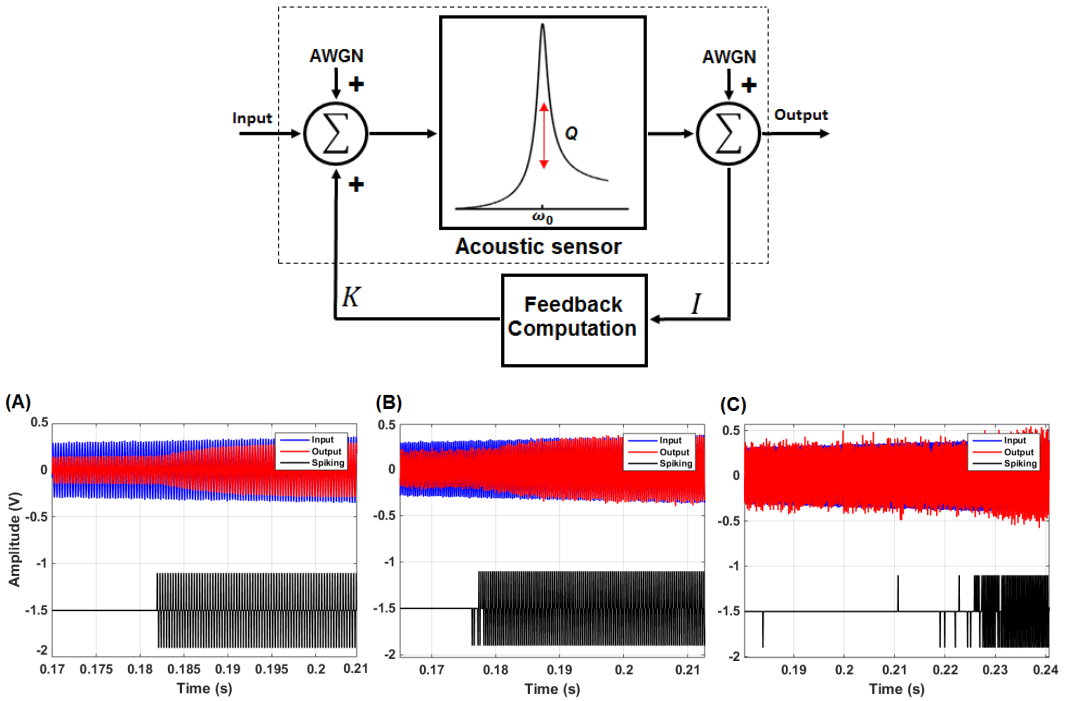

Figure 4.26: (Top) AWGN is injected to the system, which can affect the switching of the feedback mechanism (e.g., increasing uncertainty in the threshold crossing), therefore setting a random entrainment of the feedback control process at the transitory states. (Bottom) (A) SNR = 25 dB; (B) SNR = 10 dB; (C) SNR = 1 dB.

and the sensory responsiveness when compared with 1:1 mode. However, the system's critical region (β point) at 2:1 is shifted to the left of the 1:1 stability graph under the same feedback configuration (V_{th} and K).

Additionally, when inverting the polarity of the feedback signals (e.g., antiphase-locking) the system dynamics are the opposite. This means that, attenuation or suppression of signals can also be achieved by this proposed sensory system concept. Moreover, the presence of competitive signals at the input of the system give results with intermodulation output responses as a consequence of the nonlinearities imposed by the feedback control system mechanisms. The feedback dynamics were also tested with additive white Gaussian noise, which has an impact on the system's SNR, and therefore, imposes timing errors and more uncertainty in the

setting of feedback operation.

This new LIF modelling allows a better understanding of the system dynamics towards an upgrade of the purpose-built experimental embedded sensor system setup presented before, while exploiting the sensing and actuation capabilities built-in the purpose-built MEMS microphone.

Chapter 5

Combining Frequency Agile Tuning & Active Nonlinear Amplification

This chapter presents experimental results conducted to evaluate the performance of a new embedded acoustic sensor system setup that combines both, frequency agile tuning and active nonlinear amplification concept. The aim is to pursue the concept of creating a MEMS microphone framework that is able to be frequency selective, whilst also providing frequency agility and adaptive nonlinear amplification performed at the detector/sensor/transducer level, therefore, enhancing sensory responsiveness to target signals of interest. This is a bio-inspired concept and a novel methodology for audio signal processing, where "the transducer becomes part of the signal processing chain" by exploiting slow- and fast- adaptation control mechanisms (e.g., feeding back DC and AC signals) to a mechanical detector/sensor (e.g., MEMS microphone) supported by electrical systems (e.g., back-end computational systems), as illustrated in Figure 5.1.

The following sections of this chapter present a prototype study (e.g., physical model), which combines the work described in Chapters 3 and 4 by using

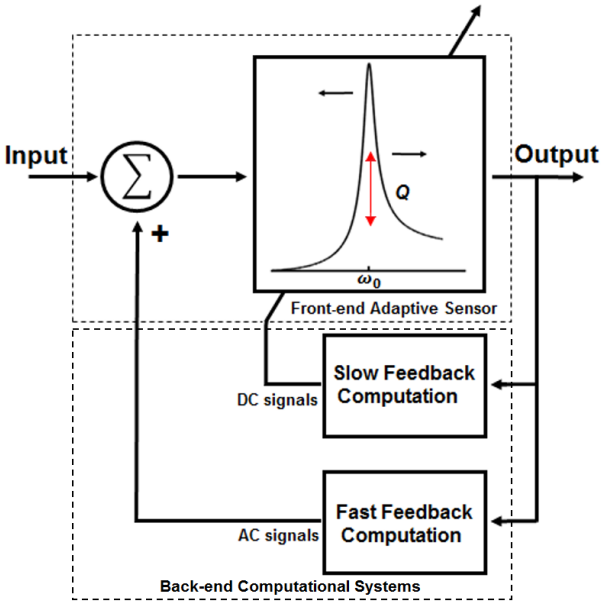

Figure 5.1: Overview of the new bio-inspired embedded acoustic sensor system, combining frequency agile tuning (e.g., exploiting "slow-feedback computation", driving DC signals to adapt the resonance frequency of the front-end transducer) and active nonlinear amplification (e.g., exploiting "fast-feedback computation", driving AC signals to adapt the Q-factor of the front-end transducer).

the hardware framework presented in Chapter 6. That is an embedded acoustic signal processing framework that integrates a new frequency selective MEMS microphone within a closed-loop system. The goal is to provide real-time peripheral signal processing capabilities, while dynamically changing the effective electromechanical characteristics of the MEMS microphone such as its spring constant and quality factor.

5.1 New Embedded Acoustic Sensor System Setup

The schematic overview of the new fully-embedded acoustic sensor system setup is shown in Figure 5.2.

This new hardware setup framework is fully described in Chapter 6, which includes details about the sensors, circuits and systems integrated in this bio-

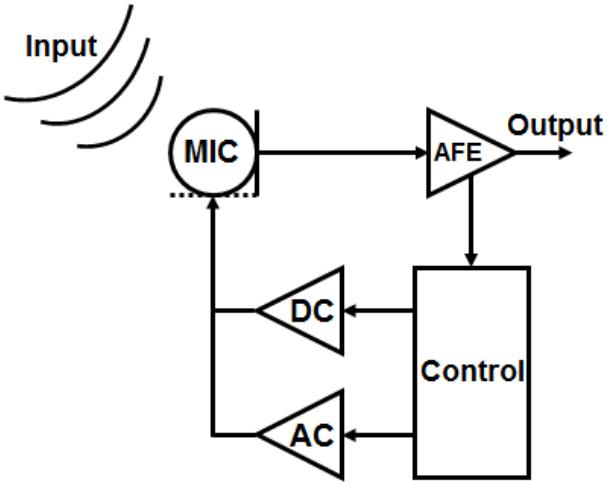

Figure 5.2: Diagram overview of a novel bio-inspired embedded acoustic sensor system setup, including a MEMS microphone within a closed-loop configuration that can be adaptable, while driving DC and AC feedback control signals.

inspired embedded acoustic sensor system as following summarizes:

- A MEMS microphone is designed (MIC: $f_0 \approx 3.3$ kHz and $Q \approx 30$) with a piezoelectric readout and a capacitive driving port, which includes both sensing and actuation capabilities in the same device;

- An analogue front-end (AFE: $\text{Gain}_{[dB]} = 65$ dB; Bandwidth = [0.25 – 25] kHz) is custom-designed in order to provide signal conditioning for the MEMS piezoelectric readout signals, providing an analogue output as a reference measurement signal of the displacements induced on the MEMS diaphragm from acoustic stimuli;

- A custom-designed DC driving circuit, which enables different levels of DC bias voltage ($\text{V}_{OUT} = [1 - 27]\ \text{V}_{DC}$). This circuit is based on a charge-pump circuit topology in order to drive the capacitive comb-fingers port of the MEMS device, for the slow-feedback signal pathway – to adapt the resonance frequency of the microphone;

- An AC driving circuit ($\text{Gain}_{[dB]} = 6$ dB, rise time = 1 μs) is designed in

order to provide the driving of the fast-feedback signals – to control the Q-factor of the microphone. This circuit is based on a standard non-inverter amplifier configuration;

- A purpose-built feedback control computational system based on a digital embedded system architecture (STM32F4 microcontroller unit) is also integrated in the experimental setup, which interfaces all the hardware blocks within a closed-loop fashion providing a platform for real-time audio signal processing and operational control;

- The revised LIF computational model, which is presented at end of Chapter 4, is executed by the computational system described in the previous point. That is a bio-inspired processing routine (e.g., neuronal based model), which is intended to be an efficient and smart generator of pulses to be entrained with the input sound signals, therefore enabling a nonlinear compressive response that is achieved by this purpose-built sensor system framework.

Experimental results are presented in order to validate the overall acoustic and electrical responses of the overall embedded sensor system. These were obtained using the following approach: the MEMS microphone is positioned and properly clamped on top of its analogue pre-amplifier PCB (presented in Chapter 6). That allowed for stable measurements of the device's response under acoustic stimuli from a standard sound transmitter (ESS HEIL Air-Motion Transformer) that is placed perpendicularly to the MEMS microphone, at a distance of 50 cm, and excited by a waveform signal generator Agilent 33250A. The output electrical signals from the MEMS piezoelectric port are conditioned by the AFE before being recorded with an oscilloscope (Tektronix DPO 2014) with a sampling frequency of 1.25 MHz. And laser Doppler vibrometer techniques were used for inspecting the displacements of the microphone diaphragm under acoustic stimuli when required. Signals are plotted using MatLab 2014b.

5.2 Experimental Results

In Chapter 4, simulated results are presented and discussed while varying several of the system parameters such as K and V_{th}, which are related to the LIF theoretical model. Some of those discussions were not fully implemented through the initial purpose-built experimental setup (e.g., using a laser controller with an optical readout from the MEMS microphone diaphragm displacements), which was used to support that study. Here, several new experimental results are presented and discussed, while varying the K and V_{th} values of the LIF system. Moreover, the output response of the system, when intentionally making it unstable or critically stable by setting a high K with a low V_{th} condition, is reported. Additionally, the active amplification response of the system that is obtained experimentally as well as its nonlinear behaviour, while applying competitive input sound signals, is also explored. These are all new experimental results that make a substantive addition to the theoretical study that was previously presented in Chapter 4.

5.2.1 Adapting the Resonance Frequency

One of the main objectives of the research reported in this thesis is the creation of a MEMS acoustic sensor system framework, which could achieve frequency agile tuning. Figure 5.3 shows an example of the frequency agile tuning response that can be achieved by this new purpose-built embedded sensor system framework. For instance four different DC bias voltages were supplied to the capacitive driving-port of the MEMS microphone, therefore, setting four different resonance frequencies to the device namely, V_{DC} = [1, 13, 23, 27], thus f_0 = [3.38, 3.42, 3.75, 3.92] kHz, respectively. Refer to Chapter 6 for further details about the MEMS microphone design, circuits and systems, and associated characterization tests.

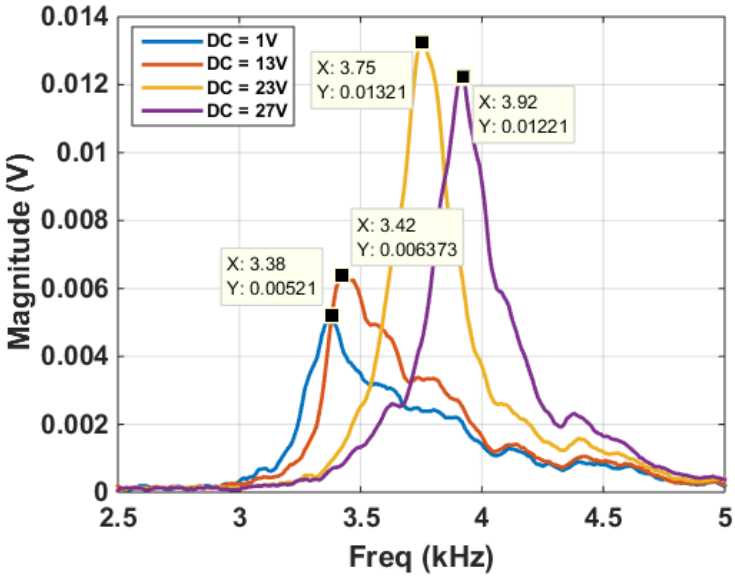

Figure 5.3: Example of the frequency agile tuning response achieved by the MEMS microphone, showing four different resonant peaks while applying four different DC bias voltages at 1, 13, 23 and 27 V_{DC}, respectively, supplied by the charge-pump circuit to the capacitive comb-driver port of the MEMS microphone. Acoustic responses resulted from a frequency sweep test applied to the closed-loop sensor system from 2.5 to 5.0 kHz.

This frequency agile tuning functionality (e.g., slow-feedback adaptation) is intentionally designed to be combined with the active nonlinear amplification capabilities of the system (e.g., fast-feedback adaptation) as described in the following.

5.2.2 Active Amplification in a MEMS Microphone

In Chapter 4, a bio-inspired active nonlinear amplification concept is presented, however some functionalities of that purpose-built system were not completely presented or tested experimentally, namely the entrainment of pulses (e.g., feedback control signals) with the input sound signals using the so-called 2:1 resonance mode (e.g., firing at twice-per-cycle) to enable active nonlinear amplification capabilities. Here, that modality is implemented and evaluation tests are presented as

illustrated in Figure 5.4, showing the active amplification and signal attenuation capabilities of this new purpose-built system, while the pulses are phase-locked with the input sound signals to enable amplification, and in anti-phase-locked to enable attenuation of signals, at different selected frequencies such as f_{in} = [3.3, 3.4, 3.7, 3.9] kHz. It is important to note that different resonance frequencies of the MEMS microphone can be selected using the technique presented previously.

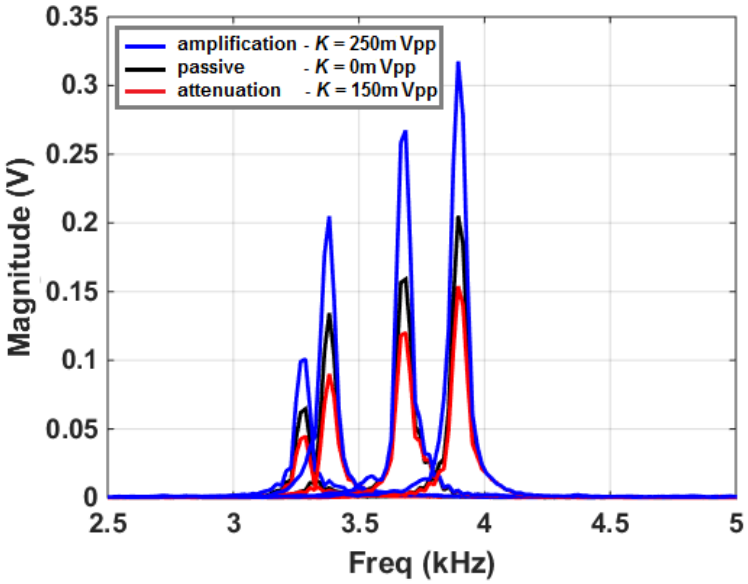

Figure 5.4: Frequency agile response and active amplification and attenuation achieved by the MEMS microphone due to feedback computation. (Black trace) without feedback operation, therefore the microphone shows its passive response at $K = 0$ mVpp; (Blue trace) with feedback operation supplying pulses in-phase with the input waveform - hence amplification at $K = \pm 250$ mVpp; and (Red trace) pulses in anti-phase with the input waveform - hence attenuation at $K = \pm 150$ mVpp.

Experimental tests show that the purpose-built system is able to attenuate signals as well. This capability can be seen while driving the system acoustically with an amplitude-modulated signal, as illustrated in Figure 5.5.

It is important to note that when the input sound signal reaches a defined threshold level that triggers feedback operation, the pulses are fired in anti-phase

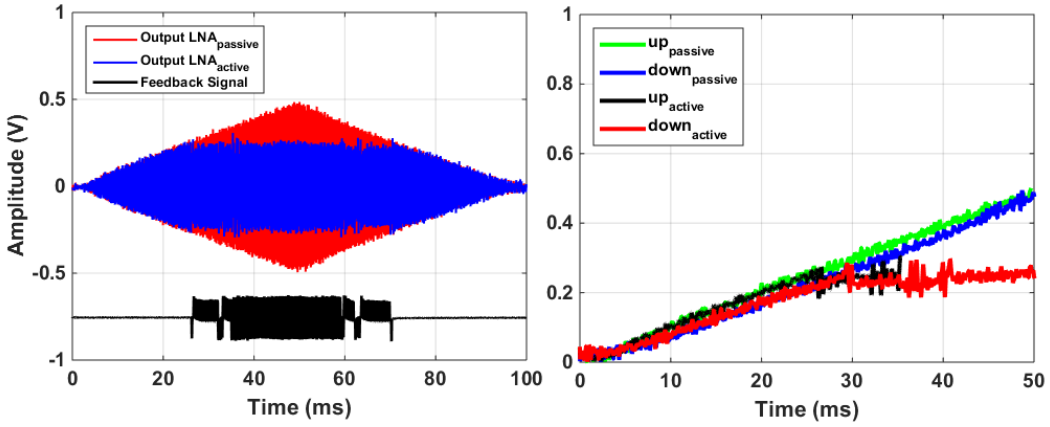

Figure 5.5: The acoustic system response is greatly affected by the polarity of the pulses that are entrained with the input signal. Test conducted under the following conditions: $f_{in} = f_0 = 3.4$ kHz, $V_{th} = 0.2$ V, $T_0 = 0.166$ ms, $\tau = dt = 20$ μs, $W = 60$ μs and $K = \pm 150$ mVpp. (Left graph) OutputLNA$_{passive}$ is the system's output response without feedback (Red trace) and OutputLNA$_{active}$ is the system's output response with feedback (Blue trace); (Right graph) Linear vs nonlinear response of the system showing the attenuation behaviour of the system.

in respect to the input waveform, therefore a limiting effect to the output system response is created (Blue trace in Figure 5.5 - left graph). That effect is not seen when the system is configured without feedback operation, therefore the output signal shows the passive response of the system (Red trace in Figure 5.5 - left graph) for comparison. The linear versus nonlinear response of the system is then shown in Figure 5.5 - right graph.

5.2.3 Compressive Nonlinear Gain

Additionally, the nonlinear compressive gain response of the system was also evaluated as illustrated in Figure 5.6, for a selected resonance frequency such as $f_0 = 3.55$ kHz. This nonlinear compressive gain functionality was predicted by the theoretical model in the MatLab simulation presented in Chapter 4. It was shown that when the K value is set higher than the input sound signal

that is presented to the front-end acoustic sensor (e.g., microphone diaphragm), the contribution of the pulsatile energy added to the system, from the feedback signal path (e.g., biphasic pulses), is higher than the reverse situation – when the input sound amplitude is higher than the feedback energy injected. Therefore, a nonlinear compressive gain response is also exhibited by this new prototyped system, following a similar experimentally determined exponential relationship as previously reported by the simulation of the theoretical model in Chapter 4.

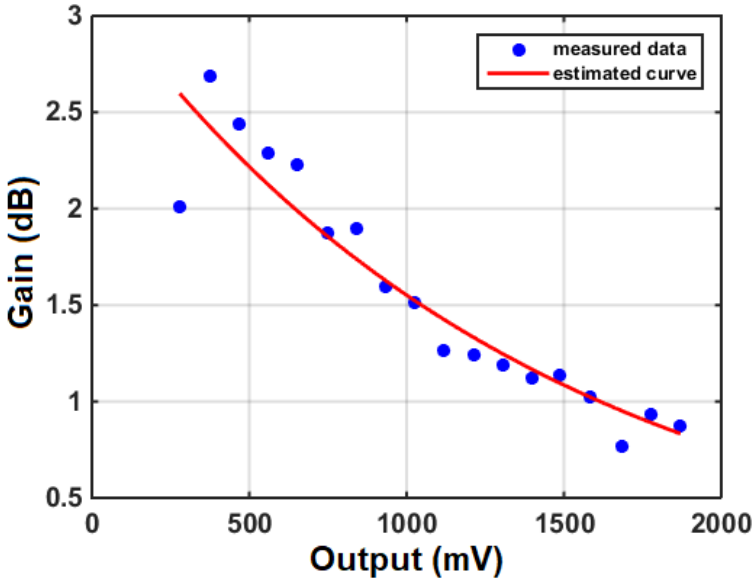

Figure 5.6: Compressive gain response (blue dots) achieved by the purpose-built experimental setup, under the following test conditions: $f_{in} = f_0 = 3.55$ kHz, $T_0 = 0.166$ ms, $\tau = dt = 20$ μs, $W = 60$ μs; $V_{th} = 0.25$ V and $K = \pm 100$ mV. (Red trace) estimated curve as an exponential fit with goodness: $sse = 0.6308$, $r^2 = 0.8932$, $dfe = 16$, $adjr^2 = 0.8865$ and $rmse = 0.1986$.

It is important to note that the x-axis in Figure 5.6 (Output) represents the electrical output signal amplitude of the MEMS microphone after conditioning (e.g., AFE output signal), which is proportional to the input sound level applied to it.

5.2.4 Hysteretic Response

The hysteretic response of the overall system is affected by different feedback configurations namely V_{th} and K values, as previously mentioned in Chapter 4. That was also tested experimentally for this new embedded system setup as presented as follows, while driving the system acoustically with amplitude-modulated signals as typically used to evaluate this kind of system dynamics. The system was set with three different feedback thresholds such as Figure 5.7 V_{th} = 0.5 V; Figure 5.8 V_{th} = 0.75 V; Figure 5.9 V_{th} = 1.0 V and Figure 5.10 V_{th} = 1.25 V, while supplying three different values of feedback signal gain ($K = \pm$[250, 200, 100] mV – [Left, Middle, Right] columns in each figure, respectively), respectively.

It is important to note that under active feedback operation (Black trace) the output response of the system is amplified (Blue trace) when compared with its passive response (Red trace) - without feedback operation, for comparison. Moreover, different K values, define different gain contributions as previously predicted by the theoretical model in Chapter 4.

Again, these results support the assumption that both the hysteretic response and the gain contribution given by the purpose-built system are greatly dependent on K and V_{th} values. It is important to note that V_{th} mainly defines the amplitude signal level in which the feedback control mechanism is triggered, whereas K mainly defines the amount of energy that is injected back to the front-end receiver (e.g., microphone's diaphragm). Therefore, the system when configured with high K values might show greater hysteretic responses, however, higher compressive gain contributions might also be achieved under those conditions. Interestingly, the system seems to set a particular output response for each input sound amplitude that is presented to it, depending on V_{th} and K values configured, as predicted by the theoretical model presented in Chapter 4.

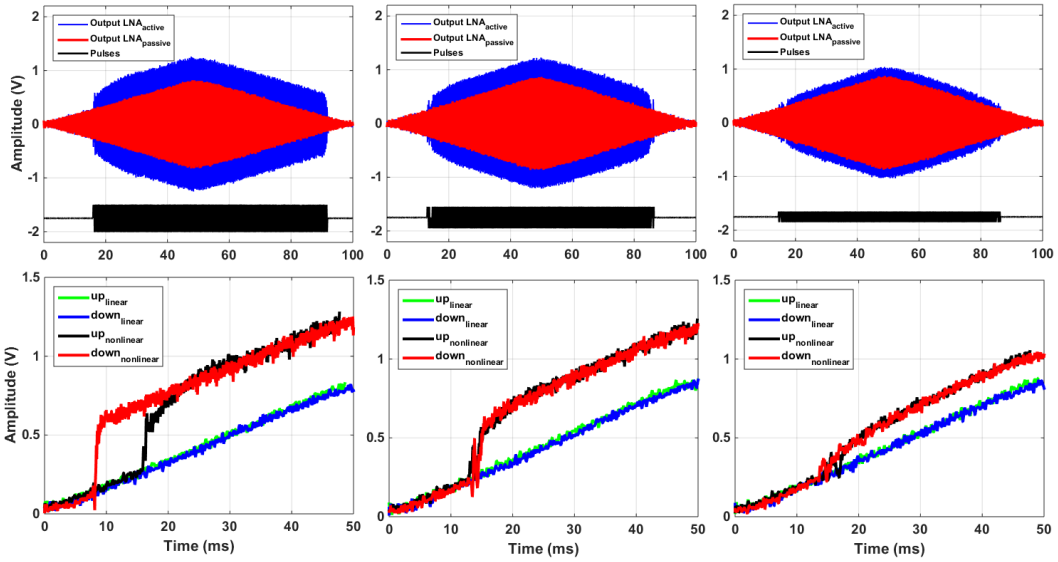

Figure 5.7: Hysteretic responses of the system when $V_{th} = 0.5$ V, while supplying three different values of feedback signal gain ($K = \pm[250, 200, 100]$ mV – [Left, Middle, Right], respectively.

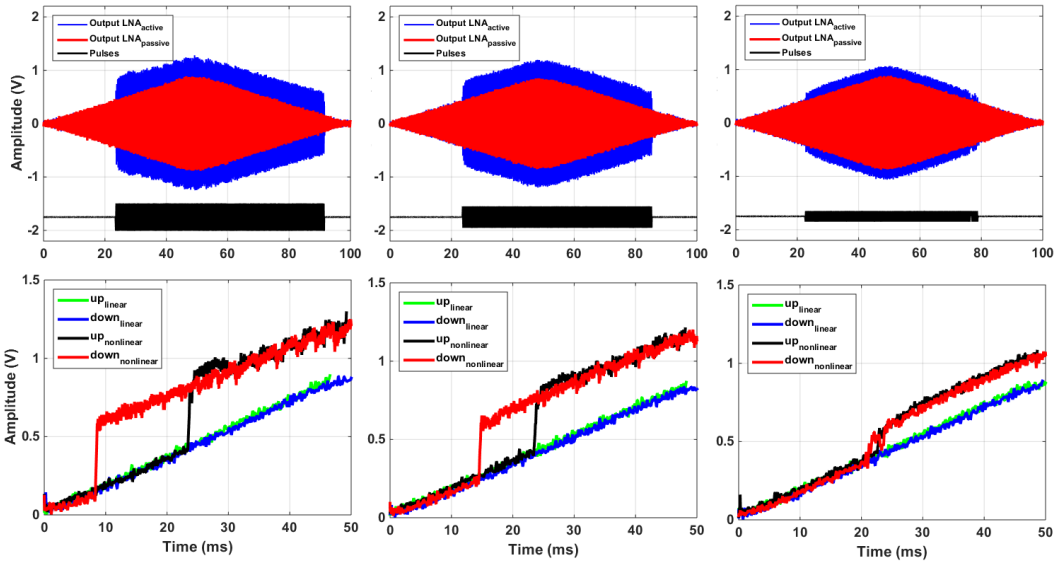

Figure 5.8: Hysteretic responses of the system when $V_{th} = 0.75$ V, while supplying three different values of feedback signal gain ($K = \pm[250, 200, 100]$ mV – [Left, Middle, Right], respectively.

5.2.5 Checking for Stability

One of the consequences of using positive feedback control techniques is that the system dynamics may become unstable (e.g., the system's output appears

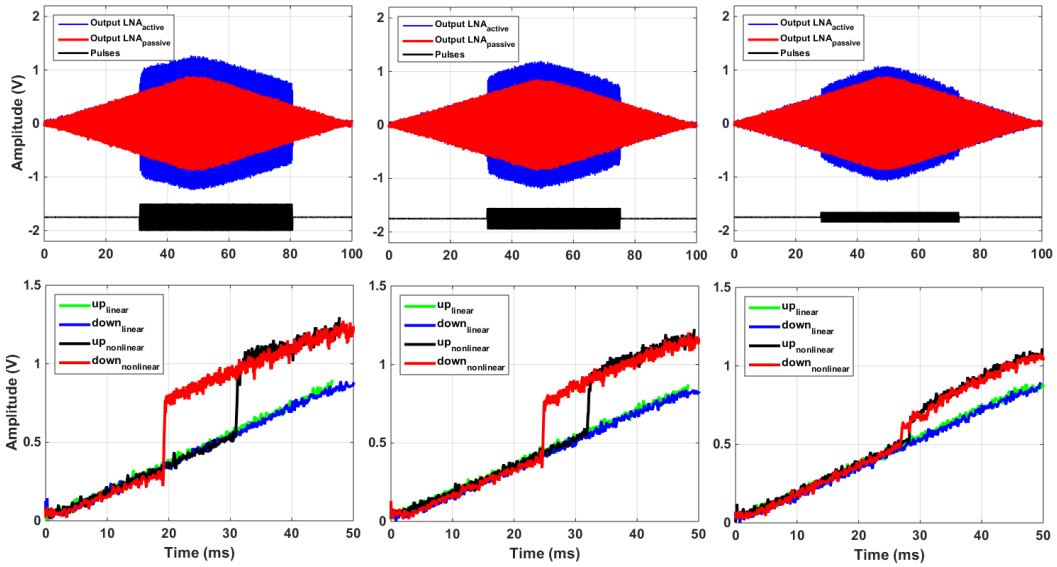

Figure 5.9: Hysteretic responses of the system when $V_{th} = 1.0$ V, while supplying three different values of feedback signal gain ($K = \pm[250, 200, 100]$ mV – [Left, Middle, Right], respectively.

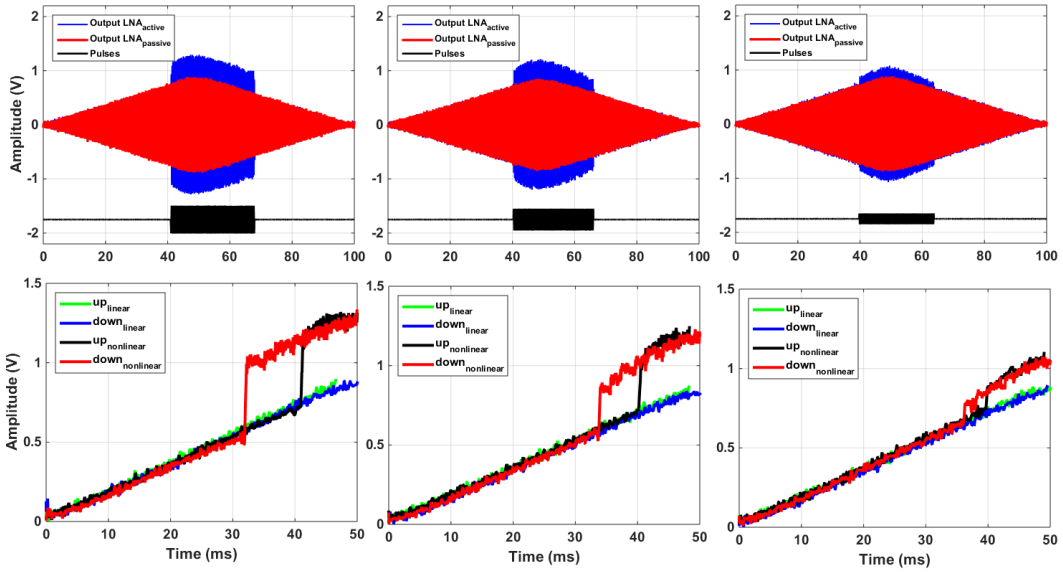

Figure 5.10: Hysteretic responses of the system when $V_{th} = 1.25$ V, while supplying three different values of feedback signal gain ($K = \pm[250, 200, 100]$ mV – [Left, Middle, Right], respectively.

to diverge without bound) or critically stable (the system's output converges to a continuous and endless oscillatory state) under certain feedback conditions.

Figure 5.11 shows some stability tests performed to the purpose-built closed-loop system, while varying K and V_{th} values. The system was intentionally placed in an uncontrolled oscillatory state (middle and right columns in Figure 5.11). That is clearly seen by the system's output response (Blue trace) that sometimes shows an uncontrolled oscillatory behaviour when compared with its under stable-control states (left column in Figure 5.11) or passive response (Red trace), and this system can present different output dynamics depending on different feedback configurations based on K and V_{th} values used. Important to note that the background noise also plays a role on the system's output dynamics. It means that if the system is operating at the edge of stability, it may transit between a stable to an unstable state, and vice-versa, depending on the statistics of the background noise within the experimental setup at a particular time moment.

Some biological acoustic sensors and systems are meant to evolve (e.g., update) their dynamical states over time. Their output responses can be self-sustained through the presence of feedback loops in the system that can result in oscillatory behaviour and nonlinear output responses. Some active systems are thought to operate near the oscillatory instability (e.g., at the critical region, Hopf bifurcation as noted in Chapter 4). Transitions beyond the critical state (e.g., β point) can occur momentarily due to the presence of noise or high feedback gain configurations set in closed-loop positive feedback systems. Therefore, their output responses may become uncontrolled with endless oscillatory responses, occasionally. However, some dynamical systems are thought to have active processes to control their internal feedback parameters in order to restore their stable or critically stable operations [133]. The fact that some biological sensors and systems may operate "at the edge of chaos" [136], is quite interesting, as it might be advantageous in terms of transmission, storage and processing of sensory information [134].

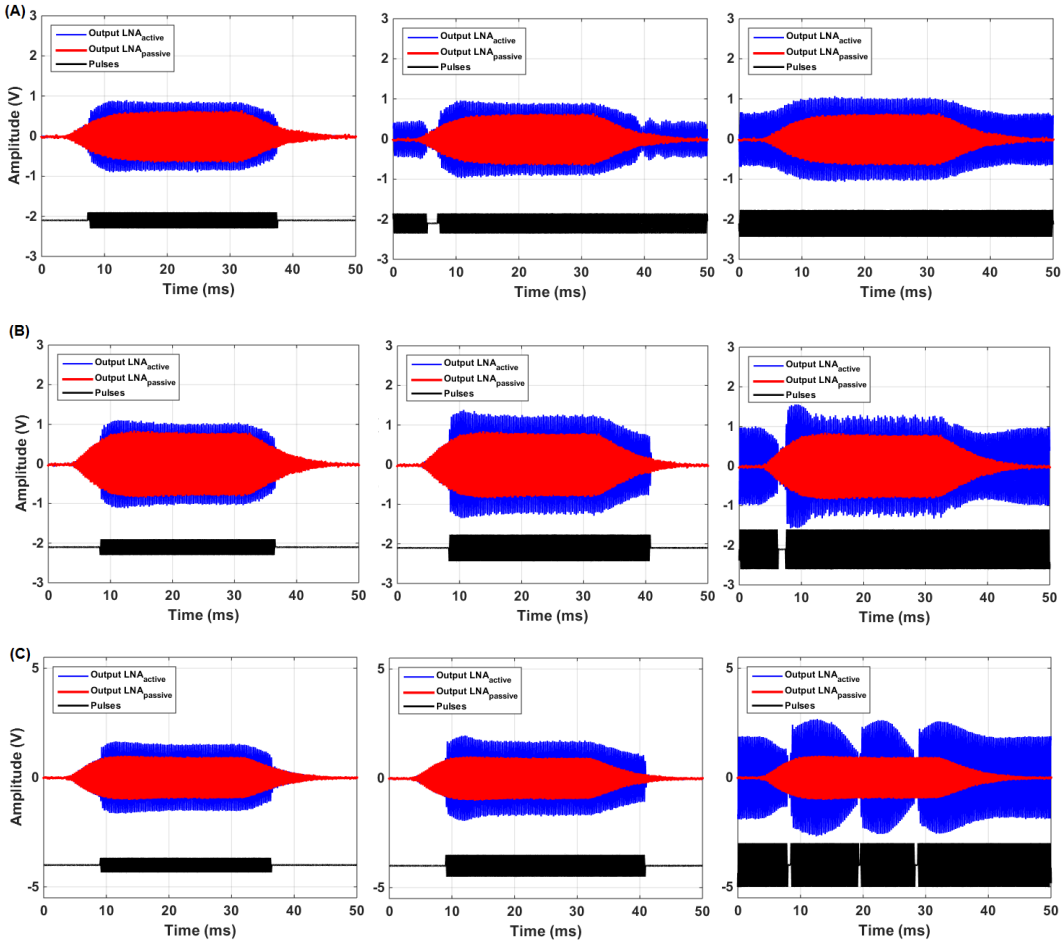

Figure 5.11: Stability of the overall sensor system under the following test conditions: $f_{in} = f_0 = 3.55$ kHz, $T_0 = 0.166$ ms, $\tau = dt = 20$ μs, $W = 60$ μs; (A) $V_{th} = 0.5$ V and $K = \pm[200, 260, 340]$ mV – [Left, Middle, Right]; (B) $V_{th} = 1.0$ V and $K = \pm[200, 340, 510]$ mV – [Left, Middle, Right]; (C) $V_{th} = 1.5$ V and $K = \pm[340, 510, 1000]$ mV – [Left, Middle, Right], respectively.

5.2.6 Intermodulation Products

Another interesting consequence of the nonlinearities imposed by the purpose-built feedback system operation is the generation of output responses as a result of intermodulation in the system when exposed to competitive input sound signals, as illustrated in Figure 5.12 and summarized in Table 5.1.

It is important to note that the presence of intermodulation of signals in this closed-loop system is a result of the nonlinear dynamics imposed by the feedback

Table 5.1: Summary of the Intermodulation as distortion products generated by the system as shown in Figure 5.12 for $\Delta f = |f_1 \breve{} f_2| = 50$ Hz, 100 Hz and 150 Hz.

	f_1	f_2	$2f_1 - f_2$	$3f_1 - 2f_2$	$2f_2 - f_1$	$3f_2 - 2f_1$
(A)	3550 Hz	3600 Hz	3500 Hz	3450 Hz	3650 Hz	3700 Hz
(B)	3550 Hz	3650 Hz	3450 Hz	3350 Hz	3750 Hz	3850 Hz
(C)	3550 Hz	3700 Hz	3400 Hz	3250 Hz	3850 Hz	4000 Hz

mechanisms exploited in this study. The presence of distortion products at the system's output were investigated over the mechanical (e.g., MEMS microphone diaphragm) and electrical (e.g., AFE output signal) block parts of the experimental setup in order to verify their occurrence. It is clear that the signals outputted by the mechanical and electrical stages are faithful matched.

5.3 Discussion

The work presented in this chapter provides a substantive addition to the theoretical study, simulations and to the initial experimental setup results that were presented in Chapter 4. Therefore, a novel bio-inspired acoustic sensor system concept was prototyped, that allow the sensor's resonance frequency to be selected through the use of slow-feedback mechanisms (e.g., DC bias signals), and whilst also manipulating the sensor's responsiveness in a nonlinear fashion to amplify or attenuate selected signals through the use of fast-feedback mechanisms (e.g., AC bias signals). Moreover, the processing time to compute the new LIF routine is 11.73 μs that was measured experimentally, and it is below 20 μs sampling time set by the acquisition task, therefore real-time signal processing is ensured.

Future investigations based on this purpose-built signal processing framework might be towards the creation of new adaptive processes, for instance dynamically changing the feedback variables - V_{th} and K values (e.g., in real-time). Furthermore, exploiting a critical sensory system architecture that potentially can be

operated at the edge of chaos, perhaps, it can provide effective computation at the sensor level, which in terms of transmission, storage and processing of acoustic information may offer some advantages.

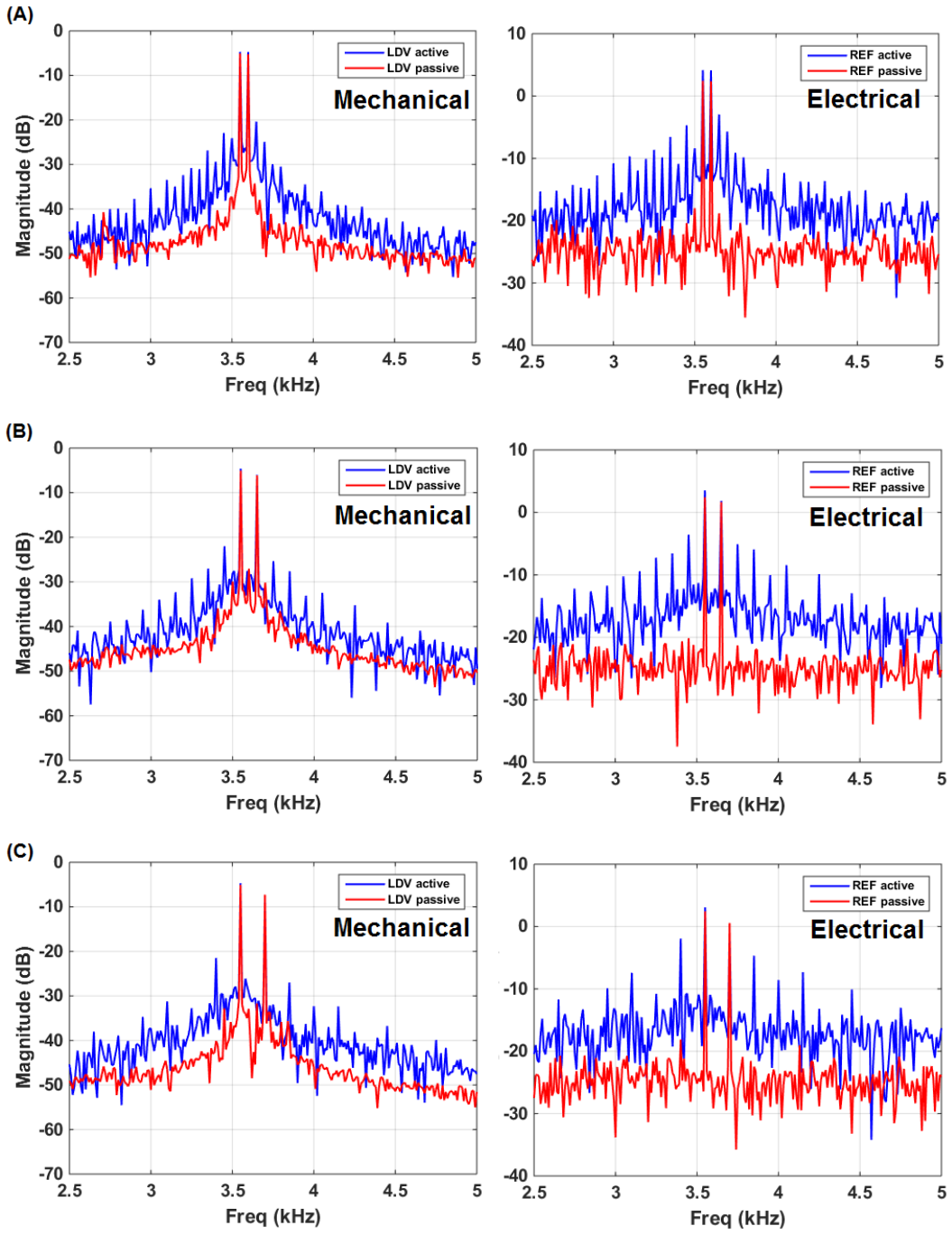

Figure 5.12: Example of distortion products recorded using LDV techniques over the microphone's diaphragm (Left-side graphs), which are also present at the electrical output signal stage (Right-side graphs). (A) Δf = 50 Hz; (B) Δf = 100 Hz; (C) Δf = 150 Hz; (Left-side graphs) LDV measurements with (Blue trace) and without (Red trace) feedback operation; (Right-side graphs) Output electrical signal recorded after the conditioning stage (e.g., AFE circuit); with (Blue trace) and without (Red trace) feedback operation.

Chapter 6

A New MEMS Microphone & Embedded System Framework

Standard MEMS microphones are generally designed with a broad frequency response in order to address multiple audio applications. When operated in typical noisy environments such microphones might be vulnerable to wideband background noise or interfering signals, which might require further signal processing techniques to remove them, generally relying on power-hungry digital signal processors (DSP). In this Chapter a new MEMS microphone framework is presented that allows a selective microphone to be placed within a closed-loop system and be dynamically adaptable to deal with some signal requirements and compatible with real-time signal processing applications.

Towards the Development of a Frequency Agile MEMS Microphone

This work aims to present an acoustic device system that can be used as a sensor while also actuated within a feedback loop system. Therefore, this sensor is capable of being dynamically adaptable. As mentioned before, biological acoustic

sensors have evolved to be adaptable through the presence of feedback mechanisms. That helps in the process of manipulating acoustic information at the sensor periphery before sending it to higher level computational systems in the auditory pathway. Clearly, this gives advantages in terms of power efficiency when there is a need to process a large amount of sensory information in a limited time frame [89]. Designing acoustic sensors such as MEMS microphones, which are inspired by nature is not new [137], [138], [139]. Moreover, two bio-inspired acoustic sensory concepts (Chapters 3 and 4) were combined and presented in Chapters 5 of this thesis – supporting the assumption of the "transducer becomes part of the signal processing chain". That can be achieved by exploiting feedback mechanisms at the sensor level in order to alter its acoustic response namely its resonance frequency and Q-factor. Therefore, this chapter aims to extend the study further by presenting a MEMS microphone signal processing framework designed to pursue both concepts combined within the same hardware platform. It includes a new MEMS microphone design with piezoelectric and capacitive sensing and actuation modalities, respectively. These two transduction modalities are required within the same device to allow its integration within a closed-loop system. Therefore, a new signal processing methodology performed at the microphone's structural level can be presented, while also using standard MEMS manufacturing techniques within an embedded system architecture.

6.1 Microphone Design and Fabrication

A MEMS microphone was designed in which comprises an 800 μm radius diaphragm, 10 μm thick membrane mounted on 6 serpentine spring arms, as illustrated in Figure 6.1.

Each of the arms is coated with a 500 nm Aluminium Nitride layer for piezoelectric transduction (e.g., sensing port), while the membrane itself is fringed

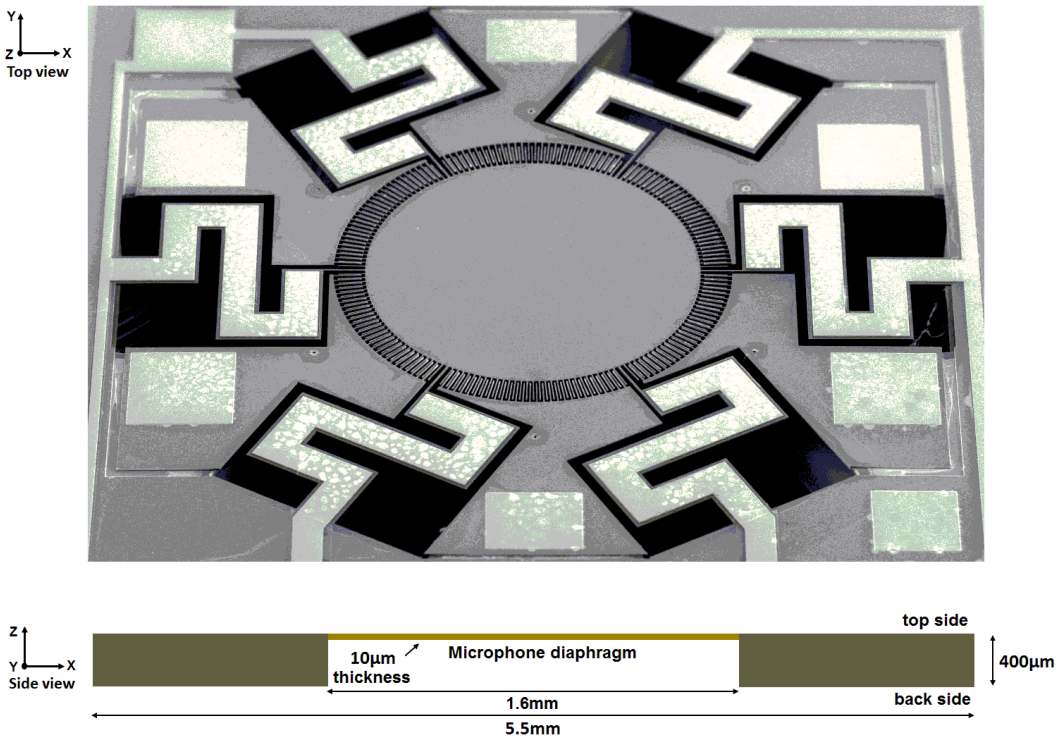

Figure 6.1: MEMS microphone (prototype I) fabricated on single crystal Silicon-On-Insulator using MEMSCAP services. (Top-view) Scanning electron microscopy picture taken tilted 50^o – $\times 30$. (Side-view) design schematic overview that shows the dimensions of the device. *Courtesy to Andrew Reid for the design of this device and Yansheng Zhang for the microscopic picture.*

by 176 (6 μm wide) capacitive comb-fingers (e.g., actuation port), interdigitated with a stator bank of comb-fingers on the surrounding die at 6 μm intervals, as shown in Figure 6.2. The device is backside etched (400 μm thick) at the moving parts to allow free release of movement.

The device was fabricated on single crystal Silicon-On-Insulator (SOI) using MEMSCAP's services (PiezoMUMPs®). In contrast to existing capacitive comb actuators and sensors the rotor combs of this device are intended to have a neutral position in plane with the stator combs, making the electromotive force from the biasing of the combs symmetrical about the z-axis. The relative thickness of the serpentine springs at multiple anchor points reduced the effect of through thickness stress gradients during fabrication to a negligible displacement around

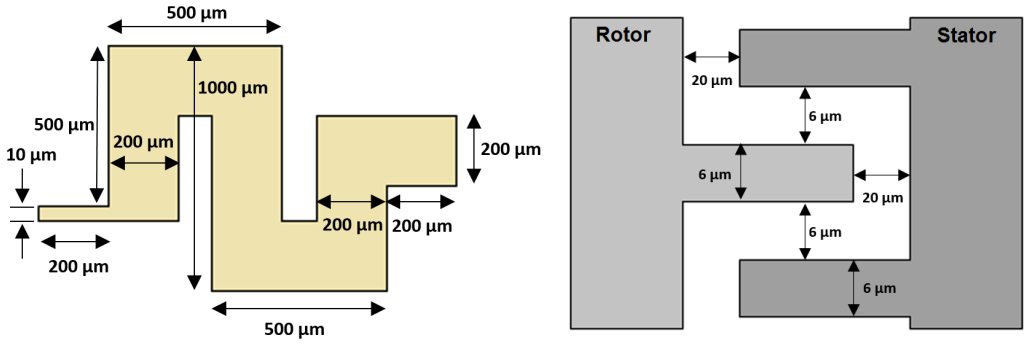

Figure 6.2: Dimensions of the serpentine spring arms (Left-side) and the capacitive comb-fingers (Right-side) used for the MEMS microphone design, respectively.

the centre of the membrane, such that the stator and rotor combs fully engaged. The device is then wire-bonded (e.g., electrical connections) to a standard PCB (see Figure 6.3) for easy access to the capacitive and piezoelectric ports before any experimental and evaluation tests as typically required.

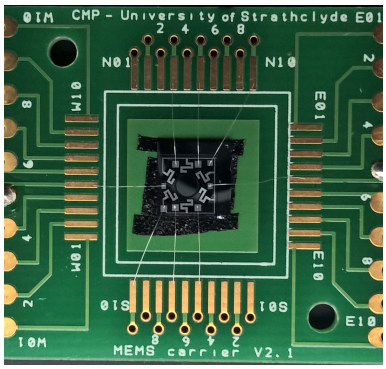

Figure 6.3: MEMS microphone is mounted on a standard PCB, before it is ready for experimentation and evaluation tests. *Courtesy to Yansheng Zhang for the mounting and wire-bonding of this device.*

6.1.1 Finite Element Modelling

In order to predict the acousto-strutural interactions in the MEMS microphone before its fabrication, finite element modelling using COMSOL Multiphysics is performed using the acoustics and structural mechanics modules. The rotational

symmetry of the device allowed the model to be constructed as a 60^o segment of the membrane containing one spring arm and associated stator and rotor combs surrounded by a cylindrical air domain, greatly reducing computation time. Simulating the effect of the constant voltage, applied at the capacitive combs, on the resonance frequency of the membrane required a moving mesh to be applied to the air domain. The minimum mesh element quality was determined to be greater than 0.1 with a minimum element size of 1 μm. A harmonic boundary load equivalent to 1 Pa was applied to the membrane surface and swept at 50 Hz intervals with varying the bias voltage from 0 to 50 V applied to the rotor combs. The membrane damping was estimated as an applied loss factor of 0.015, giving a Q-factor of 30 in this device.

The estimated resonance frequency in air for the membrane without bias was 3.15 kHz increasing to 3.25 kHz with a bias voltage of 50 V, as illustrated in Figure 6.4. Displacement at resonance was estimated at 2.6 μm for a 1 Pa load, however the net pressure from an acoustic wave is anticipated to be much lower due to the large diffraction around the membrane from a sound field at 3.0 kHz.

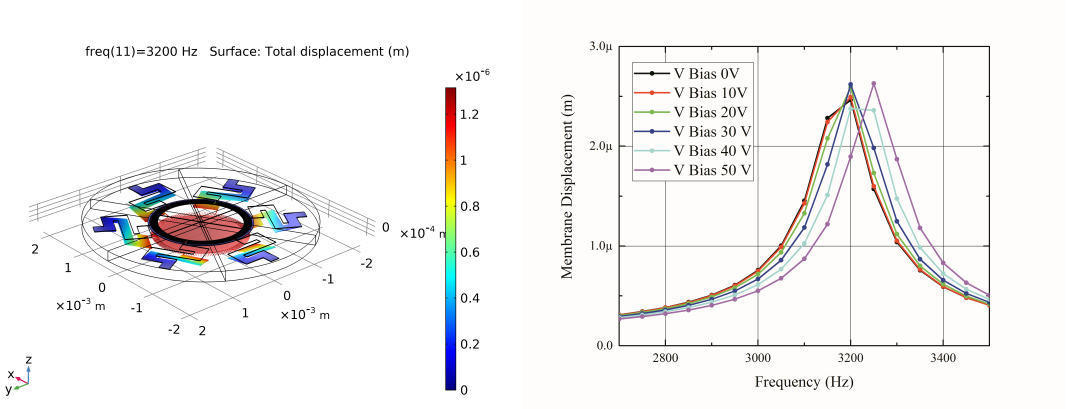

Figure 6.4: COMSOL modelling of the MEMS microphone acoustic response. (Left) simulation of membrane's displacement at predicted resonance frequency of around 3.2 kHz in response to 1 Pa boundary load. (Right) Predicted resonance frequency shift with increasing bias voltage applied to rotor combs. *Courtesy to Andrew Reid for the COMSOL modelling of this device.*

6.1.2 Experimental Evaluation

First of all, the device is positioned under a laser Doppler vibrometer stage (Polytec sensor head MSA-100-3D) to allow measurements of the motion on the microphone's diaphragm in response to acoustic stimulation, as illustrated in Figure 6.5. From this test, it was possible to determine the Q-factor of the device of approximately 30 at 3.3 kHz, which is its 1^{st} resonant mode. The movement of the membrane observed at the 1^{st} resonant mode is a piston like behaviour with symmetry about the z-axis, as expected from its design and COMSOL simulations. A 2^{nd} more responsive frequency of the structure around 9.6 kHz is also visible in Figure 6.5 (Left), which is resulted from a twisting behaviour of the springs (not exactly a typical resonant mode exhibit by circular diaphragm like structure, therefore it is not relevant for the present study).

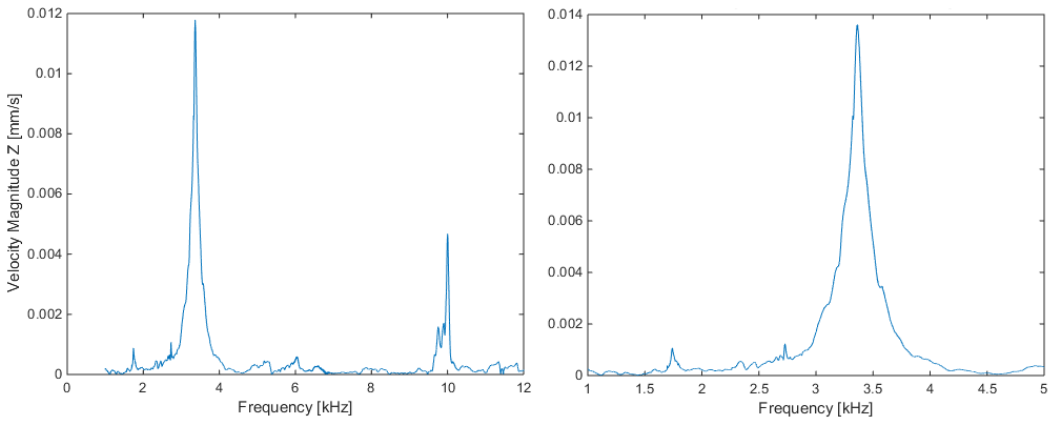

Figure 6.5: Frequency response of the microphone's diaphragm during acoustic stimuli with an AC signal sweeping across the device's bandwidth, showing higher acoustic response at 3.3 kHz and 9.6 kHz. (Left) LDV scan from 1 – 12 kHz; (Right) LDV scan from 1 – 5 kHz.

Secondly, the device is kept positioned under the laser Doppler vibrometer machine to allow measurements of the motion on the microphone's diaphragm in response to electrical stimulation (e.g., transmission mode: driving the piezoelectric layer with AC signals), while applying different DC bias voltages across the

capacitive comb-fingers, as illustrated in Figure 6.6.

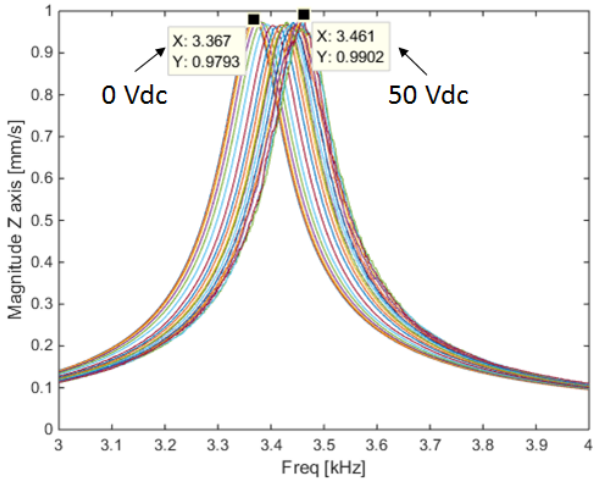

Figure 6.6: Frequency response of the microphone's diaphragm while applying different DC voltage potentials at the capacitive comb-fingers of the device and driving the piezoelectric layer with AC signals sweeping (e.g., from 3 – 4 kHz) around the device's 1^{st} resonant mode.

When the evaluation tests required sound to be driven, a sound transmitter/speaker (ESS HEIL Air-Motion Transformer) is placed perpendicularly to the microphone, at a distance of 1 m, which is excited by the internal signal generator of the laser vibrometer controller. Electrical signals from the microphone's piezoelectric layer are recorded with the acquisition laser vibrometer controller system (Polytec front-end MSA-100-3D) with a sampling frequency of 50 kHz. Therefore, laser signals resulting from the diaphragm movements and the electrical signals from the piezoelectric layer can be compared, as illustrated in Figure 6.7.

As reported in the previous study [19], the simulated and measured acoustic frequency response of such a device could be altered by changing the diaphragm's equivalent stiffness. In this new microphone's design, the stiffening effect over the microphone's diaphragm was also tested (e.g., through COMSOL simulation, and experimentally – mechanical and electrical responses) by driving the capacitive comb-fingers of the device with DC voltage potentials between 0 to 50 V with 5 V

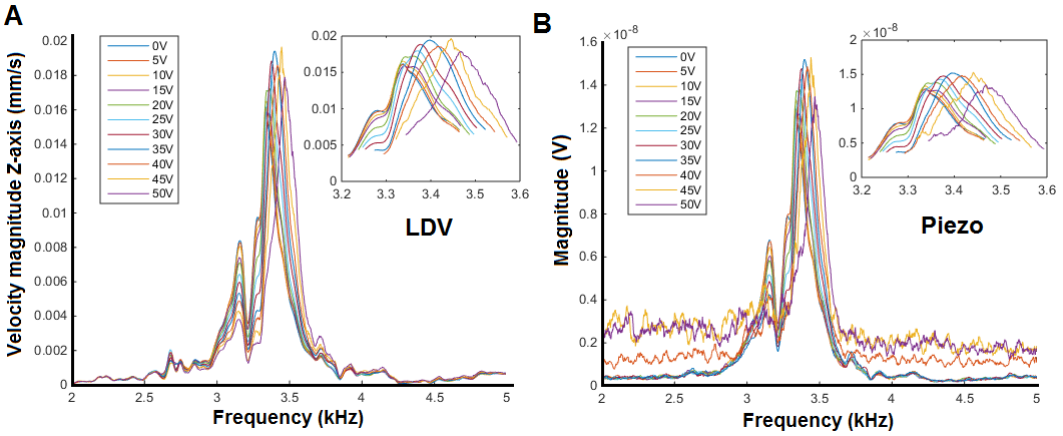

Figure 6.7: Frequency response of the microphone's diaphragm while applying different DC voltage potentials at the capacitive comb-fingers of the device. (A) Measured with LDV; (B) measured from the piezoelectric sensing port of the device. Inset graphs illustrate the zoom in between 3.2 – 3.6 kHz that closely shows the change of the resonance frequency for different applied DC bias voltages.

step increments. This resulted in an increment of the resonance frequency tested around its 1^{st} resonant mode, from around 3.34 kHz up to 3.47 kHz, respectively, as illustrated in Figure 6.8.

This initial work presents the design of a MEMS microphone with piezoelectric and capacitive sensing and actuation capabilities, which possibly allow this device to be integrated within a closed-loop system towards the creation of a frequency agile acoustic sensor system. Simulations and experimental results have shown that this 1^{st} device is able to alter its acoustic frequency response in correlation to varied DC voltage potentials applied at the capacitive port, and the piezoelectric transduction method used for sensing acoustic signals was validated through laser inspections of the diaphragm displacements. The resonance frequency (1^{st} resonant mode) was identified, which can be shifted approximately within a 130 Hz bandwidth. However, the aim is to create an adaptive tuning system across a wider frequency agile bandwidth, therefore further research work is required and addressed as follows:

- A custom-made pre-amplifier circuit is required in order to provide the

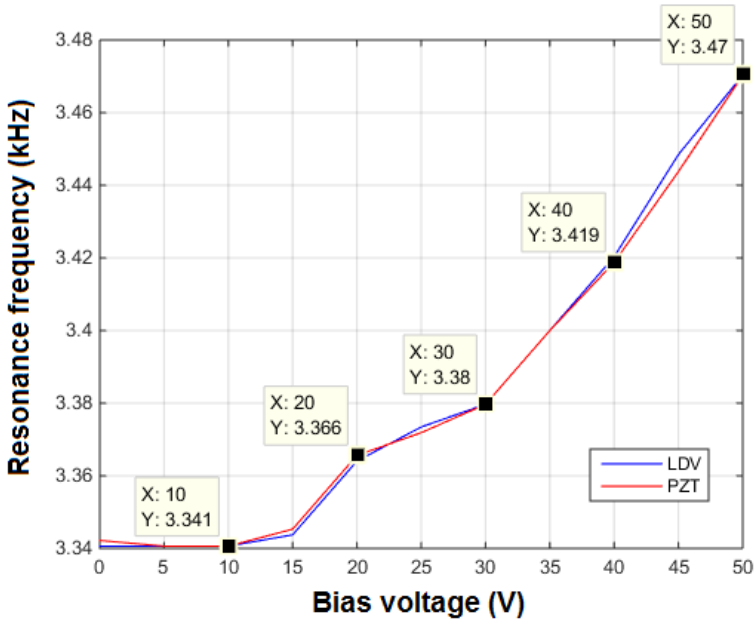

Figure 6.8: Resonance frequency shifting of the microphone's diaphragm when applying DC voltages from 0 - 50 V range. (Blue) measured with LDV; (Red) measured from the piezoelectric port of the device.

conditioning of the piezoelectric signals;

- A custom-made driving circuit is required with the possibility to vary its DC bias voltage output for the device's agile tuning modality;
- A custom-designed AC driving circuit for the device's Q-factor control modality;
- A new design of a MEMS microphone is also considered in order to increase its frequency shifting bandwidth;
- A new purpose-built embedded system setup is required in order to integrate the MEMS microphone in a closed-loop fashion and to enable real-time signal processing and experimental results.

6.1.3 Revision of the MEMS Microphone design

A new MEMS microphone was designed following the same design principles as presented in Section I. Mainly, the goal was to slightly change the design in order to increase the effect of spring stiffening, while supplying DC voltages at the capacitive comb-fingers of the device. Essentially, that can be achieved by changing the spacing/gap in between adjacent interdigital comb-fingers from 6 μm down to 3 μm, therefore increasing the equivalent capacitance of the comb-fingers structure. The remained design lines of the device were kept unaltered as presented before, as illustrated in Figure 6.9.

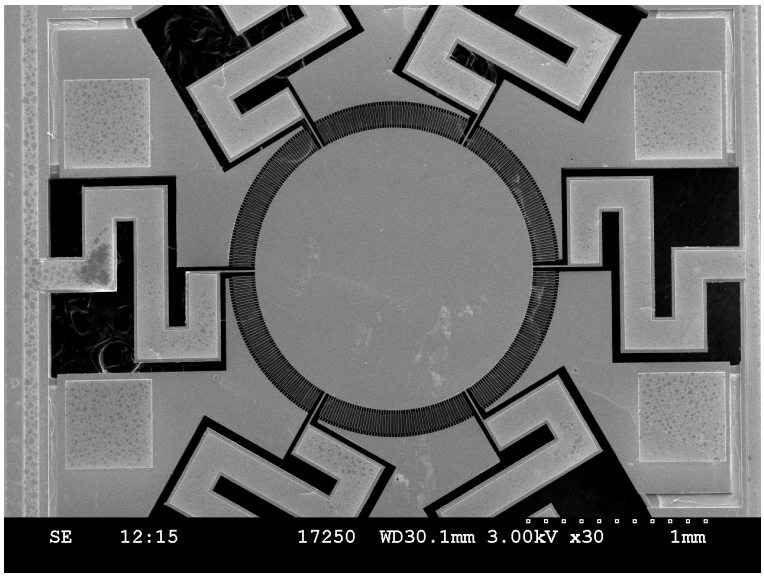

Figure 6.9: SEM picture of the new MEMS microphone (prototype II). The MEMS microphone was fabricated on single crystal Silicon-On-Insulator using MEMSCAP services. Refer to Figure 6.1 for details about dimensions. *Courtesy to Andrew Reid for the design and Yansheng Zhang for the microscopic picture of the device.*

Experimental tests revealed that this new design allows a wider resonance frequency shifting (e.g., greater stiffening effect can be achieved from the DC bias voltage applied) than the previous design, while keeping identical acoustical responses, as observed through LDV scanning (illustrated in Figure 6.10) and

described as follows.

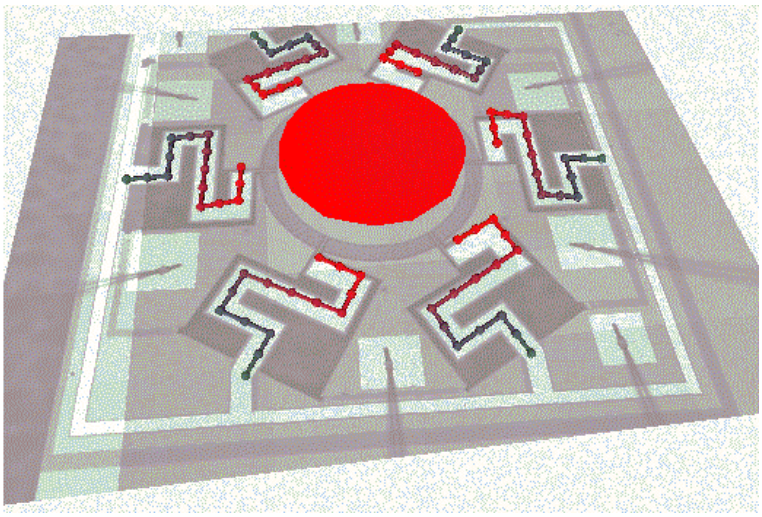

Figure 6.10: LDV scanning shows the displacements of the diaphragm symmetrical at the z-axis (e.g., piston like movements), as expected by its design. *Courtesy to Yansheng Zhang for this picture.*

In order to evaluate experimentally the stiffening effect while applying different DC voltages, the MEMS device is wire-bonded to a custom-designed AFE circuit (e.g., AFE is described in Section 6.2) and firstly tested in an open-loop configuration by applying acoustic stimuli using chirp signals ranging from 2.5 – 5 kHz, as presented in Figure 6.11.

Additionally, the equivalent impedances from the capacitive and piezoelectric ports of a MEMS device can be measured using an impedance/gain-phase analyser (4194A – Hewlett Packard), as illustrated in Figure 6.12.

Therefore, combining the real and the imaginary parts of the equivalent impedance measurements, of each sensing/actuation port, then it can be determined that the equivalent impedance of the capacitive port is about ≈300 kΩ @ 3.3 kHz, whereas the equivalent impedance of the piezoelectric port is ≈70 kΩ @ 3.3 kHz, approximately. This information is important for consideration in the design of the analogue electronic circuits (e.g., piezoelectric signal conditioning, and the capacitive driving circuits).

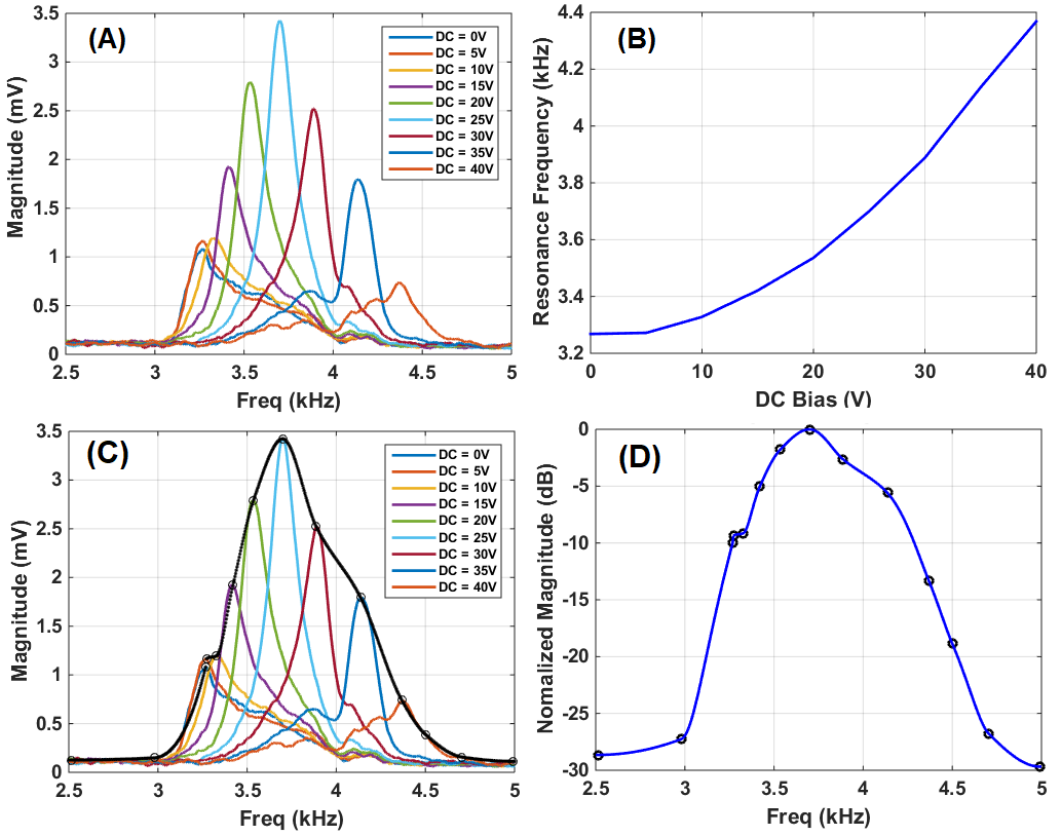

Figure 6.11: (A) Frequency response of the MEMS microphone while varying the DC bias voltage applied to the capacitive comb-fingers, showing a resonance shifting of about 1100 Hz from 3.3 kHz (at 0 V_{DC}) up to 4.4 kHz (at 40 V_{DC}), approximately. (B) Resonance frequency shifting of the microphone's diaphragm when applying DC voltages from 0 - 40 V range illustrates the stiffening effect of the diaphragm's response as suggested by the expression $K_s \propto C.V_b^2$ noted at the end of Chapter 2; (C) Illustrates the frequency shifting bandwidth of this system; (D) System's normalised magnitude response (dB scale), showing the operational-shifting bandwidth of the system at different points, for instance at -3 dB is 428 Hz, at -6 dB is 760 Hz and at -9 dB is 928 Hz.

6.2 Analogue Front-End (AFE)

A custom-designed AFE is presented in order to provide the conditioning of the output signals from the piezoelectric transduction readout of the MEMS microphone, and to ensure compatibility with the input port of the unipolar A/D converter (unipolar: 0 – 3 V, 12-bit resolution) on-board of the microcontroller

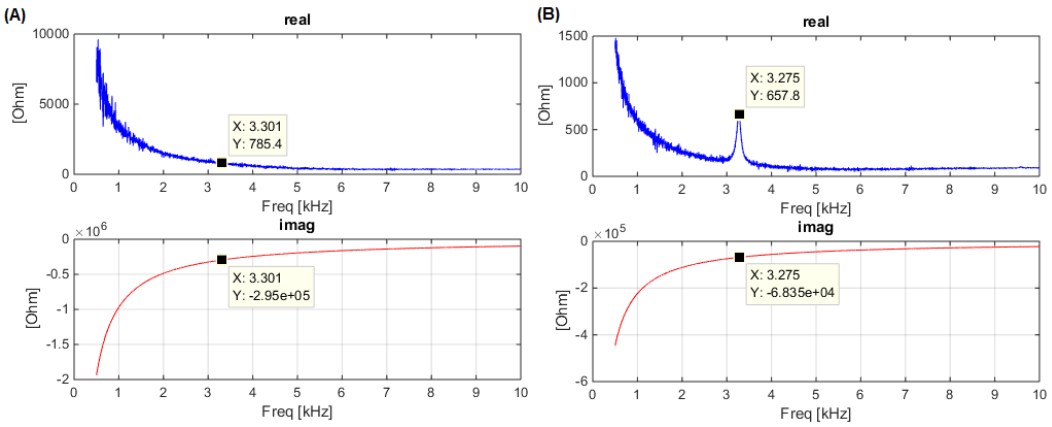

Figure 6.12: Impedance measurements of the capacitive and piezoelectric ports of a MEMS microphone. (A) Capacitive port; (B) Piezoelectric port.

STM32F4. Therefore, a pre-amplifier circuit with $\text{Gain}_{[dB]} = 65$ dB and Bandwidth = [0.25 – 25] kHz overall, and output offset voltage of 1.5 V_{DC} is designed, as illustrated in Figure 6.13.

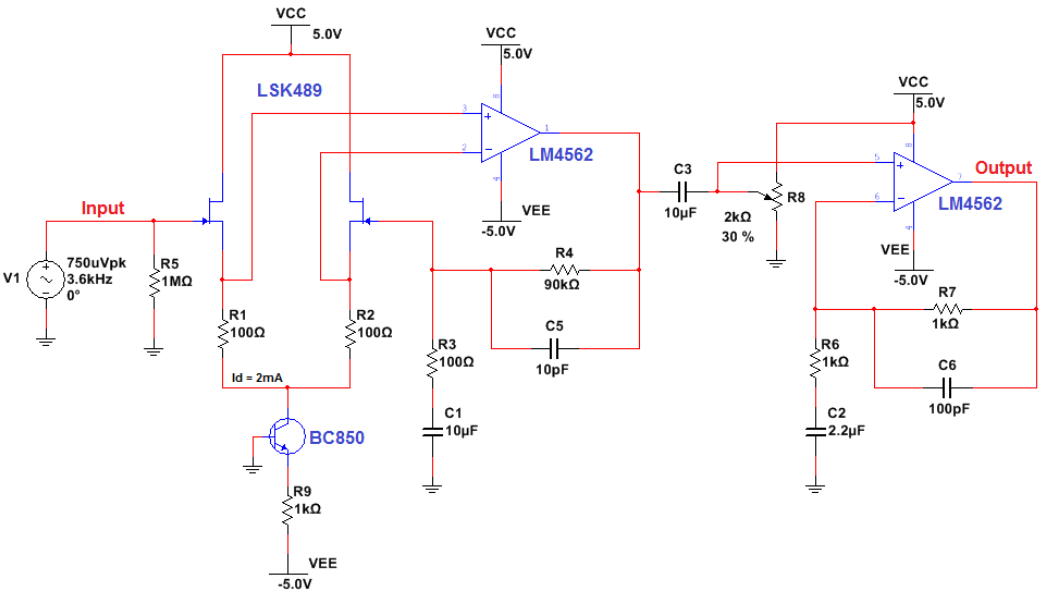

Figure 6.13: Schematic overview of the AFE circuit for the conditioning of the piezoelectric readout signals of the MEMS microphone. $\text{Gain}_{[dB]} = 65$ dB and Bandwidth = [0.25 – 25] kHz with output offset voltage of 1.5 V_{DC}.

This circuit follows the design principles of a hybrid JFET operational ampli-

fier configuration [140], [141]. It presents a differential input stage with a buffer configuration using a low-noise ($e_n = \frac{1.8nV}{\sqrt{Hz}}$ @ 1 kHz and $I_d = 2$ mA) and low-capacitance ($C_{iss} = 4$ pF @ 1 MHz) monolithic dual N-Channel JFET device (LSK489). The differential input stage is set with a drain current of 2 mA derived from the current sink circuit using a NPN BJT (BC850) and the resistor R9, which sets the source current of 4 mA that is split evenly to the two buffers (2 mA each). R5 is used as the bias resistor to set the DC voltage conditions at the gate of the JFET input circuit connected with the MEMS microphone piezoelectric output. Moreover, the gain of this hybrid input circuit stage is mainly set by the non-inverter amplifier configuration using a high-performance audio operational amplifier device (LM4562). The ratio between the resistors R4 and R3 set the gain of the circuit namely $Gain = 1 + \frac{R4}{R3}$ for this amplifier configuration and its bandwidth is limited by the resistor R3 and the capacitor C1 for the lower cut-off frequency – 0.25 kHz, approximately; and R4 and C5 limits the upper cut-off frequency – 25 kHz, approximately, as illustrated in Figure 6.14 (Bottom). The capacitor C3 blocks any DC offset from the hybrid input stage, and the potentiometer R8 provides a voltage offset shift of about 1.5 V that is required for the A/D unipolar input. The last stage of this AFE circuit is another non-inverter amplifier configuration in case extra amplification is required during the setup experimentation, maximizing as much as possible the output signal range for maximum A/D signal amplitude discrimination, as illustrated in Figure 6.14 (Top) (e.g., Transient Analysis showing the full signal excursion from 0 to 3 V @ 3.6 kHz). The gain of this last non-inverter amplifier stage is given by $Gain = 1 + \frac{R7}{R6}$, with R7 being a variable resistor (e.g., potentiometer). The capacitor C2 is used to block the gain of the circuit at low-frequencies and C6 is used to filter-out high frequency components. It is important to note that the overall bandwidth of the AFE circuit is mainly set by the first circuit stage bandwidth – the hybrid JFET - OPAMP.

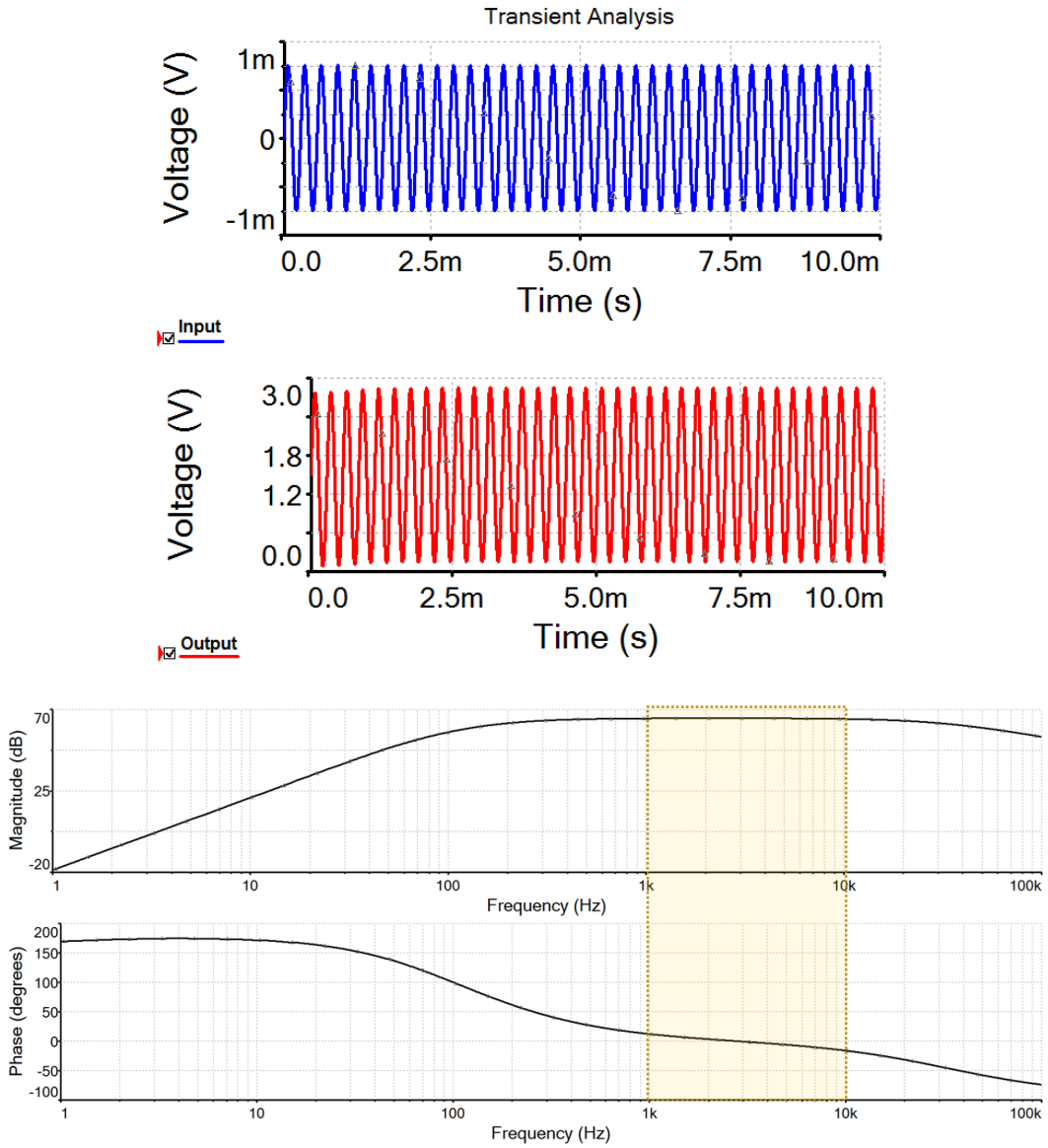

Figure 6.14: (Top graph)Transient and (Bottom graph)frequency response of the AFE circuit, showing a fast time response; flat frequency response with a quasi-linear and almost zero phase-delay between 1 – 10 kHz.

During the AFE design stage some important requirements were considered in order to maximize the performance of this circuit:

- Differential input stage is used to minimize common noise interference pick-up at the microphone level such as 50 Hz from the power line signal and the

potential electromagnetic coupling from the loudspeaker used for the testing of the experimental setup. The loudspeaker's electromagnetic interference is seen as a potential problem, which would impact substantially on the performance of the experimental setup, thus affecting the performance of the real-time signal processing algorithms and the feedback mechanisms (e.g., LIF neuronal model) presented in Chapter 5. Note that no metal shielding was used to isolate the system;

- JFET input is used to achieve as much as possible a low-noise amplifier design analogue front-end from an expected high input impedance signal source ($\approx$70 kΩ) given by the piezoelectric transduction layers of the MEMS microphone providing signal amplitudes within μV range;

- Flat frequency response given by the front-end analogue circuit covering the whole agile frequency range of the MEMS microphone such as from 2.5 kHz up to 5 kHz frequencies, and that is ensured by the AFE circuit design, as illustrated in Figure 6.14 (Bottom);

- Resistor R5 is much bigger than the equivalent impedance of the piezoelectric port of the MEMS microphone in order to minimize the effect of circuit loading - trade-off with noise (e.g., thermal noise contribution);

- Phase-delay within the agile frequency window of the MEMS microphone has to be zero or close to zero, in order to minimize any signal lag (time difference) between signals at different frequencies within that frequency window. The timing of signals in the main signal path (from microphone to AFE to computational unit) is of critical importance for reliable signal processing. That was taken in special consideration since the output of the feedback algorithms is based on the time of arrival of the input signal, for instance the LIF model is an algorithm for phase-locking. Therefore, zero

phase-delay is a requirement and that is ensured by this AFE circuit design, as illustrated in Figure 6.14 (Bottom);

- Overall, in order to reduce the contribution of the thermal-noise in the circuit, the values of all resistors were kept as low as possible, and the OPAMP device (LM4562) is low-noise.

The performance of the MEMS microphone and its AFE circuit response (e.g., sound detection and piezoelectric transduction) is satisfactory for the purposes of this study as found during evaluation tests against a gold-standard B&K reference microphone, as illustrated in Figure 6.15.

It is important to note that the AFE circuit PCB is powered by two +9 V batteries. These are set in a way to provide a bipolar DC voltage supply such as +9 V and -9 V, which is down-regulated to ± 5, respectively, using two linear voltage regulators (MIC5225: +5 V, 150 mA and MIC5270: -5 V, 100 mA) placed on the common PCB.

6.3 DC Bias Driving Circuit (Charge-Pump Circuit)

An important requirement to achieve a versatile update of the stiffening effect on the MEMS microphone acoustic response is through a circuit that can provide an adaptable DC bias voltage output. A way to achieve that is through a circuit based on a DC-DC voltage converter using a standard charge pump configuration, as illustrated in Figure 6.16.

The aim is to step-up DC voltage levels from a 3 V_{DC} supplied at the input of the circuit up to 30 V_{DC} output, which can then be the DC bias mechanism for the frequency agile MEMS microphone to operate. The working principles of the charge-pump circuit are well known in the literature, as referred to at

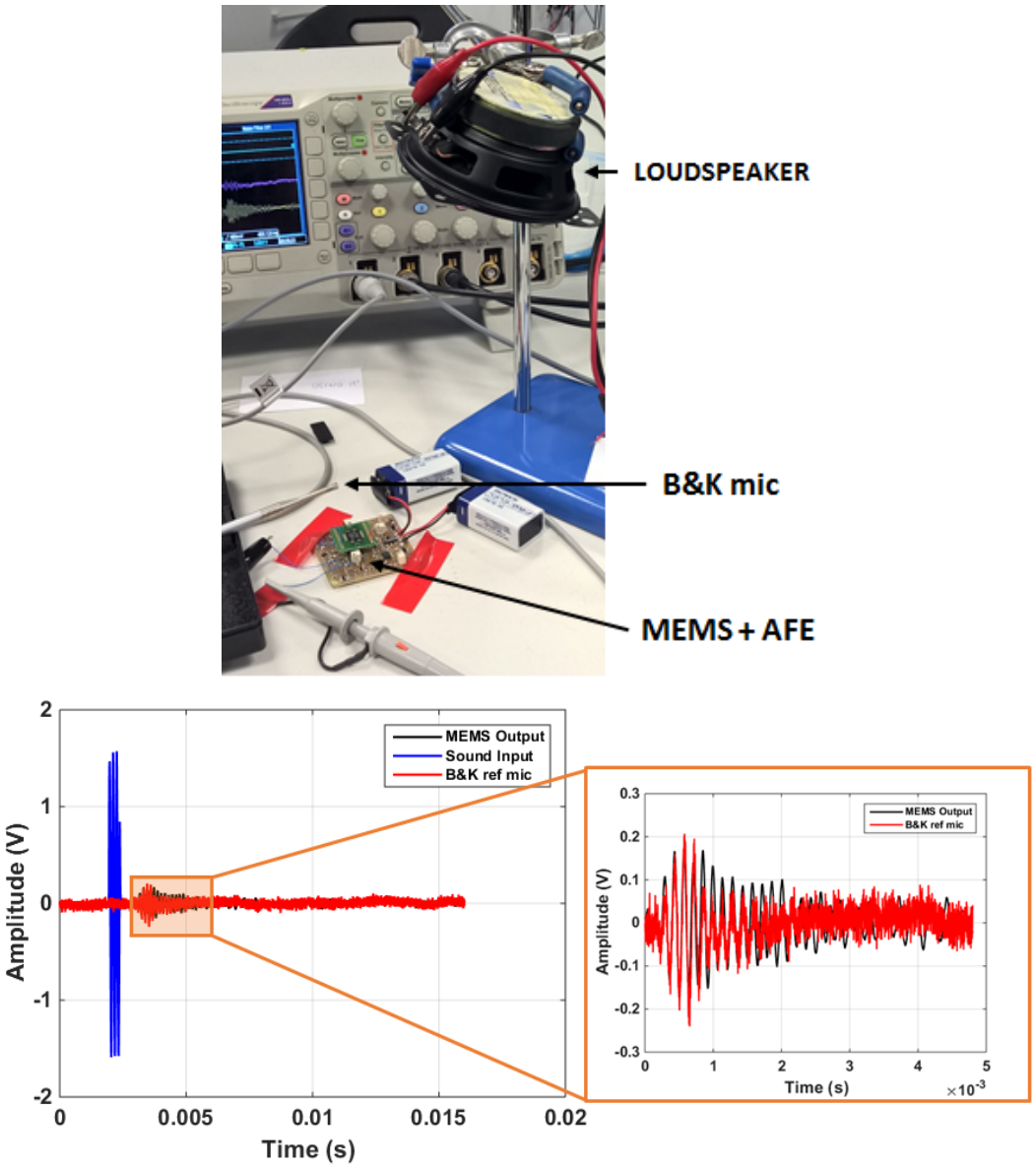

Figure 6.15: Evaluation test of the MEMS microphone and its AFE circuit response compared with the B&K reference microphone. All signals are smoothed with an average filter of N = 32 for clarity of the graphs plotted.

the end of Chapter 2. In this circuit design the voltage output signal is built up based on eleven charge pump stages (e.g., diode-capacitor) supplied by two clock sources at 1 MHz in anti-phase (e.g., with their phase reversed) provided by two on-board digital outputs of the microcontroller STM32F4. A precise 1

MHz clock mechanism is set through hardware interrupt routines using a 16-bit Timer counter.

The output voltage ($Charge_{out}$) is controlled by an On-Off mechanism (MOSFET - Q1) through a comparator device (MCP6561) set with a reference voltage level provided by the $DAC_{control}$ signal from an on-board D/A converter (e.g., on-board to STM32F4). Essentially, this circuit operation builds-up and controls its output voltage dynamically, relying on a switching mechanism by the MOSFET – Q1. Therefore, an additional filtering stage is considered in order to suppress any ripple originated from the charge-pump circuit dynamics (e.g., switching noise). Considering that, the charge-pump output voltage is then filtered by a circuit based on a capacitance multiplier using R7, C13 and Q2 at the final stage of signal regulation (refer to [142] for details about the capacitance multiplier working principles). The capacitor C9 represents the equivalent capacitance of the comb-fingers of the MEMS microphone that is interfaced with the circuit via a shunt diode and resistor R1 (e.g., for output protection).

The device U1 is a buffer circuit using an operational amplifier (OPA836) that connects to the A/D converter input on-board to the STM32F4, which is used for calibration purposes of the voltage output upon start-up stage (e.g., if required by a given application or experimental setup).

Figure 6.17 shows different output voltages (5, 10, 20 and 30 V) generated by the charge pump circuit according with the $DAC_{control}$ reference voltage signal that is applied to the comparator. Some ripple exists (green traces – $V(8)$) at the $DAC_{control}$ signal mainly due to the switching mechanism (Blue traces – $V(sw)$) at the *swi* signal – refer to Figure 6.16, which is the compactor output signal. The smoothed output voltage signals (Red traces – $V(15)$) are at the $Sensor_{in}$ signal after the capacitance multiplier stage.

Experimental tests were conducted to evaluate the response of the charge pump driving circuit with and without load (e.g., MEMS microphone), as illus-

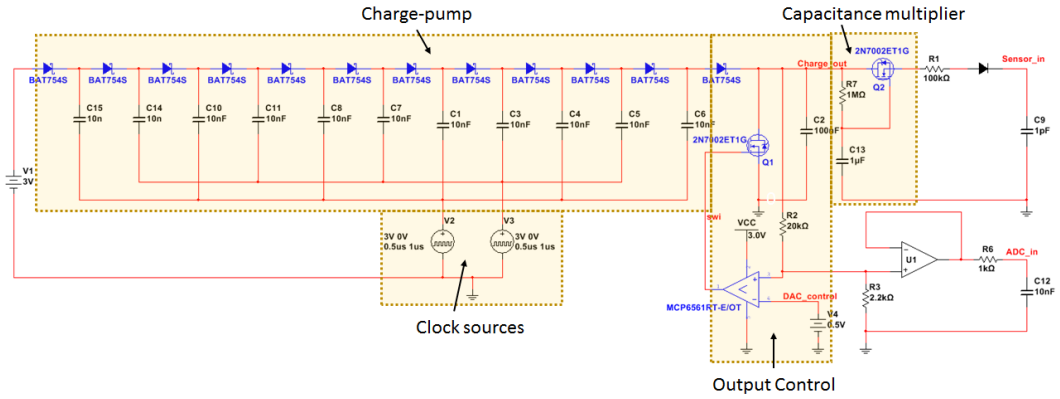

Figure 6.16: Schematic of the charge-pump (CP) circuit designed with 11 stages is used to provide an adaptive DC bias voltage to enable the MEMS microphone frequency agile tuning capabilities.

trated in Figure 6.18, and as summarized in the Table 6.1:

Table 6.1: Summary of the output response of the charge-pump circuit.

	Without Load (open-circuit)	**With Load (MEMS mic)**
Max. Output Voltage	30.2 V	27.3 V
Min. Output Voltage	1.6 V	1.9 V
Rise time	2 ms	1 s
Decay time	0 ms	7 s

Assuming all the above conditions, then the time of convergence and output voltage of this circuit is greatly dependent on the load that is connected at the output of the circuit. Essentially, there is a time spent to charge and discharge the equivalent capacitance of the MEMS comb-fingers, and there is also a drop of about 3 V_{DC} of the maximum output voltage provided by this circuit due to the loading effect from the MEMS microphone equivalent impedance.

Additionally, during the experimental tests the presence of high frequency signals (e.g., switching) at the circuit output was also investigated. Figure 6.19 shows an example of the spectrum (e.g., frequency response from 1 – 500 kHz) of the charge-pump output signal. No significant spurious potential noise was

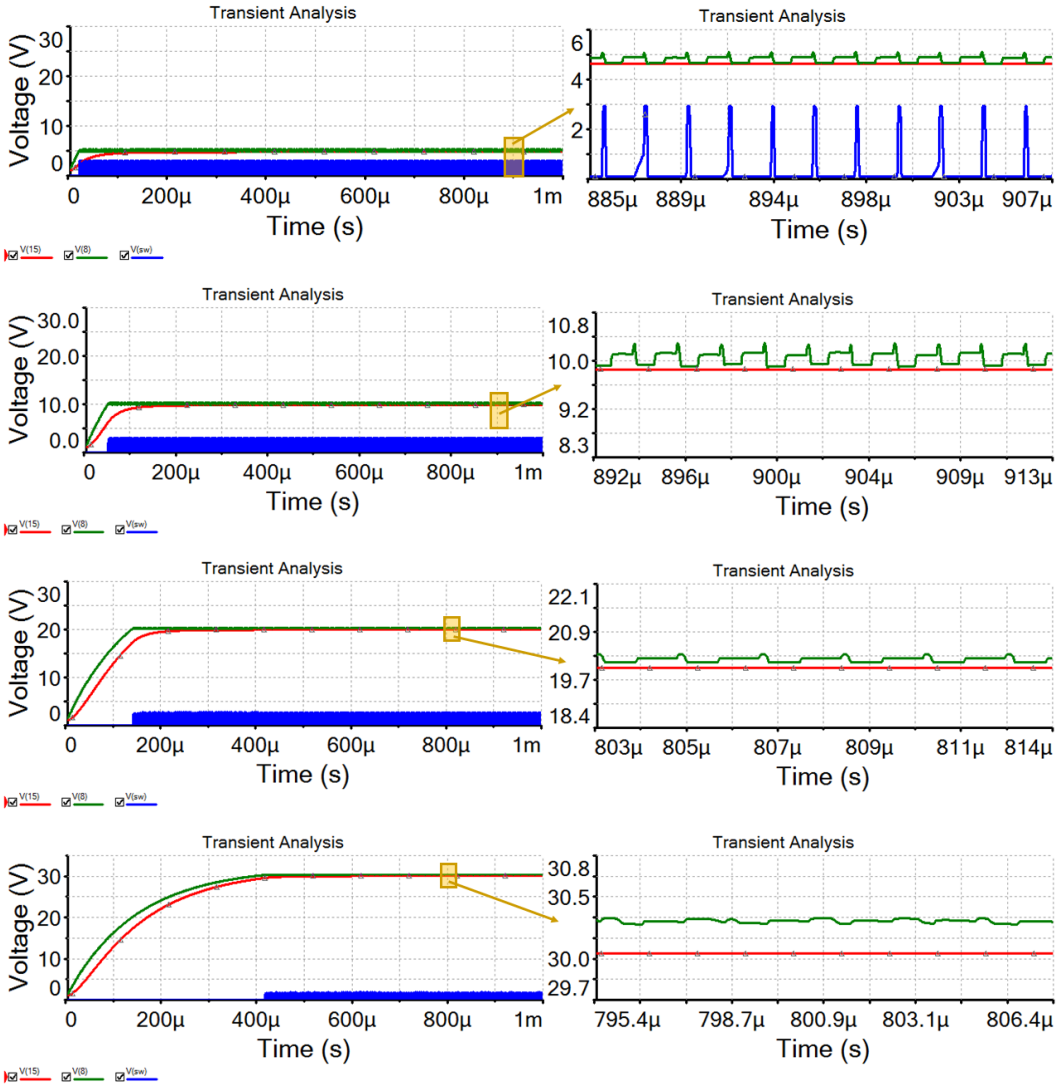

Figure 6.17: Different output voltages (5, 10, 20, 30 V – Top to Bottom, respectively) generated by the charge-pump circuit according with the $DAC_{control}$ reference voltage signal presented to the comparator's input. (Blue trace) switching mechanism to control the output voltage signal; (Green trace) output voltage of the charge-pump circuit showing some ripple due to the on-off switching mechanisms; (Red trace) smoothed output voltage of the charge-pump circuit after the ripple rejection stage (e.g., capacitance multiplier circuit).

found being generated by the internal switching signals of the circuit that could be injected to the MEMS microphone, and picked-up by the piezoelectric sensing port.

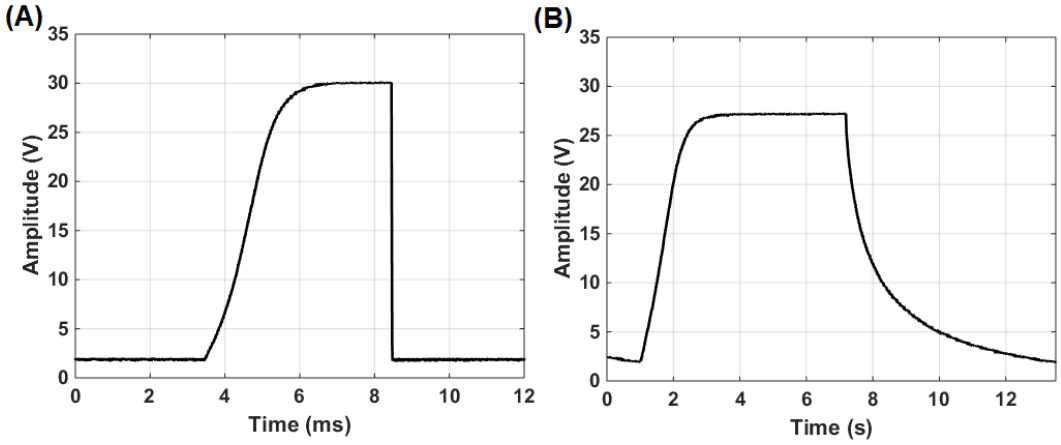

Figure 6.18: Step response of the charge pump circuit, (A) Without load (open-circuit); (B) With load (MEMS mic).

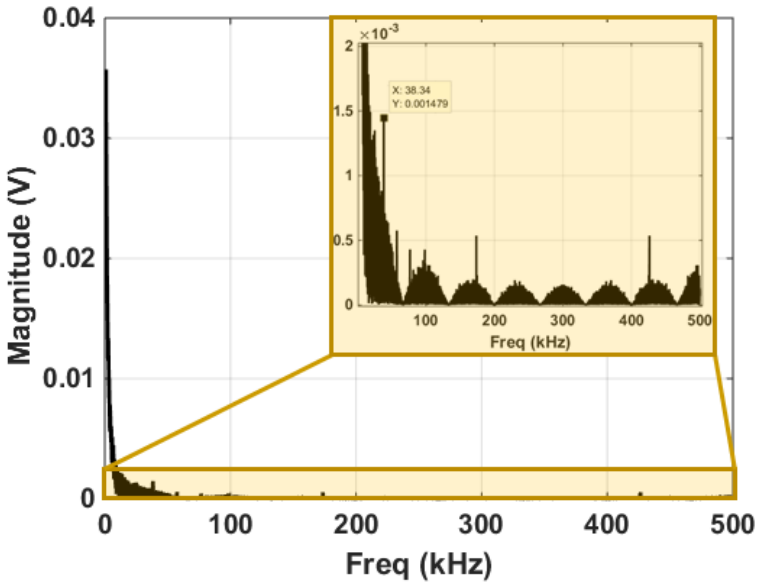

Figure 6.19: Spectrum of the charge-pump output signal, showing no significant spurious potential noise found being generated by the internal switching signals of the circuit.

6.4 AC Bias Driving Circuit (Non-inverter Amplifier Circuit)

Another important requirement for the prototype concept is to dynamically control the Q-factor of the MEMS microphone, by driving AC bias signals (e.g.,

pulses) to it. Figure 6.20 shows the AC driving circuit that was designed, which is derived from a standard non-inverter amplifier circuit configuration. The gain of this circuit can be altered by changing resistor R3 (e.g., potentiometer) while keeping R2 constant, where for R3 = R2 the gain is 2 (e.g., 6 dB). The shunt resistor R4 and the shunt capacitor C1 are for output protection, while C2 represents the equivalent capacitance of the MEMS capacitive comb-fingers port, as used for circuit simulation purposes only.

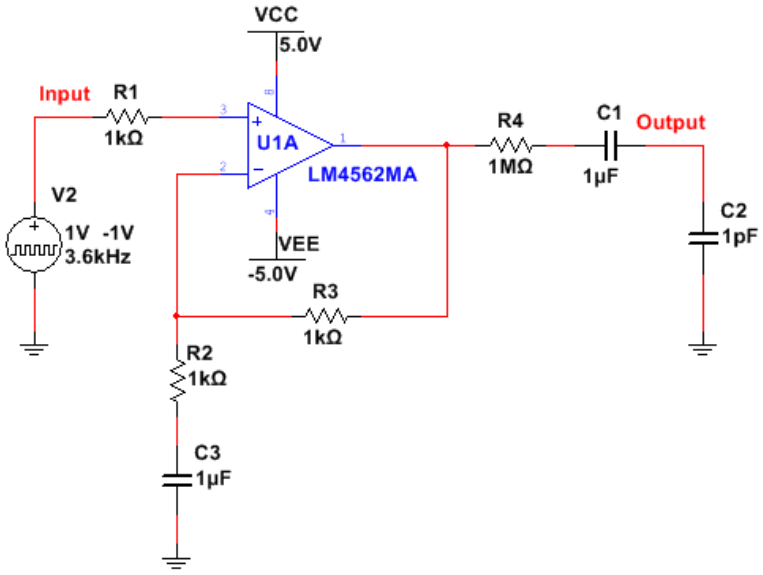

Figure 6.20: Schematic of the AC driver circuit used for the conditioning of the signal (e.g., square pulses) driven by the D/A converter on-board to the STM32F4.

It is important to highlight that the constant time of this circuit has to be fast in order to drive faithful output square-shaped pulses as required by the study present in Chapter 5. Figure 6.21 shows the response of the circuit while applying biphasic square pulses at 3.6 kHz with 30% duty-cycle, as the typical signals to be driven to the MEMS microphone enabling Q-factor control. Assuming that U1A (LM4562) is a wide-band operational amplifier device, the time response of this circuit is mainly dependent on the RC time constant imposed by the shunt components (R4 and C1 – hence rise time is 1 μs) at the circuit output, which

can be changed to well suit any particular application or experimental setup (if required).

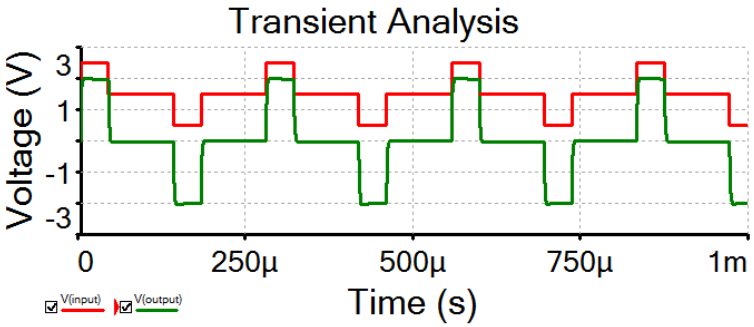

Figure 6.21: Transient time response of the AC driving circuit simulation, while applying potential spike-type signals to the MEMS microphone to enable Q-factor control. (Red trace) signal from a unipolar D/A converter; (Green trace) output signal of the AC driving circuit, showing a fast transient response, amplification ($\text{Gain}_{dB} = 6\text{dB}$; rise time $= 1\ \mu\text{s}$) and zero offset voltage output.

Experimental tests were conducted in order to evaluate the AC driving circuit with the MEMS microphone, as presented in Figure 6.22. Note that a symmetrical generation of positive and negative pulses can be provided by this AC driving circuit.

6.5 Overall Feedback System Framework

For validation purposes of the overall purpose-built sensory system, all the hardware blocks are integrated within a closed-loop configuration in order to enable the evaluation of the overall embedded feedback setup, as illustrated in the block diagram of Figure 6.23, which can provide real-time results as reported in Chapter 5.

Highlights of the embedded system setup features include: an electrical readout from the MEMS microphone's diaphragm displacements through piezoelectric transduction providing correspondent analogue output signals. Signal conditioning is performed on the piezoelectric output signals before A/D conversion (e.g.,

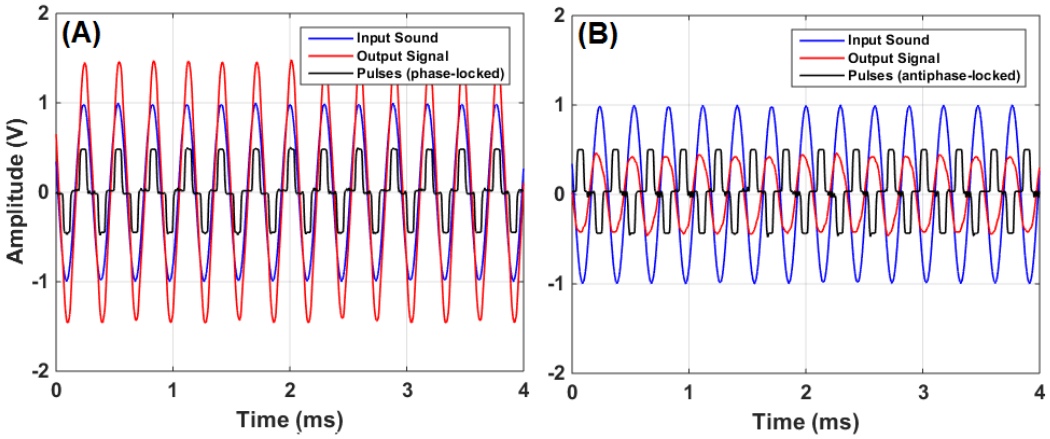

Figure 6.22: Experimental test of the AC driving circuit, showing a symmetrical generation of pulses that are being injected to the MEMS microphone. (A) Pulses in-phase with the input signal – hence output response of the MEMS microphone is amplified; (B) pulse anti-phase with the input signal – hence output response of the MEMS microphone is attenuated.

ADC2, 12-bit @ Fs = 50 kHz, unipolar: 0 – 3V). Signals are acquired and processed using a STM32F4 microcontroller (32-bit Advance Risc Machine – ARM Cortex-M4 architecture) running at 168 MHz clock-speed. Any purpose-built algorithm (e.g., LIF neuronal model) that potentially be executed inside the processing unit (CPU) can generate output signals through the on-board D/A converter (12-bit @ Fs = 50 kHz; unipolar: 0 – 3V) namely, DAC2 is used to set the spike-type signals for the AC driving circuit (e.g., fast-feedback signals path); DAC1 sets the charge-pump reference control voltage (e.g., slow-feedback signals path) and ADC1 can be used for calibration purposes of the charge-pump output signal. Overall, this feedback sensor system setup configuration allow the spring factor of the MEMS microphone to be manipulated (using DC signals) as well as enabling Q-factor control capabilities (using AC signals).

The engineered embedded sensor system is then presented in Figure 6.24. On the left-side is a PCB with the AFE circuit, AC driving circuit, on-off switch, voltage regulators for the +9 V batteries, the capacitance multiplier circuit, and the MEMS microphone (e.g., green PCB with the device at the middle) clamped

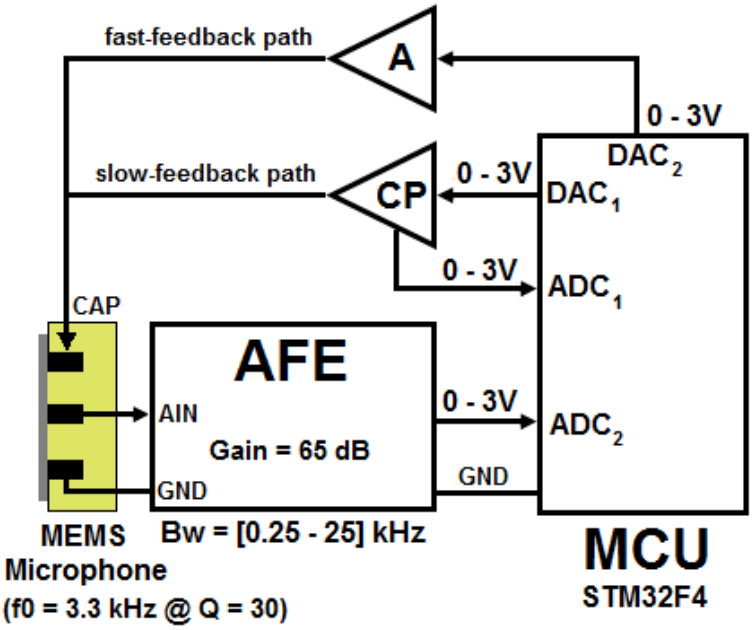

Figure 6.23: Diagram overview of the embedded acoustic sensor system to provide an experimental setup environment for real-time signal processing, where A represents the AC driving circuit and CP is the DC driving circuit connected to the CAP (capacitive port of the MEMS microphone). The piezoelectric signals from the MEMS microphone are conditioned with the AFE circuit and, therefore acquired by the STM32F4 microcontroller on-board A/D converter.

on top facing upwards; on the right-side a PCB with the microcontroller in the centre, the charge-pump circuit, a linear voltage regulator (MCP1802, +3 V, 300 mA) supplied by a + 9 V battery to power this computational unit; a 8 MHz crystal as the main clock source for the microcontroller; an on-off switch; among other peripherals for user-interface such as LEDs and a push-button.

It is important to note that the layout of these two PCBs was designed considering standard PCB design rules and following good practices on layout and routing (shown in Figure 6.25). For instance, one of the main considerations was to keep all the analogue modules and acoustic front-ends isolated (e.g., different ground planes and power supply) from the "noisy" digital modules and switching mechanisms (e.g., charge-pump voltage regulator) and main power line.

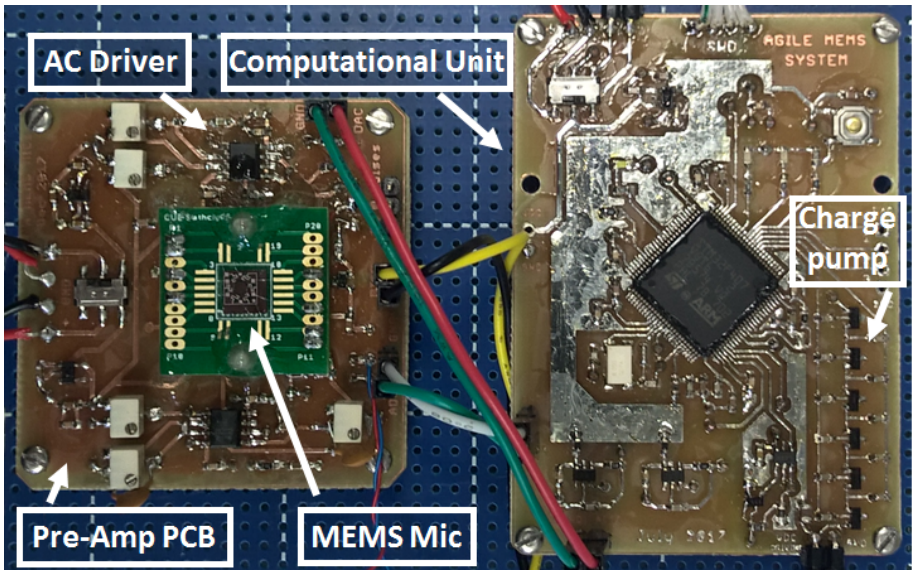

Figure 6.24: Engineered and bio-inspired electromechanical sensory system using a MEMS microphone for sound detection and transduction assisted by an embedded system process and with feedback signal computation to the microphone in order to enhance peripheral signal processing such as frequency agile tuning and active amplification.

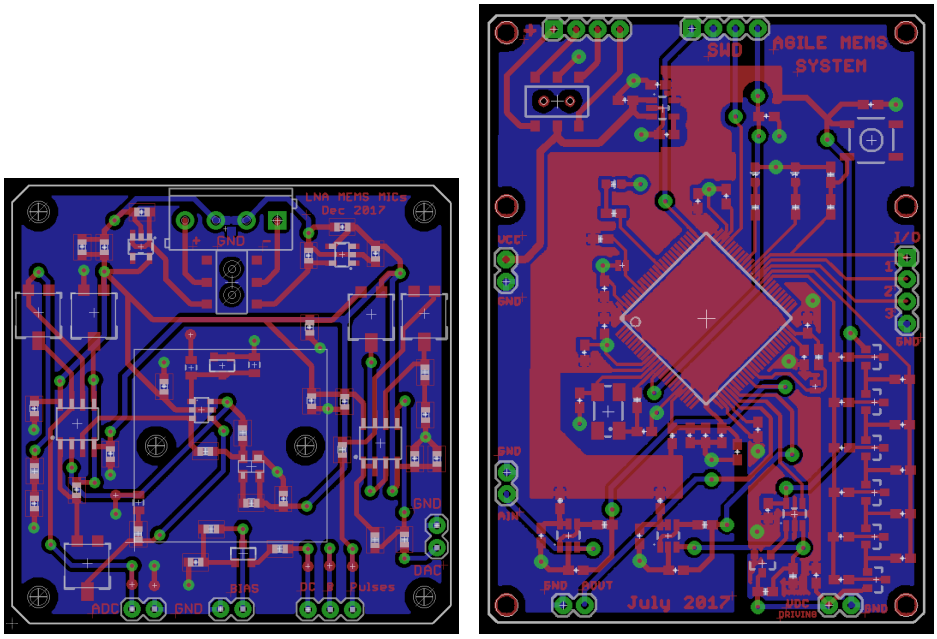

Figure 6.25: (Left-side) PCB layout of the AFE circuit and (Right-side) computational unit system.

6.6 Discussion

This chapter presents the design of a new MEMS microphone that includes sensing and actuation capabilities in order to be integrated within a closed-loop sensory system. A device that can have a selective and agile frequency response. Simulations and experimental results have shown that the resonance frequency of the MEMS microphone can be altered by applying DC voltage signals to the capacitive comb-driver port of the device and the piezoelectric transduction layers can pick-up the diaphragm displacements induced by acoustic stimulation. Piezoelectric output signals can be recorded and the response of the device was validated through laser Doppler Vibrometer techniques as well. The resonance frequency (1^{st} resonant mode) of this new device can be shifted approximately within 1100 Hz bandwidth, from 3.3 kHz up to 4.4 kHz – 0 up to 40 V_{DC}, respectively. Future research should address the impact of manufacturing process variability to the microphone's overall acoustic response associated to the resonance frequency shifting capabilities and sensitivity. Additionally, some analogue circuits were designed and presented in order to create a proper closed-loop feedback system setup for the research presented in this thesis (e.g., Chapter 5). The analogue circuit designs include:

- An AFE circuit, which provides the conditioning stage for the microphone's piezoelectric signals. The circuit design was validated through simulation as well as experimentally, while driving the MEMS microphone with acoustic signals. Note that the interface between the MEMS microphone PCB and the analogue amplifier front-end (e.g., JFET input stage) is a critical point in the setup in order to ensure reliable output signals overall. All wires should be as short as possible and the MEMS PCB has to be well-clamped to the main PCB (e.g., AFE board) in order to avoid undesired vibrations (e.g., mechanical noise) that can potentially be picked-up by the piezo layers

embedded in the microphone structure, otherwise compromising the SNR of the overall sensory system. By following the above considerations, there was no need for additional techniques to reduce electrical and mechanical noises within the experimental setup such as metal casing/box (e.g., faraday shielding) or testing the system inside anechoic chambers. Therefore, the MEMS microphone embedded system could be exposed to standard laboratory environments during all evaluation tests and data recordings. The AFE circuit designed shows robustness for the task of conditioning the piezoelectric signals from the MEMS microphone;

- A DC voltage regulator was designed based on a charge-pump circuit configuration that is capable of providing output voltage levels from 2 up to 27 V_{DC} from a 3 V_{DC} power supply. Note that this circuit is able to drive the capacitive comb-fingers of the MEMS microphone with consequent effects to the resonance frequency of the device. However, the design of this circuit can possibly be optimized in terms of output voltage level and transient time response, if required. The output voltage level can possibly be increased proportionally with the number of stages (e.g., diode-capacitor) in the circuit. And, the transient time response might possibly be improved by revising the output stage of the circuit, namely by decreasing the value of C2 as well as removing the capacitance multiplier circuit, in order to update the output response of the circuit more quickly upon requirement. Further research to revise this circuit should be considered in future work. Note that this circuit was intended to regulate a slow-feedback adaptation process, therefore, it suits the requirements of the present research;

- An AC driving circuit was designed and tested experimentally and also validated through circuit simulation. This circuit is capable of driving the MEMS microphone capacitive comb-fingers port with fast-signals such as

square-pulses. The rise time of the circuit was set to be 1 μs, which is much smaller than the width (e.g., min. 20 μs) of the pulses that are generated by the D/A converter on-board to the STM32F4;

- A new purpose-built embedded acoustic sensor system hardware framework was created integrating the new MEMS microphone and all the analogue and digital circuits and systems in a closed-loop fashion in order enable real-time signal processing for the experimental results presented in Chapter 5.

Chapter 7

Conclusions

Engineering has a lot to learn from biology. Over many millions years of evolutionary processes, nature has been developing the most efficient sensors, circuits and systems, allowing the detection, storage and manipulation of surrounding environmental information, hence enhancing the chances to survive and prosper.

First of all, this thesis starts by describing some essential background knowledge within biological sensors, circuits and systems, focusing on acoustic signals and sensory apparatus. It is clear that biological acoustic sensors and systems make use of several levels of feedback loop mechanisms in order to process peripheral sensory information. That is considered as a useful technique for signal detection and processing and therefore it is used as the backbone for the bio-inspired concepts presented in the remain chapters of this thesis. State-of-the-art engineering related to recent microphone technology was also outlined in the background knowledge chapter (e.g., Chapter 2), including some of the latest advances in designs, specifications and techniques used by the industry and sensor research community for MEMS microphones.

Secondly, the work presented in this thesis develops under the line of thought inspired by nature where a front-end acoustic detector/sensor/transducer (e.g., any acoustic sensor at audio or ultrasonic frequencies) can be placed within a

closed-loop feedback system and be part of the signal processing chain. That exploiting slow and fast adaptation processes between mechanical and electrical mechanisms to enhance peripheral sound processing. Therefore, two smart acoustic sensor system concepts were created, prototyped and validated theoretically and experimentally as the main outcomes of this Ph.D. research work.

One of the concepts presented is referred as **Frequency Agile Tuning**. This concept is based on the assumption that a front-end acoustic receiver such as a microphone is designed with a selective frequency response, and that is able to be dynamically adaptable showing different resonant tuning responses. A theoretical model for the sensor's resonance tuning response was developed following the fundamental basis as reported for the moth's hearing system. The concept was also prototyped using engineering techniques, which allowed the creation of an electromechanical sensor system framework applied to real-time signal processing environments as follows:

- A front-end acoustic receiver was fabricated using off-the-shelf materials namely, a thin Kapton membrane glued on top of a PZT stack device. This purpose-built acoustic receiver was capable of detecting and transducing sound into electrical signals through an optical readout method, whilst actuating on its piezoelectric functionalities to enable the creation of frequency agile tuning responses as similarly seen in the ears of certain moths;

- A back-end computational system setup was designed exploiting bio-inspired mechanisms based on the *Mechanoreceptor cells role* and *Neuronal cells role* to process sensory signals. Therefore, an *Adapting Control System* algorithm was presented and designed to be executed within an embedded system experimental setup, while providing results from real-time signal processing tasks.

Additionally, another smart acoustic sensor system concept was presented and

that is referred as **Active Nonlinear Amplification**. This is a bio-inspired concept based on the active processes within the mosquito's hearing system thought to be based on parametric amplification. The assumption is that the acoustic responsiveness of a front-end acoustic receiver can be adapted by exploiting the presence of fast-feedback processes injecting synchronized energy into it. A theoretical model was developed exploiting feedback computational mechanisms based on an efficient neuronal model known as a LIF neuron. The LIF model was used as a smart generator of pulses to be entrained with the front-end acoustic receiver's response within a positive feedback closed-loop system. A back-end computational system setup was prototyped using embedded system techniques, which was capable of providing a selective, nonlinear compressive gain, and hysteretic responses of a custom-made front-end acoustic sensor (e.g., MEMS microphone) from input sound signals applied to it.

Thirdly, both concepts are thought to be unconventional but advantageous techniques of signal processing achieved at the sensor level, which can be used to adapt the response of an acoustic receiver, for instance to track signals of interest. Therefore, an acoustic signal processing framework integrating a functional prototype system was proposed and prototyped to support the concepts of frequency agile tuning and active nonlinear amplification, including several sensor and system requirements that are thought to be compatible with real world system applications as the following outlines:

- Exploiting the use of recent micro fabrication techniques such as MEMS in the design of a new miniaturised microphone;
- A MEMS microphone was designed that includes sensing and actuation techniques compatible with standard sensing and actuation methodologies such as piezoelectric and capacitive, respectively;
- The MEMS microphone was designed and fabricated to ensure a high Q-

factor response and selectable resonance frequency within the audio range such as $Q = 30$ and $f_0 = [3.3 – 4.4]$ kHz, respectively, as a key innovation provided by this study;

- A new embedded system framework was created and designed using recent engineering techniques and electronic devices (e.g., ARM Cortex-M4 based computational unit) to enable efficient real-time sensor signal processing operations such as exploiting bio-inspired algorithms based on simple neuronal model computations (e.g., LIF neuronal model);

- The circuits and systems designed to support the study are meant to be in-line with state-of-the-art on circuit design techniques.

Additionally, the frequency agile tuning and active nonlinear amplification capabilities were embedded in an acoustic sensor system platform with the aim to create a MEMS microphone framework to bring forward a novel methodology for acoustics signal processing for real-time applications. Nevertheless, it is suggested for the future work that a combination of multiple adaptive smart acoustic sensors of this type can be placed in an array fashion in order to address the detection and processing of complex acoustic signals.

The technological assumption is the following: if microphones can be designed to be sensitive only at selected frequencies of interest, whilst also allowing frequency agility and adaptable sensitivities in order to track and filter specific features of interest - they have the potential to benefit a signal processing task with sophisticated signal-detection methods, low-power system consumption and reduced latency on real-time operations. Therefore, improving computational efficiency and/or accuracy in some acoustic applications such as required by wearable devices, hearing aids and cochlear implant systems, or in ultrasonic non-destructive evaluation/testing system applications.

Bibliography

[1] D. A. Russel, "Radiation from a monopole source," tech. rep., The Pennsylvania State University, 8 2001. Sound Fields Radiated by Simple Sources - Acoustics and Vibration Animations.

[2] M. F. Bear, B. W. Connors, and M. A. Paradiso, *Neuroscience: Exploring the Brain.* Wolters Kluwer, 4^{th} Edition, 2016.

[3] R. F. Lyon, *Human and Machine Hearing: Extracting Meaning from Sound.* Cambridge University Press, 2018.

[4] Breedlove, Watson, and Rosenzweig, *Biological Psychology,* 6^{th} *Edition.* Sinauer Associates, 2003.

[5] A. R. Palmer and I. J. Russel, "Phase-locking in the cochlear nerve of the guinea-pig and its relation to the receptor potential of inner hair-cells," *Hearing Research*, vol. 24, no. 1, pp. 1–15, 1986.

[6] M. E. Novis and Y. Ma, "Neurons & synapses." Emaze, 2018.

[7] G. W. Jenkins and G. J. Tortora, *Anatory and Physiology: From Science to Life,* 3^{rd} *Edition.* John Wiley & Sons, Inc., 2013.

[8] R. C. Law, "Volley theory." Wikipedia, November 2016. (contribution).

[9] J. F. C. Windmill and J. C. Jackson, *Mechanical Specializations of Insect Ears. In: Insect Hearing.* Springer Handbook of Auditory Research, 2016.

[10] J. F. C. Windmill, J. C. Jackson, E. J. Tuck, and D. Robert, "Keeping up with bats: Dynamic auditory tuning in a moth," *Current Biology*, vol. 16, no. 24, pp. 2418–2423, 2006.

[11] K. Fish, T. Schwalger, B. Linder, A. V. M. Herz, and J. Benda, "Channel noise from both slow and adaptation currents and fast currents is required to explain spike-response variability in a sensory neuron," *The journal of Neuroscience*, vol. 32, no. 48, pp. 17332–17344, 2012.

[12] J. C. Jackson, J. F. C. Windmill, V. G. Pook, and D. Robert, "Synchrony through twice-frequency forcing for sensitive and selective auditory processing," *PNAS*, vol. 106, no. 25, pp. 10177–10182, 2009.

[13] D. Avitabile, M. Homer, A. R. Champneys, J. C. Jackson, and D. Robert, "Mathematical modelling of the active hearing process in mosquitoes," *J. R. Soc. Interface*, vol. 7, pp. 105–122, 2010.

[14] J. Tiete, F. Domínguez, B. da Silva, A. Touhafi, and K. Steenhaut, "Mems microphones for wireless applications," *Wireless MEMS Networks and Applications, Elsevier Ltd.*, vol. 117, no. 195, 2017.

[15] "Acoustic mems and audio solutions," tech. rep., Yole Developpement, 4 2017. www.yole.fr - www.i-micronews.com.

[16] C. Lie and V. B. Mungurwadi, *Foundation of MEMS 2nd ed., International ed.* Upper Saddle River, N. J.: Prentice Hall, 2012.

[17] R. J. Littrell, *High Performance Piezoelectric MEMS Microphones*. PhD thesis, University of Michigan, USA, 2010.

[18] D. Hah, P. R. Patterson, H. D. Nguyen, H. Toshiyoshi, and M. C. Wu, "Theory and experiments of angular vertical comb drive actuators for scanning

micromirrors," *IEEE Journal of Selected Topics in Quantum Electronics*, vol. 10, no. 3, pp. 505–513, 2004.

[19] W. Cui, S. Q. Miles, R. N., and D. Homentcovsci, "A bio-inspired miniature comb sense differential microphone diaphragm," *Proceedings on the ASME 2010 International Mechanical Engineering Congress & Exposition IMECE2010*.

[20] J. F. Dickson, "On-chip high-voltage generation in mnos integrated circuits using an improved voltage multiplier technique," *IEEE Journal of Solid-State Circuits*, vol. 11, no. 3, pp. 374–378, 1976.

[21] J. C. Jackson, *Experimental and theoretical investigations into the active nonlinear processes of mosquitoes audition*. PhD thesis, School of Biological Sciences, University of Bristol, 2007.

[22] S. Brand, T. Appenroth, F. Naumann, W. Steller, M. J. Wolf, P. Czurratis, F. Altmann, and M. Petzold, "Acoustic ghz-microscopy and its potential applications in 3d-integration technologies," *Proceedings on IEEE Electronic Components and Technology Conference*, 2015.

[23] L. E. Kinsler, A. R. Frey, A. B. Coppens, and J. V. Sanders, *Fundamentals of Acoustics,* 4^{th} *Edition*. John Willey & Sons, 2000.

[24] T. D. Rossing, *Springer Handbook of Acoustics,* 2^{nd} *Edition*. Springer-Verlag New York, 2014.

[25] J. Schnupp, I. Nelken, and A. King, *Auditory Neuroscience: Making Sense of Sound*. The MIT Press, 2012.

[26] G. M. Ballou, *Handbook for Sound Engineers,* 5^{th} *Edition*. Focal Press, 2015.

[27] R. H. Wiley and D. G. Richards, "Physical constraints on acoustic communication in the atmosphere: Implications for the evolution of animal vocalizations," *Behav. Ecol. Sociobiol.*, vol. 3, pp. 69–94, 1978.

[28] C. M. Harris, "Absorption of sound in air versus humidity and temperature," *NASA Contractor Report*, January 1967.

[29] V. E. Ostashev and D. K. Wilson, "Formulation of sound propagation and scattering in forests as a radiative transfer theory," *Journal of the ASA*, vol. 140, no. 3194, 2016.

[30] B. C. J. Moore, *An introduction to the physiology of hearing.* Emerald Group Publisher, 6^{th} Edition, 2012.

[31] D. D. Yager, "Structure, development, and evolution of insect auditory systems," *Microscopy Research and Techniques*, vol. 47, no. 6, pp. 380–400, 1999.

[32] G. A. Manley, A. N. Lukashkin, P. Simões, G. W. S. Burwood, and I. Russel, "The mammalian ear: Physics and the principles of evolution," *Acoustics Today Spring*, vol. 4, no. 1, pp. 8–16, 2018.

[33] K. D. Roeder, "Aspects of the noctuid tympanic nerve response having significance in the avoidance of bats," *Journal of Insects Physiology*, vol. 10, no. 4, pp. 529–532, 1964.

[34] W. Bialek, *Biophysics – searching for principles.* Princeton University Press, 2012.

[35] H. Kurokawa and R. L. Goode, "Sound pressure gain produced by the human middle ear," *Otolaryngol. Head Neck Surg.*, vol. 113, no. 4, pp. 349–355, 1995.

[36] G. v. Békésy, *Experiments in hearing*. New York: McGraw-Hill, 1960.

[37] D. Purves, G. J. Augustine, D. Fitzpatrick, W. C. Hall, A. LaMantia, and L. E. White, *Neuroscience,* 5^{th} *Edition*. Sinauer Associates, 2018.

[38] S. Mukerji, A. M. Windsor, and D. J. Lee, "Auditory brainstem circuits that mediate the middle ear muscle reflex," *Trends in Amplification*, vol. 14, no. 3, pp. 170–191, 2010.

[39] D. Pérez-González and M. S. Malmierca, "Adaptation in the auditory system: an overview," *Frontier in Integrative Neuroscience*, vol. 8, no. 19, 2010.

[40] A. Møller, *The Acoustic Middle Ear Muscle Reflex. In: Auditory System. Handbook of Sensory Physiology*, vol. 5. Springer, Berlin, Heidelberg, 1974.

[41] A. J. Hudspeth, "Making an effort to listen: Mechanical amplification in the ear," *Neuron*, vol. 59, no. 4, pp. 530–545, 2008.

[42] D. Kemp, "Otoacoustic emissions," *Encyclopedia of Neuroscience*, pp. 317–326, 2009.

[43] C. Liu, E. Glowatzki, and P. A. Fuchs, "Unmyelinated type ii afferent neurons report cochlear damage," *Proc. Natl Acad. Sci. USA*, vol. 112, no. 47, pp. 14723–14727, 2015.

[44] J. J. Guinan, "Olivocochlear efferents: anatomy, physiology, function, and the measurement of efferent effects in humans," *Ear & Hearing*, vol. 27, no. 6, pp. 589–607, 2006.

[45] C. A. Mead, "Neuromorphic electronic system," *Proceedings on IEEE*, vol. 78, no. 10, pp. 1629–1636, 1990.

[46] R. Sarpeshkar, *Efficient Precise Computation with Noisy Components: Extrapolating From an Electronic Cochlea to the Brain*. PhD thesis, California Institute of Technology, Pasadena, California, April 1997.

[47] C. E. Shannon, "Communication in the presence of noise," *Proceedings of the IEEE*, vol. 86, no. 2, pp. 447 – 457, 1998.

[48] R. Sarpeshkar, "Analog versus digital: Extrapolating from electronics to neurobiology," *Neuronal Computation*, vol. 10, no. 7, pp. 1601–1638, 1998.

[49] L. A. Jeffress, "A place theory of sound localization," *Journal of Comparative and Physiological Psychology*, vol. 41, no. 1, pp. 35–39, 1948.

[50] A. A. Faisal, L. P. J. Selen, and W. D. M., "Noise in the nervous system," *Nature Reviews Neuroscience*, vol. 9, no. 4, pp. 292–303, 2008.

[51] A. W. Bronkhorst, "The cocktail-party problem revised: early processing and selection of multi-talker speech," *Atten. Percept. Psychophys.*, vol. 77, no. 5, pp. 1465–1487, 2015.

[52] K. Dierkes, B. Lindner, and F. Jülicher, "Enhancement of sensitivity gain and frequency tuning by coupling of active hair bundles," *PNAS*, vol. 105, no. 48, pp. 18669–18674, 2008.

[53] D. Robert and R. R. Hoy, *Auditory Systems in Insects. In: Invertebrate Neurobiology*, vol. 49. Cold Spring Harbor Laboratory Press, 2007.

[54] G. S. Pollack, A. C. Mason, A. N. Popper, and R. R. Fay, *Insect Hearing*. Springer Handbook of Auditory Research, 2016.

[55] D. Robert, N. Mhatre, and T. McDonagh, "The small and smart sensors of insect auditory systems," *Proceedings of IEEE Sensors*, 2010.

[56] H. M. Moir, J. C. Jackson, and J. F. C. Windmill, "Extremely high frequency sensitivity in a 'simple' ear," *Biology Letters*, vol. 9, no. 4, 2013.

[57] J. Guerreiro, J. C. Jackson, and J. F. C. Windmill, "Simple ears inspire frequency agility in an engineered acoustic sensor system," *IEEE Sensors Journal*, vol. 17, no. 22, pp. 7298–7305, 2017.

[58] J. C. Jackson and D. Robert, "Nonlinear auditory mechanism enhances female sounds for male mosquitoes," *PNAS*, vol. 103, no. 45, pp. 16734–16739, 2006.

[59] D. Avitabile, M. Homer, J. C. Jackson, D. Robert, and A. R. Champneys, "Modelling the active hearing process in mosquitoes," *AIP Conference Proceedings*, vol. 1403, pp. 447–452, 2011.

[60] M. Andrés, M. Seifert, C. Spalthoff, B. Warren, L. Weiss, D. Giraldo, M. Winkler, S. Pauls, and M. C. Göpfert, "Auditory efferent system modulates mosquito hearing," *Cell Press, Current Biology*, vol. 26, no. 15, pp. 2028–2036, 2016.

[61] N. Mhatre and D. Robert, "A tympanal insect ear exploits a critical oscillator for active amplification and tuning," *Cell Press, Current Biology*, vol. 23, no. 19, pp. 1952–1957, 2013.

[62] A. L. Hodgkin and A. F. Huxley, "A quantitative description of membrane current and its application to conduction and excitation in nerve," *Journal of Physiol.*, vol. 117, pp. 500–544, 1952.

[63] A. A. Lazar, "Time encoding with an integrate-and-fire neuron with a refractory period," *Neurocomputing*, vol. 58, no. 60, pp. 53–58, 2004.

[64] E. M. Izhikevich, "Simple model of spiking neurons," *IEEE Trans. Neural Netw.*, vol. 14, no. 6, pp. 1569–1572, 2003.

[65] E. A. Lopez-Poveda and A. Eustaquio-Martin, "A biophysical model of the inner hair cell: The contribution of potassium currents to peripheral auditory compression," *JARO*, vol. 7, pp. 218–235, 2006.

[66] M. Rudnicki, O. Schoppe, M. Isik, F. Volk, and W. Hemmert, "Modelling auditory coding: from sound to spikes," *Springer, Cell Tissue Res.*, vol. 361, pp. 159–175, 2015.

[67] J. Guerreiro, A. Reid, J. C. Jackson, and J. F. C. Windmill, "Active hearing mechanisms inspire adaptive amplification in an acoustic sensor system," *IEEE Transactions on Biomedical Circuits and Systems*, vol. 12, no. 3, pp. 655–664, 2018.

[68] M. J. Skocik and L. N. Long, "On the capabilities and computational costs of neurons," *IEEE Trans. Neural Netw. Learn. Syst.*, vol. 25, no. 8, pp. 1474–1483, 2014.

[69] P. Loizou, "Mimicking the human ear," *IEEE Signal Process. Mag.*, vol. 15, no. 5, pp. 101–130, 1998.

[70] B. S. Wilson and M. F. Dorman, "Cochlear implants: A remarkable past and brilliant future," *Hearing Research*, vol. 242, no. 1-2, pp. 3–21, 2008.

[71] R. Sarpeshkar, R. F. Lyon, and C. A. Mead, "A low-power wide-dynamic-range analog vlsi cochlea," *Analog Integrated Circuits Signal Process.*, vol. 16, pp. 245–274, 1998.

[72] M. W. Baker and R. Sarpeshkar, "Low-power single-loop and dual-loop agcs for bionic ears," *IEEE Journal of Solid-State Circuits*, vol. 41, no. 9, p. 1983 – 1996, 2006.

[73] S. Wang, T. J. Koickal, G. Enemali, L. Gouveia, L. Wang, and A. Hamilton,

"Design of a silicon cochlea system with biologically faithful response," *Proceedings on IEEE IJCNN*, p. 1 – 7, 2015.

[74] E. Farquhar and P. Hasler, "A bio-physically inspired silicon neuron," *IEEE Transactions on Circuits and Systems – I Regular Papers*, vol. 52, no. 3, pp. 477 – 488, 2005.

[75] S. Wang, T. J. Koickal, A. Hamilton, E. Mastropaolo, R. Cheung, A. Abel, L. S. Smith, and L. Wang, "A power-efficient capacitive read-out circuit with parasitic-cancellation for mems cochlea sensors," *IEEE Transactions on Biomedical Circuits and Systems*, vol. 10, no. 1, p. 25 – 37, 2016.

[76] L. Wang, T. J. Koickal, A. Hamilton, E. Mastropaolo, R. Latif, R. Cheung, M. Newton, and L. S. Smith, "A low-noise interface circuit for mems cochlea-mimicking acoustic sensors," *Proceedings on IEEE ISCAS*, pp. 1151–1154, 2012.

[77] R. Fakoor, X. He, I. Tashev, and S. Zarar, "Reinforcement learning to adapt speech enhancement to instantaneous input signal quality," Proceedings on 31^{st} Conference on Neural Information Processing Systems, Long Beach, CA, USA, 2017.

[78] C. Breithaupt and R. Martin, "Statistical analysis and performance of dft domain noise reduction filters for robust speech recognition," pp. 365–368, Proceedings 9^{th} ICSP, 2006.

[79] Z. Zhang, J. Geiger, J. Pohjalainen, A. E. Mousa, W. Jin, and B. Schuller, "Deep learning for environmentally robust speech recognition: An overview for recent developments," *Journal ACM Transactions on Intelligent Systems and Technology*, vol. 9, no. 5, 2018.

[80] A. Wang, "The shazam music recognition service," *Communications of the ACM*, vol. 49, pp. 44–48, 2006.

[81] A. Wang, "An industrial strength audio search algorithm," *Proceedings on International Society for Music Information Retrieval (ISMIR) Conference*, 2003.

[82] Z. Wu and Z. Cao, "Improved mfcc-based feature for robust speaker identification," *Tsinghua Science and Technology*, vol. 10, pp. 158–161, 2005.

[83] J. M. Kates, *Digital Hearing Aids*. Plural Publishing, Inc., 2008.

[84] C. D. Salthouse and R. Sarpeshkar, "Jump resonance: A feedback viewpoint and adaptive circuit solution for low-power active analog filters," *IEEE Trans. Circuits and Systems*, vol. 53, no. 8, pp. 1712–1725, 2006.

[85] K. Aono et al., "Exploiting jump-resonance hysteresis in silicon auditory front-ends for extracting speaker discriminative formant trajectories," *IEEE Trans. Biomedical Circuits and Systems*, vol. 7, no. 4, pp. 389–400, 2013.

[86] T. Rodriguez and R. Garcia, "Theory of q control in atomic force microscopy," *Applied Physics Letters*, vol. 82, no. 26, pp. 4821–4823, 2003.

[87] H. S. R. A. Prakash, G. and R. Reifenberger, "Theoretical basis of parametric-resonance-based atomic force microscopy," *Phys. Rev. B*, vol. 79, no. 094304, 2009.

[88] W. M. Waters and G. Linde, "Frequency-agile radar signal processing," *IEEE Transactions on Aerospace and Electronic Systems*, vol. 15, no. 3, pp. 459–464, 1979.

[89] R. Sarpeshkar, *Ultra-Low Power Bioelectronics: Fundamentals, Biomedical Applications, and Bio-Inspired Systems*. Cambridge University Press, 2010.

[90] A. Dehé, M. Wurzer, M. Füldner, and U. Krumbein, "The infineon silicon mems microphone," *Proceedings on AMA Conference*, 2013.

[91] J. Lewis and B. Moss, "Mems microphones, the future for hearing aids," *Analog Dialogue*, vol. 47, no. 11, 2013.

[92] G. E. Moore, "Cramming more components onto integrated circuits," *IEEE Solid-States Circuits Society Newsletter*, vol. 11, no. 3, 2006. Reprinted from Electronics. Vol. 38, no. 8, 1965.

[93] G. W. Elko, F. Pardo, D. Lopez, D. Bishop, and P. Gammel, "Capacitive mems microphone," *Bell Labs Technical Journal*, vol. 10, no. 3, pp. 187–198, 2005.

[94] P. R. Scheeper, A. G. H. van der Donk, W. Olthusis, and P. Bergveld, "A review of silicon microphones," *Sensor and Actuators*, 1994.

[95] J. Bergquist, F. Rudolf, J. Maisana, F. Parodi, and M. Rossi, "A silicon condenser microphone with a highly perforated backplate," *Intern. Conf. on Solid-State Sensors and Actuators, Dig. Tech. Papers*, p. 266–269, 1991.

[96] G. M. Sessler and J. E. West, "Self-biased condenser microphone with high capacitance," *J. Acoust. Soc. Am.*, vol. 34, pp. 1787–1788, 1962.

[97] D. Hohm and G. M. Sessler, "An integrated silicon-electret condenser microphone," *Proceedings on 11th Intern. Congr. Acoust.*, vol. 6, pp. 29–32, 1983.

[98] "Infineon application note: An558 v1.0 2018-01-16," 2018.

[99] S. Chowdhury, M. Ahmadi, and W. C. Miller, "Nonlinear effects in mems capacitive microphone design," *Proceedings on International Conference on MEMS, NANO and Smart Systems (ICMENS'03)*, 2003.

[100] J. Segovia-Fernandez, S. Sonmezoglu, S. T. Block, Y. Kusano, J. M. Tsai, R. Amirtharajah, and D. A. Horsley, "Monolithic piezoelectric aluminum

nitride mems-cmos microphone," *Proceedings on IEEE Solid-state Sensors, Actuators and Microsystems Conference*, 2017.

[101] Y. Zhang, R. Bauer, J. F. C. Windmill, and D. Uttamchandani, "Multi-band asymmetric piezoelectric mems microphone inspired by the ormia ochracea," *Proceedings on IEEE 29th Intern. Conf. on MEMS*, 2016.

[102] I. Patel, "Ceramic based intelligent piezoelectric energy harvesting device," *Advances in Ceramics - Electric and Magnetic Ceramics, Bioceramics, Ceramics and Environment*, 2011.

[103] J. F. C. Windmill, A. Zorab, D. J. Bedwell, and D. Robert, "Nanomechanical and electrical characterization of a new cellular electret sensor-actuator," *Nanotechnology*, vol. 19, no. 3, 2008.

[104] J. Jung, W. Lee, W. Kang, E. Shin, J. Ryu, and H. Choi, "Review of piezoelectric micromachined ultrasonic transducers and their applications," *Journal of Micromechanics and Microengineering*, vol. 27, no. 113001, 2017.

[105] "Vesper technologies, inc.," 2018. http://vespermems.com/. Accessed 29 Jan 2018.

[106] D. Damjanovic, "Hysteresis in piezoelectric and ferroelectric materials," *The Science of Hysteresis, Elsevier Inc.*, vol. 3, pp. 337–465, 2005.

[107] C. Wang, K. Lau, and Q. Wang, "Dynamic hysteresis and scaling behaviours of lead-free 0.94bi0.5na0.5tio3–0.06batio3 bulk ceramics," *RSC Adv.*, vol. 6, no. 30148, 2016.

[108] F. Mateen, J. Boales, S. Erramilli, and P. Mohanty, "Micromechanical resonator with dielectric nonlinearity," *Nature Microsystems & Nanoengineering*, vol. 4, no. 14, 2018.

[109] J. Lewis, "Understanding microphone sensitivity," *Analog Dialogue 46-05 Back Burner*, 2002.

[110] V. Tarnow, "The lower limit of detectable sound pressures," *Journal of the Acoustical Society of America*, vol. 82, pp. 379–381, 1987.

[111] T. B. Gabrielson, "Mechanical-thermal noise in micromachined acoustic and vibration sensors," *IEEE Transactions on Electron Devices*, vol. 40, no. 5, pp. 903–909, 1993.

[112] J. B. Johnson, "Thermal agitation of electricity in conductors," *Physical Review*, vol. 32, pp. 97–109, 1928.

[113] H. Nyquist, "Thermal agitation of electric charge in conductors," *Physical Review*, vol. 32, pp. 110–113, 1928.

[114] M. Vorlander, *Acoustic Measurements, In: Handbook of Engineering Acoustics*. Springer, 2013.

[115] R. L. S. Pierre and D. J. Maguire, "The impact of a-weighting sound pressure level measurements during the evaluation of noise exposure," *Proceedings on NOISE-CON*, 2004.

[116] A. Kamenov, *Digital Signal Processing for Audio Applications*. 2014.

[117] M. Pedersen, W. Olthuis, and P. Bergveld, "High-performance condenser microphone with fully integrated cmos amplifier and dc-dc voltage converter," *Journal of Microelectromechanical Systems*, vol. 7, no. 4, pp. 387–394, 1998.

[118] F. A. Levinson, "Ultra-low-noise high-input impedance amplifier for low-frequency measurement applications," *IEEE Transactions on Circuits and Systems I*, vol. 55, no. 7, pp. 1815–1822, 2008.

[119] T. Starecki, "Analog front-end circuitry in piezoelectric and microphone detection of photoacoustic signals," *Int. J. Thermophys., Springer*, vol. 35, no. 11, pp. 2124–2139, 2014.

[120] S. Peng, M. S. Qureshi, P. E. Hasler, A. Basu, and F. L. Degertekin, "A charge-based low-power high-snr capacitive sensing interface circuit," *IEEE Transactions on Circuits and Systems – I: Regular Papers*, vol. 55, no. 7, 2008.

[121] M. Garcia-Rodriguez, J. Garcia-Alvarez, Y. Yanez, M. J. Garcia-Hernandez, J. Salazar, A. Turo, and J. A. Chavez, "Low cost matching network for ultrasonic transducers," *Proceedings on International Congress on Ultrasonics, Elsevier Procedia*, 2009.

[122] L. Jerad, "Analog and digital mems microphone design considerations," *Technical Article MS-2472, Analog Devices, Inc.*, 2013.

[123] W. Cui, S. A. Jones, R. N. Miles, F. L. Degertekin, N. Hall, and B. Bicen, "Optical sensing in a directional microphone inspired by the ears of the parasitoid fly, ormia ochracea," *Proceedings on 19th IEEE Conference on MEMS*, 2006.

[124] R. N. Miles, Q. Su, W. Cui, M. Shetye, F. L. Degertekin, B. Bicen, C. Garcia, S. Jones, and N. Hall, "A low-noise differential microphone inspired by the ears of the parasitoid fly ormia ochracea," *Journal of Acoust. Soc. Am.*, vol. 125, no. 4, pp. 2013–2026, 2009.

[125] V. P. Jaecklin, C. Linder, N. F. de Rooij, and J. M. Moret, "Micromechanical comb actuators with low driving voltage," *Journal of Micromechanics and Microengineering*, vol. 2, no. 4, pp. 250–255, 1992.

[126] S. Gupta, T. Pahwa, R. Narwal, B. Prasad, and D. Kumar, "Optimizing

the performance of mems electrostatic com drive actuator with different flexure springs," *Proceedings on COMSOL Conference*, 2012.

[127] A. H. Alameh, A. Robichaud, and F. Nabki, "A reconfigurable charge pump in 0.13 μm cmos for agile mems actuation," *Proceedings on 21st IEEE International Conference on Electronics, Circuits and Systems*, vol. 11, no. 3, pp. 374–378, 1976.

[128] A. Chaigne, *Structural Acoustics and Vibrations.In: Handbook of Acoustics, 2nd Edition.* Springer, 2014.

[129] A. C. Serra, F. Alegria, R. Martins, and M. F. da Silva, "Analog-to-digital converter testing: new proposals," *Elsevier New Trends in ADC Testing and Modelling*, vol. 26, no. 1, pp. 3–13, 2004.

[130] R. Domingo-Roca, J. C. Jackson, and J. F. C. Windmill, "Bioinspired 3d-printed piezoelectric device for acoustic frequency separation," *Proceedings on IEEE Sensors Conference*, 2017.

[131] H. V. Vargas, E. Wu, R. N. Miles, and J. Qu, "Robust control design for resonance damping of a directional microphone," *Proceedings of 17th World Congress The International Federation of Automatic Control, Seoul, Korea*, pp. 4424–4429, 2008.

[132] E. Wu, R. N. Miles, and J. Huang, "Robust control design for resonance damping of a directional microphone," *American Control Conference, Marriott Waterfront, Baltimore, MD, USA*, pp. 3415–3422, 2010.

[133] A. Pikovsky, M. Rosenblum, and J. Kurths, *Synchronization: A Universal Concept in Nonlinear Sciences.* Cambridge Univ. Press, 2001.

[134] T. A. J. Duke and F. Jülicher, "Critical oscillators as active elements

in hearing. in: Active processes and otoacoustic emissions in hearing," *Springer Handbook of Auditory Research*, vol. 30, pp. 63–92, 2007.

[135] P. M. Simoes, R. A. Ingham, G. Gibson, and I. J. Russel, "A role for acoustic distortion in novel rapid frequency modulation behaviour in free-flying male mosquitoes," *Journal of Experimental Biology*, vol. 219, p. 2039 – 2047, 2016.

[136] C. G. Langton, "Computing at the edge of chaos: phase transitions and emergent computation," *Physics D.*, vol. 42, p. 12–37, 1990.

[137] R. N. Miles and R. R. Hoy, "The development of a biologically-inspired directional microphone for hearing aids," *Audiology Neurotology*, vol. 11, no. 2, pp. 86–94, 2004.

[138] A. Reid, J. F. C. Windmill, and D. Uttamchandani, "Bio-inspired sound localization sensor with high directional sensitivity," *Elsevier Procedia Engineering*, vol. 120, pp. 289–293, 2015.

[139] Y. Zhang, R. Bauer, J. C. Jackson, W. M. Whitmer, J. F. C. Windmill, and D. Uttamchandani, "A low-frequency dual-band operational microphone mimicking the hearing properties of ormia ochracea," *Journal of Microelectromechanical Systems*, vol. 99, pp. 1–10, 2018.

[140] B. Cordell, "Low-noise dual monolithic jfet," tech. rep., 2017. LSK489 Application Note.

[141] G. Alexandrov and N. Carter, "Some tips on making a fetching discrete amplifier," *Analog Dialogue*, vol. 47, no. 10, pp. 1–10, 2013.

[142] P. Horowitz and W. Hill, *The Art of Electronics, 3rd Edition.* Cambridge Univ. Press, 2015.